STRUCTRE OF SUPERDEFORMED BANDS NEAR THE N=80 SHELL GAP

By

GREG HACKMAN, B.Sc.

A Thesis
Submitted to the School of Graduate Studies
in Partial Fulfillment of the Requirements
for the Degree
Doctor of Philosophy

McMaster University

SUPERDEFORMED BANDS NEAR N=80

Doctor of Philosophy (1995) McMaster University
(Physics) Hamilton, Ontario

TITLE: Structure of Superdeformed Bands
Near the N=80 Shell Gap

AUTHOR: Greg Hackman, B.Sc., University of Alberta

SUPERVISOR: Professor J.C. Waddington

NUMBER OF PAGES: xvi, 245

Abstract

As part of a systematic survey of superdeformation in nuclei in the vicinity of ^{143}Eu, six superdeformed bands in ^{142}Sm, ^{142}Eu and ^{144}Eu have been studied by their γ–ray decay following heavy-ion fusion-evaporation reactions. All of these bands are based on a "second minimum" shell gap associated with the superdeformed (2:1 prolate ellipsoid of rotation) nuclear shape at neutron number N=80 and proton number Z=63. The first band in ^{142}Sm and the band in ^{142}Eu have been studied with the 8π spectrometer, while the bands in ^{144}Eu and the excited band in ^{142}Sm have been discovered with the GAMMASPHERE array. The γ–ray decays of these superdeformed structures are compared to collective rotational models, and specifically to state-of-the-art Cranked Shell Model (CSM) calculations for Nilsson, Woods-Saxon, and Hartree-Fock models of the nuclear potential. The predicted roles of specific orbitals in the $A\sim140$ mass region are compared to quantities derived from the experiments and where possible, configurations with respect to an ^{143}Eu core are proposed.

The first ^{142}Sm band consists of 19 γ-ray transitions with an intensity of 0.5% of the reaction channel, and its behaviour is best described in the calculations as an ^{143}Eu superdeformed core with a hole in an N_{osc}=5 proton orbital. The second excited band consists of 15 transitions with an intensity $\sim$ 20% that of the first band, of which the transitions above $\sim$ 1 MeV are identical in energy to those in a ^{146}Gd band. This new band, which represents the second example of a two-proton, two-neutron identical bands pair, is most likely a ^{146}Gd superdeformed core with four holes in low N_{osc} orbitals. Structures based on simple excitations of the proton hole of the first band likely comprise a quasi-continuum ridge structure.

The ^{142}Eu band has 15 transitions and an intensity of 1.2%. The detailed behavior of this band suggests that its configuration is an N_{osc}=5 neutron hole in the ^{143}Eu core. Such a configuration is not predicted to be energetically favourable.

The three ^{144}Eu bands all have population intensities of < 0.2 % relative to the reaction cross-section. Two of the ^{144}Eu bands, with 17 and 18 transitions respectively, are quite likely N_{osc}=6 neutron particle states coupled to the ^{143}Eu core. The behavior of the third band indicates occupation of an N_{osc}=7 neutron intruder which does not influence the shape of the ^{143}Eu core.

Acknowledgements

In the past four years I have enjoyed the company of many friends and colleagues who have been willing to share their wisdom and give me a good running start on a research carreer. I only hope that I can give as many of them as possible the credit they deserve.

First I thank my wife, Heather, for her patience and support, for sharing the joys of research with me, and for helping me get through some of the harder times, especially during writing-up. Without her, I don't know if I would have got through this all in one piece. Heather, I love you.

No one could ask for a better supervisor than Dr. Jim Waddington. He is a peach; kind, accessible, and infinitely reasonable. He bent over backwards to see this project through, making sure that I had the best data in the world, and access to the best resources to analyse and interpret it. His ability to see beyond the status quo and come up with ingenious new ways of looking at things were behind the novel analysis techniques developed in the course of this project. In addition to being an exceptional physicist and teacher, he's a good friend, and I thank him and Sue for making us feel welcome in their home.

One of the better choices Jim made in his carreer was to hire Dr. Simon Mullins as a research associate. Simon arrived at McMaster roughly the same time I did, and promptly began to teach me everything he knew about the cranked shell model, cricket and Deep Purple. This thesis reflects a portion of the much larger project envisioned and led by Simon, and it's been a pleasure working with him on it. I also thank him for introducing me to the varied and many characters in the business, often well before I ever met them in person.

I've also made friends amongst my fellow graduate and undergraduate students, namely Ahmed, Leif, Johnny Nimbin, Guillame, Carl and Jamie at McMaster and Jim and Mario at Toronto, and with M. le prof Stephane Flibotte and Dr. Jon

Wilson. Special mention goes to Daniel Prevost and Dean Haslip. Daniel taught me everything I ever wanted to know about the computers or swearing in French. I value his friendship and I hope we can work together again somewhere down the line. The only way to describe Dean is, "He's good." As an undergraduate summer student, he accomplished more than some graduate students ever will. ANDband is his baby, and I (and the whole community) owe him, big-time.

Much of the experimental work was done at Chalk River. In addition to thanking the operators and crew for providing beams, I also thank David Ward for guidance in philosophy, natural and otherwise. When it comes to gamma rays, I don't think there's too many rocks he hasn't turned over. I thank him for sharing his vast experience and wisdom, and also for often-entertaining discussions about life, the universe, and everything. I also thank David Radford for sharing his expertise on analysis (that is, fixing my level scheme), and for Radware in general.

This project benefited enormously from associations with international collaborators. Gracious thanks to Dr. Bob Wadsworth for leading the ^{142}Sm GAMMASPHERE experiment and inviting the McMaster delegation to participate. Thanks to the operations crew of the 88-inch cyclotron of Lawrence Berkeley Laboratories, and to the all the members of the GAMMASPHERE team at LBL, especially Dr. Augusto Machiavelli for his vigilance in making sure GAMMASPHERE was in perfect working order and Dr. Rod Clark for cheerful assistance above and beyond the call of duty (what distance?). Thanks also to Drs. Jerzy Dudek and Jacek Dobaczewski for providing the HF codes prior to general release. Special thanks to Jacek for taking valuable time from his Oak Ridge visit (winter 1994) to teach me how to use the `hf46b.f` code and how to understand its output, and also for teaching me the valuable lesson, "don't always believe the Routhians."

Assorted random "thank-you"s to Dr. Bernard Haas, Wendy and everyone in the office, the Dalewood badminton gang, Neil Peart, and Honda.

Thanks to the taxpayers of Canada who, through the auspices of NSERC, found it worthwhile to provide post-graduate scholarship and travel funds for my research work.

This work is dedicated to the memory of Iris Schonert.

Table of Contents

Abstract iii

Acknowledgements v

Chapter 1:

Introduction 1

- 1.1. Fission Isomers and the Second Well 3
- 1.2. High-Spin Superdeformation 5
- 1.3. Decay Out from Superdeformed Bands 7
- 1.4. Identical Bands 9
- 1.5. Neutron Number 80 11

Chapter 2:

Theory of Superdeformed Rotational Bands 12

- 2.1. Deformed Nuclei and Rotational Behavior 12
  - 2.1.1. Quadrupole Deformation Parameters 13
  - 2.1.2. Intrinsic, Rotational and Total Angular Momenta 16
- 2.2. Deformed Nuclear Mean Fields 22
  - 2.2.1. Nilsson Model 22
  - 2.2.2. Woods-Saxon Potential 24
  - 2.2.3. Strutinsky Shell Correction 28
  - 2.2.4. Hartree-Fock method with Skyrme interaction 29
- 2.3. The Cranking Model 34
  - 2.3.1. The Cranking Hamiltonian 34
  - 2.3.2. Aligned Spin and Rotational Frequency 35
  - 2.3.3. Signature 38

2.3.4. Moments of Inertia 40
2.3.5. Effective alignment 42
2.4. Pairing 49
2.5. Pseudo-Spin 52
2.6. Population and Observation of Superdeformed States 54
2.6.1. Heavy-Ion Fusion-Evaporation Reactions 54
2.6.2. Gamma-Ray Cascades 57
2.6.3. The Magic Triangle 61

Chapter 3:

Gamma-ray Detector Arrays 65
3.1. Detection of γ–rays 65
3.1.1. Detector materials 65
3.1.2. Compton Suppression 68
3.2. The 8π Array 71
3.2.1. Detector geometry 71
3.2.2. Ge, BGO and Master Trigger Electronics 71
3.2.3. CAMAC Booster (CAB) 78
3.2.4. Computer Control, Acquisition 79
3.3. The GAMMASPHERE Array 80
3.4. Calibration 83
3.4.1. Energy calibration 83
3.4.2. Efficiency 84
3.5. X-ray absorbers 88

Chapter 4:

Experimental Results: Superdeformed Bands 90

4.1. Motivation: the $N = 80$ Shell Closure 90
  4.1.1. Shell Gaps near ^{143}Eu 90
  4.1.2. Single-particle landscape 94
  4.1.3. Total Routhian surfaces 96
  4.1.4. Spins 96
4.2. Experimental program 99
4.3. Superdeformation in ^{142}Sm 102
  4.3.1. Experiments and Data Reduction 102
  4.3.2. ^{142}Sm yrast SD band A: 8π Results 104
  4.3.3. ^{142}Sm SD band A: GAMMASPHERE results 107
  4.3.4. ^{142}Sm excited SD band B 114
  4.3.5. Quasi-continuum in ^{142}Sm 116
4.4. Superdeformation in ^{142}Eu 121
4.5. Superdeformation in ^{144}Eu 125
  4.5.1. Discovery and Assignment of ^{144}Eu SD Bands 125
  4.5.2. Intensities 130
  4.5.3. Spins 133
4.6. Search for Superdeformation in ^{141}Pm, ^{144}Sm 135
4.7. Summary 136
Chapter 5:
Interpretation: Single-Particle Structure 137
5.1. Dynamic Moments of Inertia 137
5.2. A Few Words on Hartree-Fock Calculations 141
  5.2.1. Quadrupole Constraints and Iterations 141
  5.2.2. Vacua 142

5.3. ^{142}Sm 143
    5.3.1. Yrast configuration: Band A 143
    5.3.2. Excited band: Band B 147
    5.3.3. Energetics and the Quasi-Continuum 154
    5.3.4. Conclusions for ^{142}Sm 156
5.4. ^{142}Eu 158
5.5. ^{144}Eu 162
    5.5.1. Band C Crossing: Pairing or $N_{\rm osc} = 7$ intruder? 162
    5.5.2. Anomalous Low $\mathcal{J}^{(2)}$ bands A and B 165
    5.5.3. Spins 170
5.6. Summary: Is ^{143}Eu A Suitable Core? 171

Chapter 6:

Conclusions and Future Prospects 173
6.1. Summary 173
6.2. Future Prospects 174
    6.2.1. More Bands, More Nuclei 175
    6.2.2. Spins and Parities 176
    6.2.3. Deformations and DSAM 176
    6.2.4. 2p2n Identical Bands 177

Appendix A:

Non-SD Decay Schemes 179

Appendix B:

Background Subtraction 191
B.1. The Global Operator Method 191
    B.1.1. Origin of the “Smooth” Background 191

B.1.2. Gating on γ rays and the Normalized Smooth Background ϕ 193

B.1.3. Background Operator in γ^n Coincidence Histograms 196

B.2. Background Subtraction of Gated Spectra 201

B.2.1. One $n-1$-gated spectrum 201

B.2.2. Sums of Gates 204

B.2.3. Gated Matrices 209

B.3. The Operator Method in Action 210

Appendix C:

SD Search Algorithm 216

Appendix D:

8π *vs.* GAMMASPHERE: Sensitivity 220

Appendix E:

Intensity Measurements 225

E.1. Model SD Band Intensity Profile 225

E.2. Implementation 228

Appendix F:

Symbols 231

References 234

List of Figures

Figure 1.1: Independent *vs.* Collective Behavior 2
Figure 1.1.1: Fission isomer 4
Figure 1.1.2: Deformed Harmonic Oscillator 6
Figure 1.2.1: Highlights in the history of high-spin SD 8
Figure 1.3.1: Decay Out of SD states 10
Figure 2.1.1: Schematic of β-γ deformation plane 14
Figure 2.1.2: Angular Momenta in Rotating Nuclei 18
Figure 2.1.3: Coupling limits, particle-rotor model 20
Figure 2.2.1a: Nilsson diagram, $50 \leq Z \leq 82$. 25
Figure 2.2.1b: Nilsson diagram, $82 \leq N \leq 126$. 26
Figure 2.2.2: Woods-Saxon potential 28
Figure 2.3.1: Calculated effective alignment 44
Figure 2.3.2: Experimental effective alignment 45
Figure 2.6.1: Fusion-Evaporation Reactions 56
Figure 2.6.2: Fusion barrier 57
Figure 2.6.3: γ-ray cascades from HI,xn reactions 58
Figure 2.6.4: Rotational structure in γ–γ matrix 62
Figure 2.6.5: Yrast diagram for SD states 64
Figure 3.1.1: Attenuation coefficients, detector materials 67
Figure 3.1.2: Compton suppression 69
Figure 3.1.3: 8π HPGe and Anti-Compton Shield 70
Figure 3.2.1: The 8π Spectrometer 72
Figure 3.2.2: 8π BGO electronics (part I) 74
Figure 3.2.3: 8π BGO electronics (part II) 75
Figure 3.2.4: 8π HPGe and Anti-Compton electronics 76
Figure 3.2.5: 8π Master Trigger 77
Figure 3.3.1a: GAMMASPHERE energy and master trigger electronics 81

Figure 3.3.1b: GAMMASPHERE slow trigger electronics and data flow 82
Figure 3.4.1: GAMMASPHERE ADC non-linearity 84
Figure 3.4.2: 8π efficiency calibration 86
Figure 3.4.3: GAMMASPHERE efficiency calibration 87
Figure 3.5.1: Effect of X-ray absorber on efficiency 89
Figure 4.1.1: Woods-Saxon Levels *vs.* β_2 92
Figure 4.1.2: ^{143}Eu single-particle Routhians 93
Figure 4.1.3: Cranked Woods-Saxon Levels *vs.* β_2 95
Figure 4.1.4: TRS plot for ^{143}Eu 97
Figure 4.1.5: TRS plots for ^{142}Sm, ^{142}Eu, ^{144}Eu 98
Figure 4.3.1: H and K, ^{142}Sm 8π experiment 103
Figure 4.3.2: ^{142}Sm SD band A, (8π) 106
Figure 4.3.3: ^{142}Sm SD band γ-ray spectra (GAMMASPHERE) 110
Figure 4.3.4: Clean double-gate list, ^{142}Sm band A 111
Figure 4.3.5: Intensity profile, ^{142}Sm 112
Figure 4.3.6: Decay-out, ^{142}Sm band A 113
Figure 4.3.7: Clean double-gates list, ^{142}Sm band B 115
Figure 4.3.8: SD Ridge (8π) 116
Figure 4.3.9: ^{142}Sm Ridge Structure 118
Figure 4.3.10: ^{142}Sm ridge intensity 119
Figure 4.3.11: Ridge in anti-coincidence with ^{142}Sm band A 120
Figure 4.4.1: H distributions from ^{142}Eu experiment 122
Figure 4.4.2: ^{142}Eu SD band, γ–ray spectrum 123
Figure 4.5.1a: ^{144}Eu SD band A 127
Figure 4.5.1b: ^{144}Eu SD band B 128
Figure 4.5.1c: ^{144}Eu SD band C 129
Figure 4.5.2: Clean double-gates triangles, ^{144}Eu SD bands 130
Figure 4.5.3: Intensity profile, ^{144}Eu 131
Figure 5.1.1: Dynamic M.o.I. of SD bands in vicinity of ^{143}Eu 138

Figure 5.3.1: ^{142}Sm yrast SD band (band A) dynamic M.O.I. 145
Figure 5.3.2: ^{142}Sm band B Δi_x and E 148
Figure 5.3.3: ^{146}Gd band 2 dynamic M.o.I. *vs.* HF calculations 150
Figure 5.3.4: Routhians for ^{142}Sm excited configuration 152
Figure 5.3.5: Dynamic M.o.I. of ^{142}Sm ridge structure 156
Figure 5.4.1: Calculated Energies, ^{142}Eu 159
Figure 5.4.2: Effective alignments (experimental and Nilsson), ^{142}Eu 160
Figure 5.4.3: Effective alignments (experimental and HF), ^{142}Eu 161
Figure 5.5.1: ^{144}Eu band C dynamic M.o.I. 163
Figure 5.5.2: ^{144}Eu band C Woods-Saxon M.o.I. 164
Figure 5.5.3: ^{144}Eu band C effective alignment 166
Figure 5.5.4: ^{144}Eu bands A,B dynamic M.o.I 167
Figure 5.5.5: N_{osc}=6 neutron crossings 168
Figure 5.5.6: ^{144}Eu bands A, B WS M.o.I. calculations 169
Figure 6.2.1: HF calculated proton Q_{20} values 177
Figure A.1: Typical GAMMASPHERE ^{142}Sm non-SD spectra 182
Figure A.2: Propsed (non-SD) level scheme for ^{142}Sm 186
Figure B.1.1: EI-43 LEVIT8R smooth background 194
Figure B.1.2: Simple gating example 195
Figure B.3.1: EG-II Commissioning Run: γ^4 214
Figure B.3.2: EG-II Commissioning Run: γ^5 215
Figure E.1: Schematic of intensity profile for SD bands 226

List of Tables

Table 2.3.1: Signature and Angular Momentum Quantum Numbers 39

Table 4.2.1: $A\sim140$ SD experimental studies 100

Table 4.2.2: $A\sim140$ SD experimental studies II 101

Table 4.3.1: HPGe multiplicities, GS experiments 105

Table 4.3.2: ^{142}Sm SD bands (from GAMMASPHERE) 108

Table 4.4.1: ^{142}Eu SD band, 8π 124

Table 4.5.1: ^{144}Eu SD bands (from GAMMASPHERE) 132

Table 4.7.1: Summary of experimental results, SD bands 136

Table 5.6.1: Valence Particle Configurations 172

Table 5.6.2: Configurations in terms of X, Y 172

Table A.1: $A\sim140$ level scheme, γ-ray decay references 180

Table A.2a: Non-SD γ-ray characteristics, ^{142}Sm 187

Table A.2b: (continued) 188

Table A.2c: (continued) 189

Table A.3: Alternate angular correlations, ^{142}Sm 190

Table D.1: Comparison of 8π and GAMMASPHERE sensitivities 223

Chapter 1.
Introduction

The atomic nucleus is a unique quantum system which exhibits a wide variety of behavior. In particular, the heavy nuclei, with masses on the order of one hundred times that of the hydrogen atom, exhibit a rich variety of excitation modes. The nucleon-nucleon interaction has been thoroughly studied, for example from scattering experiments or from quantum chromodynamic theory. However, the details of the strong force are of little help in understanding why, or predicting when, the nucleons in a finite nuclear system might behave as independent particles or as a collective coherent unit, cf. Figure 1.1. The intellectual challenge lies in the fact that nuclei are finite quantum systems which are too small to be statistical systems, yet are too large to be few-body systems. More precisely, the number of nucleons, A, in a heavy nucleus is small enough that the approximation $A \to \infty$ is often inappropriate, yet an exact many-body wave function would be so complicated that one could not extract useful observables.

There are two important approximations which greatly simplify the problem of nuclear structure. The first is that individual nucleons move in some sort of *mean field* generated by the rest of the nucleons in the system. For a single nucleon, its interactions with the rest of the nucleons in a heavy nucleus can be treated in a summed and averaged way as a single potential. A second approximation is to assume that the behavior of the atomic nucleus is dominated by only a few valence particles, and that the remainder of the nucleons are part of an inert fermionic core. The bulk properties of the nucleus can be described by treating this core as a quantum liquid drop, and the detailed behavior of the system can be determined by perturbations due to the valence particles whose properties are given by a shell

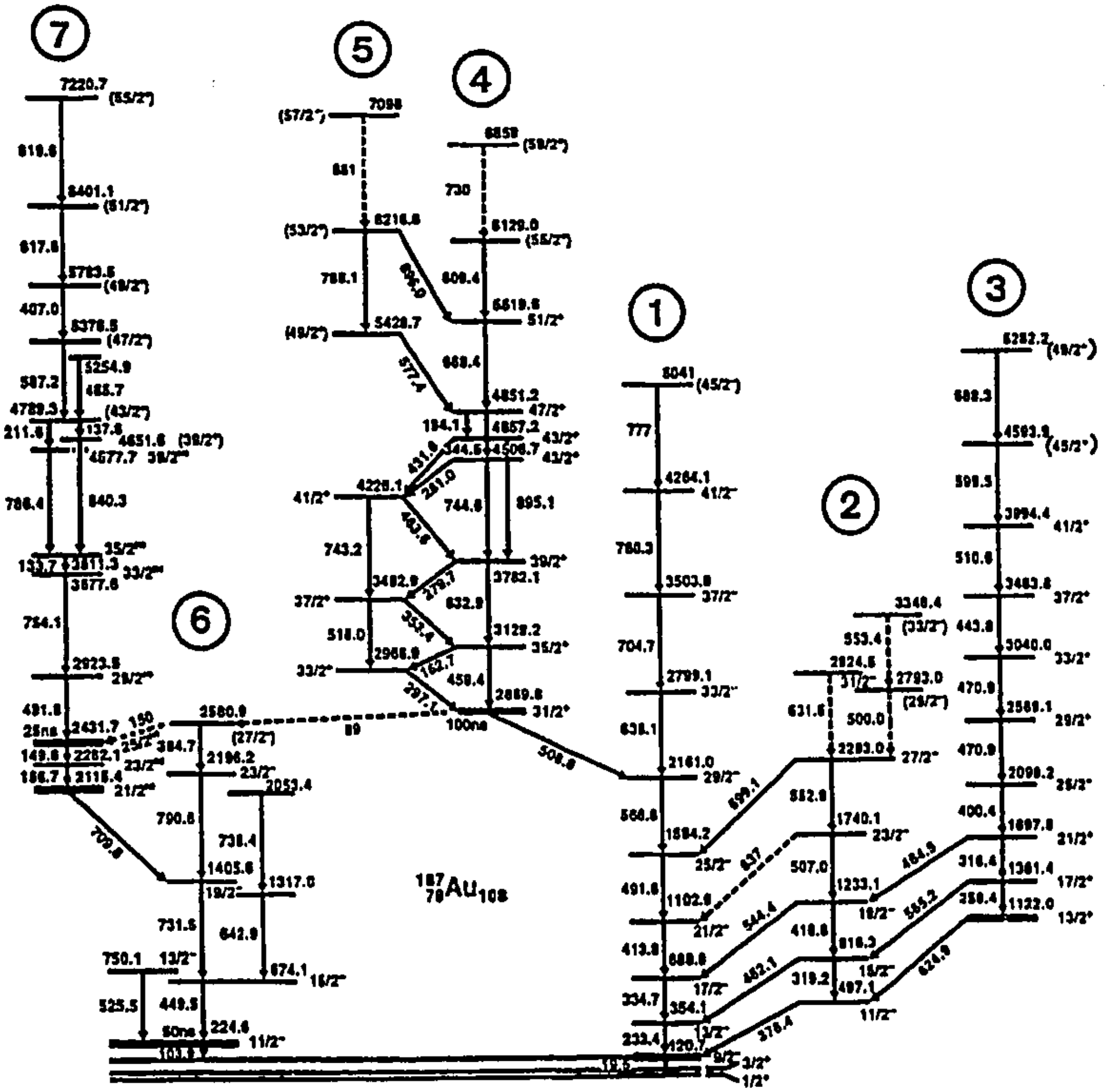

Figure 1.1: An example of the coexistence of individual and collective behavior in the same nuclear system is shown in this level scheme of ^{187}Au deduced from γ-ray decay. The regular pattern of levels in structures 1, 2 and 3 are indicative of collective rotation, while the irregular pattern in structures 6 and 7 arises from non-collective rearrangements of individual particles. Structure 4/5 is a collective rotor which undergoes a single-particle re-arrangement with increasing rotation. From [Joh 87].

model. This approach has been triumphant in many aspects of nuclear structure, including the subject of this work, superdeformation. Superdeformation is a term applied to excited states of a nuclear system which are highly deformed, and these states can only be observed because they have a special stability associated with the valence particles.

The purpose of this thesis is to attempt to identify the valence particles of superdeformed nuclear systems at high spin with a neutron number of approximately N=80 in the vicinity of $^{143}_{63}\mathrm{Eu}_{80}$. These nuclei fall between two well–established regions of superdeformation, namely those with approximately 130 and 150 nucleons. These two regions have distinct behaviors which are determined by their valence particle structure, so one of the questions to be answered is how these intermediate N=80 nuclei are related to the $A\sim130$ or $A\sim150$ regions.

The remainder of Chapter 1 will introduce briefly the topics associated with nuclear superdeformation and review some of its history. In Chapter 2, a more detailed treatment the theory of nuclear structure relevant to this thesis will be presented. Also in Chapter 2, some of the theory relevant to the population and observation of superdeformed states will be given. Chapter 3 describes the instrumentation, namely large arrays of gamma-ray spectrometers, which were used in this study. The experimental results, which are described in Chapter 4, are interpreted in Chapter 5, and probable valence particle configurations are proposed. Conclusions and future prospects are presented in Chapter 6.

1.1. Fission Isomers and the Second Well

The first discovery of superdeformation was the fission isomers of the actinide region with neutron number N in the range 144 to 148, such as ^{232}Th and ^{236}U [Pol 62]. In the liquid-drop model of fission (see for example [PB 75], Chapter 12 or [RS 80], Sect. 1.6, and references therein), the stretching and ultimately the separation of the nucleus into two drops was parametrized by deformation coordinates.

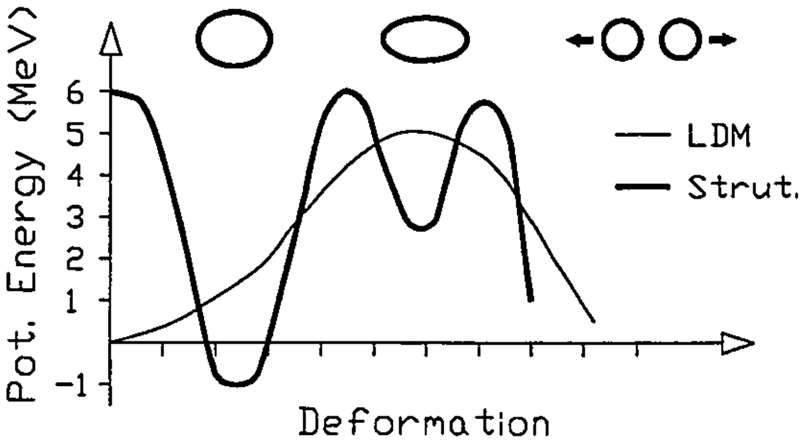

Figure 1.1.1: Schematic of the potential energy as a function of a deformation parameter for a typicial fission-isomer nucleus with 144 to 148 neutrons. Shell effects modify the liquid-drop energy (narrow line) to give a second well at superdeformation (thick line). As the system attempts to execute a trajectory from a low-deformed state to the two-drop system, it can get trapped in the superdeformed well. Adapted from [PB 75].

The fission process itself was actually a tunneling process as the nucleus executed a trajectory in this deformation space, from nearly-spherical states through a potential barrier to a two-nucleus system. Strutinsky [Str 67, Str 68] showed that in the fission isomer systems, a "second minimum" occurred in deformation space corresponding to a 2:1 prolate ellipsoid of rotation, that is, a shape like a Canadian football. This minimum appeared due to large gaps in single-particle level density at the Fermi surface which are brought about by deformation. As the fissioning nucleus tunneled from its near-spherical state to the scission point, it would get "trapped" in states in this second well. This was a beautiful example of the coexistence and interplay of the macroscopic (fissioning liquid drop) and microscopic (shell gaps) degrees of freedom in finite nuclear matter.

This discussion has identified the two characteristics which define a superdeformed state. It is highly deformed with axis ratios approximately 2:1, and it exists in a secondary potential well in deformation space with barriers against fission or against decay to lower-deformed states. The (exact) 2:1 axis ratio is known to be important in anisotropic harmonic oscillator systems, where it yields new regions of low level density with new magic numbers differing from the traditional harmonic oscillator shell gaps. These shell gaps and the deformation at which they exist will be somewhat different in a real nuclear system. For example, spin-orbit coupling can change the prolate superdeformed shell gap at particle number 140 of Figure 1.1.2 to $\sim 144 - 148$, corresponding to the neutron number of the fission isomers. The essential physics, however, is in the origin of the second minimum, namely the shell gaps which reduce the energy of the highly deformed system and the height of barriers between these highly deformed states and either spherical states or fissioned systems. Second-minimum states are often classified as superdeformed even if the nuclear shape is not exactly 2:1.

1.2. High-Spin Superdeformation

As the theoretical tools for high-spin nuclear structure were developed, it became clear that rotation could induce second minima [Ben 75, Nee 75, Ben 81, Dud 82, DN 85]. A long series of collective rotational states could be built upon intrinsic superdeformed configurations within this second well. The predicted spins and excitation energies of such states were such that the best means of populating the superdeformed (SD) bands was by heavy-ion fusion-evaporation reactions. Because the potential well would present a barrier against decay to fissioned systems or to less-deformed configurations, it was expected that the dominant decay mode would be in-band γ ray transitions. Experimental verification of the predictions of high-spin SD would have to await the implementation of the so-called "second generation" of γ-ray spectrometer arrays. Highlights in the history of high-spin superdeformation are shown in Figure 1.2.1 and discussed below.

The first evidence of high-spin superdeformation is usually attributed to the prominent γ–γ energy correlations, measured with the TESSA-2 spectrometer

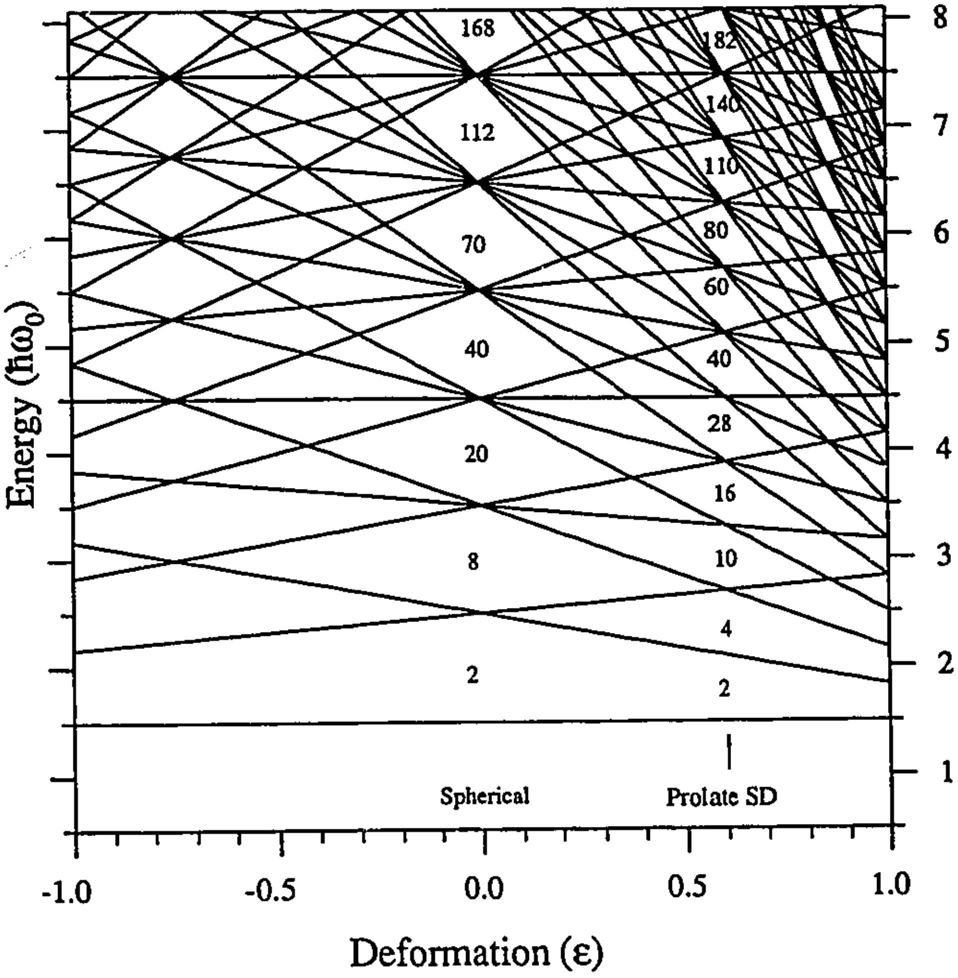

Figure 1.1.2: Evolution of levels, shell gaps and magic numbers in a deformed harmonic oscillator potential, where ϵ is a parameter which increases in magnitude with deformation. The location of the 2:1 prolate superdeformed (SD) shape and the new magic numbers at that deformation are indicated. Adapted from [SRN 72].

at Daresbury (UK), in the emissions from high-spin states of ^{152}Dy [Nya 84]. This nucleus also happened to be one of the best predicted cases for superdeformation. A so-called "ridge structure" was discovered which was interpreted as the $(J+2) \rightarrow J \rightarrow (J-2)$ decay of superdeformed states. The difference between the coincident

γ rays which comprised this ridge were consistent with a rigid rotor in the shape of a 2:1 prolate ellipsoid.

The first high-spin second-minimum rotational band observed by a cascade of discrete γ rays was in ^{132}Ce [Nol 85]. This beautiful "picket fence" spectrum, observed with TESSA-2, was interpreted as a the de-excitation of a rapidly rotating nuclear system with the shape of a 3:2 prolate ellipsoid. Higher energy transitions correspond to faster rotation and higher angular momentum. The number of γ-ray lines in the spectrum is evidence that the configuration is stabilized by a deep second minimum. At the time the ^{132}Ce band was not identified as a superdeformed band, since its deduced deformation was lower than 2:1. As was suggested earlier, the deformation is simply one of the consequences of the essential physics of the second minimum.

A discrete rotational band in ^{152}Dy [Twi 86] based on the 2:1 prolate ellipsoid shape and observed with TESSA-3, is often quoted as the first high-spin SD band. The subsequent discovery of an SD band in ^{149}Gd with the 8π spectrometer [Haa 88] led to a better understanding of the best means of populating superdeformed states [Tar 88], which in turn launched a flurry of intense study of superdeformed bands in nuclei with masses $A{\sim}150$ based on shell gaps at 86 neutrons and 66 protons. The discovery of superdeformation in ^{191}Hg [Moo 89] with the Argonne–Notre Dame γ-ray array opened a new region of superdeformation near $A{\sim}190$ based on proton number 80. Excitations within the second minima yield multiple discrete-line SD bands within the same nucleus, as was first observed in ^{153}Dy [Joh 89].

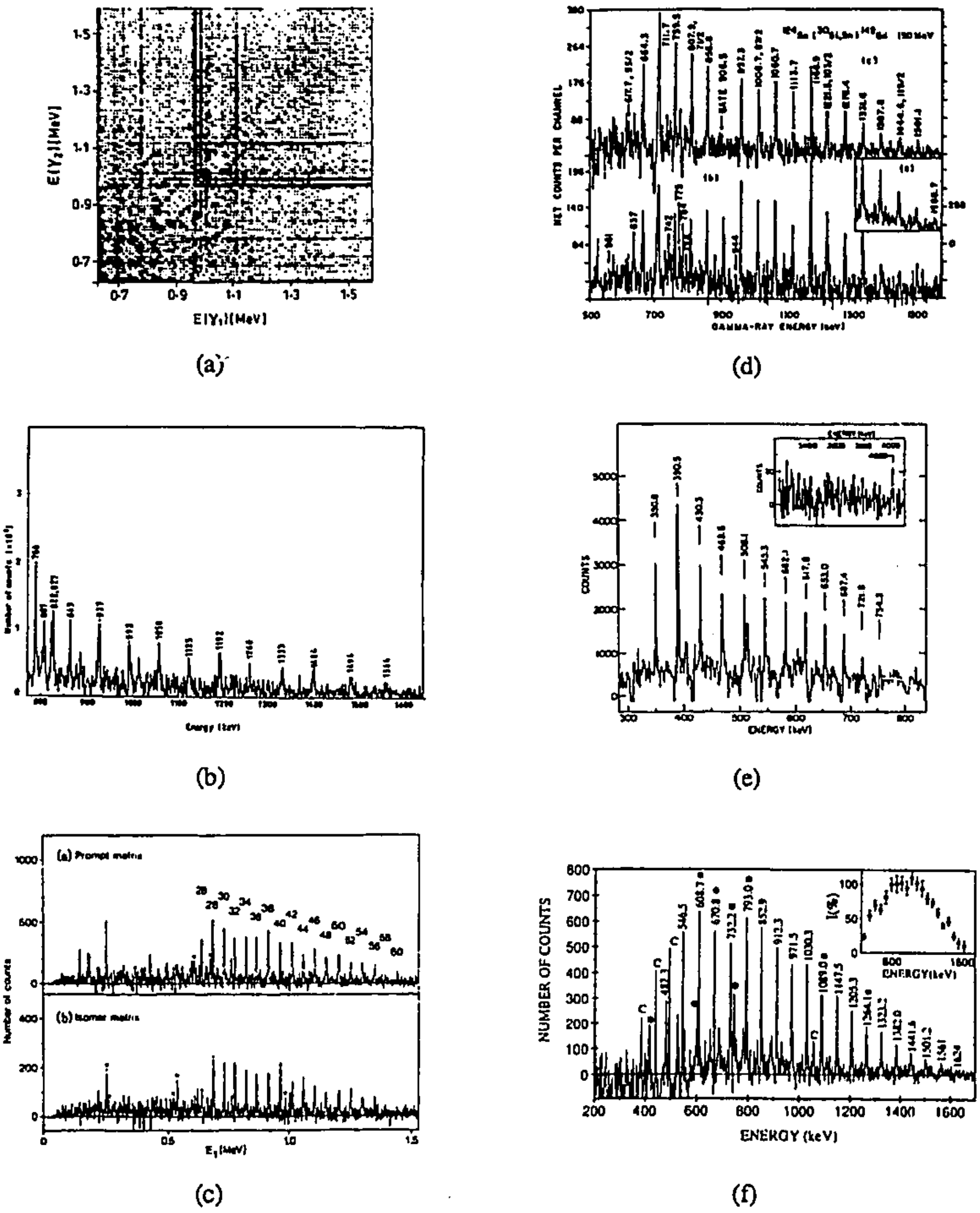

(a) (b) (c) (d) (e) (f)

Figure 1.2.1: A brief history of high-spin superdeformation: (a), ^{152}Dy ridge [Nya 84]; (b), ^{132}Ce SD band [Nol 85]; (c), ^{152}Dy SD band [Twi 86]; (d), ^{149}Gd SD band [Haa 88]; (e), ^{191}Hg SD band [Moo 89]; (f), ^{143}Eu SD band [Mul 91].

1.3. Decay Out from Superdeformed Bands

Since the second minimum in high-spin bands is enhanced by rotation, it follows that as a SD band de-excites, its rotation will slow down and the barriers of the potential well will eventually disappear. More precisely, the barrier becomes low enough to permit tunneling to spherical or less deformed states (see Figure 1.3.1), often called normal-deformed (ND) states. This means that the very regular pattern of peaks in the γ-ray spectrum is suddenly cut off at some lower limit of γ-ray energy. The level density of the ND states is so high that the decay spreads out over several possible branches, which converge again at lower excitation. This is another feature common to all SD bands, that the decay from SD to ND states is extremely complicated and fractionated. Unfortunately, the spins, parities and excitation energies of states can only be deduced from γ-ray decay if the decay paths are well characterized. If individual decay paths cannot be established, direct measurements cannot be made. Recently progress has been made in identifying the decay paths in $A{\sim}130$ nuclei [Lun 95]. However, in the $A{\sim}150$ and $A{\sim}190$ SD bands, these decay paths remain elusive. More clever techniques of deducing the properties of these decay paths without directly observing them have placed limits on the spins and energies [Ata 93, Hen 94], but definitive, unambiguous measurements have not been made.

1.4. Identical Bands

The discovery of a superdeformed band in ^{151}Tb which decays by a sequence of γ rays with exactly the same energies within experimental uncertainties as the ^{152}Dy yrast superdeformed band [Byr 90] has launched an enormous experimental and theoretical effort on the so-called *identical bands* phenomenon. These are pairs of bands in nuclei *of different mass* which decay by γ–ray transitions whose energies, to within $\sim 0.1\%$, are exactly the same or differ by $\pm\frac{1}{4}$ or $\frac{1}{2}$ of consecutive γ-ray energy differences. Indeed, most of the SD bands in the $A{\sim}150$ region can be thus

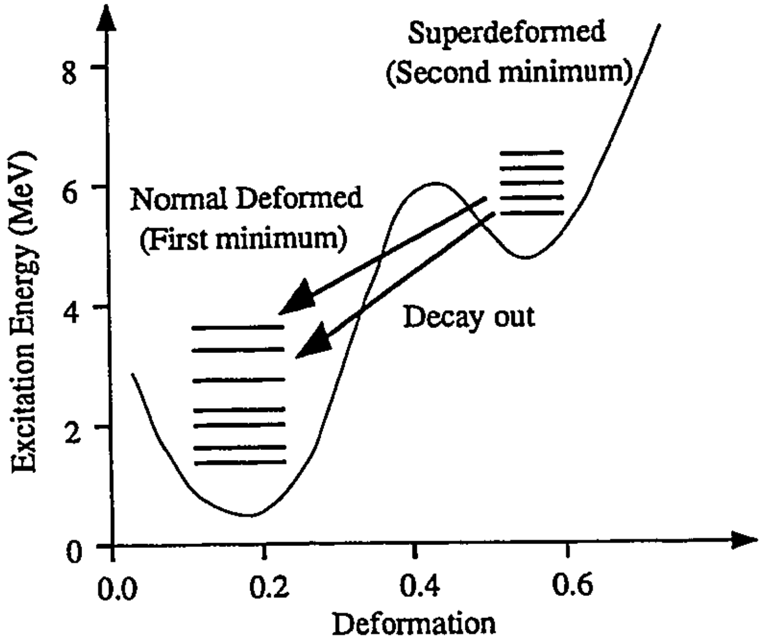

Figure 1.3.1: Schematic diagram of the decay-out of SD to ND states. Reproduced from [Wil 94].

related to bands in neighboring or nearby nuclei of different mass, and the same is true of $A\sim190$ SD bands.

As is a recurrent theme in nuclear physics, there is a macroscopic and a microscopic component to the phenomenon. The spacing of consecutive transitions within a band is interpreted as the inverse of the moment of inertia. This macroscopic quantity depends on both mass and deformation, so bands with identical spacing but different mass might involve a convenient change in deformation. Microscopically, it appears that the occupation of certain orbitals has no effect on the moment inertia of the overall system. Furthermore, there are special "magic" orbitals which, occupied or not, have no effect on the de-excitation γ-ray energies either, yielding *isospectral* bands. Further details of the identical bands phenomenon must be postponed until the pertinent theory is introduced. However it must be re-iterated that the prevalence of SD identical bands is still largely a mystery and has led to a re-examination of all rotational behavior, not just at superdeformations.

1.5. Neutron Number 80

The SD shell gap at particle number 80 exists for both neutrons and protons. In the proton case, it is this gap which gives rise to the mercury SD bands. It had been long predicted that the N=80 neutron shell gap would also produce SD second wells, and the best case was deemed to be ^{144}Gd. However this band eluded detection by the second-generation γ-ray spectrometers [Viv 86, Sch 87]. The first N=80 superdeformed band was discovered in ^{143}Eu [Mul 91].

The primary goal of this thesis is to study the interplay between macroscopic and microscopic effects in superdeformation based on the N=80 shell gap, or more precisely, the valence particle configuration of SD bands in nuclei in the vicinity of ^{143}Eu. The detailed motivation for studying superdeformation near N=80 will be revisited in Chapter 4, following the review of theoretical and experimental techniques of the following two chapters.

Chapter 2.
Theory of Superdeformed Rotational Bands

Superdeformed bands exist and are stabilized against decay by fission or by γ-ray decay to less-deformed states by a combination of collective and single-particle effects. This chapter summarizes the theoretical tools pertinent to the study of this intricate interplay. After reviewing the fundamentals of deformed and rotating nuclei, three forms of the nuclear mean field will be presented, with special emphasis on their contemporary use in superdeformation studies. The cranking model and the transformation from the laboratory to intrinsic frame will be discussed from both a theoretical and experimental perspective. The chapter will close with a brief review of the population and subsequent electromagnetic decay of superdeformed states.

The contents of this chapter are based largely on the relevant discussions in Ring and Shuck [RS 80]. Unless otherwise noted, this excellent work should be considered as a citation for all equations and derivations in this chapter.

2.1. Deformed Nuclei and Rotational Behavior

There are two distinct modes which describe the ways in which a nuclear system can form a state with high angular momentum I. In collective rotational motion, the liquid drop itself rotates. The total angular momentum comes from the coupling of the collective rotation to the intrinsic single-particle states of the rotating core, and the excitation energies of such states go as $I(I+1)$, as would be expected classically for a rotor. Since the shape is determined by the wave functions, rotation can only have an effect on the observables (energy eigenfunctions) if the wave functions themselves are not invariant under rotation. That is, an ellipsoidal (oblate or prolate), axially symmetric nucleus cannot rotate collectively about its axis of symmetry. The most commonly-observed rotational states are those where a prolate shape revolves about an axis perpendicular to its main symmetry axis.

By contrast, in the second mode of high angular momentum the nuclear liquid drop does not rotate collectively. Rather, the angular momentum of the nuclear system is determined simply by the coupling of angular momenta of a few valence nucleons. The least energetic state of a given angular momentum J is called the *yrast* state. The energy of these yrast states, produced through particle-hole excitations, is approximately given by $\hbar^2 J(J+1)/2\mathcal{J}^{(2)}$, as would be expected for a rotational system. A plot of yrast state energies *vs.* $J(J+1)$, the *yrast diagram*, shows that the points will be scattered about a straight line.

The astute reader will have noticed the use of both J and I to refer to the angular momentum of a nuclear system in the previous paragraphs. In the discussions which follow, J always refers to angular momentum in the laboratory frame. As a quantum number, J has integer values for even-A systems and half-integer values for odd-A systems, as expected for fermions. Furthermore it can refer to both collective rotational and non-collective states. I, on the other hand, will only refer to the angular momentum of systems in rotational models. In some models it does not refer to real states or to eigenvalues of the nuclear Hamiltonian.

2.1.1 Quadrupole Deformation Parameters

Before further discussing the behavior of a deformed nucleus it is worthwhile to establish the popular conventions for describing the shape of a model nuclear system. The nucleus does not have a sharp boundary between nuclear matter and empty space (cf. electron scattering experiments, [Hof 56]), so the term "nuclear shape" may be more correctly identified as corresponding to a half-density surface or to a model-dependent equipotential surface.

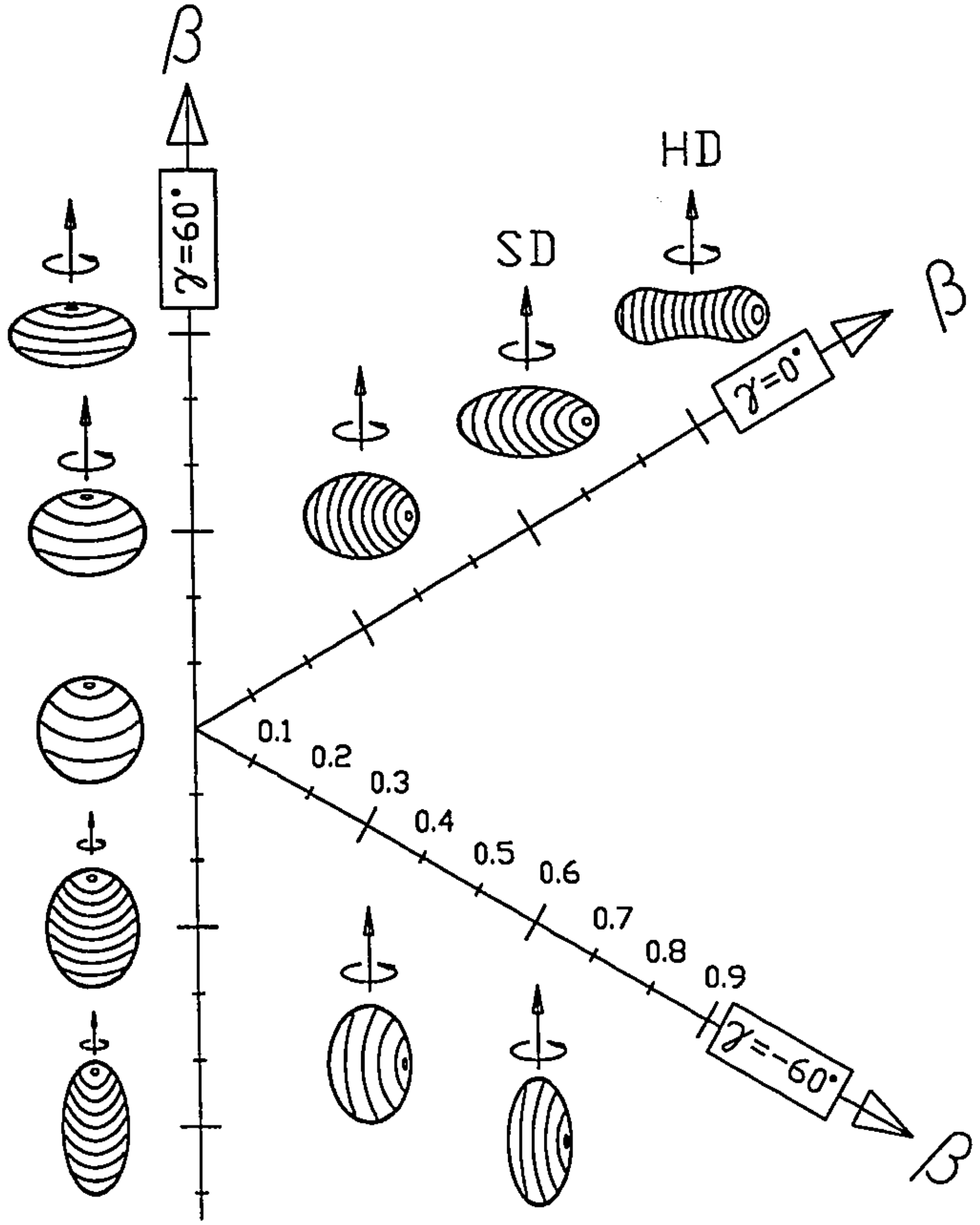

Figure 2.1.1: Schematic of (β, γ) quadrupole deformation space, with examples of axially symmetric shapes shown. Equatorial lines encircle the axis of full rotational symmetry. The rotation axis is taken to be the 1-axis. Collective rotation is forbidden when the rotation and rotational symmetry axes coincide, *i.e.* $\gamma = 60°$ or $-120°$.

The position R of the surface of a general nuclear shape Ξ can be described in terms of a multipole expansion,

$$R = R(\theta, \phi) = R_0 \left(1 + \sum_{\lambda=0}^{\infty} \sum_{\mu=-\lambda}^{\lambda} \alpha^*_{\lambda\mu} Y_{\lambda\mu}(\theta, \phi) \right). \tag{2.1.1}$$

Here R_0 is the radius of a sphere which encloses the same volume as $R(\theta, \phi)$, and α_{00} is fixed by this volume condition. An ellipsoidal shape is approximated by a quadrupole ($\lambda = 2$) deformation. The five $\alpha_{2\mu}$ coefficients are fixed by two parameters β and γ known as the Hill-Wheeler coordinates, [HW 53]

$$\alpha_{20} = \beta \cdot \cos\gamma, \tag{2.1.2a}$$

$$\alpha_{2\pm1} = 0, \tag{2.1.2b}$$

$$\alpha_{2\pm2} = \frac{1}{\sqrt{2}}\beta \cdot \sin\gamma. \tag{2.1.2c}$$

All of the shapes described by (β, γ) are invariant to a parity transformation, rotation of 180° about an intrinsic axis, or reflection through a plane which includes two major axes. Figure 2.1.1 demonstrates special cases in the (β, γ) plane. It is traditional to select the 1-axis of the body-fixed (1-2-3) coordinate system as the axis of rotation. Shapes along the $\gamma = 0$, $\beta > 0$ ray correspond to axially symmetric, prolate "football-shaped" nuclei rotating collectively about a short axis, and a superdeformed prolate shape (axis ratio 2:1:1) corresponds to the coordinates $\beta \sim 0.6$ and $\gamma = 0$. The oblate non-collective shapes are described along the $\gamma = 60°$ ray, and the oblate collective and prolate non-collective shapes exist at $\gamma = -60°$ and $-120°$ respectively. Shapes along all of these rays will still have one axis of full rotational ($\mathcal{D}_\infty$) symmetry. Between these rays are the triaxial shapes. These are roughly ellipsoidal shapes where no two major axes are the same length.

The moment of inertia $\mathcal{J}_\kappa$ of a rotating nucleus of one of the above shapes depends on whether we treat the liquid drop as an irrotational superfluid,

$$\mathcal{J}^{\text{irr}}_\kappa = \frac{3}{2\pi} m A R_0^2 \beta^2 \sin^2\left(\gamma - \frac{2\pi}{3}\kappa\right), \tag{2.1.3}$$

or as a rigid body,

$$\mathcal{J}_{\kappa}^{\text{rot}} = \frac{2}{5} m A R_0^2 \left(1 - \sqrt{\frac{5}{4\pi}}\beta \cos\left(\gamma - \frac{2\pi}{3}\kappa\right)\right), \tag{2.1.4}$$

where m is the mass of a nucleon, $R_0 = A^{1/3} r_0$, with $r_0 \sim 1.3$ fm, and $\kappa = 1, 2$, or 3 for the axis of the intrinsic frame. Real nuclei have moments of inertia somewhere between these limits. It is important to note that both Eqs. (2.1.3) and (2.1.4) depend on particle number and scale as $A^{5/3}$. So if two nuclei differing by ΔA nucleons have the same deformation parameters, one would expect that the moments of inertia would differ by

$$\frac{\Delta\mathcal{J}}{\mathcal{J}} \simeq \left(\frac{5}{3}\right)\frac{\Delta A}{A}. \tag{2.1.5}$$

In nuclei with $A{\sim}140$, this corresponds to $\Delta\mathcal{J}/\mathcal{J} \sim 1.2\%$ per nucleon.

A shape described by purely $\lambda = 2$ deformations does not describe a pure ellipsoid, and as β increases this discrepancy becomes quite important. The 3:1:1 prolate (hyperdeformed) shape, $\beta \sim 0.9$, looks more like a dumbbell than an ellipsoid. Introduction of hexadecapole terms $Y_{4\mu}$ can better reproduce the ellipsoidal shape. One popular form of representing the hexadecapole deformation component is as single parameter β_4. The coefficients of the $Y_{4\mu}$ terms are given, for example, in [WD 85].

2.1.2 Intrinsic, Rotational and Total Angular Momenta

One model of representing the nuclear Hamiltonian is to separate it into a collective component and an intrinsic component,

$$\begin{aligned} H &= H_{\text{coll}} + H_{\text{int}} \\ &= \hbar^2 \sum_{k=1}^{3} \frac{R_k^2}{2\mathcal{J}_k} + H_{\text{int}} \end{aligned} \tag{2.1.6}$$

if a suitable transformation of coordinates for H_{int} is available. For example, H_{int} could be expressed in terms of a "body-fixed" intrinsic coordinate system which rotates with the nucleus. Figure 2.1.2 demonstrates the various angular momenta and their projections associated with a prolate, ellipsoidal, rotating liquid drop nucleus, where the intrinsic frame is fixed so that the long axis of the ellipsoid and the 3-axis coincide. It should be noted that different authors use different labels for these axes. For example, in both Chap. 4 of [BM 75] and Chap. 2 of [RS 80], the coordinate systems are chosen such that in Figure 2.1.2, the 1 axes of the intrinsic frame would coincide with the z axis of the laboratory frame, rather than the x axis. Unless stated explicitly otherwise, the orientation of the frames of reference portrayed in Figure 2.1.2 applies in this thesis.

For generalized rotational behavior we consider first only the total angular momentum operator $\vec{I}^2$ and the angular momentum projection operators along the x axis of the laboratory system and the 3 axis of the intrinsic system, $\widehat{J}_x$ and $\widehat{I}_3$. These operators have eigenvalues I, M and K respectively. Wave functions may be represented as Wigner rotation functions [BM 75],

$$|\Psi^I_M\rangle = \sum_K c_K |IMK\rangle, \tag{2.1.7}$$

where

$$|IMK\rangle = \sqrt{\frac{2I+1}{8\pi^2}} D^{I*}_{MK}\left(\vec{\Omega}\right) \tag{2.1.8}$$

with $\vec{\Omega}$ being the three Euler angles.

In the *particle-plus-rotor model*, most of the nucleons comprise the rotating collective core and the remaining (valence) particles are considered separately. The angular momentum associated with the collective rotation of the core is given by $\vec{R}$. The particles near the Fermi surface (that is, those near the last, highest-energy occupied level) are treated separately, and the angular momentum of these valence particles is $\vec{j}$. The projection of the total angular momentum $\vec{I}$ onto the 3-axis is K. For a valence particle, the projection of $\vec{j}$ onto the 3-axis is denoted Ω. The orbital and spin angular momenta of the valence particles are $\vec{l}$ and $\vec{s}$, and the projections onto the 3-axis are Λ and Σ respectively.

In the special case of axial symmetry about the 3-axis, $\mathcal{J}_1 = \mathcal{J}_2 \equiv \mathcal{J}$, and the vector $\vec{R}$ can have no component along the 3-axis. Axial symmetry means

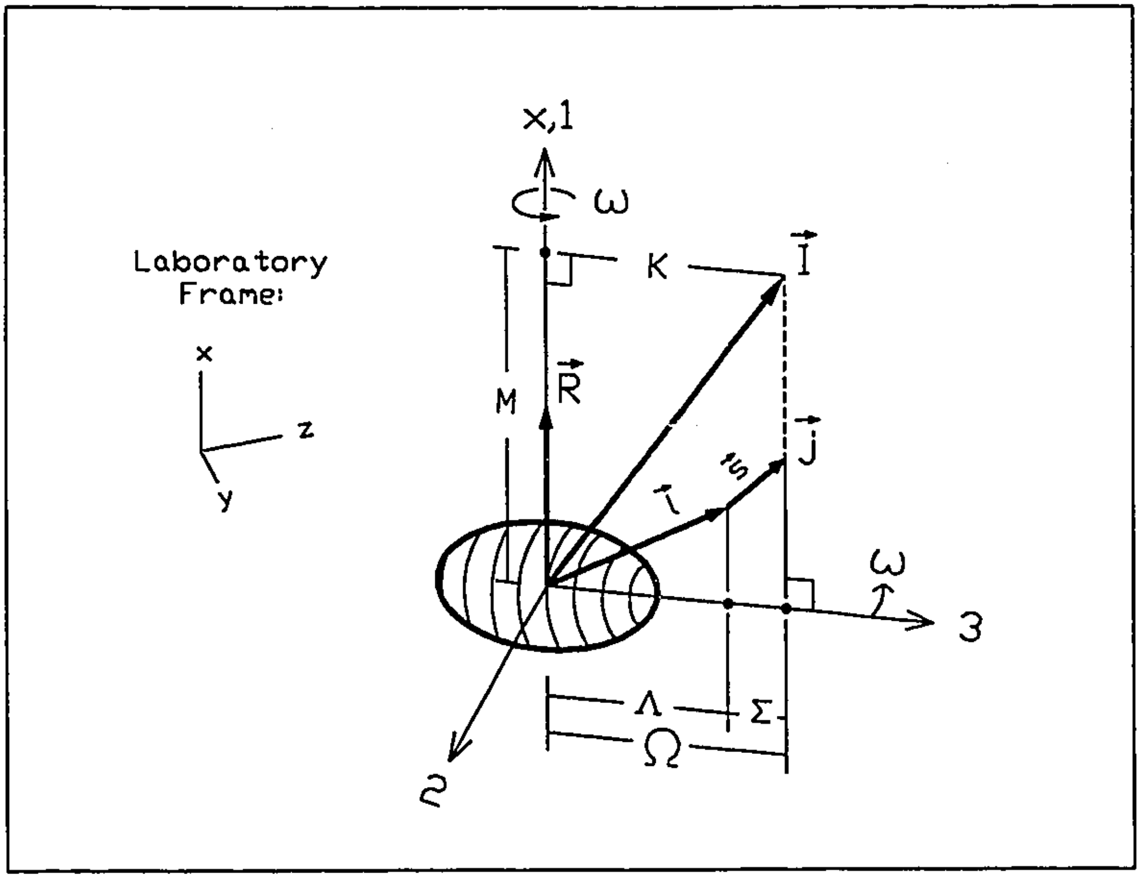

Figure 2.1.2:
Angular momenta, projections, and laboratory and intrinsic frames for a rotating prolate nucleus.

invariance under any arbitrary rotation about a given axis, *e.g.* $\gamma = 0$ shapes have axial symmetry about the 3-axis. If the system is invariant under such a rotation, then the observable (the Hamiltonian) must also be invariant, hence R_3 must vanish, which in turn means $K = \Omega$. The collective part of Eq. (2.1.6) is recast by substituting $\vec{R} = \vec{I} - \vec{j}$, which gives

$$H_{\text{coll}} = \frac{\vec{I}^2 - {I_3}^2}{2\mathcal{J}} \tag{2.1.9a}$$

$$+ \frac{1}{2\mathcal{J}}\left(j_1^2 + j_2^2\right) \tag{2.1.9b}$$

$$- \frac{1}{\mathcal{J}}\left(I_1 j_1 + I_2 j_2\right). \tag{2.1.9c}$$

The first term, often called the rotational term, is the total angular momentum perpendicular to the 3-axis, that is, the rotational angular momentum of the core plus the valence particle angular momentum projected onto the rotation axis. The $j_1^2 + j_2^2$ term acts only on the single-particle degrees of freedom, that is, on the valence nucleon or nucleons which are not part of the collective core, and so is often moved to the intrinsic part of the Hamiltonian or neglected outright (cf. [BM 75], p. 201). The third term is the Coriolis interaction term. This connects states with $\Delta K = \pm 1$, and to the first-order, it therefore only gives diagonal matrix elements for the $K = 1/2$ components of the wave function. This is more apparent when it is re-written in terms of ladder operators,

$$H_{\text{Coriolis}} = -\frac{1}{2\mathcal{J}}\left(I_+ j_- + I_- j_+\right). \tag{2.1.10}$$

For a purely collective core which is static in the intrinsic frame, $K = 0$, and the wave function is $|\Psi\rangle = c|IM0\rangle$. To preserve the same symmetries in the intrinsic frame as in the laboratory frame, the system is restricted to spins and parities $\{0^+, 2^+, 4^+ \ldots\}$. By contrast, if $K \neq 0$, the same symmetries can still be preserved for spin $I \in \{|K|, |K|+1, |K|+2, |K|+3, \ldots\}$. However it has become customary to classify these states as separate bands $\{|K|, |K|+2\ldots\}$ and $\{|K|+1, |K|+3\ldots\}$. This will be discussed in more detail in Sect. 2.3.

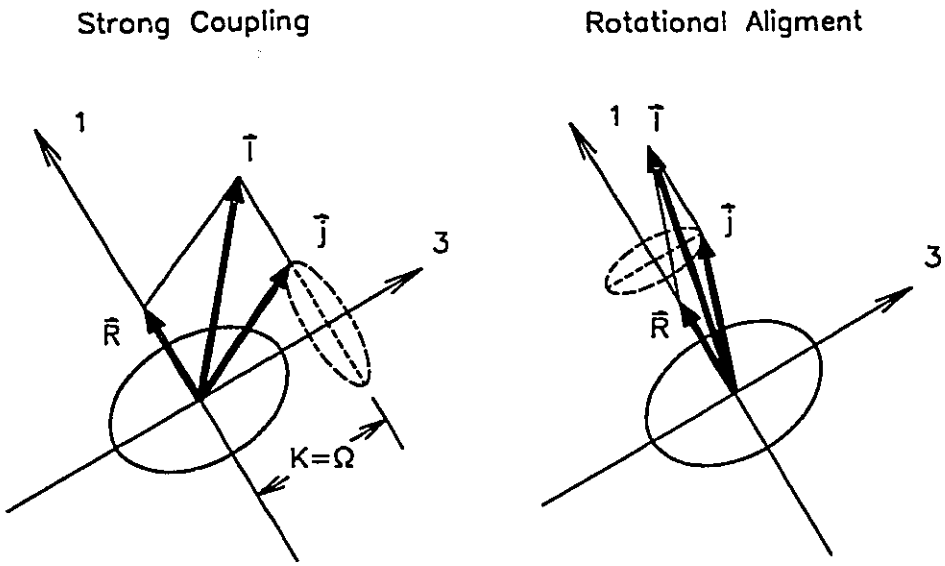

Figure 2.1.3: Strong coupling and rotational aligment limits of the particle-rotor model. Adapted from [RS 80].

There are two useful limits to the axially-symmetric particle-rotor model, shown schematically in Figure 2.1.3. For simplicity this discussion will focus only on a single valence particle beyond the collective core. In the *rotational alignment* limit, which applies to high-j orbitals, the matrix elements of the Coriolis force are greater than the level splitting arising from deformation. Qualitatively, the most energetically favoured states become those whose angular momentum $\langle\vec{j}\rangle$ is nearly parallel to the total angular momentum vector $\vec{I}$. As the Coriolis mixing introduces more of the aligned components into the single-particle wave functions, and the expectation value $\langle j_x\rangle$ for that wave function becomes more parallel (*aligns*) to the rotation axis. In this limit the rotational angular momentum becomes a good quantum number, and the energies of states are given by $E = E_0 + \hbar^2 R(R+1)/\mathcal{J}$, where $R = 0,\ 2,\ 4, \ldots$ and E_0 is the eigenvalue of H_{int}.

In the *strong coupling* limit, the Coriolis elements remain small relative to deformation-induced splitting. The Coriolis term can then be treated as a first-order perturbation, and the energies are

$$E(I) = E_0 + \frac{\hbar^2}{2\mathcal{J}}\{I(I+1) - \frac{1}{4} + a \cdot \left(I + \frac{1}{2}\right)(-1)^{(I+\frac{1}{2})}\}, \tag{2.1.11}$$

where the decoupling parameter a for a valence particle in orbital $|\phi\rangle$,

$$a = i\langle\phi|j_+ e^{-i\pi j_1}|\phi\rangle, \tag{2.1.12}$$

is non-zero only if there is some $K = \frac{1}{2}$ component to the wave function. In this model, the difference in energy between states of spin I and $I-2$ within a rotational band is

$$E(I) - E(I-2) = \frac{\hbar^2}{\mathcal{J}}\left[2I - 1 + a \cdot (-1)^{I+\frac{1}{2}}\right]. \tag{2.1.13}$$

2.2. Deformed Nuclear Mean Fields

Efforts to form a theoretical understanding of superdeformation typically rely on mean-field calculations, see for example the review article [AFN 90]. The fundamental assumption is that interactions of any one nucleon with the rest of the nucleons in the system are dominated by the two-body component, which in turn means that the sum of these interactions may be expressed as a single "mean field" potential $V(\vec{r})$, where $V(\vec{r})$ depends on and resembles the shape of the nucleus. Theoretical calculations used in the study of superdeformation are primarily based on one of the Nilsson model [Rag 93a], the Woods-Saxon potential [NWJ 89, WD 85], and the Hartree-Fock method with Skyrme effective interactions [BFH 87, BFH 91, Flo 95, DD 95]. The details and relative advantages and disadvantages of these methods will be compared and reviewed below.

2.2.1 Nilsson Model

The Nilsson model [Nil 55] has endured as a successful tool for understanding the behavior of deformed nuclei, mainly because of its inherent simplicity. The Nilsson single-particle Hamiltonian,

$$\begin{aligned} H_{Nils}(\epsilon) &= H_0 + C\vec{l}\cdot\vec{s} + D\vec{l}^2 \\ H_0 &= -\frac{\hbar^2}{2M}\nabla^2 + \frac{1}{2}M\omega_0^2\left(\left(x^2+y^2\right)\left(1+\frac{1}{3}\epsilon\right)^2 + z^2\left(1-\frac{2}{3}\epsilon\right)^2\right) \end{aligned}$$

is essentially just that of an anisotropic harmonic oscillator H_0, with phenomenological corrections. The oscillator frequencies are given in terms of a deformation parameter ϵ,

$$\begin{aligned} \omega_1 = \omega_2 &= \omega_0 \cdot \left(1+\frac{1}{3}\epsilon\right) \\ \omega_3 &= \omega_0 \cdot \left(1-\frac{2}{3}\epsilon\right) \\ \hbar\omega_0 &= 41A^{-\frac{1}{3}}\mathrm{MeV}. \end{aligned}$$

The equipotential surface described by the potential energy portion of H_0 is an ellipsoid of rotation, axially symmetric about the 3 axis and with a ratio of major to minor axis lengths of $\omega_1 : \omega_3$. The relationship between ϵ for the ellipsoid and β_2 for a quadruploid is

$$\epsilon = \frac{3}{4}\sqrt{\frac{5}{\pi}}\beta_2 - \frac{75}{224\pi}\beta_2^2 - \frac{81}{128\pi}\sqrt{\frac{5}{\pi}}\beta_2^3 + \ldots \tag{2.2.1}$$

The spin-orbit coupling is introduced by the $\vec{l} \cdot \vec{s}$ term. The harmonic oscillator potential is "flattened out" by the $\vec{l}^2$ term, which decreases the energy of high-l states in the same manner as expected of more square-well-like potentials. The parameters C and D are fit to experimental data.

The primary attraction of the Nilsson Hamiltonian is that it and its associated wave functions are straightforward to manipulate and interpret. In the limit of extreme deformation the correction terms become negligible, and the Hamiltonian is a nearly pure anisotropic harmonic oscillator. In this limit the wave functions are characterized by the asymptotic Nilsson quantum numbers,

$$\lim_{\epsilon \to \infty} |\psi\rangle \equiv |\,[N_{\text{osc}} n_3 \Lambda]\, \Omega^{\pi}\rangle. \tag{2.2.2}$$

The first two numbers, N_{osc} and n_3, are the total number of oscillator quanta (nodes in the wave function) and the number of quanta along the 3-axis of the state. The orbital and total angular momenta projections onto the 3-axis are given by Λ and Ω, and $\Omega - \Lambda = \pm 1/2 \equiv \Sigma$ is the projection of the nucleon intrinsic spin onto the 3-axis. (See Figure 2.1.2.) The parity of the state is simply $\pi = (-1)^{N_{\text{osc}}}$, and is often omitted from the label.

The Nilsson diagram of Figure 2.2.1 shows the evolution of states as a function of deformation. At zero deformation the states are just the familiar $2j+1$ degenerate shell model states. With increasing prolate deformation these subshells split into $j + \frac{1}{2}$ doubly-degenerate states. The energies of states of $n_3 = 0$ from a given multiplet rise most rapidly with increasing ϵ, while those with the highest n_3 fall most rapidly. This is easy to understand in the asymptotic limit. The energy of the anisotropic, axially symmetric harmonic oscillator is $n_3\hbar\omega_3 + (N_{\text{osc}} - n_3)\hbar\omega_1$, and since $\omega_3 < \omega_1$ for $\epsilon > 0$ (prolate deformations), the states of higher n_3 will have lower total energy.

From the isotropic harmonic oscillator model, one expects that for a given isospin (either neutrons or protons), the states near the Fermi surface should all have the same *natural* parity. States which have the opposite, or *unnatural*, parity are referred to as *intruder* orbitals. The natural parity states will mix, but because the nuclear interaction conserves parity, the intruder orbitals will maintain almost pure shell-model wave functions. Increasing prolate deformation can bring a high-N_{osc}, high-n_3 states of unnatural parity to the Fermi surface. These intruder orbitals tend to dominate the structure of rotational bands. An unnatural parity high-N_{osc}, low-n_3 state which is brought up to the Fermi surface due to deformation is known as an "extruder."

The limitations of the Nilsson model are as follows:

- The potential is not finite for large r, so the tails of the wave functions are incorrect (this problem becomes more serious for excited states);
- The $\vec{l}^2$ term is artificial and tends to cause the model to overestimate moments of inertia;
- The spin-orbit term is only correct for the spherical case $\epsilon = 0$, where $\vec{s} \cdot (\vec{p} \times \vec{\nabla} V)$ really does reduce to $\vec{l} \cdot \vec{s}$;
- The ordering of levels is wrong for very heavy nuclei (Pb region), and an additional correction must be included;
- There is no intrinsic self-consistency between the parametrized shape of the potential (given by ϵ) and the spatial probability of the final wave functions.

Despite these limitations the Nilsson model has still served well in contemporary studies of $A{\sim}150$ superdeformed nuclei [Rag 93a, Fli 95].

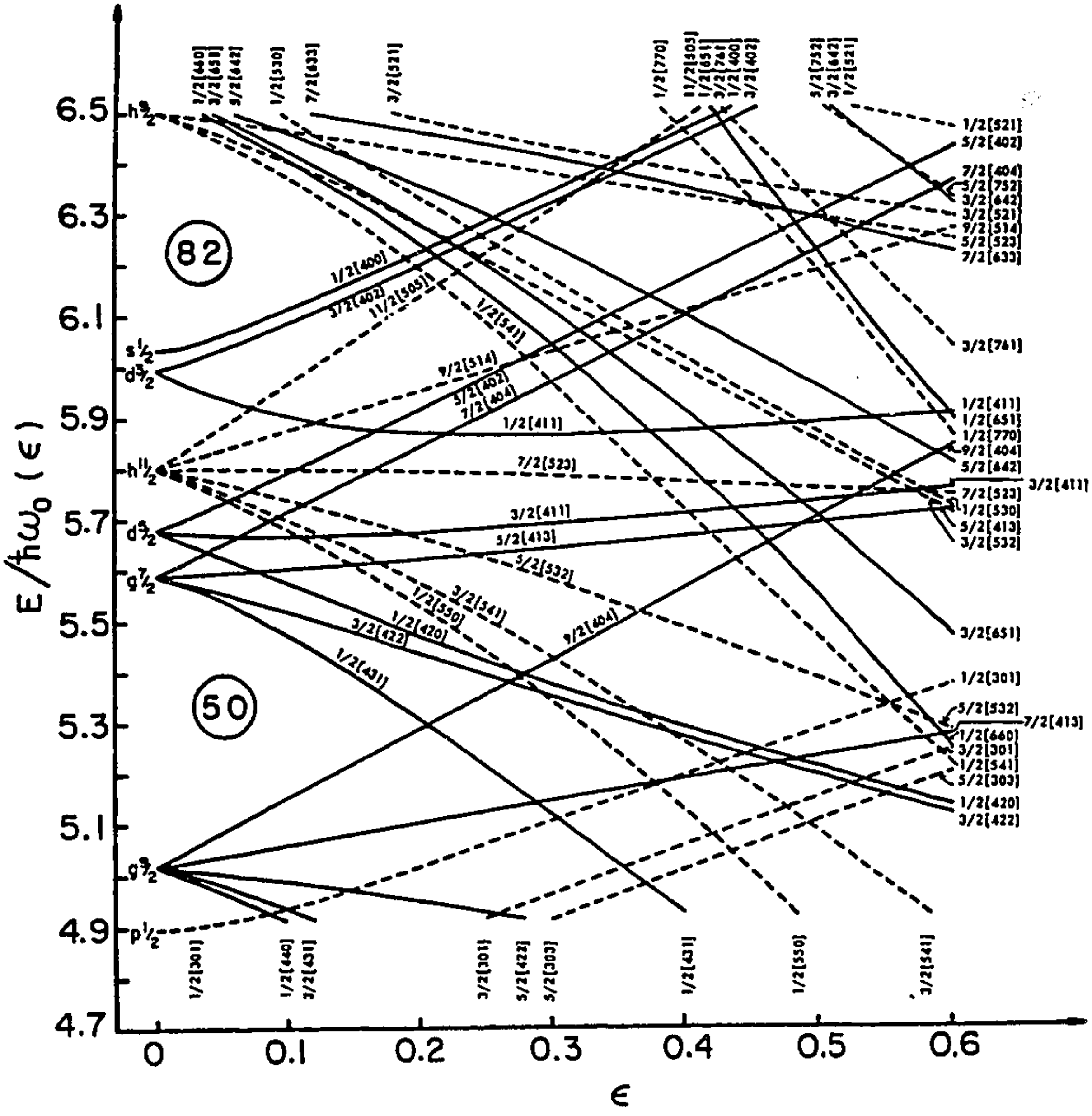

Figure 2.2.1a: Nilsson diagram for protons, $50 \leq Z \leq 82$. [LS 78]

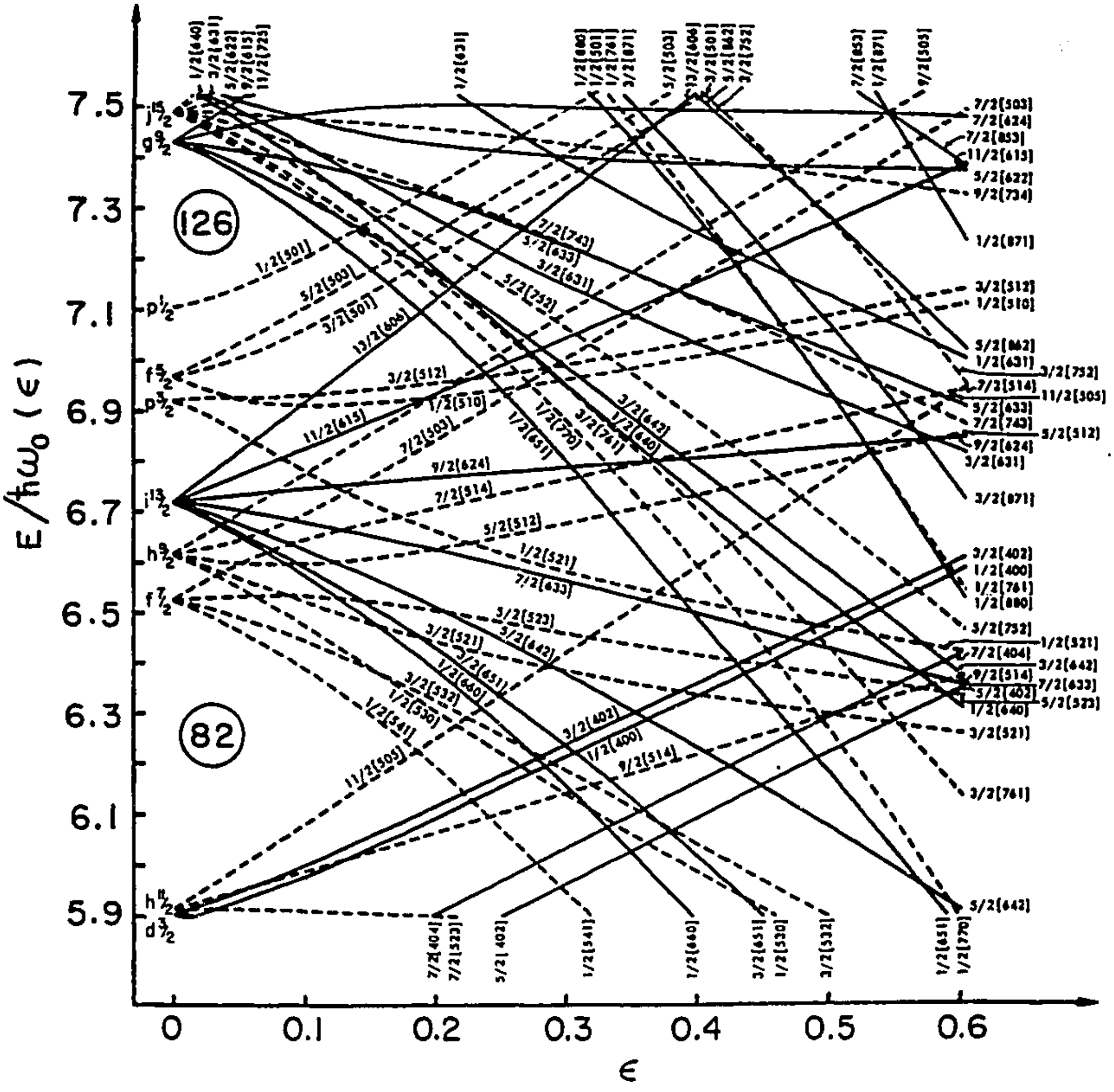

Figure 2.2.1b: Nilsson diagram for neutrons, $82 \leq N \leq 126$. [LS 78]

2.2.2 Woods-Saxon Potential

The Woods-Saxon potential [WS 54] approximates the spatial density distribution of nuclear matter. In the mean-field ansatz, this should be a better approximation than the modified harmonic oscillator. The nuclear surface $\Xi(\vec{\beta}, r_0)$ is determined as in Sect. 2.1.1, where $\vec{\beta}$ represents all of the deformation parameters. Then the potential as a function of position depends on the shortest distance from the point $\vec{r}$ to the surface Ξ, [DSW 81]

$$V(\vec{r}; \Xi) = \frac{V_0}{(1 + \exp\left[\mathrm{dist}(\vec{r}, \Xi)/a\right])}, \tag{2.2.3}$$

where a determines how rapidly the potential falls off to zero. At any point on the surface, the potential is $\frac{1}{2}V_0$. For a spherical nucleus, the distance function reduces to $r - R_0$ and the potential $V(r)$ looks like the example shown in Figure 2.2.2. The spin-orbit term is given by

$$-\lambda\left(\frac{\hbar}{2mc}\right)^2\left(\vec{\nabla}V(\vec{r}; \Xi_{SO}) \times \vec{p}\right) \cdot \vec{s}\left(\frac{2}{\hbar^2}\right) \tag{2.2.4}$$

where λ is a strength parameter.

The parameter sets used in [DSW 81] and [NWJ 89] select three different values of r_0, the phenomenological nucleon radius, to determine potentials for the neutrons (Ξ_n) and protons (Ξ_p) and for the potential used the spin-orbit term Ξ_{SO}. Unless otherwise stated, the Woods-Saxon calculations quoted in this work used the parameter sets and computer codes of [NWJ 89].

The Woods-Saxon Hamiltonian and wave functions are somewhat more complex than the Nilsson Hamiltonian, and as such the computations are more technically difficult and not quite so transparent. However it is free of the deficiencies of the Nilsson model (except for the density self-consistency problem), which is reflected in better reproduction of observed moments of inertia. The wave function can still be characterized by a major oscillator number N_{osc} as in the Nilsson model, and it is customary to label orbitals the same as the most-similar Nilsson

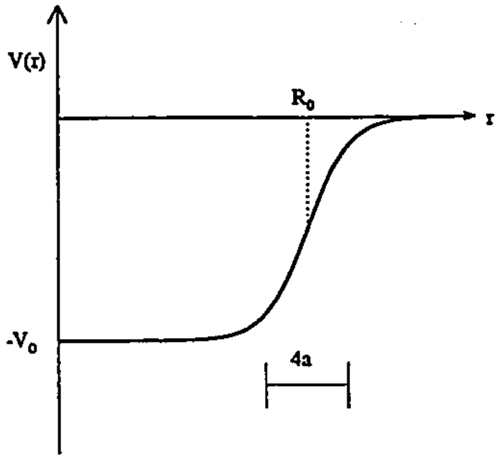

Figure 2.2.2: Schematic of the Woods-Saxon potential $V(r)$ for spherical nuclei, $R_0 = r_0 A^{\frac{1}{3}}$.

wave function, *i.e.*, $[N_{\mathrm{osc}} n_3 \Lambda]\Omega$. Another popular convention, especially for large deformations, is to label a state as N_k, the k^{th} lowest-lying state with $N_{\mathrm{osc}} = N$.

2.2.3 Strutinsky Shell Correction

Neither the Nilsson nor Woods-Saxon calculations are able to predict, by themselves, the energies of deformed nuclear states. Although shell gaps can be reproduced by these calculations, the level spacing (or equivalently, level density) is, on the average, wrong. The liquid drop model, on the other hand, can be used to calculate the average binding energies of nuclei but has no means of accounting for the special stability at shell gaps. Strutinsky [Str 67] proposed a means of combining the two models by essentially replacing the (incorrect) smooth part of the shell-model energies,

$$E_{\mathrm{shell}} = \delta E_{\mathrm{shell}} + E_{\mathrm{shell}}^{\mathrm{smooth}} \tag{2.2.5}$$

with the liquid-drop energy, giving

$$\begin{aligned} E_{\mathrm{better}} &= E_{\mathrm{shell}} - E_{\mathrm{shell}}^{\mathrm{smooth}} + E_{\mathrm{LDM}} \\ &= \delta E_{\mathrm{shell}} + E_{\mathrm{LDM}}. \end{aligned} \tag{2.2.6}$$

The shell model energy of N like particles (neutrons or protons), which is a sum of individual energy eigenvalues e_k, can be written in terms of an integral with a density of states $g(e)$ which is a delta function at the shell-model energies,

$$E_{\text{shell}} = \sum_{k=1}^{N} e_k \tag{2.2.7a}$$

$$= \int^{\lambda} e\, g(e)\ de, \tag{2.2.7b}$$

$$g(e) = \sum_{k=1}^{N} \delta\left(e - e_k\right), \tag{2.2.7c}$$

where λ, the Fermi level energy, lies somewhere above e_N but below e_{N+1}. The density of states is convolved with a smoothing function,

$$\widetilde{g}\,(e) = \sum_{k=1}^{N} S(e - e_k)\,. \tag{2.2.8}$$

The smoothing function $S(e)$ has a characteristic width of approximately $\gamma_S \simeq \hbar\omega_0$, the same order as the width of any expected shell gap. Often it is taken as the product of a Gaussian and a Laguerre polynomial. The Laguerre factor reduces the detailed dependence of the results on γ_S. A new Fermi surface $\widetilde{\lambda}$ is calculated by enforcing the condition

$$N = \int^{\widetilde{\lambda}} \widetilde{g}(e)\ de. \tag{2.2.9}$$

The smooth component of the shell-model energy, then, is calculated as

$$E_{\text{shell}}^{\text{smooth}} = \int^{\widetilde{\lambda}} e\, \widetilde{g}(e)\ de. \tag{2.2.10}$$

For rotating nuclei, an angular momentum density function $g_{\mathcal{J}}(e)$ is smoothed in a similar manner and an angular momentum shell correction is applied [And 76].

2.2.4 Hartree-Fock method with Skyrme interaction

The problems of shape self-consistency and incorrect smooth level density are avoided when the Hartree-Fock [Har 28, Foc 30] equations are solved iteratively. What follows is by no means a rigorous derivation of the Hartree-Fock (HF) method, but is simply an attempt to indicate some of its critical features. Detailed derivations may be found in Chap. 5 of [RS 80] or Chap. 10 of [PB 75].

In the HF procedure, one starts with an orthogonal basis set $\{\chi_l\}$, for example the single-particle eigenfunctions from the Nilsson or Woods-Saxon Hamiltonians. From these states it will be necessary to construct a new, optimized set of wave functions $\{\phi_k\}$,

$$\phi_k = \sum_l D_{kl} \chi_l, \tag{2.2.11}$$

which will be eigenvalues of the eventual HF Hamiltonian,

$$h\phi_k = e_k \phi_k. \tag{2.2.12}$$

The goal of the HF procedure is to find the wave functions $\{\phi_k\}$ such that all particle-hole matrix elements vanish, that is, states above the Fermi surface do not interact with states below through one-particle, one-hole couplings.

If the creation/annihilation operators corresponding to the wave functions of the original basis set χ_l are $c_l{}^+/c_l$, then the HF creation operators are defined as

$$a_k{}^+ = \sum_l D_{kl} c_l{}^+ \tag{2.2.13}$$

and the antisymmetric HF wave function is

$$|\mathrm{HF}\rangle = |\Phi(1 \ldots A)\rangle = \prod_{i=1}^{A} a_i{}^+ |\mathrm{vacuum}\rangle. \tag{2.2.14}$$

The intensities of the original basis set states in the HF wave function are expressed in a density matrix

$$\rho_{ll'} = \langle \mathrm{HF}| c_{l'}{}^+ c_l |\mathrm{HF}\rangle. \tag{2.2.15}$$

In the χ basis, the total energy of the HF wave function is

$$E^{\mathrm{HF}}[\rho] = \sum_{kl} t_{kl}\rho_{kl} + \frac{1}{2}\sum_{ijkl} \rho_{ki}\bar{v}_{ijkl}\rho_{lj} \tag{2.2.16}$$

where t and $\bar{v}$ are the properly antisymmetrized matrix elements of kinetic energy and two-body interactions, respectively.

In the $\{\phi_k\}$ basis, the ρ matrix would be diagonal and would contain only ones and zeroes for occupied or unoccupied ϕ_k states. The energy is minimized,

$$\delta E = E[\rho + \delta\rho] - E[\rho] = 0, \tag{2.2.17}$$

under the constraint that $\rho + \delta\rho$ must itself be diagonal in the ϕ basis. A new matrix h is introduced,

$$\begin{aligned} h_{kk'} \equiv& \frac{\partial E^{\mathrm{HF}}[\rho]}{\partial \rho_{kk'}} \\ =& t_{kk'} + \sum_{ll'} \bar{v}_{kl'k'l}\rho_{ll'} \\ =& t_{kk'} + \Gamma_{kk'}, \end{aligned} \tag{2.2.18}$$

where Γ is referred to as the self-consistent field. It turns out that ρ and h commute, so they can be diagonalized simultaneously. The result is the final set of Hartree-Fock equations,

$$\sum_{l'} \left(t_{ll'} + \sum_{i=1}^{A} \sum_{pp'} \bar{v}_{lp'l'p} D_{pi} D^{*}_{p'i} \right) D_{l'k} = \epsilon_k D_{lk}, \tag{2.2.19}$$

which is a non-linear eigenvalue problem. The coefficients D_{lk} fully determine the HF basis set $\{\phi_k\}$ and therefore $|\mathrm{HF}\rangle$.

So far the discussion of HF has dealt with static systems. A rotating nuclear system can be treated in the more general time-dependent HF prescriptions, where one works with the Schrödigner equation of time evolution of the density matrix

$$i\hbar\frac{\partial \rho}{\partial t} = [h, \rho] \tag{2.2.20}$$

or within the cranking model of Sect. 2.3.

The Skyrme effective interaction [Sky 56, Sky 59] has proven to be an especially useful form for the interaction $\bar{v}_{ijkl}$, partly because of its treatment of density–dependent forces which arise from the tensor and short–range repulsive nature of the nucleon–nucleon interaction. The two- and three-body components are given by

$$\begin{aligned} V(1,2) =& t_0 \left(1 + x_0 P^\sigma\right) \delta\left(\vec{r}_1 - \vec{r}_2\right) \\ & + \tfrac{1}{2} t_1 \left[\delta\left(\vec{r}_1 - \vec{r}_2\right) \vec{k}^2 + \vec{k}^2 \delta\left(\vec{r}_1 - \vec{r}_2\right)\right] \\ & + t_2 \vec{k} \delta\left(\vec{r}_1 - \vec{r}_2\right) \vec{k} \\ & + i W_0 \left(\vec{\sigma}^{(1)} + \vec{\sigma}^{(2)}\right) \vec{k} \times \delta\left(\vec{r}_1 - \vec{r}_2\right) \vec{k}, \qquad (2.2.21a) \\ V(1,2,3) =& t_3 \delta\left(\vec{r}_1 - \vec{r}_2\right) \delta\left(\vec{r}_2 - \vec{r}_3\right) \qquad (2.2.21b) \end{aligned}$$

where

$$\vec{k} = \frac{1}{2i}\left(\vec{\nabla}_1 - \vec{\nabla}_2\right) = \frac{\vec{p}}{\hbar} \qquad (2.2.22)$$

is the relative momentum operator. The three-body term, Eq. (2.2.21b), is an effective density dependent potential. The set of parameters t_0, t_1, t_2, t_3, and W_0 are fit to reproduce experimentally observed static and low-energy properties of nuclei.

Because of the δ-function nature of the Skyrme effective interaction, it is convenient to compute matrix elements for this interaction in spatial coordinates. Specifically, the Hamiltonian will depend on six functions which can be calculated directly from the single-particle matrix ρ:

- particle density $\rho(\vec{r})$,
- kinetic energy density $\tau(\vec{r})$,
- spin density $\vec{s}(\vec{r})$,
- momentum density $\vec{j}(\vec{r})$,
- spin current tensor $J_{\mu\nu} = [(\nabla_\mu - \nabla'_\mu)\vec{s}_\nu(\vec{r},\vec{r}')]_{\vec{r}=\vec{r}'}$,
- vector kinetic energy density $\vec{T}(\vec{r}) = [\nabla \cdot \nabla' \vec{s}(\vec{r},\vec{r}')]_{\vec{r}=\vec{r}'}$.

Expressions for the Skyrme Hamiltonian density function are derived in [VB 73] for the static case and [Eng 75] for the time-dependent case.

Without any further constraints, the wave functions which solve the HF equations represent the *ground states* of nuclear systems. Expectation values such as energy and deformation can be evaluated from the HF wave functions. To calculate excited states, further constraints must be imposed, such as parity, angular momentum, and quadrupole deformation. A straightforward example is for an even-even nucleus which is deformed in its ground state. If the HF wave functions constrained to spins and parity $J^\pi = 2^+, 4^+, \ldots$, the energy spectrum would correspond to the excited states based on the rotation of the intrinsic $K = 0$ ground state. Application of the cranking model (to be described in Sect. 2.3) can be viewed as a constraint, in the sense that it assumes ahead of time that the final wave function corresponds to a collective rotor. The cranked HF–Skyrme codes employed in this work, which constrain quadrupole deformation, parity, signature (see Eq. (2.3.20)) and rotational frequency, are those of Dobaczewski and Dudek [DD 95]. The basis states $\{\chi_k\}$ are calculated in a Woods-Saxon potential. The (SkM*) [Bar 82] parameter set was employed for the Skyrme force in the time-dependent Hamiltonian. This state-of-the-art code is especially attractive for use in high-spin work because it takes full account of all time-dependent terms, unlike *e.g.* [BFH 87] and [BFH 91] where certain terms related to the spin-orbit coupling were omitted to facilitate the computations.

2.3. The Cranking Model

Although the cranking model was first introduced by Inglis in 1954, [Ing 54] its value as an analytical tool was made clear 18 years later when it was demonstrated that the backbending phenomenon [JRS 71, JRH 72] could be described by the alignment of a pair of nucleons to the rotation axis due to the Coriolis force [SS 72]. The cranking model is the semiclassical transformation of the nuclear Hamiltonian to the body-fixed (intrinsic) frame of the rotating model nucleus. The real intellectual triumph of the cranking model is in the ability to transform the quantities measured in the laboratory frame, namely spin and excitation energies deduced from γ–ray energies, into this intrinsic reference frame [BF 79]. This section describes the cranking model and the means of interpreting experimental data in terms of this model.

2.3.1 The Cranking Hamiltonian

The cranking model supposes that the mean-field Hamiltonian retains the same form in the intrinsic frame. Given a time-dependent single-particle potential $V(\vec{r}, t)$ which rotates in space with an angular velocity ω,

$$V\left(\vec{r}, t\right) = V\left(r, \theta, \phi - \omega t\right) \tag{2.3.1}$$

the Hamiltonian is given by

$$\hat{h}\left(t\right) = \frac{\hat{p}^2}{2m} + V\left(r, \theta, \phi - \omega t\right). \tag{2.3.2}$$

The time dependence of V may be removed by introducing the (unitary) screw transformation appropriate for fermions,

$$U = e^{i\omega t\ \hat{j}_x/\hbar} \tag{2.3.3}$$

with the boundary condition

$$U\hat{h}\left(t\right)U^{-1} = \hat{h}\left(0\right). \tag{2.3.4}$$

The Schrödinger representation of the time evolution is

$$\hat{h}(t)\,\phi(t) = i\hbar\frac{\partial\phi(t)}{\partial t} \tag{2.3.5}$$

and applying the screw transformation yields

$$U\hat{h}(t)\,U^{-1}U\phi(t) = i\hbar U\frac{\partial\phi(t)}{\partial t}. \tag{2.3.6}$$

If we use the transformed wave function

$$\tilde{\phi} = U\phi \tag{2.3.7}$$

and recognize that

$$\frac{\partial\tilde{\phi}}{\partial t} = U\frac{\partial\phi}{\partial t} + \frac{\partial U}{\partial t}\phi \tag{2.3.8}$$

Eq. (2.3.6) may be written (also with Eq. (2.3.4)

$$\hat{h}(0)\,\tilde{\phi} = i\hbar\frac{\partial\tilde{\phi}}{\partial t} + \omega\hat{j}_x\tilde{\phi}$$

or in a form more like Eq. (2.3.5),

$$i\hbar\frac{\partial\tilde{\phi}}{\partial t} = \left(\hat{h}(0) - \omega\hat{j}_x\right)\tilde{\phi}. \tag{2.3.9}$$

The operator in parentheses and its eigenvalue are referred to as the single-particle Routhians,

$$e' = \hat{r}\tilde{\phi}.$$

Summing over all occupied single-particle states gives the total Routhian operator,

$$\hat{R} = \hat{H}(0) - \omega\hat{J}_x \tag{2.3.10}$$

where $\hat{J}_x = \sum_{i=1}^{A}\hat{j}_x^{(i)}$, the sum of the x component of angular momenta for all nucleons in the system.

2.3.2 Aligned Spin and Rotational Frequency

Bengtsson and Frauendorf [BF 79] proposed a prescription for transforming experimental data from the laboratory frame to the intrinsic frame. Substituting the eigenvalues of the operators, Eq. (2.3.10) may be written

$$E'(\omega) = E(\omega) - \omega I_x(\omega) \tag{2.3.11}$$

where $I_x(\omega)$ is the experimental spin J projected on the laboratory frame x-axis. The I_x of that state J is given by

$$I_x(J) = \sqrt{(J)(J+1) - K^2} \tag{2.3.12a}$$

$$\simeq \sqrt{\left(J + \frac{1}{2}\right)^2 - K^2} \tag{2.3.12b}$$

$$\simeq \left(J + \frac{1}{2}\right), \qquad J \gg K \tag{2.3.12c}$$

where Eq. (2.3.12b) incorporates a semi-classical approximation for the eigenvalue of the angular momentum squared operator, $\langle J^2 \rangle = J(J+1) \sim (J+\frac{1}{2})^2$. For the very high spins typical of superdeformed states, the K^2 term becomes negligible and the approximation of Eq. (2.3.12c) is appropriate. The choice of nomenclature I_x, rather than J_x or I_1, is intended to indicate that this quantity is neither an intrinsic nor a laboratory-frame quantum number. However it is constrained in terms of the laboratory frame operator, $I_x = \langle \hat{J}_x \rangle$.

The angular frequency as a function of I is deduced from the canonical equation

$$\omega(I) = \frac{\partial E(I)}{\partial I_x(I)} \tag{2.3.13}$$

recast in finite form,

$$\omega(I) = \frac{E(J+1) - E(J-1)}{I_x(J+1) - I_x(J-1)}. \tag{2.3.14}$$

For a single stretched E2 ($\Delta J{=}2$) γ-ray transition between rotational states,

$$\omega(I) = \frac{E_\gamma(J+1 \to J-1)}{I_x(J+1) - I_x(J-1)} \tag{2.3.15a}$$

$$\sim \frac{E_\gamma(J+1 \to J-1)}{2\hbar}, \qquad I \gg K \tag{2.3.15b}$$

where Eq. (2.3.15b) applies the high-spin limit of Eq. (2.3.12c). The reader should again notice the distinction between J and I, namely that I does not refer to a real state but instead to an interpolation, for the purposes of the transformation to the intrinsic frame, between physical, observed, laboratory-frame states $J+1$ and $J-1$. In this sense, $I = J$.

It is customary to report $\hbar\omega$ with dimensions of energy, *e.g.*

$$\hbar\omega \simeq \frac{E_\gamma}{2}. \tag{2.3.16}$$

The experimental Routhian, given by

$$\begin{aligned} E'(I) &= E(I) - \omega(I)\, I_x(I) \\ &= \frac{1}{2}\left(E(J+1) + E(J-1)\right) - \omega(I)\, I_x(I) \end{aligned} \tag{2.3.17}$$

essentially measures the energy of the system in the rotating frame. Since both I_x and ω are functions of I, and since ω is conventionally treated as an independent variable in calculations, I_x is often taken to be a function of rotational frequency, $I_x(\omega)$.

A further quantity of interest is the aligned spin,

$$i_x(\omega) = I_x(\omega) - I_x^{ref}(\omega) \tag{2.3.18}$$

where $I_x^{ref}(\omega)$ is a smooth reference function which models the angular momentum associated with the collective rotation and possible shape evolution of the nuclear matter. It is often given in terms of Harris parameters[Har 65]

$$I_x^{ref}(\omega) = \mathcal{J}_0\omega + \mathcal{J}_1\omega^3 \tag{2.3.19}$$

where $\mathcal{J}_0$ and $\mathcal{J}_1$ are normally chosen to fit the rotational structure (if any) based on the ground state intrinsic structure of the nucleus or of a nearby even-even nucleus. The quantity i_x is the angular momentum which has not been associated with the the collective rotation of the fully paired, ground-state core. This quantity is sensitive to a sudden change in structure such as a configuration change or pair alignment and is a valuable tool in understanding the single-particle structure of rotational bands.

2.3.3 Signature

The cranking Hamiltonian is no longer invariant under time-reversal. As a consequence, it is also not invariant under rotations of 180° about the intrinsic 2 or 3 axes. Even for axially symmetric systems, K can therefore not be a good quantum number. However, if the intrinsic Hamiltonian is invariant under the 180° rotation about the 1 axis, then the laboratory-frame quantity *signature* remains a good quantum number,

$$r|\Psi\rangle = \exp\left(-i\pi\hat{J}_x\right)|\Psi\rangle. \tag{2.3.20}$$

(The signature quantum number r here is not the same as the Routhian operator $\hat{r}$.) The eigenvalues are ±1 and $\pm i$, which can be expressed in terms of the signature exponent α,

$$r = \exp(-i\pi\alpha)\,, \tag{2.3.21}$$

which is integer or half-integer. The quantity α is not strictly defined, since one can add or subtract some integer multiple of two without changing r; however, it is often a more convenient quantum number than r because it is additive. Since the signature and $\hat{J}_x$ operators commute, their eigenvalues will be related. In fact, the signature exponent is related to the total angular momentum by the selection rule

$$\alpha \bmod 2 = I \bmod 2. \tag{2.3.22}$$

The relationship between r, α and permitted values of I are listed in Table 2.3.1. In this work, the signature exponent α will be called simply the signature, and r

r	α	I
1	0	$0, 2, 4, \ldots$
$-i$	$+\frac{1}{2}$	$\frac{1}{2}, \frac{5}{2}, \frac{9}{2}, \ldots$
-1	± 1	$1, 3, 5, \ldots$
i	$-\frac{1}{2}$	$\frac{3}{2}, \frac{7}{2}, \frac{11}{2}, \ldots$

Table 2.3.1: Relationship between signature and angular momentum quantum numbers.

will be referred to as the signature eigenvalue. As a shorthand notation, the sign of the signature of an orbital may be expressed as a subscript in parenthesis, *e.g.* $\pi[301]\frac{1}{2}_{(+)}$ refers to an $\alpha = +\frac{1}{2}$ proton level which evolved from the $[301]\frac{1}{2}$ orbital as ω was increased from 0.

In the cranking Hamiltonian with nonzero ω, the only good quantum numbers for the single-particle states will, in fact, be signature and parity. At $\omega = 0$, two states $|j, m\rangle$ and $|j, -m\rangle$ are degenerate. Since m will be some half-integer, the signatures of these two single-particle states will be opposite. Such a pair of states will be called *signature partner* states. At low frequency, where K is still very nearly a good quantum number (for an axially symmetric Hamiltonian), the Coriolis force will split pairs of $K = 1/2$ orbitals (see Eq. (2.1.10)). The angular momentum vectors of these states are nearly parallel or antiparallel to the cranking axis, that is, $j = |m|$. The $+m$ state will fall in energy with increasing ω due to the $-\omega j_x$ term, and is said to be favoured, while the $-m$ state rises. The signature of the favoured state, $\alpha = m \bmod 2$ is equal to the modulo 2 of the angular momentum,

$$\alpha_{\text{favoured}} = j \bmod 2. \tag{2.3.23}$$

This favoured signature applies to *all* states from the same subshell, that is, those which evolved, under the influence of deformation and rotation, from the same

$2j+1$ multiplet of spherical shell-model states. However, aside from this low-frequency Coriolis splitting, states of different signature and parity (α, π) cannot interact. Therefore it is appropriate, especially at high spin, to classify states by their signature and separate them into $\Delta I = 2$ bands. This classification is further justified by the fact that, as will be explained in Sect. 2.6.2, the decay of the high-spin states of these bands is dominated by $\Delta I = 2$ transitions, which conserve signature.

A special case of bands called ***signature partner bands*** have the distinctive feature that the average of the energies of consecutive $\Delta I = 2$ transitions in one band is exactly equal to the energy of a transition in the other band. In other words, the peaks in the γ-ray spectrum of one band are at the midpoint between peaks in the other. This occurs when both signatures $(\alpha = \pm\frac{1}{2})$ of a $|j, \pm m\rangle$ pair remain degenerate with rotational frequency (*i.e.* their wave functions contain no $K = \frac{1}{2}$ component). The eigenvalues of the single-particle Routhians, $\hat{r} = e - \omega \hat{j}_x$, will be exactly the same. In the high-spin limit of $I_x = I$, this furthermore means that $I(\omega)$ and its inverse function $\omega(I)$ would be the same for both configurations. The spin sequence of the two bands, $I + \frac{1}{2} \ldots$ and $I - \frac{1}{2} \ldots$, define interleaved sampling points of $\Delta I = 1$ for $\omega(I)$. Thus the emitted $\Delta I = 2$ γ rays $(E_\gamma = 2\hbar\omega)$ follow the previously-mentioned mutual midpoint pattern. If instead the $|j, \pm m\rangle$ levels are *split* by the Coriolis force, the spectra from the rotational bands built on these two possible configurations will not follow the special midpoint pattern.

The existence of signature partner bands is often taken as strong evidence that the two bands involve the two signatures of a pair of $K \neq \frac{1}{2}$ orbitals. A weaker statement which is sometimes made, is that if a band is observed with *no* evidence of a signature partner band, that the valence particle configuration must involve orbitals which are split.

2.3.4 Moments of Inertia

One of the features of superdeformed bands is that when the inner barrier becomes low enough that γ–ray decay to non-SD states begins to compete with in-band transitions, the de-excitation paths are so numerous that no direct *linking transitions* can be observed. As a consequence the spins of superdeformed states cannot be established uniquely and unambiguously from γ rays alone. However there exists a mechanical quantity, the dynamic moment of inertia $\mathcal{J}^{(2)}$, which can be measured without explicit knowledge of the spins of the states in a rotational band.

The rotational term of the collective Hamiltonian, Eq. (2.1.9a), is essentially that of a perfect rotor if $\mathcal{J}$ is constant,

$$E = \frac{\hbar^2}{2\mathcal{J}} J\,(J+1)\,.$$

This inertial parameter can be calculated from single-particle wave functions with the Inglis formula,

$$\mathcal{J}_{\text{Inglis}} = 2 \cdot \sum_{mi} \frac{|\langle m|J_x|i\rangle|^2}{\epsilon_m - \epsilon_i} \tag{2.3.24}$$

where the index m is for all states above the Fermi surface and i, all states below. However, the cranking model provides a somewhat more transparent means of calculating moments of inertia and extracting useful values experimentally.

To study the changes in the rotating system we consider the kinematic $\mathcal{J}^{(1)}$ and dynamic $\mathcal{J}^{(2)}$ moments of inertia,

$$\mathcal{J}^{(1)} = \frac{I}{\omega} = I\left(\frac{\partial E}{\partial I}\right)^{-1} \tag{2.3.25a}$$

$$\mathcal{J}^{(2)} = \frac{\partial I}{\partial \omega} = \left(\frac{\partial^2 E}{\partial I^2}\right)^{-1}. \tag{2.3.25b}$$

These expressions have also been recast in terms of the first and second derivative of energy as a function of spin, to demonstrate that the quantity $\mathcal{J}^{(2)}$ will be the more sensitive to deviations of the nuclear system from pure rotational behavior.

Since in the cranking model ω is an independent parameter, these quantities become simple functions which are easily extracted from calculations. To evaluate these values experimentally, we again consider the high-spin limit. For one stretched E2 γ-ray transition between states J and $J-2$, the $\mathcal{J}^{(1)}$ value is estimated from first differences:

$$\begin{aligned} E_J - E_{J-2} &= \frac{\hbar^2}{2\mathcal{J}^{(1)}}\left[J\,(J+1) - (J-2)\,(J-1)\right] \\ E_\gamma &= \frac{\hbar^2}{2\mathcal{J}^{(1)}}\,(4J-2) \\ \mathcal{J}^{(1)} &= \frac{\hbar^2}{E_\gamma}\,(4J-2)\,. \end{aligned} \tag{2.3.26}$$

This is defined at $\hbar\omega = E_\gamma/2$. From two γ rays cascade $(J+2)\rightarrow J\rightarrow(J-2)$, the second difference of the energy of the states from the difference of the γ-ray energies gives an expression for $\mathcal{J}^{(2)}$,

$$\begin{aligned} E_{\gamma 1} - E_{\gamma 2} &= \frac{\hbar^2}{2\mathcal{J}^{(2)}}\left[(4\,(J+2)-2) - (4\,(J)-2)\right] \\ \Delta E_\gamma &= \frac{\hbar^2}{2\mathcal{J}^{(2)}}\left[(4\,(J+2)-2) - (4\,(J)-2)\right] \\ \mathcal{J}^{(2)} &= \frac{4\hbar^2}{\Delta E_\gamma}. \end{aligned} \tag{2.3.27}$$

This function, which is defined at $\hbar\omega = (E_{\gamma 1} - E_{\gamma 2})/4$, is independent of the actual spins of the states J. As was mentioned before, this quantity will also be the most sensitive to changes in the collective rotational behavior which may arise due to changes in the internal (*e.g.* single-particle) structure.

2.3.5 Effective alignment

Although the $\mathcal{J}^{(2)}$ values may be used to infer the systematics of single-particle occupancy in rotational structures, they are not themselves a direct measurement of the single particles themselves. For this the effective alignment $\Delta i_x(\omega)$ is introduced. It is defined as the difference in the angular momentum between two systems at a given rotational frequency. Like the dynamic moment of inertia, the experimental value is deduced from differences in consecutive γ-ray energies, see Eq. (2.3.34). Figs. 2.3.1 and 2.3.2 should be adequate to explain how to extract and interpret this value, but for completeness a rigorous derivation is also presented.

Consider the specific example of two yrast bands A and B (note Roman letters) in neighbouring nuclei of mass $A+1$ and A, respectively (note Italic letters). Rather than use the Harris formula, Eq. (2.3.19), one could instead use the measured characteristics of band B to study band A. The difference in spin projected along the rotation axis,

$$\Delta i_x(\omega) = I_x^{\mathrm{A}}(\omega) - I_x^{\mathrm{B}}(\omega) \tag{2.3.28}$$

is identical to the difference in aligned spins, $i_x^{\mathrm{A}} - i_x^{\mathrm{B}}$, if the same (*e.g.* Harris) reference parameters are used. If band B is a robust deformed core (for example, is doubly-magic) then one estimates that the wave function of that core is not substantially modified by the existence of an additional nucleon. Then for the band A one can immediately see that

$$\begin{aligned} \Delta i_x &= I_x^{\mathrm{A}}(\omega) - I_x^{\mathrm{B}}(\omega) \\ &= \sum_{i=1}^{A+1} \langle j_x^{(i)} \rangle - \sum_{i=1}^{A} \langle j_x^{(i)} \rangle . \\ &= \langle j_x^{(A+1)} \rangle \end{aligned}$$

This means that in the case of a well-defined, stable core, $\Delta i_x(\omega)$ directly measures the j_x of the extra nucleon. In this work, the band which we compare to a core or reference will be referred to as a target band, *e.g.* band A in the above example.

Since cranking calculations are normally done at a set of fixed frequencies $\{\omega\}$, the projection of spin I_x extracted from these calculations may be interpolated to continuous functions $I_x^{tgt}(\omega)$ and $I_x^{ref}(\omega)$. Then $\Delta i_x(\omega)$ is also a continuous function. This is demonstrated schematically in Figure 2.3.1. Similarly, the observation of a γ ray samples the experimental function $I_x'(\hbar\omega = E_\gamma/2)$. The lowest-lying γ ray, with energy $E_{\gamma 0}$, is the transition between states of spin $\hbar(I_0+2)$ and $\hbar I_0$, and samples the projected spin I_x of the artificial state $\hbar(I_0+1)$ at frequency $\hbar\omega_0 = E_{\gamma 0}/2$

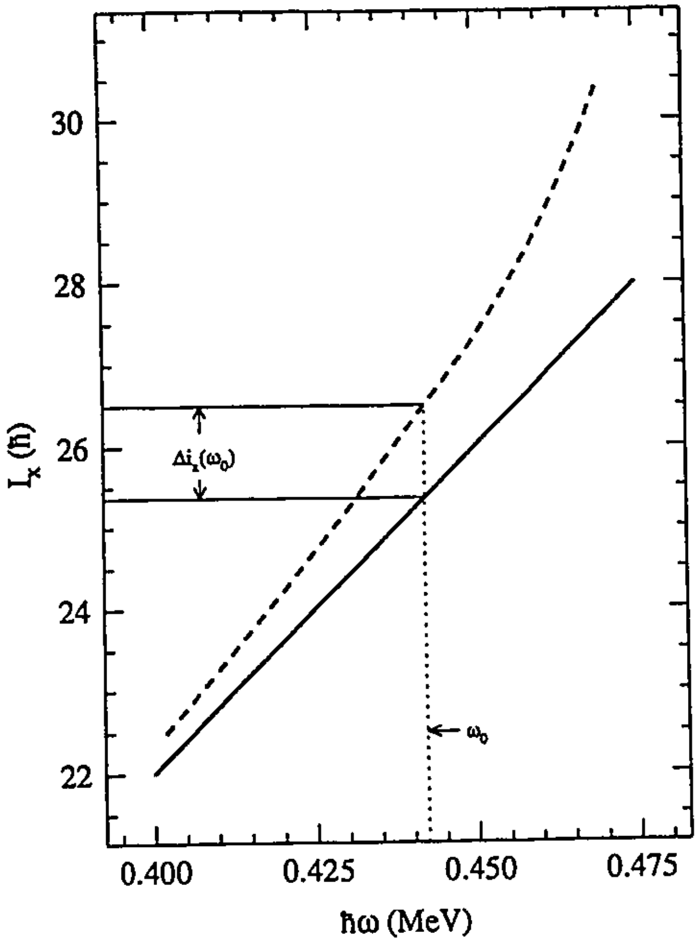

Figure 2.3.1:
Schematic of effective alignment $\Delta i_x(\omega)$ extracted from a pair of calculated $I_x(\omega)$ functions.

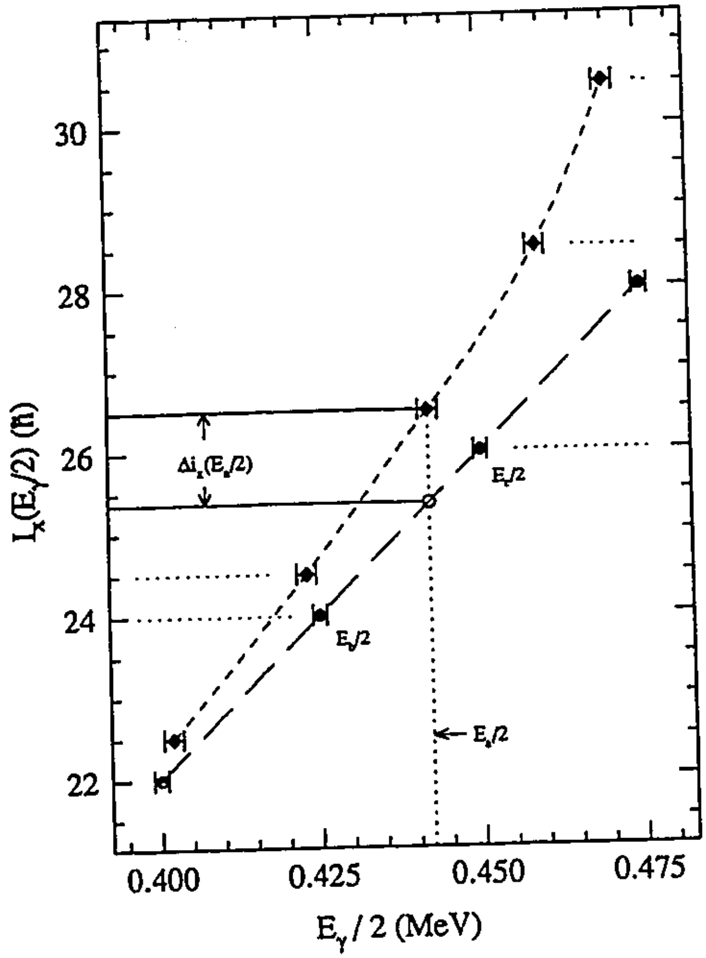

Figure 2.3.2:

Schematic of effective alignment $\Delta i_x(\omega)$ extracted from experimental data. The target band, denoted by diamond symbols, has a signature α which is $1/2\hbar$ greater than the reference band, denoted by circles, so the data points for the reference lie at $I_x^{ref} \simeq I^{ref} = I_0, I_0 + 2\hbar, \ldots$ while the target band points are at $I_x^{tgt} \simeq I^{tgt} = I_0 + 1/2\hbar, I_0 + 5/2\hbar, \ldots$.

(see Eq. (2.3.12)). The projected spin associated with the first γ ray, then, is given by

$$I'_x\left(E_{\gamma_0}\right) = I'_x(0) = I'_0 + (3/2)\,\hbar \tag{2.3.29}$$

following the high-spin expression Eq. (2.3.12c). For the higher-lying γ rays,

$$I'_x\left(E_{\gamma_k}\right) = I'_x(k) = I'_0 + (3/2 + 2k)\,\hbar. \tag{2.3.30}$$

At a frequency given by $E_{\gamma_a}^{tgt}$, the function $I'^{tgt}_x(E_{\gamma_a}^{tgt}) = I'^{tgt}_x(a)$, but it is unlikely there will be a sampling point (*i.e.* a γ ray) of exactly that energy in the reference $I'^{ref}_x(a)$. Instead the reference function must be interpolated, for example by the lowest-order terms of a Taylor expansion,

$$I'^{ref}_x(a) = I'^{ref}_x(b) + \left(E_{\gamma_a}^{tgt} - E_{\gamma_b}^{ref}\right)\cdot\frac{\partial I'^{ref}_x}{\partial E_\gamma^{ref}}(a). \tag{2.3.31}$$

If the target γ-ray's energy $E_{\gamma_a}^{tgt}$ is between two γ rays in the reference $E_{\gamma_b}^{ref}$ and $E_{\gamma_c}^{ref}$,

$$\frac{\partial I'^{ref}_x}{\partial E_\gamma^{ref}}(a) \simeq \frac{I'^{ref}_x(c) - I'^{ref}_x(b)}{E_{\gamma_c}^{ref} - E_{\gamma_b}^{ref}}, \qquad E_{\gamma_b}^{ref} \le E_{\gamma_a}^{tgt} \le E_{\gamma_c}^{ref}, \tag{2.3.32}$$

and furthermore, if $E_{\gamma_b}^{ref}$ and $E_{\gamma_c}^{ref}$ are consecutive decays in the reference band (*i.e.* $c = b + 1$), then $\Delta I'_x = 2\hbar$ in the high spin limit. The full expression for the reference band, then, is

$$\begin{aligned} I'^{ref}_x(a) = {}& I'^{ref}_0 + \left(3/2 + 2b + 2\frac{\left(E_{\gamma_a}^{tgt} - E_{\gamma_b}^{ref}\right)}{\left(E_{\gamma_c}^{ref} - E_{\gamma_b}^{ref}\right)}\right)\hbar, \\ & E_{\gamma_b} \le E_{\gamma_a} \le E_{\gamma_c}, \\ & c = b + 1. \end{aligned} \tag{2.3.33}$$

The $3/2\hbar$ terms cancel in the calculated effective alignment and the result is

$$\Delta i_x\left(E_\gamma^{tgt}(a)\right) = \left(I'^{tgt}_0 - I'^{ref}_0\right) + 2\hbar(a-b) + 2\hbar\left(\frac{E_{\gamma_a}^{tgt} - E_{\gamma_b}^{ref}}{E_{\gamma_c}^{ref} - E_{\gamma_b}^{ref}}\right). \tag{2.3.34}$$

Figure 2.3.2 shows a schematic case of a reference band with a constant $\mathcal{J}^{(1)}$ so that I'^{ref}_x is a linear function of E_γ. The target band is in a nucleus which differs by one nucleon from the reference band, such that the signature of the target band is 1/2 larger than the reference band. Thus the sampled I_x for the reference band follows a pattern $I, I+2\hbar, I+4\hbar\ldots$ while the target band data points go as $I+1/2\hbar, I+5/2\hbar, I+9/2\hbar\ldots$.

If the reference and target band both follow the same projected spin function $I_x(\omega)$, but the target band is in a nucleus differing by one nucleon (hence $I^{tgt} = I^{ref} \pm 1/2\hbar$), one can work backwards from Eq. (2.3.34) to see that the energies of the γ rays in the target band would be equal to those of the reference γ rays plus or minus one-quarter of the difference in consecutive γ–ray energies. (This could also be seen by reading off the values of $\hbar\omega = E_\gamma/2$ on the x-axis of Figure 2.3.2 for $I_x = I, I+1/2, I+2$.) These are the "quarter-point" bands. By the same argument, isospectral bands in nuclei A and $A+1$ would have to have an effective alignment of $1/2\hbar$.

This definition of effective alignment is favoured in studies of A~150 superdeformed nuclei [Rag 93a]. A similar quantity which is more popular in the A~190 superdeformed region, the "incremental alignment," [Ste 90] is defined simply as

$$\Delta i_{\mathrm{inc}} = 2\frac{\Delta {E_\gamma}^{\mathrm{tgt}}}{E_{\gamma_b}^{\mathrm{ref}} - E_{\gamma_c}^{\mathrm{ref}}} \qquad (2.3.35)$$

where ΔE_γ is the difference between E_{γ_a} and E_{γ_b} or E_{γ_c}, whichever is closer. This quantity is restricted to values between -1 and $+1$, and makes no assumptions about the spins of the states in the bands. Throughout this work the effective alignment will be used, not the incremental alignment.

The definition of Δi_x in Eq. (2.3.34) implies that the spins of the states in both the reference and target, or more precisely, the difference in bandhead spins ΔI_0 must be known. As was pointed out before, spins of states in superdeformed bands are not known. However, there are certain selection rules which may be followed in assigning a possible ΔI_0 between two bands. Clearly the first consideration is that if the two bands are in nuclei differing by an odd number of nucleons, then ΔI_0 must be a half-integer multiple of $\hbar$, while if the two bands differ by an even number of nucleons, ΔI_0 must be an integer multiple of $\hbar$. When comparing the experimental Δi_x to theoretical configurations which differ in signature by $\Delta\alpha$, there is an additional constraint $\Delta I_0 \bmod 2 = \Delta\alpha$. This will not uniquely define ΔI_0, but one can predict a value for ΔI_0 on the basis of which value best fits the calculated Δi_x in a given model. This synthesis has been applied with great success in the $A{\sim}150$ region [Haa 93, Fli 95]. In these works, a self-consistent assignment of ΔI_0 values between bands were proposed which reproduced the experimentally observed effective alignments for the 13 superdeformed bands reported in the Gd isotopes.

2.4. Pairing

The mean-field discussions so far have only dealt with single-particle phenomena, that is, particle-hole correlations. By themselves, single-particle models cannot reproduce either the odd-even mass difference of the ground states of nuclei, nor can they explain why all even-N, even-Z nuclei have ground states with $J^\pi = 0^+$. In addition, the observed moments of inertia of low-lying rotational bands is somewhat less than calculated by single-particle models; instead they are somewhere between the expected values for rotational flow and irrotational flow. All of these effects are ascribed to pairing correlations.

Following the simplistic, semi-classical description of pairing in [Cas 90], consider two nucleons near the Fermi surface in some sort of mean field. The matrix element for a short-range residual attraction $V_{\rm short}$ between these two particles is largest for pairs of orbits which intersect or, equivalently, whose wave functions overlap. Classically the angular momentum vectors of such orbits would be nearly parallel or anti-parallel. In terms of angular momentum wave functions, the largest matrix element $\langle j_1 m_1 | V_{\rm short} | j_2 m_2 \rangle$ occurs when the orbitals have the same j and nearly the same absolute value of $|m|$.

For heavy nuclei, the proton orbitals near the Fermi surface have different wave functions (different j) than the neutron wave functions, hence the matrix element for proton-neutron pairs is negligible (although for $N \sim Z$ light or exotic heavy nuclei these may become important [Cam 94, Jan 93]) . This leaves proton-proton and neutron-neutron systems. Since nucleons are fermions and obey the Pauli exclusion principle, two like nucleons cannot have the same wave function. Therefore the largest matrix elements occur for the $|j, m\rangle |j, -m\rangle$ system of like particles, and such a system is called a *pair*. Semi-classically these wave functions correspond to orbits in the same plane but in opposite directions, *i.e.*, one orbit is time-reversed to the other. A time-reversed orbit is often denoted by an overbar, *e.g.* $|\psi\rangle$ and $|\bar{\psi}\rangle$. The pairs couple to a net angular momentum and parity 0^+.

If, for example, V_{short} is taken as an attractive delta function $-G\delta(\vec{r}_2 - \vec{r}_1)$ for one single-particle j subshell, energies of the the $J = 0$ many-body state will be reduced in energy while the $J = 2, 4, \ldots$ states remain degenerate. In the ground state of an even-N, even-Z system, all of the nucleons can "pair off" such that the angular momentum and parity of the ground state is also 0^+, as is observed.

These pairs themselves can interact and scatter, which will mix their $|j, \pm m\rangle$ components. However in the single-particle ansatz the absolute value of the amplitude of any of the single-particle wave functions must be either one or zero, that is, the orbital must be occupied or empty. Pair mixing implies that the single-particle states involved in these correlations would have fractional amplitude, that is, would be partially occupied. Therefore, pairing cannot be treated in detail in a strict single-particle formalism. Partial occupation numbers are treated by applying the BCS theory of metallic superconductors [BCS 57], but by considering angular rather than linear momentum [BMP 58]. In this model the interactions between the available pair states results in the pairing gap Δ, which is the even-odd mass difference. From this gap, the single-particle occupation amplitudes are calculated. Then the Bogolyubov transformation [Bog 58] recasts the paired wave function as occupied or unoccupied "quasi-particle" states which are linear combinations of the single-particle wave functions. Quasi-particles are, in this approximation, non-interacting. The energies of the quasi-particle states are given in terms of renormalized single-particle energies e'_ν, the Fermi energy λ and the pairing gap,

$$E_\nu = \sqrt{(e'_\nu - \lambda)^2 + \Delta^2}. \tag{2.4.1}$$

If the nucleus is rotating, then the time-reversed orbitals, which are degenerate in the static case, will be split. This weakens the pairing between these two orbitals. Eventually the two particles will no longer be bound by the residual interaction, and the wave function of the $|j, -m\rangle$ single particle will evolve to a state with the maximum m permitted by the exclusion principle. That is, the particle in the pair whose angular momentum was anti-parallel to the rotation axis, now attempts to align to it. If this occurs over a short range of increasing angular momentum, then the rotational angular momentum can actually decrease as it is transferred to the broken pair. The rotational frequency, and hence γ-ray energy, also decreases. This is often called "backbending," since the γ-ray spectrum appears to switch back upon itself. If the effect is more spread out and occurs over several states, then the γ-ray spacing will be compressed and the moment of inertia will briefly rise.

As rotation increases, more of these pairs will weaken and eventually break. Since the number of available pair states decreases, the pairing gap also decreases. When it reaches zero, there is no more pairing. It is estimated that pairing correlations will be fully quenched above $\sim 30\hbar$ [DS 80]. For $A{\sim}140 - 150$ nuclei, pairing should only be important in the lowest observed states of superdeformed bands (cf. [Cur 95]).

2.5. Pseudo-Spin

As was mentioned previously, the Nilsson model has the advantage of simple wave functions from which calculated values are easily extracted. In the case of the decoupling parameter Eq. (2.1.12),

$$a = \langle [N_{\mathrm{osc}} n_z \Lambda]\, \Omega | j_+ e^{-i\pi j_1} | [N_{\mathrm{osc}} n_z \Lambda]\, \Omega \rangle,$$

it is non-zero only for $\Omega = \frac{1}{2}$ states. In the asymptotic limit of extreme deformation ($\epsilon \rightarrow \infty$) it reduces simply to

$$a_{\mathrm{asymp}} = (-1)^{N_{\mathrm{osc}}}\,, \mathrm{iff}\ \ \Omega = \frac{1}{2}\ \ \mathrm{and}\ \ \Lambda = 0. \tag{2.5.1}$$

However detailed calculations for finite deformations did not reflect the expected trends from the asymptotic expression. Instead, it turned out that the exact decoupling parameters were better modeled in the asymptotic limit if ***pseudo-spin*** quantum numbers were used [HA 69, AHS 69]. The pseudo-spin scheme evolved from the observation that the Nilsson levels $[N_{\mathrm{osc}} n_z (\Lambda - 2)](\Omega = (\Lambda - 2) + \frac{1}{2})$ and $[N_{\mathrm{osc}} n_z \Lambda](\Omega = \Lambda - \frac{1}{2})$ were almost degenerate. If one uses the pseudo-spin Nilsson quantum numbers,

$$\widetilde{N} = N_{\mathrm{osc}} - 1, \tag{2.5.2a}$$

$$\widetilde{n} = n_z, \tag{2.5.2b}$$

$$\widetilde{\Lambda} = \Lambda - 1, \tag{2.5.2c}$$

then these two orbitals can be thought of as having identical pseudo-orbital quantum numbers and opposite pseudo-intrinsic spin $\widetilde{\Sigma} = \pm\frac{1}{2}$. Note that Ω is unchanged by the transformation to pseudo-spin.

Orbitals with $\Lambda = 1$ and $\Omega = \frac{1}{2}$ will not have pseudo-spin partners, but because they become $\widetilde{\Lambda} = 0$, these are the orbitals which will have non-zero decoupling parameters in the asymptotic limit. For example, a $[301]\frac{1}{2}$ orbital would be expressed in the pseudo-Nilsson quantum numbers as $[\widetilde{200}]\frac{1}{2}$, while a $[411]\frac{1}{2}$ orbital becomes $[\widetilde{310}]\frac{1}{2}$. In the latter ($\widetilde{N} = 3$) case, the asymptotic decoupling parameter would be $\widetilde{a}_{\rm asymp} = -1$. Experimentally, the decoupling parameter for a $\pi[411]\frac{1}{2}$ band in ^{177}Lu was measured to be -0.91 [EH 75], rather than $a_{\rm asymp} = 0$ as would be expected from the asymptotic limit of conventional Nilsson numbers. It was also demonstrated, for low-j orbitals in the moderately-deformed $155 < A < 185$ nuclei, that the values of a calculated from Nilsson wave functions with finite deformation were closer to the pseudo-spin asymptotic values than the standard values [BHM 82].

The previous discussion has ignored the question of whether or not the asymptotic limit of the pseudo-spin coupling scheme is relevant for SD bands. Experimentally, the observation of isospectral pairs of SD bands along the $N = 86$ chain of isotones [Byr 90] is partially explained by invoking pseudo-spin, and the decoupling parameters a deduced from γ-ray energies were consistent with $\widetilde{a}_{\rm asymp}$. The theoretical justification, and further details about pseudo-spin and the pseudo-$SU(3)$ symmetry, can be found in [Naz 90] and references therein. It must be pointed out that pseudo-spin by itself cannot explain identical $\mathcal{J}^{(2)}$ values between bands.

2.6. Population and Observation of Superdeformed States

Until now the discussion has focussed on the theoretical tools pertinent to the *structure* of superdeformed states. Experimentally, these highly-excited states can be populated in fusion-evaporation reactions. A beam of heavy ions with a velocity of a few percent of the speed of light is directed upon a target material. If a beam nucleus comes close enough to a target nucleus, the two nuclei may fuse and form a compound system. An off-center collision will impart angular momentum to the system. The highly-excited system may then fission, or it may evaporate particles as it cools down. The residual system will still be highly excited and will emit γ rays. The details of fusion-evaporation reactions (Figure 2.6.1) and γ-ray decay (Figure 2.6.3) will be briefly reviewed in this section.

2.6.1 Heavy-Ion Fusion-Evaporation Reactions

The fusion-evaporation reactions which were just described will now be considered in some depth. The de Broglie wavelength in the centre of mass frame, $\lambdabar = \hbar/\sqrt{2E_{\mathrm{c.m}}\mu}$ where μ is the reduced mass, is quite small compared to the typical size of the nuclei themselves. The total reaction cross-section is given by a sum over partial waves. But if one assumes that all partial waves contribute fully up to a cutoff l_{max} with no contribution beyond that limit, the total cross section reduces to $\sigma_R = \pi\lambdabar^2(l_{\mathrm{max}}+1)$ [Szy 83]. The value of l_{max} itself is estimated as [DS 80]:

$$l_{\mathrm{max}} = 0.219\,(R_{\mathrm{int}})\left[\mu\left(E_{\mathrm{c.m.}} - V\left(R_{\mathrm{int}}\right)\right)\right]^{\frac{1}{2}} \tag{2.6.1}$$

where R_{int} is the approach distance in fm, μ is in atomic mass units, and $E_{\mathrm{c.m.}}$ and $V(R_{\mathrm{int}})$ are in MeV. R_{int} is estimated as sum of the radii target and beam nuclei with a small correction for tunneling effects,

$$R_{\mathrm{int}} = 1.16\left(A_1^{1/3} + A_2^{1/3} + 2\right)\ \mathrm{fm}. \tag{2.6.2}$$

The $V(R_{\mathrm{int}})$ term is the Coulomb barrier,

$$V\left(R_{\mathrm{int}}\right) = 1.44\frac{Z_1 Z_2}{R_{\mathrm{int}}}\ \mathrm{MeV}. \tag{2.6.3}$$

Eq. (2.6.1) for $l_{\max}$ includes all possible partial waves, including the highest ones which will dominantly contribute to particle transfer or deep inelastic scattering rather than full fusion, hence this estimate for $l_{\max}$ and for the the total reaction cross section is an upper limit for fusion reactions.

Following fusion, the most likely processes are fission and particle evaporation. The latter typically occurs on a time scale of 10^{-17} to 10^{-18} seconds, and the former depends on the barrier height which itself depends on the angular momentum of the system. When the barrier height for fission and the neutron binding energy are approximately equal ($\sim$8 MeV), the two processes have roughly the same cross section. Figure 2.6.2 demonstrates a calculated curve of the angular momentum at which a nuclear liquid drop of mass A has an 8 MeV barrier against fission. Above this line, fission dominates; below, particle evaporation will dominate. In the $A\sim140$ region this boundary is around $70\hbar$ [DS 80].

The compound system can cool most rapidly by particle evaporation, *i.e.* by the emission of neutrons, protons and alpha particles. Usually neutron evaporation is the dominant process because protons and alpha particles must overcome the Coulomb barrier which is not present for neutrons, but in reactions involving very high center of mass energies or highly neutron-deficient compound systems, the charged-particle cross sections become important. As each neutron (or charged particle) is emitted it carries away its binding energy, some kinetic energy, and a very small amount of angular momentum from the system, see Figure 2.6.1. Evaporation can only continue so long as final states in the residual nucleus are available. Recall that the yrast line, the minimum-energy state at a given angular momentum, behaves approximately like a rigid (cold) rotor. No states exist below this line, so the evaporation process stops when the residual nucleus is less than one particle binding energy above the yrast line. The kinetic energy and angular momentum carried off by evaporated particles could be calculated in a statistical model [Hil 79] but an appropriate rule of thumb for designing an experiment with specific spin-energy entry conditions is to take the values of the total kinetic energy

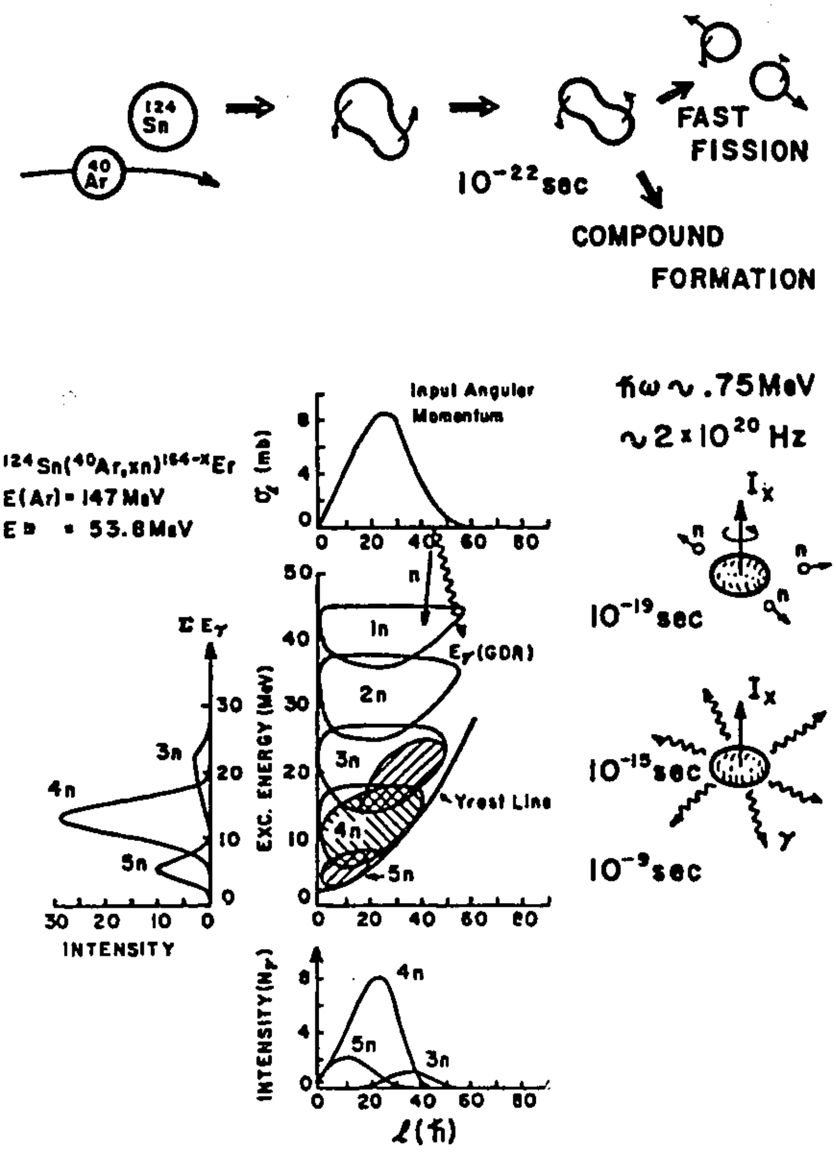

Figure 2.6.1: Statistical model calculations for heavy-ion fusion-evaporation reaction leading to high-spin states. Shaded regions will not emit any more particles and decay by γ-ray emission. Taken from [Hil 79].

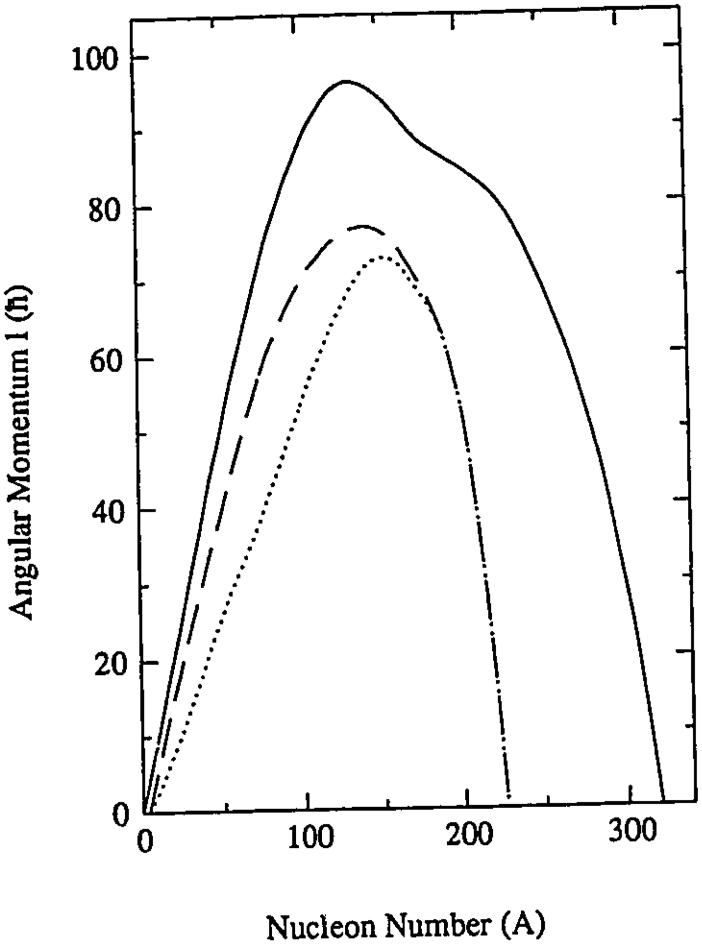

Figure 2.6.2: Solid line, angular momentum at which calculated fusion barrier disappears for nuclear liquid drops of various masses. Dashed line, fusion barrier of 8 MeV. Dotted line, estimate of boundary between particle evaporation (above) and γ-ray emission (below). Adapted from [DS 80].

and angular momentum removed by a given xn evaporation as 1.5 MeV of kinetic energy and $1\hbar$ of angular momentum per neutron.

2.6.2 Gamma-Ray Cascades

The γ rays emitted by the residual nucleus as it decays to the ground state fall into three distinct categories:

- statistical

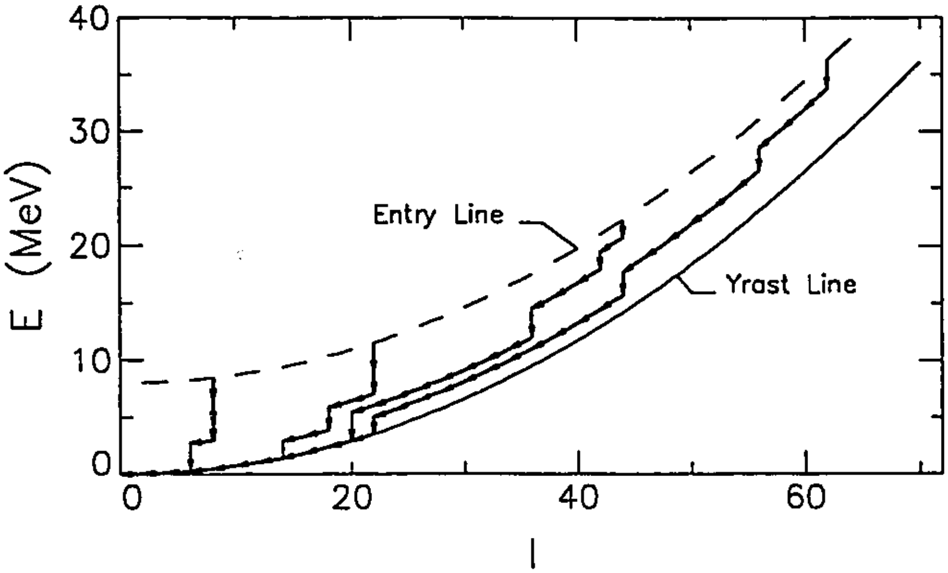

Figure 2.6.3: Typical γ-ray cascades, following particle evaporation, which de-excite a nucleus to its ground state after a heavy-ion reaction. Statistical transitions, which remove energy but very little angular momentum from the system, are indicated by the vertical arrows. Quasi-continuum collective transitions run parallel to the yrast line. The transitions nearest to the yrast line have the highest intensity and are most likely to be observed as discrete peaks. From [DS 80].

- quasi-continuum collective
- near-yrast

These are illustrated schematically in Figure 2.6.3. This thesis emphasizes the near-yrast transitions, although quasi-continuum will also be examined in limited scope.

The electromagnetic interaction in nuclei is described in detail in [PB 75]. Like any quantal transition, γ-ray decay from one nuclear state to another is characterized by a transition probability T which is related to the transition width Γ and mean lifetime τ by

$$T = \frac{\Gamma}{\hbar} = \frac{1}{\tau}. \tag{2.6.4}$$

The decay probability is proportional to Γ and is determined by the matrix element H_{if}^{EM} between the final and initial states,

$$T \propto |\langle f|H^{\mathrm{EM}}|i\rangle|^2. \tag{2.6.5}$$

The electromagnetic interaction operator may be expanded in terms of multipole operators $\mathcal{M}_{slm}$, where l and m are familiar angular momentum quantum numbers associated with the electromagnetic field and the s subscript indicates whether the transition is electric or magnetic in character. The parity of the operator is

$$\pi = (-1)^l, \qquad \text{electric} \tag{2.6.6a}$$

$$= (-1)^{l-1}, \qquad \text{magnetic.} \tag{2.6.6b}$$

Often the orientation of neither the initial nor final states are of interest, and the multipole operators are summed over all possible m values. The factors which relate to the details of the initial and final states are conveniently expressed as a reduced transition probability $B(sl)$,

$$B\left(sl, J_i \rightarrow J_f\right) = \frac{1}{2J_i+1} \cdot \sum_{m_f,m_i} |\langle J_f m_f|\mathcal{M}_{sl(m_f-m_i)}|J_i m_i\rangle|^2, \tag{2.6.7}$$

where J_i and J_f are the total angular momenta of the initial and final states respectively. Then the transition rate between the two states for one transition type sl is given, in full, by

$$T(sl) = \frac{1}{\hbar} \cdot \frac{8\pi (l+1)}{l\,[(2l+1)!!]^2} \cdot \left(\frac{E_\gamma}{\hbar c}\right)^{(2l+1)} \cdot B(sl)\,. \tag{2.6.8}$$

The total transition rate includes all sl combinations which satisfy selection rules of angular momentum, determined by the vector addition rule $l \geq |J_f - J_i|$, and parity. When $l = |J_f - J_i|$, the transition l is said to be *stretched.* The transition between two states J^+ and $(J-1)^-$ must be a parity-changing transition with at least one unit of angular momentum. A stretched electric dipole (E1) transition satisfies these criteria, as does a magnetic quadrupole (M2) transition, but the matrix elements are so small for M2 transitions that the E1 rate (usually) overwhelmingly dominates the total transition rate. Similarly, the transitions between J^+ and $(J-1)^+$ states could be an admixture of E2 and stretched M1 transition types. In deformed nuclei the E2 transition probability is enhanced, as will be discussed shortly, and so the the E2 and M1 transition rates can be comparable.

In the special case of a rotating deformed nucleus, the $B(\mathrm{E2})$ value can be expressed in terms of the deformation parameter β. The simplest case is that of in-band transitions of an axially symmetric $K = 0$ rotational structure. In this case, Eq. (2.6.7) reduces quite simply to a collective and intrinsic component. The collective part becomes a Clebsch-Gordon coefficient, so for the an intrinsic wave function $|X\rangle$,

$$B\,(\mathrm{E2}) = |\langle J_i 200|J_f 0\rangle|^2 \cdot |\langle X|Q'_{20}|X\rangle|, \tag{2.6.9}$$

where $Q'_{20} = {r'}^2 Y_2^0(\theta', \phi')$ is the electric quadrupole operator in the intrinsic frame. The intrinsic quadrupole moment of a $K = 0$ band is defined as

$$Q_0 = \sqrt{\frac{16\pi}{5}} \cdot \langle X|Q'_{20}|X\rangle, \tag{2.6.10}$$

As an approximation, the electric charge density of the nucleus can be considered constant, $\rho = 3Ze/4\pi R_0^3$, within the volume enclosed by $\Xi(\beta)$. The integral over that volume,

$$Q_0 = \int^{\Xi(\beta)} \rho \cdot {r'}^2 \cdot Y_{20}\,(\theta', \phi')\, dV$$

reduces, after non-trivial algebra, to

$$Q_0 = \frac{3}{\sqrt{5\pi}} Z e R_0^2 \beta\,(1 + 0.36\beta + \ldots) \tag{2.6.11}$$

and it becomes clear that the $B(\mathrm{E2})$ value,

$$B\,(\mathrm{E2}) = \left(\frac{5}{16\pi}\right) Q_0^2 \cdot |\langle J_i 200|J_f 0\rangle|^2, \tag{2.6.12}$$

to first order anyway, is proportional to the deformation β squared.

Far above the yrast line, the level densities are so high that the exact character of the γ-ray decay is dominated by the density of possible final states.

These ***statistical transitions*** are mostly E1 in nature. No one decay path dominates over the others, so the states de-excite by an uncorrelated continuum of γ rays up to the particle binding energy. Once the decay approaches the yrast line, however, the level density is so small that finite, well-defined decay branches emerge. These ***near-yrast*** transitions yield discrete transitions which dominate the γ–ray spectrum. A rotational cascade would appear as a "picket-fence" spectrum, or as a distinct grid pattern in a γ–γ correlation matrix as demonstrated in Figure 2.6.4, while transitions in a non-collective regime would be scattered throughout the spectrum.

Somewhere between these two extremes exist the quasi-continuum γ rays. These arise when there are a number of intrinsically distinct but macroscopically similar rotational configurations which exist in a region where the level density is so high that any one intrinsic structure has little chance of being populated, yet still low enough that transitions within one band compete favourably with statistical decay. The in-band transitions are strongly correlated, in that the difference in γ–ray energies is fixed by the dynamic moment of inertia, Eq. (2.3.27). In a γ–γ energy-correlation plot, these transitions would appear as a ridge of enhanced intensity along the $E_x - E_y = n(4\hbar/\mathcal{J}^{(2)})$ line, where n is some nonzero integer. One may imagine this as several grids like the one in Figure 2.6.4 with different $E_{\gamma 0}$ superimposed upon one another. The number of in-band transitions is limited by the level density, so the large n peaks will be attenuated. A spectrum of $\Delta E_\gamma = E_{\gamma 1} - E_{\gamma 2}$, the so-called ridge projection, will yield equally-spaced peaks (except at $\Delta E_\gamma = 0$) which decrease in intensity with increasing ΔE_γ.

2.6.3 The Magic Triangle

When considering superdeformed states, the yrast diagram of Figure 2.6.3 must be slightly modified. A superdeformed liquid drop would have a higher excitation energy than a spherical one, due to the surface term of the liquid drop model. However, because the moment of inertia of the SD system is higher, the $I(I+1)$ parabola will be more shallow than for the ground-state deformation. That

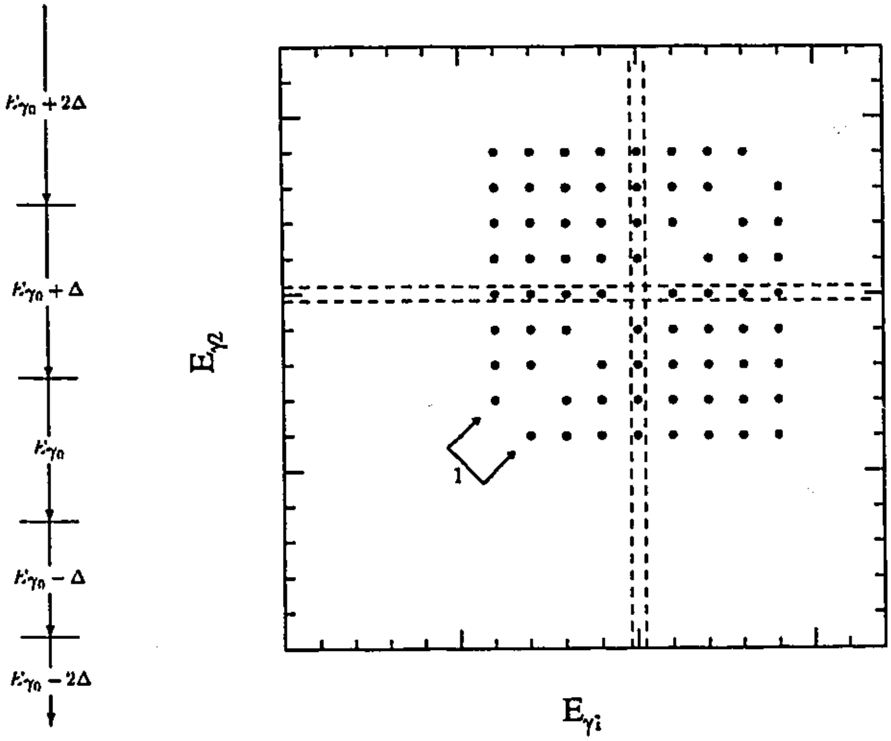

Figure 2.6.4: Rotational cascade in a γ–γ correlation matrix. Any two gamma rays detected in coincidence from the de-excitation of a regular rotor $E \propto I(I+1)$ will appear in the gamma-gamma matrix on a square lattice symmetric about but excluding points on the $E_{\gamma 1} = E_{\gamma 2}$ diagonal, where the spacing is fixed by $\mathcal{J}^{(2)}$.

is, the energy of low-deformation or spherical states increases more rapidly with angular momentum than the SD states. Eventually the two parabolas will cross, and the SD configuration becomes yrast, as shown in Figure 2.6.5. If the excitation energy of the residual system is too high, it will tend to form ND states. Taras *et al.* [Tar 88] showed that SD states were best populated by choosing a "cold" reaction, that is, one which, after particle evaporation, was high in angular momentum but not so high in total excitation energy. Then at the highest spins, the residual system would already be below the ND yrast line and it would have form an SD state. The region of the (E^*, I) bounded by the ND yrast line, the SD yrast line, and the fission limit is referred to as the *magic triangle*, and SD states are optimally fed when the entry conditions of the residual system has the most overlap with that triangle. Figure 2.6.5 also shows the region of high level density through which the γ–ray flux from the SD band decays to ND states.

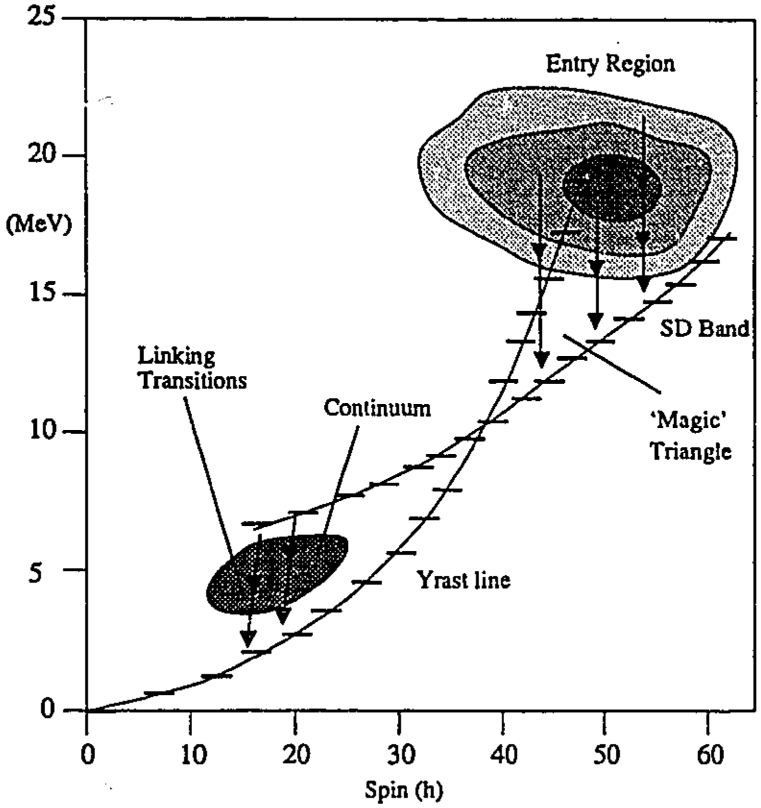

Figure 2.6.5: Yrast diagram appropriate for superdeformations, showing the yrast lines for ND and SD, the magic triangle, and the γ-ray flux from SD to ND states. Reproduced from [Wil 94].

Chapter 3.
Gamma-ray Detector Arrays

The studies of superdeformation reported in this work were performed with state-of-the-art γ-ray multi-detector arrays, namely the Canadian 8π spectrometer [Tar 83, Mar 87] and an early implementation of the American GAMMASPHERE [DD 88, Lee 90]. The former is the finest of the "second-generation" γ-ray arrays, which were optimized for the efficient detection of γ–γ coincidences. The latter is an example of a "third-generation" spectrometer where the main design criterion was to maximize the number of coincident γ rays measured in a single event.

3.1. Detection of γ–rays

Gamma rays are detected by their electromagnetic interaction with the electrons in a detector material. The three interaction processes are the photoelectric effect, Compton scattering, and pair production. In the photoelectric effect, the photon is absorbed and all of its energy is transferred to an electron in the detector material. In a Compton scattering process, the photon will transfer some of its energy and momentum to the electron. Finally, γ rays with energies above 1.022 MeV can spontaneously lose that amount of energy and generate an electron-positron pair. A single γ–ray entering a detector material can undergo several such interactions, for example, a Compton-scattered photon may then subsequently be absorbed photoelectrically in a different part of the detector.

3.1.1 Detector materials

Figure 3.1.1 shows the linear attenuation coefficients of the four detector materials that are most popular in nuclear structure studies, namely, hyperpure germanium (HPGe) semiconductor and sodium iodide (NaI), bismuth germanate (BGO) and barium fluoride (BaF_2) scintillators. The 8π and GAMMASPHERE arrays use BGO and HPGe as active detection materials.

HPGe detectors are used as massive photodiodes. A reverse bias of 2000–4000 V is applied across a cylindrical crystal typically $\sim$ 5 cm tall and wide. When a γ ray interacts with the detector by the photoelectric effect or by Compton scattering, the electron will then decelerate by scattering off of the electrons in the material and promoting particle-hole pairs to the conduction band. These are swept up by the electric field in the crystal. The charge collected at either the cathode or the anode is directly proportional to the total energy deposited in the crystal (neglecting effects like charge trapping at impurity sites). The main attraction of HPGe detectors is their excellent energy resolution, typically a 1.0 MeV γ ray will yield a peak in the pulse-height spectrum which is 2.0 keV wide [SS 88]. This resolution is adequate for studying the detailed structure of near-yrast states. As is evident in Figure 3.1.1, the photoelectric absorption cross section falls below the Compton scattering cross section for γ-ray energies above 200 keV. If the γ ray interacts by Compton scattering, the scattered photon may subsequently be absorbed photoelectrically, or it may escape the crystal altogether. The pulse height for the latter detection reflects not the energy of the incoming γ ray but only that fraction which was transferred to the electron. Similarly, the interacting electron itself may escape the crystal before it has come to rest. In an energy spectrum, the ratio of the proper energy measurement counts in the photoelectric peak to total detections (the peak-to-total ratio P/T) is only about 20% for a γ-ray of 1 MeV in an HPGe detector such as that used in the 8π array. This quantity P/T is not to be confused with the absolute photopeak detection efficiency. The latter is reported as

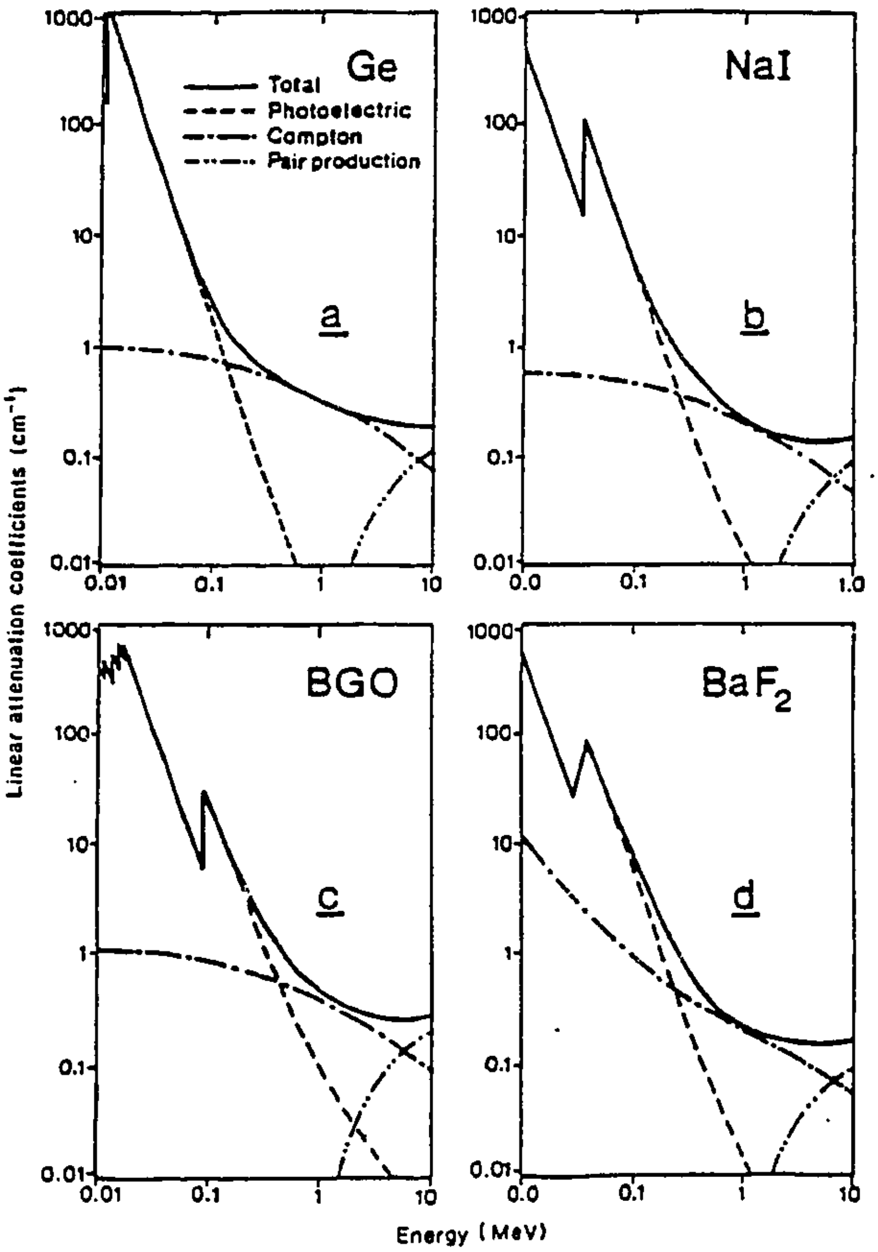

Figure 3.1.1: Linear attenuation coefficients as a function of γ-ray energy for a) germanium, b) sodium iodide, c) bismuth germanate, and d) barium fluoride [SS 88].

the rate in the 1.33 MeV ^{60}Co photopeak from a source 25 cm away divided by the same rate for a 7.62 cm × 7.62 cm cylindrical NaI scintillation crystal ([Kno 89], p. 431).

By contrast, BGO scintillators have much better photoelectric and total absorption. However they also have inferior energy resolution, since the γ-ray energy must first be converted to optical photons, which in turn must be detected in a phototube or photodiode before a pulse height is obtained. Unlike HPGe detectors, where the energy full width at half-maximum (FWHM) of a γ-ray photopeak is limited largely by the physics of semiconductors, the resolution of a specific BGO γ-ray detector depends on its geometry and optics (*i.e.*, coupling of scintillation photons to an optical detector). As such, BGO detectors are not normally of much use for detailed structure spectroscopy. Their high absorptive power does make them suitable for Compton suppression of HPGe detectors (see Sect. 3.1.2), sum-energy and multiplicity measurements (see Figure 4.3.1), and giant resonances. The latter is a class of highly excited modes which typically decay by γ rays on the order of $\sim$ 10 MeV.

3.1.2 Compton Suppression

As was indicated in Sect. 3.1.1, the main source of false energy measurement in HPGe detectors is Compton scattering out of the crystal. An auxiliary set of detectors surrounding the crystal, called an anti-Compton shield, can be used to veto Compton-scattered events. If a γ ray Compton scatters from the HPGe crystal into the anti-Compton shield and interacts with one of the detectors, then there will be coincident pulses from both detectors, whereas if the γ ray is fully absorbed in the HPGe crystal, there will be no signal in the shield. Electronically or in subsequent logic, the HPGe signal can be declared void when it is observed in coincidence with a pulse from one of the shield detectors. This is known as Compton suppression, and can improve the P/T ratio of an HPGe detector such as the ones in the 8π from 20% to $\sim$ 55% [NGT 85] (see Figure 3.1.2).

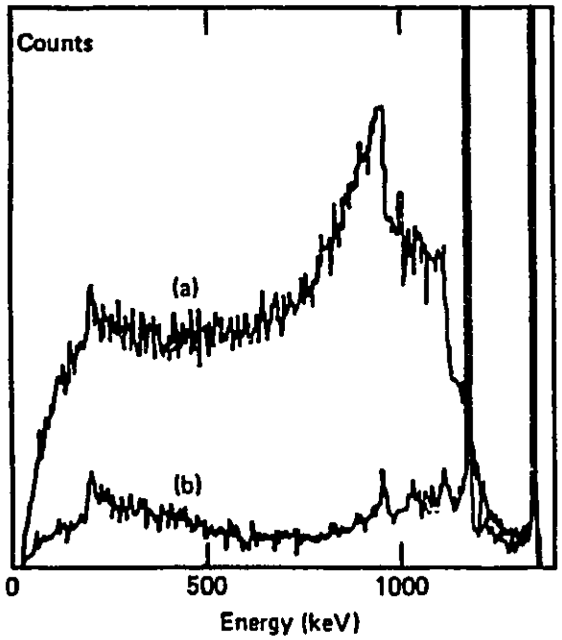

Figure 3.1.2: Pulse height spectra from ^{60}Co γ-ray source, (a) no Compton suppression, (b) Compton suppression enabled. From [NGT 85].

Figure 3.1.3 shows an HPGe assembly with its anti-Compton shield. Because of its high attenuation coefficient, BGO is used as the active material in these shields to maximize Compton suppression efficiency in a minimum of space. The forward-scattered γ rays (up in Figure 3.1.3) will have higher energy than the back-scattered rays, so there is more material behind the HPGe crystal. This "axial-symmetric" geometry is favoured because it allows the closest, most symmetric arrangement of the complete assemblies.

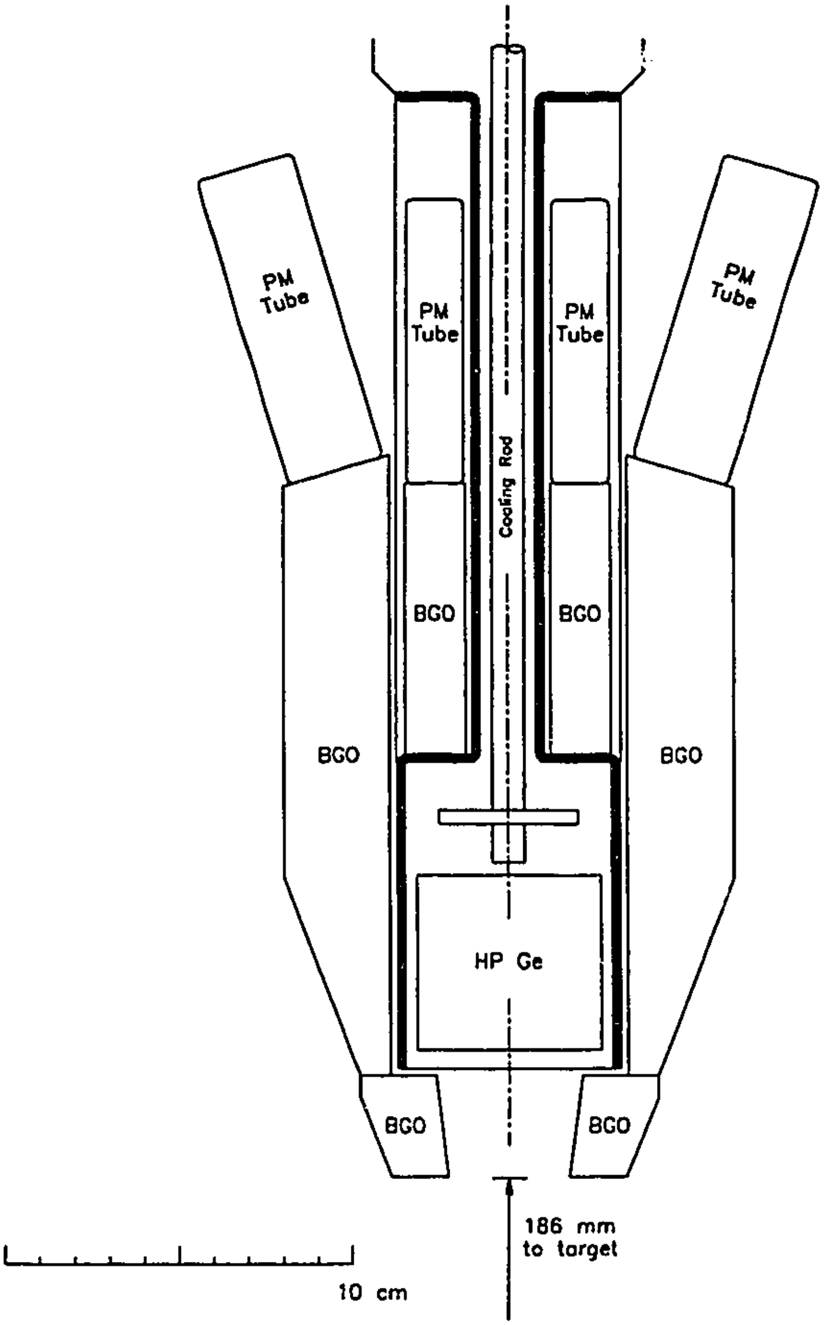

Figure 3.1.3: 8π HPGe detector and anti-Compton shield assembly, including phototubes for scintillator detectors and cryogenics system. Diagram based on [Tar 83].

3.2. The 8π Array

The 8π γ-ray spectrometer, part of the TASCC facility at AECL Chalk River Laboratories, was initially designed as a general-purpose γ–ray array but with emphasis on detections of events with high γ–ray multiplicity, namely high-spin reactions. The detector array was designed to measure, with high efficiency, two γ-ray energies with high resolution from each fusion-evaporation event. The electronics performs a number of low-level hardware checks before it declares an event valid. This avoids unnecessary dead time associated with analog-to-digital conversion of unwanted events.

3.2.1 Detector geometry

The 8π γ-ray spectrometer consists of a 72-element BGO inner ball (sometimes also called the BGO core), twenty HPGe (22% efficiency) detectors with Compton suppression shields, and associated electronics. The geometry is icosahedral with three BGO elements, one viewing port, and one HPGe assembly for each of the triangular faces. The remaining 12 BGO elements are at the vertices of the icosahedron; two of these elements are on the beam axis, and at least one of them must be removed for the beam line entrance. Usually the beam is stopped (dumped) inside the ball but beyond the sight of the viewports, but if there is some reason to dump the beam outside of the array, the other beam-axis BGO element must be removed. The ball elements form a shell with an inner radius of $\sim$ 11 cm and thickness of 7 cm which subtends a 95% solid angle. The 20 viewports which perforate the shell subtend a solid angle of 0.25% each. The centres of these viewports are in four rings of five about the beam axis at 37°, 79°, 101° and 143° measured from the target position at the centre of the ball. Each HPGe system is mounted flush against the BGO ball at a viewport. (See Figure 3.2.1.)

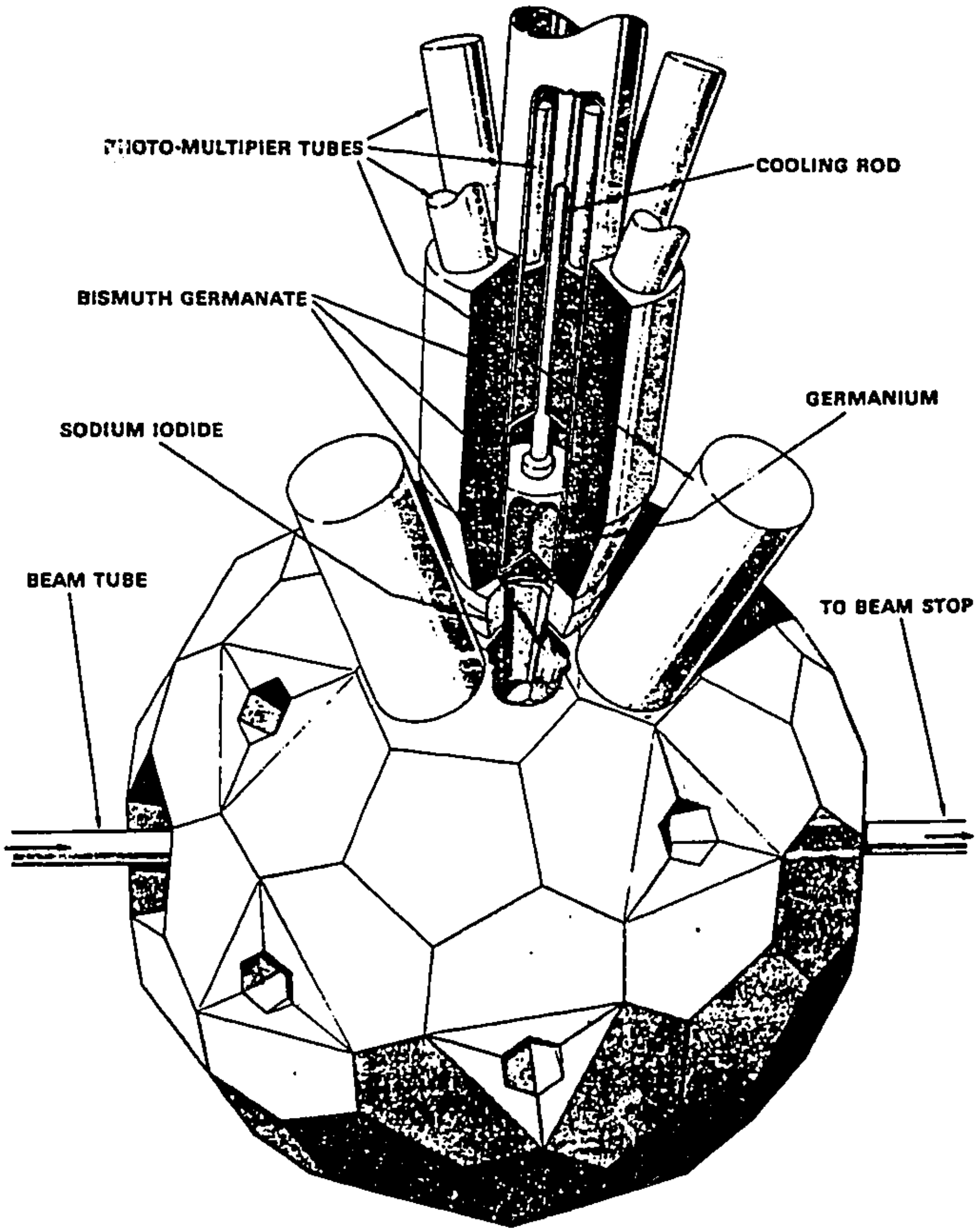

Figure 3.2.1: Diagram of 8π inner BGO ball with cutaway view of HPGe-Anti-Compton assembly. From [Tar 83].

3.2.2 Ge, BGO and Master Trigger Electronics

The electronics and acquisition system of the 8π were designed for maximum flexibility in implementing trigger conditions for event selection. It is perhaps easiest to understand the electronics by way of example, specifically a heavy-ion fusion-evaporation event. The typical 25 γ rays which are emitted within the coincidence timing resolution of the system can be considered as simultaneous, and they are referred to as a *prompt burst* or flash. Similarly, the transitions which might follow an isomeric decay may be considered as one flash as well, the *delayed burst.*

When a prompt burst occurs, some number of the BGO elements K_{prompt} will produce pulses. All pulses which pass a discriminator are converted to 0.25 V square-wave signals, and these are summed together to give an analog K_{hardware} multiplicity signal. This signal is fanned out to, amongst others, a discriminator which is set to fire for analog sum signals corresponding to some minimum K_{hardcut} (Figure 3.2.2).

Simultaneously, if a pulse is observed in the HPGe assemblies, without any signal from the Compton shield, then the HPGe signal is deemed to be good and a logic pulse is generated. These pulses are processed by a math-logic unit to calculate an analog signal corresponding to the number of good HPGe signals (Figure 3.2.4). For the high-spin experiments performed in this research, K_{hardcut} was set to ~ 10 and the minimum HPGe level was set to 2.

These two signals are then forwarded to the *master trigger* (Figure 3.2.5). If both the BGO flash and HPGe$\geq$2 signals are present, the CAB is not busy (see Sect. 3.2.3), and other auxiliary conditions are met, then the event is declared valid. This initiates further detailed event processing. The master trigger can be either cleared or cancelled by *pre-* or *post-pile-up* conditions. A second discriminator generates a *ball pile-up* signal when K_{hardware} exceeds a limit $K_{\text{p.u.}}$. The purpose of this signal is to reject events where a second γ–flash occurred too close to the main flash, for example, if two fusion-evaporation reactions occurred within one

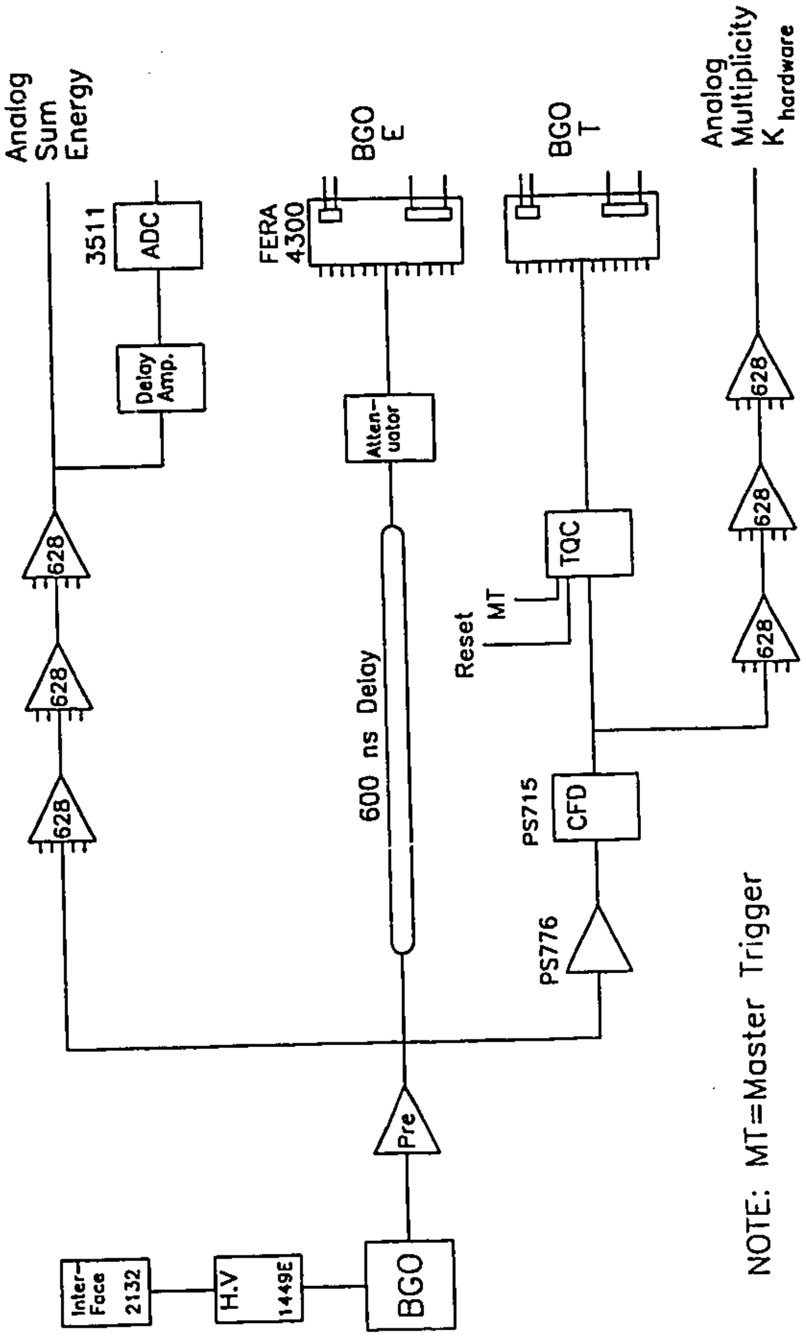

Figure 3.2.2: 8π BGO electronics, part I. This shows the discriminator and energy/time conversion modules for each individual BGO element. The series of 628 summing amplifier units evaluate in hardware the analaog multiplicity K_{hardware} and the sum-energy in the BGO ball. Updated from [Rad 85].

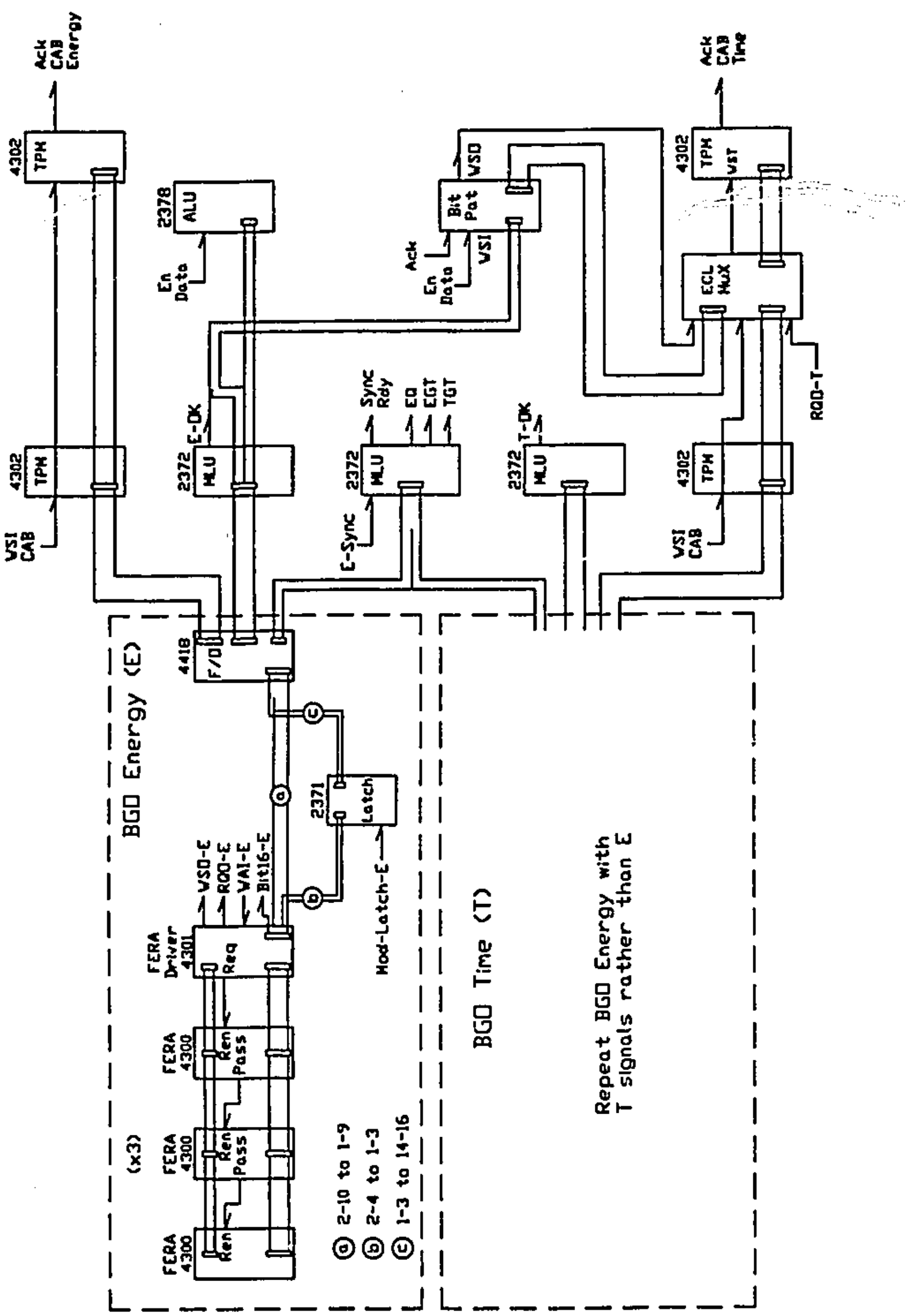

Figure 3.2.3: 8π BGO electronics, part II. This schematic shows the details of the FERA module readouts. [Rad 85]

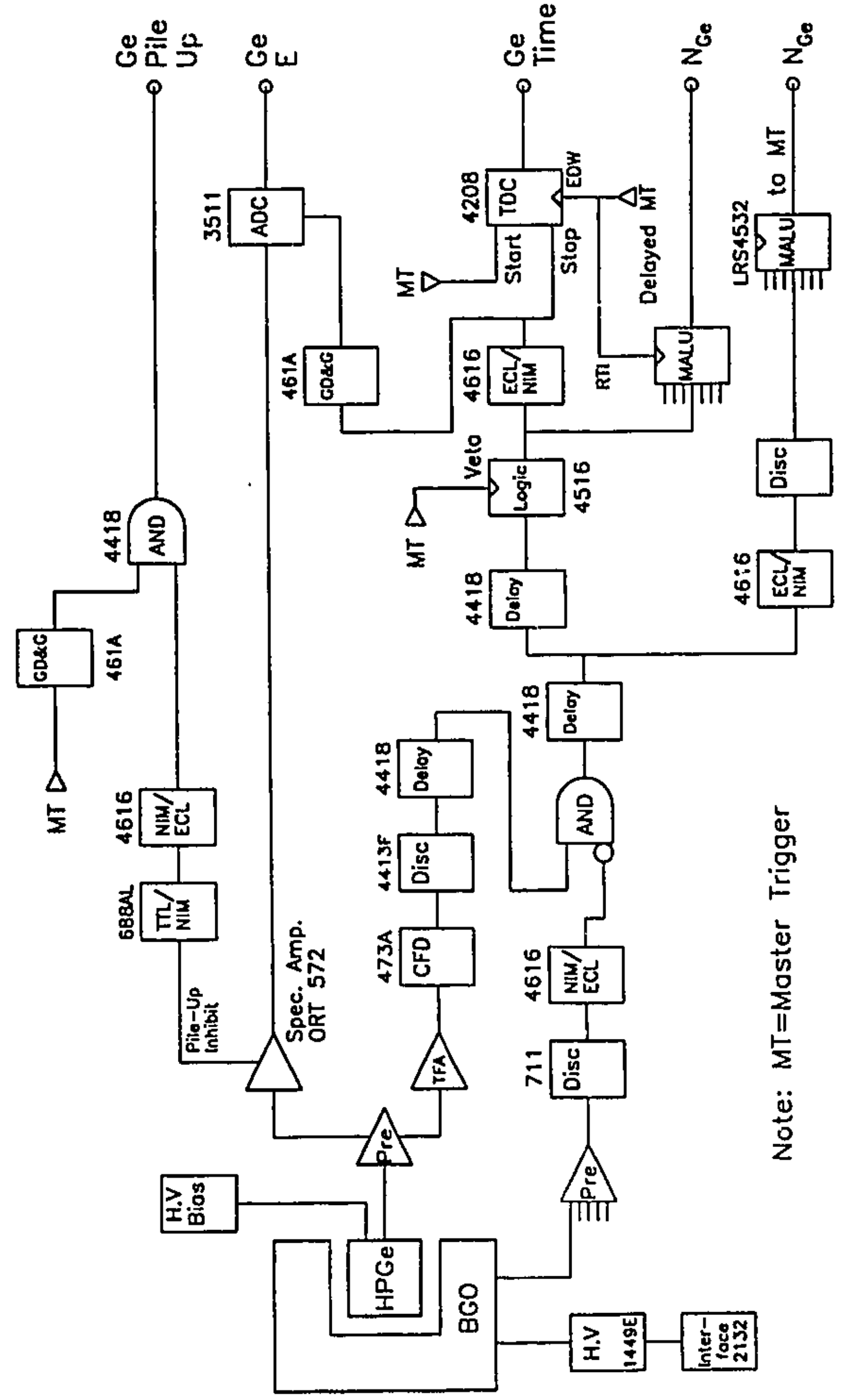

Figure 3.2.4: Schematic of 8π HPGe and anti-Compton electronics. [Rad 85]

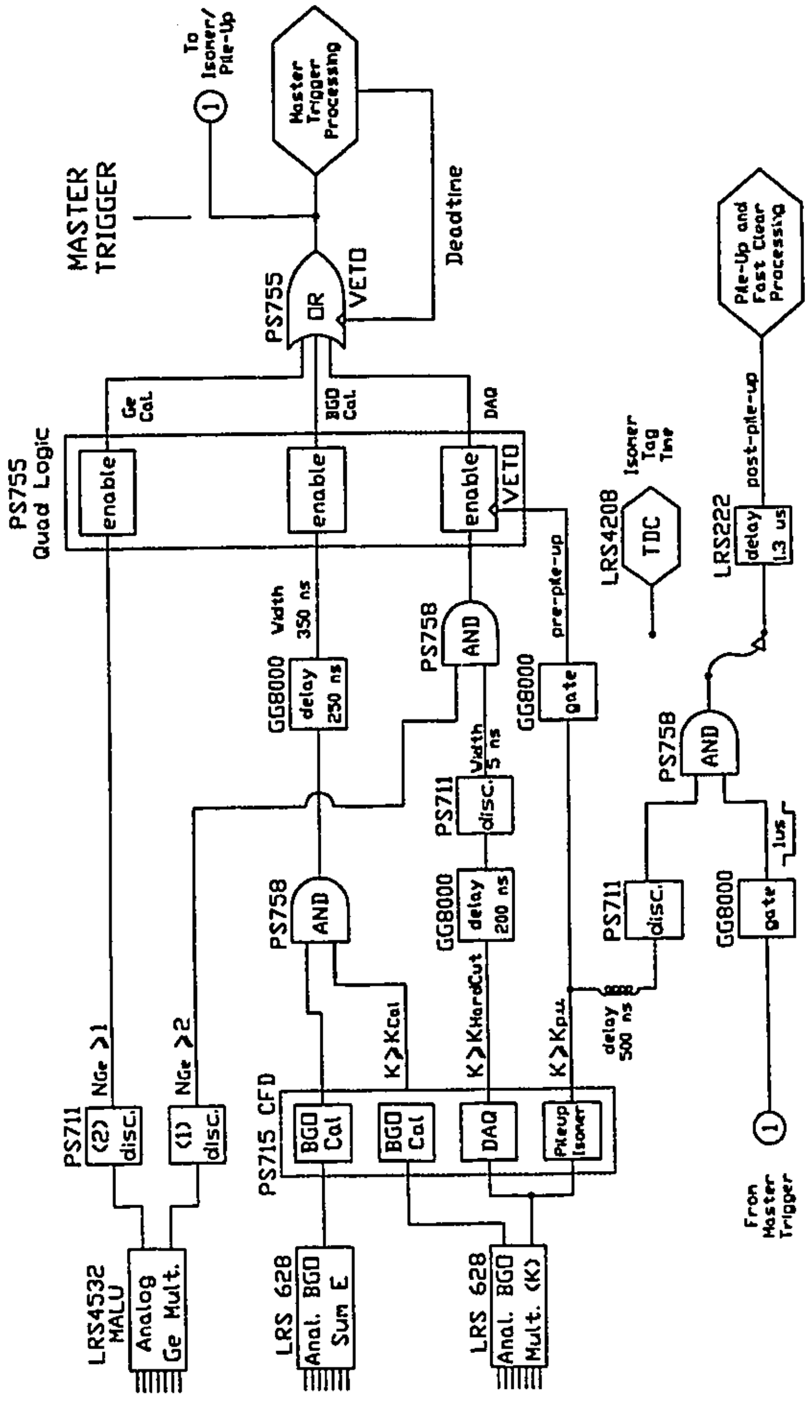

Figure 3.2.5: Schematic of 8π master trigger. This diagram is an update based on [Rad 85].

microsecond of each other. This signal generates the pre-pileup gate which vetos without delay the master trigger (the inputs to which are themselves delayed). The pile-up discriminator signal is also delayed for use as an isomer tag, but in these experiments it was employed as a post-pileup signal. In this case the master trigger will have already started the event cycle, so the post-pileup initiates a *fast clear* of the event processing modules.

The master trigger signals the electronics to begin digitizing the analog pulse heights. The HPGe pulses are shaped and amplified with standard spectroscopy modules, and these outputs are resolved with 13-bit analog to digital converters (ADC) units. The HPGe times are also measured relative to the master trigger. BGO energies and times relative to the master trigger are converted with 9-bit FERA ADC modules (Figure 3.2.3). Once these conversions are concluded, the data are read by the CAB.

3.2.3 CAMAC Booster (CAB)

The CAB, or CAMAC Booster, is a very fast microprocessor unit which is compatible with standard electronics modules. This unit reads the outputs from the ADC and FERA modules, and then performs a host of checks, calculations and on-line corrections, including:

- HPGe pile-up rejection;
- HPGe gain-offset energy correction;
- BGO digital sum-energy;
- detector hit patterns;
- timing corrections and gating.

The CAB uses the pile-up rejection signals from the HPGe spectroscopy amplifiers to reject any measurements which were accompanied by this signal. The HPGe amplifiers are only coarsely adjusted to roughly equivalent ADC dispersions for all of the detectors, so the CAB performs the fine gain-matching. The CAB can also be programmed to do an on-line Doppler correction. Similarly, the timing measurements are adjusted and digital coincidence windows are enforced on the BGO times to calculate digitally the multiplicity K and sum-energy H. Finally, the CAB is programmed to present the data to the local network in an appropriate format. For the 8π experiments described in this work a standard CAB program was used.

3.2.4 Computer Control, Acquisition

The 8π used two computers, a DEC LSI-11 for control and a Perkin-Elmer 3230 for acquisition. The LSI-11, which has since been replaced by a MicroVAX workstation, ran the cryogenic control system and also was used to configure the programmable logic units in the acquisition, including the high-voltage modules for the BGO ball and suppressor phototubes. During an experiment, it also monitored the CAB output, and calculated the coefficients for the HPGe fine gain-matching and Doppler correction. The Perkin-Elmer received the CAB data output from the local network and wrote it to magnetic tape. It also performed some simple on-line gated histograming.

3.3. The GAMMASPHERE Array

The GAMMASPHERE array [DD 88] is, in many ways, somewhat simpler than the 8π spectrometer. It is designed have high efficiency for very high-fold events by maximizing the solid angle viewed by the HPGe units. As a consequence there is no inner ball, and the acquisition electronics are greatly simplified. When completed it will consist of 110 HPGe detectors, each with a photopeak efficiency of $\sim$ 70% relative to the NaI standard, and associated suppression shields in a spherical geometry. At the time of the experiments cited in this work, it was situated at the 88-inch cyclotron facility of Lawrence Berkeley Laboratories. Thirty-four detectors and shields were mounted in a prototype frame. Fourteen were at positions corresponding to the forward-most locations in the final design ($\sim 30°$), fourteen at the backward-most positions ($\sim 150°$), and six at 90° to the beam axis.

The HPGe amplifier and anti-Compton electronics were fundamentally similar to the 8π, see Figure 3.3.1. The fast outputs from the HPGe amplifiers which pass the anti-Compton suppression check generated a fast multiplicity signal N_{fast}. The HPGe timers were started at the cyclotron RF pulse which immediately followed an $N_{\mathrm{fast}} \geq 3$ signal. Programmable post-amplifiers performed analog gain matching on the slow amplifier pulse before it was converted to a digital signal. Finally, HPGe pile-up rejection was done in a slow multiplicity unit. When $N_{\mathrm{slow}} \geq 3$, then a triple-coincidence event was fully validated and the digitized detector ID, energy and time were transferred to a MicroVAX workstation which then wrote the data to tape. [Lee 94]

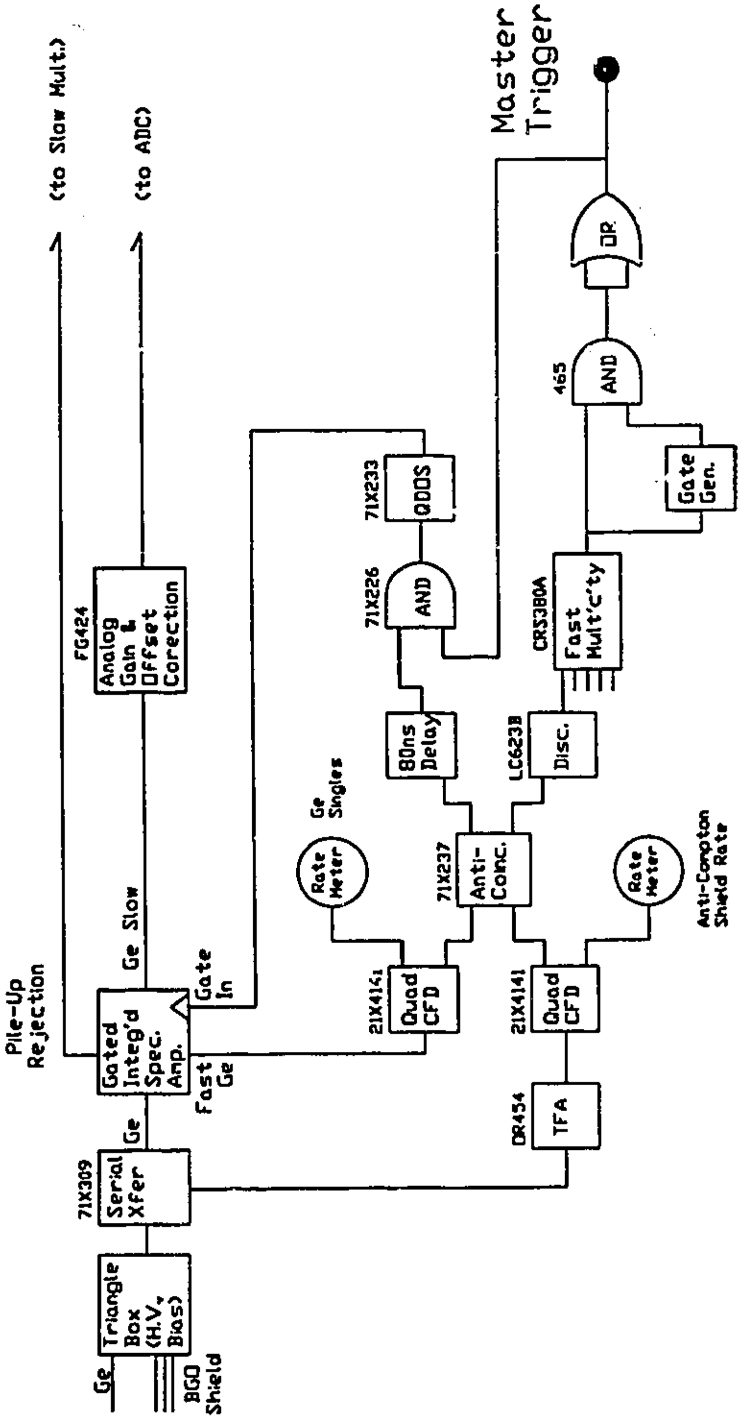

Figure 3.3.1a: Schematic of GAMMASPHERE HPGe energy measurement and master ("fast") trigger electronics in the early implementation configuration. Diagram based on [Lee 94].

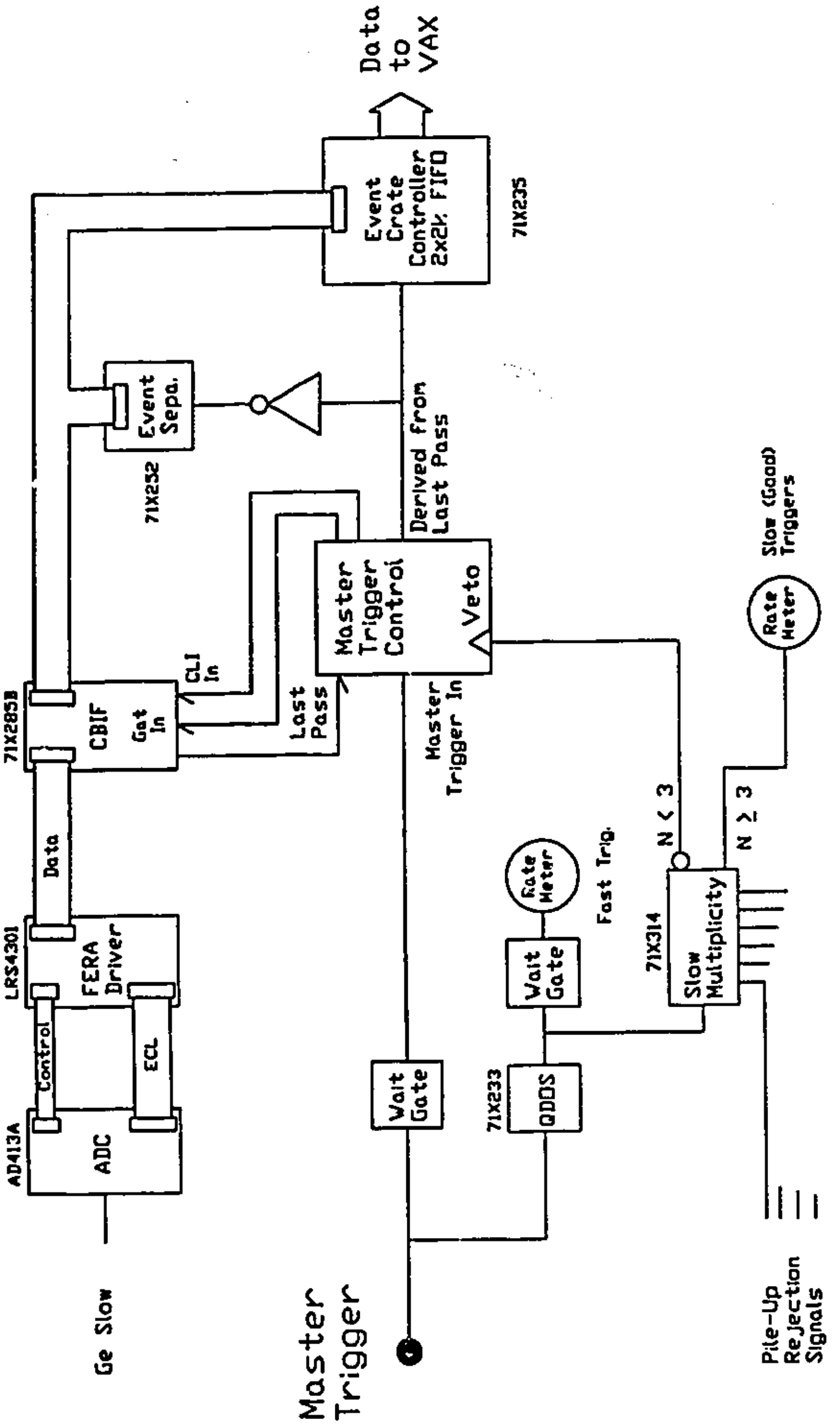

Figure 3.3.1b: Schematic of GAMMASPHERE HPGe slow trigger electronics and data flow control in the early implementation configuration. Diagram based on [Lee 94].

3.4. Calibration

Prior to detailed analysis of the results of an experiment, it is necessary to know the energy and relative efficiency response functions of the detector array. These may be measured with standard γ-ray sources. In principle these measurements are specific to a given experimental setup, and indeed are considered as part of the experiment itself. However even in details the procedures for calibration measurements are largely invariant from one experiment, or even one array, to the next. For that reason, the calibration methods will be described in general, with some illustrative examples from specific experiments.

3.4.1 Energy calibration

The digitized γ-ray energy can be expressed as a polynomial of the channel x,

$$E_\gamma = a + bx + cx^2 + \ldots \tag{3.4.1}$$

with $a = c = \ldots = 0$ for an ideal ADC. Prior to the experiment, the detectors and their electronics are adjusted for a nominal gain b_{nom}. A source is selected which has at least two strong γ rays which subtend a substantial fraction of the energy range of interest. For rare-earth spectroscopy, suitable choices are ^{88}Y (898, 1836 keV) and ^{207}Bi (569, 1063 and 1770 keV). The ADC readings from the detectors are histogramed for several minutes until the peak centroids can be measured reliably. The locations of these peaks are compared to where they should have been for the ideal response. New gain-offset coefficients are calculated and programmed into the appropriate component of the acquisition system, *e.g.* the CAB for the 8π HPGe detectors. This *gain matching* procedure is also performed at the end of an experiment prior to a detailed calibration, and also during the experiment as necessary.

In the GAMMASPHERE experiments, gain matching was also performed by monitoring the locations of two peaks in on-line spectra at the end of a four-hour cycle. If either or both peaks had moved more than two full channels from

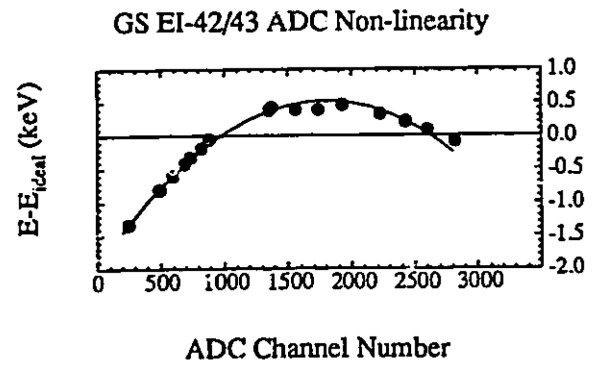

Figure 3.4.1: Differential non-linearity of GAMMASPHERE early-implementation ADCs. The data points are the difference, in keV, between the energies of ^{152}Eu source calibration peaks and the value measured from their centroids in the spectrum assuming an ideal ($a = c = 0$, $b = 0.5$ keV/channel) ADC response. The curve is the difference between the adopted gain function and the ideal ADC response as a function of ADC channel.

its reference position, the centroids of the on-line peaks were used to calculate new gain coefficients for the programmable amplifiers. The on-line spectra were then cleared for the start of the next cycle.

The detailed evaluation of the coefficients in Eq. (3.4.1) is performed with a spectrum from a multiple γ-ray source. ^{152}Eu is a suitable source, since it has several strong γ rays ranging from 122 to 1408 keV. The centroid positions of the peaks are measured and fit against their accepted energy values. The detailed calibration for GAMMASPHERE requires a second-order polynomial expansion, demonstrated in Figure 3.4.1. However, according to Prévost [Pre 92], the 8π ADCs are sufficiently linear that after a two-peak gain and offset adjustment for $b_{\rm nom}$, non-zero fitted values for a and c and deviations of b from $b_{\rm nom}$ are statistically insignificant.

3.4.2 Efficiency

The energy dependence of the photopeak efficiency for a Ge detector is modeled by the function of Radford [Rad 95a],

$$\epsilon = \exp\left(\left[\left(A + Bx + Cx^2\right)^{-G} + \left(D + Ey + Fy^2\right)^{-G}\right]^{-1/G}\right), \tag{3.4.2}$$

with

$$x = \frac{E_\gamma}{100\ \mathrm{keV}}, \qquad y = \frac{E_\gamma}{1000\ \mathrm{keV}}. \tag{3.4.3}$$

The A, B and C factors determine the low-energy efficiency roll-off due to photon absorption in the HPGe housing or X-ray absorbers (see Sect. 3.5), and D, E and F describe the high-energy efficiency decrease due to Compton scattering and pair production. The G parameter defines the transition from one regime to the other. Like the detailed energy calibrations, efficiency measurements are also performed with multiple γ-ray sources. To match the experimental conditions, the source is mounted on a target frame and installed in the same manner as the experimental target. Again ^{152}Eu is an appropriate source material, and the γ rays from ^{133}Ba are useful for establishing the shape of the curve in the transition region. The measured peak areas from the source are compared to published intensities to extract efficiencies at fixed sampling points, and the parameters of Eq. (3.4.2) are fit to these data. Sample relative efficiency curves as a function of γ-ray energy are given in Figure 3.4.2 and Figure 3.4.3.

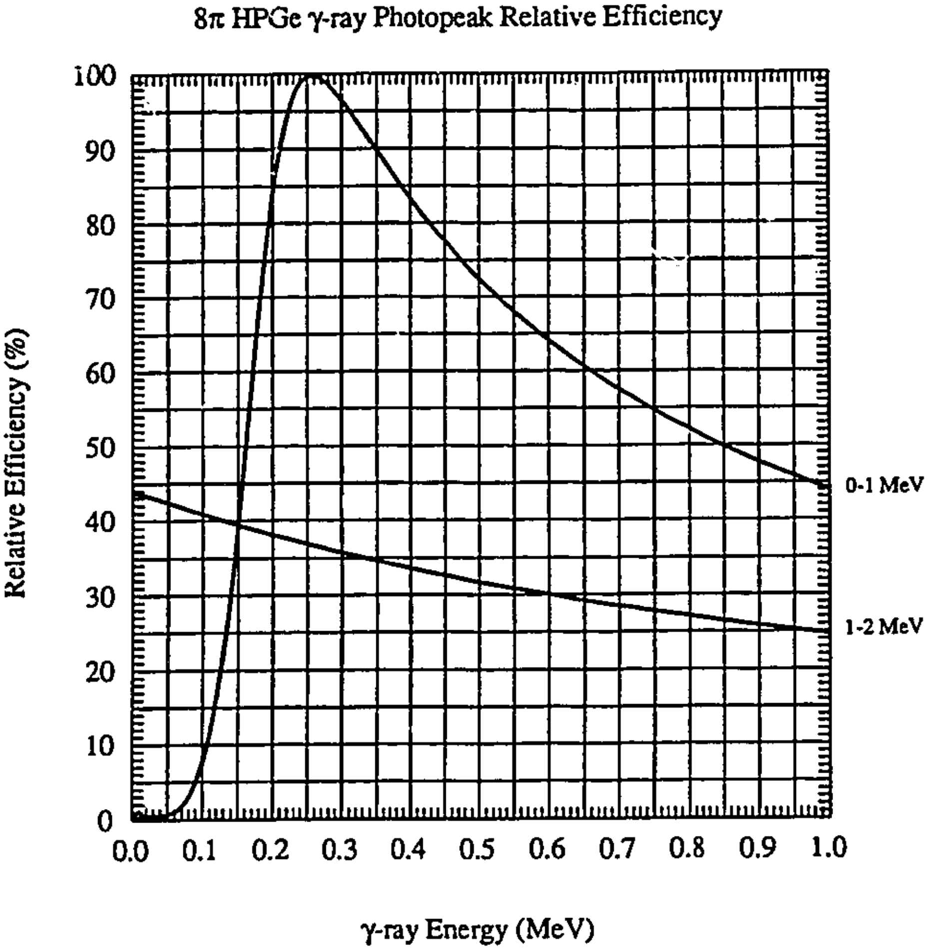

Figure 3.4.2: Relative single γ-ray photopeak detection efficiency as a function of γ-ray energy, normalized to 100 at maximum, of the entire 8π array as configured for the ^{142}Sm experiment, with a Cd-Pb X-ray absorption shroud around the target chamber.

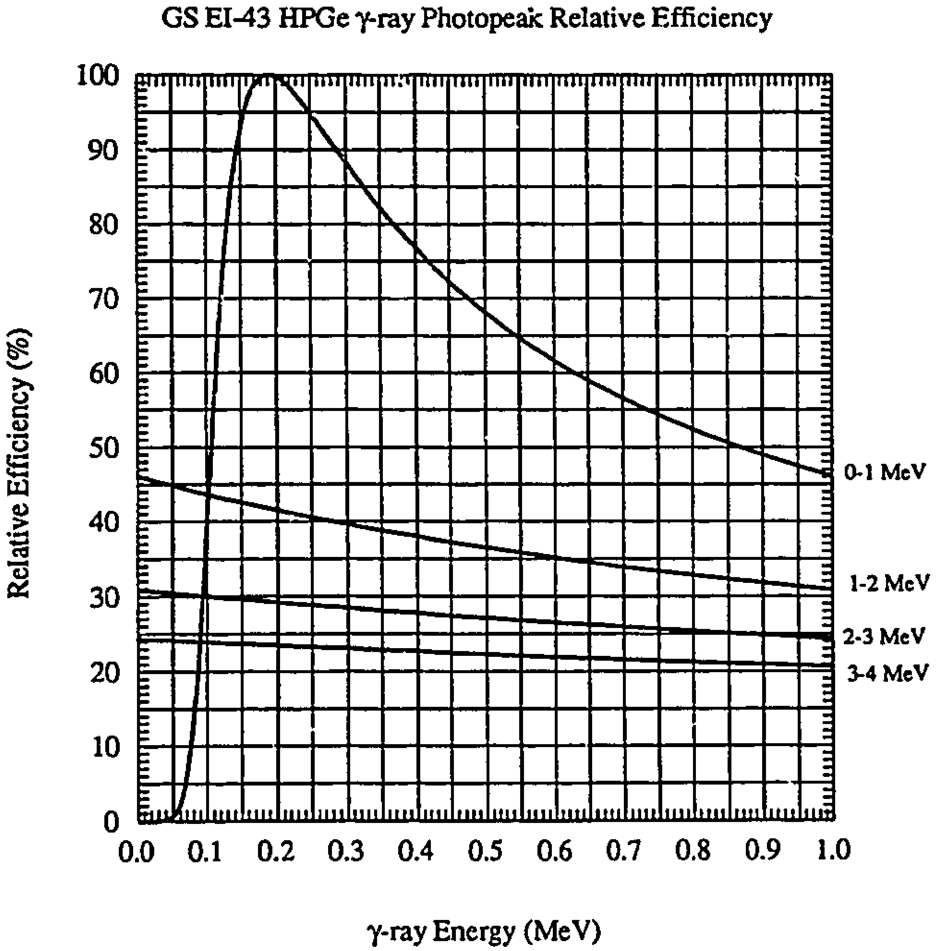

Figure 3.4.3: Relative single γ-ray photopeak detection efficiency as a function of γ-ray energy, normalized to 100 at maximum, of the entire GAMMASPHERE array in its EI42/EI43 configurations.

3.5. X-ray absorbers

A common experimental technique is to place X-ray absorber material between the γ-ray source (the target chamber) and the HPGe detectors. This can be used to attenuate photons which are of little interest anyway, namely X-rays and, in the case of SD studies, low-energy γ rays. Figure 3.5.1 shows the dramatic effect of an X-ray absorber on the efficiency curve fitted to a ^{152}Eu source spectrum. Because of scattering of high-energy γ rays from the absorber material, the P/T ratio for a single γ–ray will be increased. However, the overall sensitivity of the apparatus can be improved due to decreased double-γ hit degradation, namely γ-ray summing and HPGe pile-up. Similarly the ADC circuitry spends less time making unnecessary γ–ray energy measurements, so the loss of useful events to dead time is also decreased.

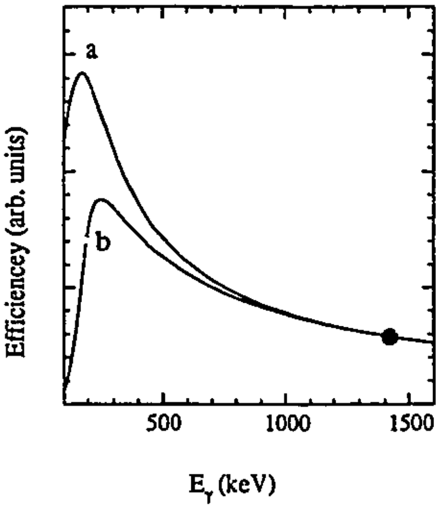

Figure 3.5.1: Effect of X-ray absorber on relative efficiency curve measured for an 8π detector with a ^{152}Eu source. (a), no absorbers; (b), with an absorber of Pb-Cd-Cu metal sheets, each 0.5 mm thick. Curves are normalized to be equal at the ^{152}Eu 1408 keV calibration point denoted by the large circle.

Chapter 4.
Experimental Results: Superdeformed Bands

The results of γ–ray studies of superdeformation in the $N = 80$ region are discussed in this chapter. After reviewing the motivation for performing these studies, the experiments themselves will be discussed. Two superdeformed bands have been identified and assigned to ^{142}Sm. One has been found in ^{142}Eu, and three have been assigned to ^{144}Eu.

4.1. Motivation: the $N = 80$ Shell Closure

The purpose of this investigation was to probe the structure of superdeformed nuclei in the A~140 region, especially in the vicinity of ^{143}Eu. In particular, it was anticipated that a comparison of SD bands in different nuclei could yield information on the roles of specific single-particle orbitals. Calculations which reproduced the features of superdeformed bands in the vicinity of ^{152}Dy also predicted another set of highly deformed structures based on a neutron shell gap at N=80, see Figure 4.1.1. A shell gap at the same proton number (Z=80) gives rise to the A~190 SD bands.

4.1.1 Shell Gaps near ^{143}Eu

The best cases for superdeformation are those with both neutron and proton shell gaps, so based on Figure 4.1.1 one would anticipate that the best cases for $N = 80$ SD would be either Z=64 ^{144}Gd or Z=62 ^{142}Sm. The first N=80 SD band discovered was in the Z=63 isotone, ^{143}Eu [Mul 91]. Its single-particle structure as calculated in a cranked Hartree-Fock self-consistent field is shown in Figure 4.1.2. It has one N_{osc}=6 proton intruder orbital occupied, which in the conventional nomenclature is $\pi 6^1$. In terms of Nilsson labels, this is the favoured signature of the $[660]\frac{1}{2}$ doublet. This pair of orbitals is interesting on a number of counts. First of all, since they have a large n_3, their single-particle energy relative to other orbitals near the Fermi surface is strongly dependent on the shape of the mean field. Secondly, since they are $K = \frac{1}{2}$ orbitals, they will be strongly split by the Coriolis force even at the lowest frequencies. This will drive the favoured-signature orbital well below the Z=63 Fermi surface. Finally, if both of these orbitals are occupied as they would be in ^{144}Gd, then they will couple to a $J = 0$ pair at low rotational frequency. This pair is predicted to break at $\hbar\omega = 0.4$ MeV [NWJ 89].

It is interesting to note that because of the influence of rotation on the N_{osc}=6 proton orbitals, the proton shell gap may actually be more appropriately taken as Z=63 over the rotational frequency range typical for SD shapes, rather than either Z=64 or Z=62. Figure 4.1.3 is a plot much like Figure 4.1.1 but at a fixed, non-zero cranking frequency, which shows how the shell gaps change for rotating systems. The measured moment of inertia of the ^{143}Eu SD band is remarkably constant.

It should be pointed out that it is not common to choose a nucleus with odd A as a core. At zero rotational frequency, all single-particle levels are doubly degenerate, so shells are not really "closed" unless both levels are occupied. The Coriolis force removes this degeneracy, so at high spins it is conceivable that regions of low single–particle energy density could exist at odd particle numbers. A more

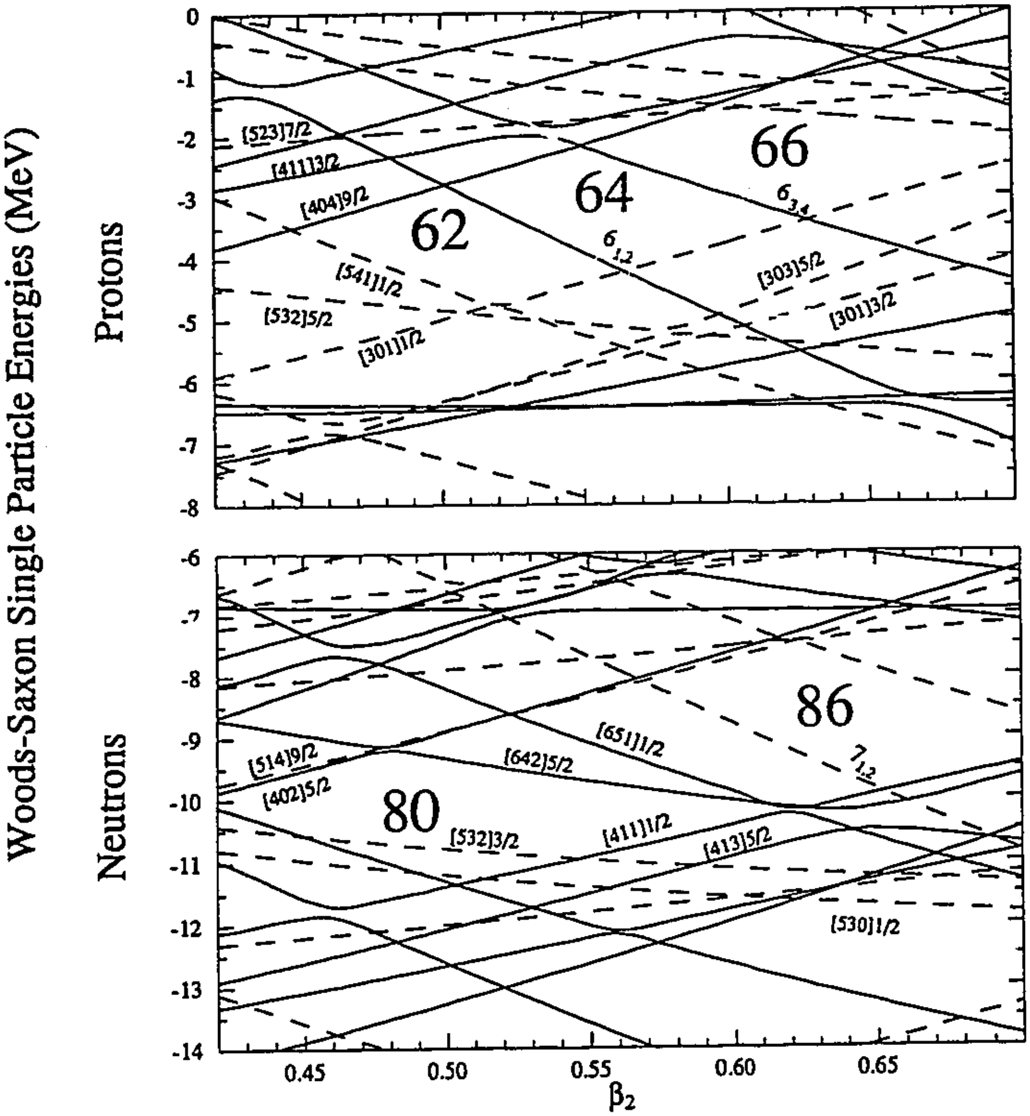

Figure 4.1.1: Single-particle level spectrum as a function of deformation calculated for a Woods-Saxon potential [NWJ 89] clearly shows shell gaps at zero rotational frequency for N=80 and Z=64 or Z=62 at $\beta_2 \sim 0.5$.

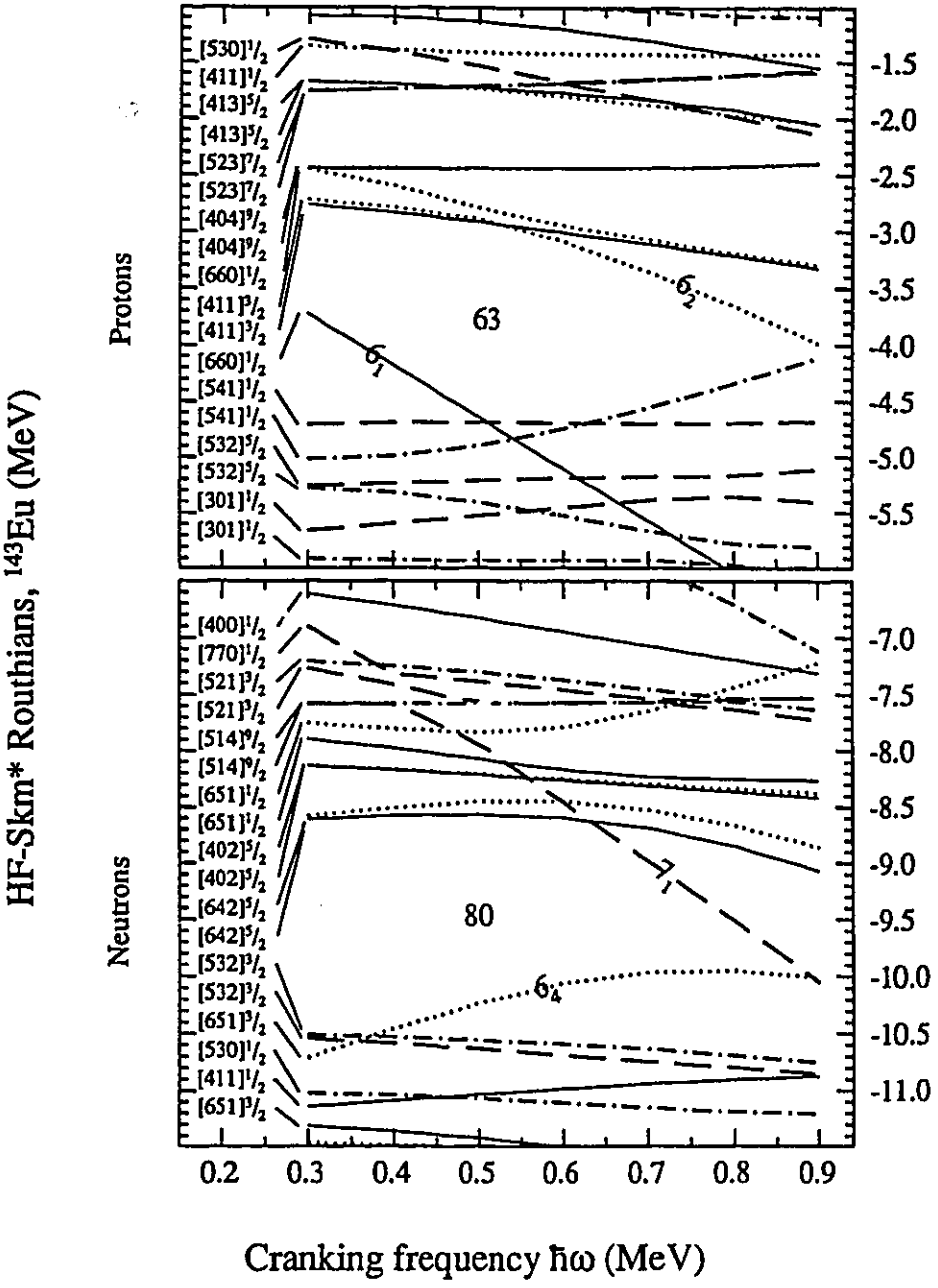

Figure 4.1.2: Single-particle Routhians for ^{143}Eu calculated with the self-consistent cranked Hartree-Fock code of [DD 95]. The line type indicates the parity and signature exponent (π, α) of the single-particle wave function: $(+, +\frac{1}{2})$, solid; $(+, -\frac{1}{2})$, dotted; $(-, +\frac{1}{2})$, dot-dashed; $(-, -\frac{1}{2})$, dashed. Single-particle states are labeled by the Nilsson numbers which best approximate the HF wave function at low rotational frequency. Important high-j intruder orbitals are also labeled by 6_1 and 6_2 (protons) and $\nu 6_4$ and $\nu 7_1$ (neutrons).

subtle difficulty with choosing an odd–A core is that full quantum-mechanical treatments of the particle-rotor couplings are more complicated and clumsy. But the cranking model is semi-classical, and so in this approximation there is no reason not to chose an odd nucleus as a core if it exhibits rigid behavior. For this reason, it has been proposed that ^{143}Eu could be taken as an inert, doubly-magic core, and it is expected that neighbouring nuclei could be interpreted as particle-rotor couplings to the ^{143}Eu SD structure.

4.1.2 Single-particle landscape

Inspection of Figs. 4.1.2 and 4.1.3 will yield some insight into the sort of bands which might be observed. Considering first the proton Routhians of Figure 4.1.2, there are four $N_{\text{osc}}=5$ orbitals just below the Fermi surface. A ^{142}Sm yrast band would have a hole in one of these orbitals relative to ^{143}Eu, and excited bands would likely be based on simply moving this hole amongst these orbitals. About 1 MeV below the Fermi surface are the $[301]\frac{1}{2}$ orbitals, which are responsible for the isospectral pair of bands in ^{151}Tb and ^{152}Dy [Byr 90]. Hence there could be a possibility of observing such an isospectral pair in ^{142}Sm–^{143}Eu. Turning to the neutrons, the fourth $N_{\text{osc}}=6$ orbital is just below the $N=80$ neutron shell gap. In Figure 4.1.2 this $(\pi,\alpha)=(+,-\frac{1}{2})$ state evolves from the unfavoured signature of the static $(\omega = 0)$ $[651]\frac{3}{2}$ doublet, and according to the calculations, one would expect that this state is the most likely unoccupied level in ^{142}Eu relative to ^{143}Eu. Above the $N=80$ gap is the distinctive $N_{\text{osc}}=7$ neutron intruder orbital which is believed to be occupied in all of the gadolinium superdeformed bands. At high frequencies this would appear to be the most likely orbital occupied by the 81st neutron in ^{144}Eu. Amongst the positive-parity orbitals above the neutron gap are the set of four $N_{\text{osc}}=6$ orbitals which seem to be responsible for some of the anomalies in the $\mathcal{J}^{(2)}$'s of the $^{146\rightarrow148}$Gd SD bands [Haa 93], which could appear in ^{144}Eu excited SD structures. It should be noted that Figure 4.1.2 is the *self-consistent* solution

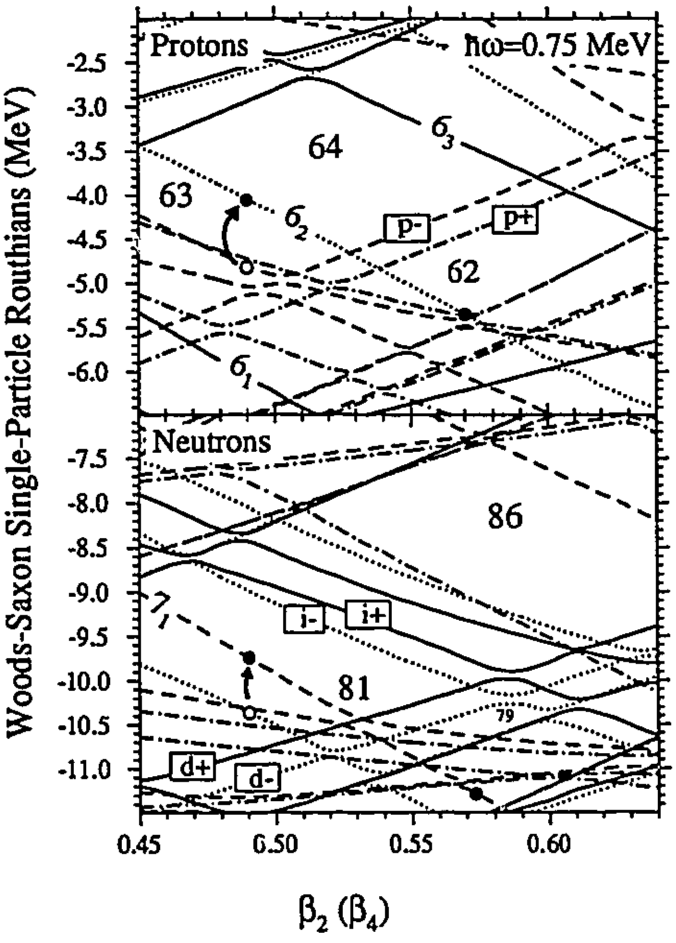

Figure 4.1.3: Cranked single-particle level spectrum as a function of deformation at a rotational frequency of $\hbar\omega = 0.75$ MeV, calculated for a Woods-Saxon potential [NWJ 89]. Parity and signature are indicated by line type as in the previous figure. Intruder orbitals in the protons ($6_1, 6_2, 6_3$) and neutrons (7_1), as are the $\alpha = \pm 1$ signature partners of the proton $[301]\frac{1}{2}$ (p±), neutron $[411]\frac{1}{2}$ (d±), and neutron $N_{osc}=6$ (i±) orbitals. Shell gaps near $Z \sim 62, 64$ and $N \sim 80$ are also identified. Circles and curved arrows will be discussed in Sect. 5.3.2.

to HF equations. Since adding or removing particles will change the mean field, a similar figure for neighbouring nuclei would differ in details.

4.1.3 Total Routhian surfaces

Finally there is the question of whether these shell gaps are sufficient to produce well-defined second minima which are stable enough to permit in-band γ-ray decay to compete favourably with fission or decay to less-deformed states. The energy of a given (N, Z) system may be calculated as a function of the (β, γ) deformation coordinates. To account for rotation the calculations may either be constrained to solutions with a fixed angular momentum, or they may be performed with the cranking Hamiltonian at a fixed rotational frequency for a given signature and parity. A 2D surface plot of the latter is called a *total Routhian surface* (TRS), and the location and depth of minima in this surface determine the favoured shapes of the system and their stability. The TRS diagram for ^{143}Eu, Figure 4.1.4, shows how with increasing frequency, a local SD minimum at $(\beta, \gamma) \sim (0.5, 0)$ appears and becomes an absolute minimum at $\hbar\omega = 0.60$ MeV. Similar calculations for ^{142}Sm, ^{142}Eu, and ^{144}Eu (Figure 4.1.5) all exhibit the same SD minimum.

4.1.4 Spins

One further incentive for using ^{143}Eu as a rigid-rotor reference is that an indirect measurement has been made which constrains the spin of the SD states to within $\sim 1\hbar$. By measuring $E_{\gamma 1} + E_{\gamma 2}$ correlations, Ataç *et.al* [Ata 93] found two-γ decay paths from SD bands to the normal-deformed structure. The decay paths were found to be consistent with a total $\Delta J = 3$, *e.g.* consecutive stretched E2–E1 transitions, if the final state of the last known SD transition (483 keV) decayed to a $J_0 = 37/2\hbar$ SD state. This assumed spin also happens to be consistent with the occupation of the $\pi 6_1$ intruder, and so will be accepted throughout this thesis.

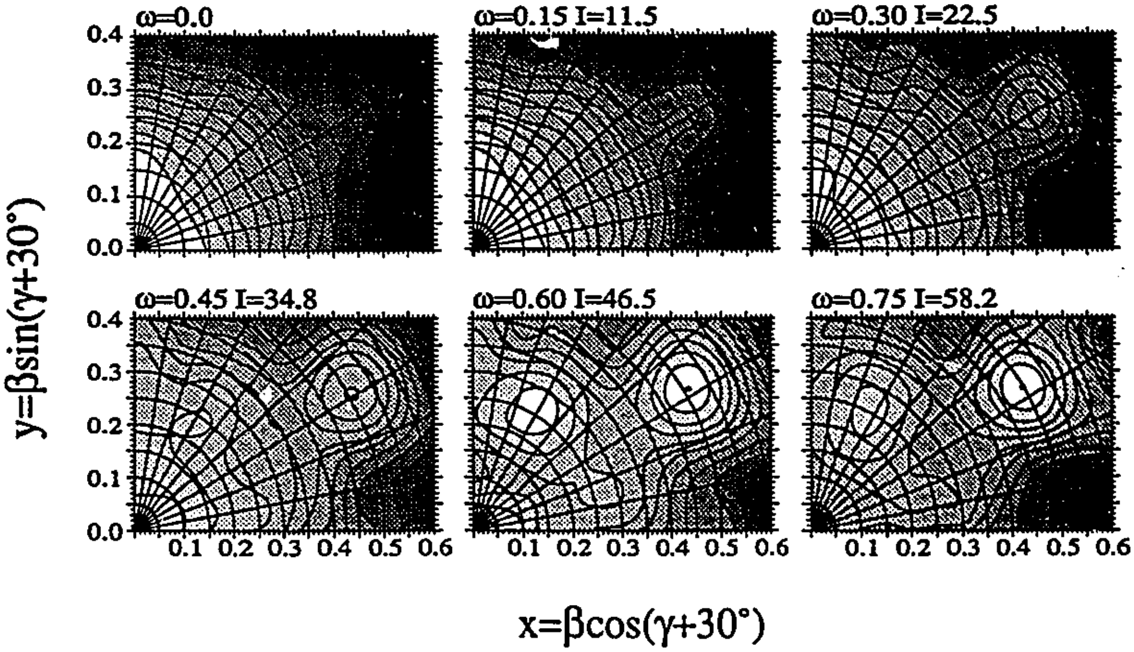

Figure 4.1.4: Total Routhian Surface (TRS) plot for ^{143}Eu, Woods-Saxon mean field with pairing at six rotational frequencies. The configuration was constrained to $(\pi, \alpha) = (+, +\frac{1}{2})$, which would correspond to $\pi 6^1$, *i.e.* occupation of the first N_{osc}=6 proton intruder beyond the core. The gray-scale goes from white at the minimum energy on the plot to black at 15 MeV and higher. Contour lines are plotted every 0.8 MeV. The cranking frequency ω is expressed in MeV/$\hbar$. The angular momentum I is estimated for the SD minimum near $(\beta, \gamma) = (0.5, 0)$, if it exists.

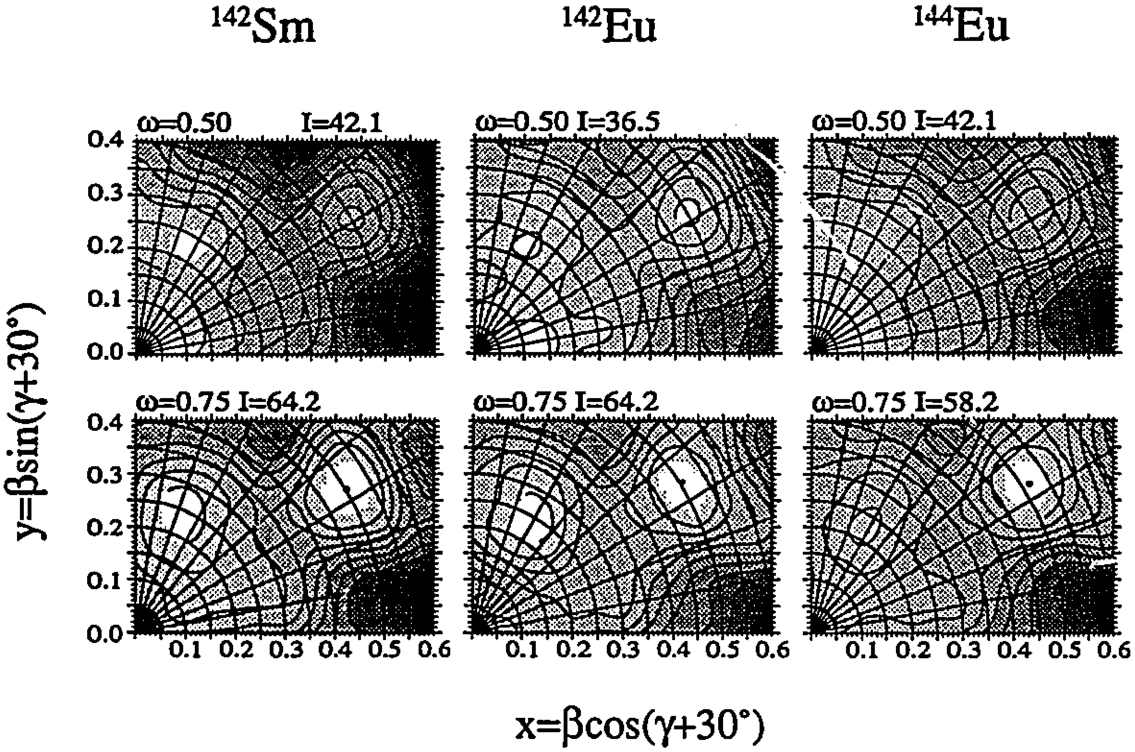

Figure 4.1.5: Selected TRS plots as in Figure 4.1.4, but for two frequencies each (0.50 and 0.75 MeV/$\hbar$) for ^{142}Sm $(\pi,\alpha) = (-,0)$, ^{142}Eu $(\pi,\alpha) = (+,0)$, ^{144}Eu $(\pi,\alpha) = (+,0)$.

4.2. Experimental program

The experiments which comprise this thesis are part of an ongoing systematic study of A~140 superdeformation, and so some of the results presented here have already been reported elsewhere. Table 4.2.1 reviews the experiments of this work. Also listed are other $A \sim 140$ studies in which SD bands have been reported, and data on these bands are taken from the listed references.

Assuming that the superdeformed bands all exist in roughly the same region of the yrast diagram, the beam, beam energy and target should be selected to best match some optimal entry conditions of excitation energy E^* and maximum angular momentum $l_{\max}$. To this end the experiments were designed to best match the E^* and $l_{\max}$ of the first ^{143}Eu experiment [Mul 91]. The data listed in Table 4.2.1 do *not* include any corrections for the kinetic energy or angular momentum which the evaporated particles remove from the system. In the design of these experiments it was assumed each evaporated neutron would remove 1.5 MeV of kinetic energy and 1 $\hbar$ of angular momentum on average from the compound system. However, in [Haa 93], it was proposed that for the neutron-evaporation reactions in the gadolinium isotopes which populated SD bands, the evaporated neutrons had a total kinetic energy of $\sim$ 13 MeV, regardless of how many of them there were. For comparisons sake, the reactions of Table 4.2.1 are listed again in Table 4.2.2 with the above parameters.

Finally it should be noted that these estimates do not include any correction for beam energy loss in the target material. For all of the experiments in this thesis, the targets have consisted of two self-supporting foils of enriched material, each typically $\sim$ 500 μg/cm^2 thick. The beam will lose an average of $\sim$ 5 MeV as it passes through the targets, and the real E_{lab} for a single fusion-evaporation event will depend on where within the target the reaction occurred. Thus the average E^* will be on the order of 1 MeV less than reported in these tables. This uncertainty is less than that for the total kinetic energy of the evaporated particles, and the

Experiments reported in this thesis						
Nuclide	Reaction	E_{lab} (MeV)	E^* (MeV)	l_{max} ($\hbar$)	Array	Ref.
^{142}Sm	^{124}Sn(^{24}Mg,6n)	145	50	70	8π	[Hac 93]
	”	”	”	”	GS	[Hac 95]
^{142}Eu	^{120}Sn(^{27}Al,5n)	152	47	71	8π	[Mul 95]
^{144}Eu	^{122}Sn(^{27}Al,5n)	142	39	64	8π	[Mul 94]
	”	”	”	”	GS	
^{141}Pm	^{124}Sn(^{23}Na,6n)	135	48	67	8π	
^{144}Sm	^{124}Sn(^{26}Mg,6n)	145	49	72	8π	
Other investigations:						
^{142}Eu	^{110}Pd(^{37}Cl,5n)	160	30	60	Ga.Sp.	[Ata 94]
^{143}Eu	^{110}Pd(^{37}Cl,4n)	160	42	60	Tessa3	[Mul 91]
	”	”	”	”	Nordball	[Ata 93]
^{144}Gd	^{100}Mo(^{48}Ti,4n)	221	54	82	Ga.Sp.	[Lun 94]
^{145}Gd	^{114}Cd(^{36}S,5n)	182	50	82	Ga.Sp.	[DeA 95]
^{145}Tb	^{112}Sn(^{37}Cl,2p2n)	187	56	75	8π	[Mul 94]
	^{118}Sn(^{31}P,4n)	160	39	63	8π	”
^{146}Gd	^{110}Pd(^{40}Ar,4n)	180	43	63	Osiris	[Heb 90]
	”	175	46	67	”	[Rza 91]
	^{122}Sn(^{29}Si,5n)	155	49	71	8π	[Haa 93]

Table 4.2.1: List of $A \sim 140 - 150$ high-spin superdeformation experiments in specific nuclei, including the reaction, entry conditions, spectrometer array facility utilized, and reference where the results were reported. The reaction nomenclature is *target (beam,evaporated particles)*. Beam energy is E_{lab}. The E^* and l_{max} values reported do *not* include kinetic energy or angular momentum removed by the evaporated particles.

effect on l_{max} is less than the uncertainty introduced by the R_{int} approximation, Eq. (2.6.2).

Experiments reported in this thesis							
		E_{lab}	E^*(MeV)			l_{max}	
Nuclide	Reaction	(MeV)	(a)	(b)	(c)	(a)	(b)
^{142}Sm	^{124}Sn(^{24}Mg,6n)	145	50	41	37	70	64
^{142}Eu	^{120}Sn(^{27}Al,5n)	152	47	40	34	71	66
^{144}Eu	^{122}Sn(^{27}Al,5n)	142	39	32	26	64	58
^{141}Pm	^{124}Sn(^{23}Na,6n)	135	48	39	35	67	61
^{144}Sm	^{124}Sn(^{26}Mg,6n)	145	49	40	36	72	66
Other investigations							
^{142}Eu	^{110}Pd(^{37}Cl,5n)	160	30	23	17	60	55
^{143}Eu	^{110}Pd(^{37}Cl,4n)	160	42	36	29	60	56
^{144}Gd	^{100}Mo(^{48}Ti,4n)	221	54	48	41	82	78
^{145}Tb	^{112}Sn(^{37}Cl,2p2n)	187	56	27*	20*	75	71
	^{118}Sn(^{31}P,4n)	160	39	33	26	63	59
^{146}Gd	^{110}Pd(^{40}Ar,4n)	175	46	40	33	67	63
	"	180	43	37	30	63	59
	^{122}Sn(^{29}Si,5n)	155	49	41	36	71	66

Table 4.2.2: As Table 4.2.1, but with l_{max} and E^* calculated with: (a), no kinetic energy or angular momentum removed by the evaporated particles; (b), 1.5 MeV and $1\hbar$ per particle; (c), 13 MeV total kinetic energy [Haa 93] and $1\hbar$ per particle. Values of E^* marked with asterisks (*) have an additional 23 MeV removed corresponding to twice the Coulomb barrier for protons in the residual system, calculated by Eqs. (2.6.2) and (2.6.3).

4.3. Superdeformation in ^{142}Sm

Two separate experiments were performed to populate superdeformed structures in ^{142}Sm. In both cases, a beam of ^{24}Mg at 145 MeV was directed upon a stack of two ^{124}Sn targets enriched to $> 98\%$. The first SD band of ^{142}Sm was found with the 8π spectrometer, while the second experiment performed with GAMMASPHERE revealed a second, very weak band.

4.3.1 Experiments and Data Reduction

In the 8π experiment, the target foils were nominally $\sim 380\ \mu$g/cm^2 each, mounted on standard 8π frames. The beam was provided by the MP tandem accelerator of the TASCC facility at Chalk River Laboratories. A Pb-Cd X-ray absorber shroud was installed around the target chamber. The minimum accepted HPGe multiplicity was 2, and the analog BGO multiplicity triggers K_{hardcut} and $K_{\text{p.u.}}$ were both set to 11. Although ^{142}Sm contains two long isomers of 480 and 175 ns, the delayed burst following the decay of these low-spin states would not have sufficient γ-ray multiplicity to be used as an efficient isomer trigger. Therefore the delayed $K_{\text{p.u.}}$ signal was used for ball post-pile-up rejection. After the HPGe detectors were gain-matched with a ^{88}Y source, an empirical v/c was calculated from the in-beam Doppler shift of the 1418 keV transition in the 7n reaction channel ^{141}Sm. This value of 1.7% was loaded into the CAB for subsequent acquisition, and a total of $\sim 350 \times 10^6$ events were written to tape.

Off-line the 8π data were replayed into standard γ–γ matrices, 4096×4096 channels at 0.5 keV/channel, with a software restriction on the HPGe timing to a 50 ns window. The optimal H and K cuts were first determined by inspecting these quantities in coincidence with known lines in ^{142}Sm and the strongest competing reaction channel ^{141}Sm, as demonstrated in Figure 4.3.1. For all detailed analysis the ball condition $H > 18$ MeV was required. It is estimated that this condition rejected 60% of all γ–γ coincidences, including $> 95\%$ of all ^{141}Sm events and

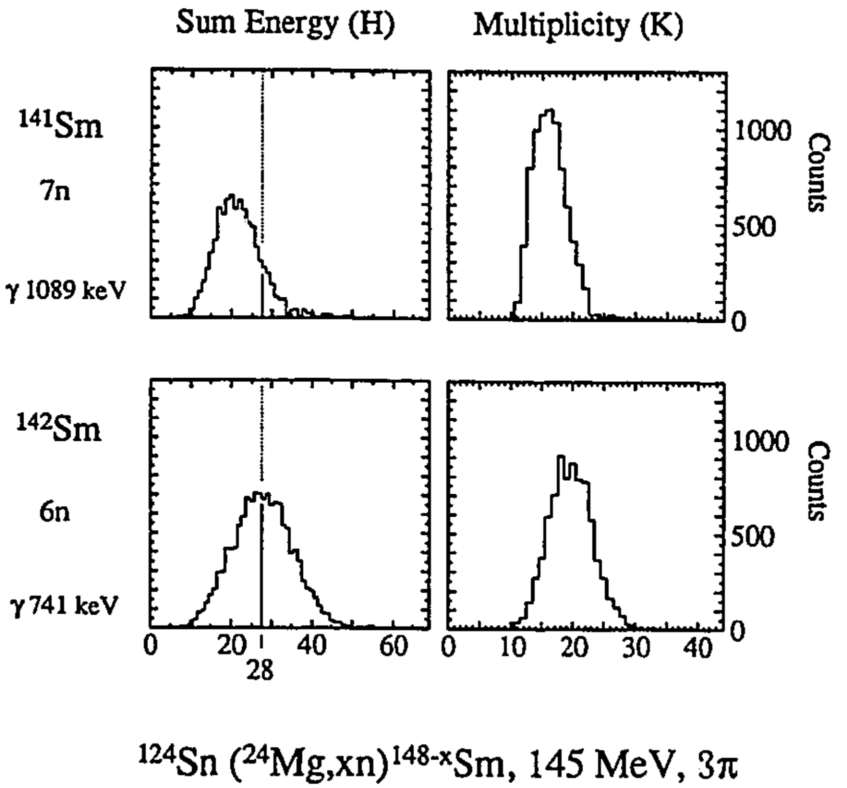

Figure 4.3.1: Sum-energy H and multiplicity K distributions measured in the 8π BGO ball during the ^{142}Sm experiment, gated on strong γ-ray transitions in the 6n and 7n reaction channels. The H scale is a standard contracted dispersion of approximately 0.625 MeV/channel.

$\sim$ 50% of all ^{142}Sm events. This dramatically improved the P/T ratio in the total projection, since it effectively eliminated a strong reaction channel and all of its associated smooth background. It should be noted that evaporation reactions involving the same number of particles, *e.g.* 6n, p5n and α5n, have about the same entry conditions, and so will appear the same in H and K distributions.

In the GAMMASPHERE experiment, two stacked targets of $\sim$ 500 μg/cm^2 $>$ 98% ^{124}Sn were bombarded with an identical beam and energy, provided by the 88-Inch Cyclotron at Lawrence Berkeley Laboratories. After gain-matching with a ^{207}Bi source for a nominal gain $b_{\mathrm{nom}} = 0.5$ keV/channel, the expected v/c was calculated assuming that the beam had already passed through one target foil, and this correction was loaded into the programmable amplifiers. Subsequently the 274 keV transition in ^{142}Sm and the 1418 keV transition in ^{141}Sm were monitored for on-line drift corrections. A total of 1.1×10^9 triple- and higher-fold γ-ray coincidences were measured in the HPGe array and written to tape.

Off-line, the data on tape were sorted in three separate modes. First, the experimental data tapes were pre-sorted to filter out measurements from detectors which were deemed to be unreliable or incorrect. For example, the gain of one detector was very sensitive to the operation of the cryogenics system, so rather than attempt to correct gain fluctuations which would occur on a time scale of two hours, any measurements from that detector were simply discarded in the pre-sort. The remaining good triple- or higher-fold measurements were written to a second tape in a simple event format consisting of HPGe multiplicity and energy ADC data. These ***skimmed data*** tapes were then used for all subsequent analysis. High-fold ($n > 3$) events were unpacked to $\binom{n}{3}$ triple-coincidence data, and then all γ^3 data were sorted into CUBEAID [KPW 92] and LEVIT8R [Rad 95a] histograms. The former was restricted to a 1024 channel range from 640 to 1663 keV at a fixed gain of 1 keV/channel, while the latter spanned the energy range 80 to 1750 keV with a non-linear dispersion chosen to give a FWHM of 2.7 channels over the entire energy range. The skimmed data tapes themselves were replayed for analysis of higher-fold coincidences. The distribution of HPGe multiplicities, both raw and unpacked from higher-fold events, are listed in Table 4.3.1.

4.3.2 ^{142}Sm yrast SD band A: 8π Results

The code SDSLICE, described in Appendix C, was used to search the $H > 18$ MeV γ–γ matrix from the 8π experiment for candidate superdeformed bands. From these, a series of mutually coincident γ rays with a spacing of ~ 61 keV was found. This cascade was eventually extended to twelve certain and two tentative

GAMMASPHERE HPGe Event Multiplicities ($\times 10^6$)				
	^{142}Sm		^{144}Eu	
Fold	Raw	Unpacked	Raw	Unpacked
3	784	2922	792	2960
4	277	971	280	990
5	71	234	71	241
6	14.9	42.5	15.3	44.2
7	2.5	5.3	2.7	5.6
8	0.3	0.3	0.4	0.4

Table 4.3.1: Distribution of HPGe coincidence multiplicity for GAMMASPHERE ^{142}Sm and ^{144}Eu experiments. The raw column lists the real number of γ^k events after pre-sorting, the unpacked column lists the number of γ^k events including those unpacked from higher-fold γ^n events, $k \leq n \leq 8$.

transitions, see Figure 4.3.2. Of these, only the 981 keV transition was clean enough to observe much of the band in a single gate. Gates placed on the full width of the remaining peaks were contaminated, that is, they included some part of the peak from other discrete transitions with nearly the same energy. The gates used to generate the sum spectrum in Figure 4.3.2 were 4 keV wide, or approximately $0.5 \times$ FWHM, and were offset to select that portion of the SD transition which was least contaminated.

Assignment of weak structures such as this superdeformed band to a given nucleus is difficult [Mul 94, Haa 93], especially in γ–γ data. It is usually not sufficient, and in fact can be grossly misleading, to rely on coincident low-spin transitions for assignment to a given species. For example, even in Figure 4.3.2, lines from both ^{142}Sm and ^{141}Sm are observed in the spectra. In such a case, the BGO ball can provide additional information. A second γ–γ matrix with an $H > 14$ MeV condition was generated, and a sum-of-gates spectrum with the same gates was extracted. With this restriction, most ^{142}Sm and $\sim 50\%$ of ^{141}Sm events are accepted, so if the SD band is in ^{141}Sm, the number of counts in the SD transition peaks should be enhanced by a factor of 10, relative to the first matrix. The $H > 14$ MeV spectrum certainly was not enhanced by this great of a factor, in fact

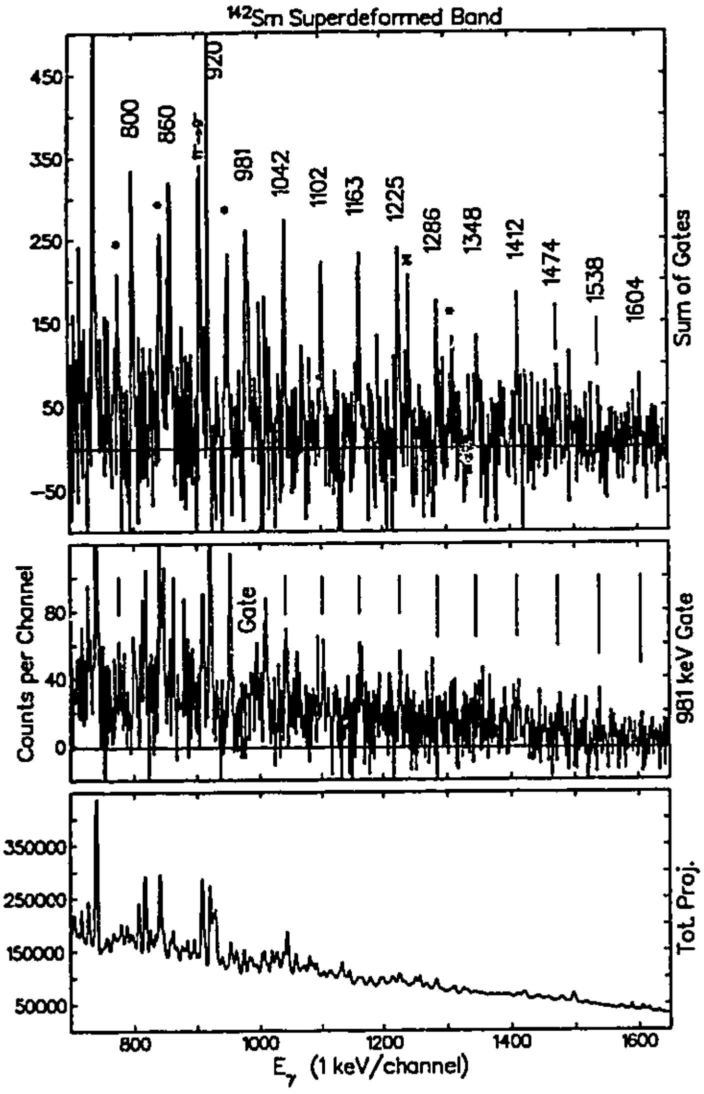

Figure 4.3.2: Partial γ-ray spectrum of the ^{142}Sm first superdeformed band (SD band A) as observed with the 8π spectrometer in the $H > 18$ MeV matrix. Top panel, sum of gates spectrum, with some ^{142}Sm lines indicated by * and a strong ^{141}Sm line indicated by a %. Also the 907 keV $11^+ \rightarrow 9^+$ transition in ^{142}Sm is identified. Middle panel, gate on the 981 keV transition. The spectrum has been contracted from 0.5 keV/channel to 1 keV/channel. The total projection (bottom panel) was used as a background spectrum for both SD-gated spectra. Energies of SD band members have typical uncertainties of 1 keV.

the peaks had less than twice as many counts in them, which would be expected for a structure in ^{142}Sm. As was implied earlier, the same argument could be used to assign the band to ^{142}Pm rather than ^{141}Pm, the pxn channels; however there was no evidence of ^{142}Pm in the $H > 28$ MeV matrix, so this possibility was discounted.

The intensity of the band was estimated by first establishing an empirical plateau region. From the spectrum gated by the 981 keV transition, the number of counts in the four higher transitions up to 1224 keV were consistent with having identical intensity, after efficiency factors were considered. This established the upper part of the plateau. Then from a sum of gates on this upper plateau it was possible to show that the counts in the 980 keV transition were consistent with having full plateau intensity, that is, there was no decay out of the band from the initial state of the 980 keV transition. Thus these five transitions were all assumed to have an intensity I_{SD}. The number of counts in these peaks in a sum-of-plateau-gates spectrum were then efficiency corrected and compared to the intensity of the 920-439 keV coincidence, which was taken from [Lac 84] to be $\sim 16\%$ of the ^{142}Sm cross-section. This coincidence was chosen because its decay path avoids the $J^{\pi} = 13^{-}$ 3 ns isomeric state. The coincidence intensity for decay paths through such a state would be attenuated in a self-supporting target experiment, because the residual nucleus will recoil beyond the focus of the collimated HPGe detectors on a time scale comparable to the mean lifetime of the isomer. Based on these coincidence measurements, ^{142}Sm SD band A was assigned an intensity of $(0.5 \pm 0.1)\%$ relative to all fusion-evaporation events leading to a ^{142}Sm residual nucleus.

4.3.3 ^{142}Sm SD band A: GAMMASPHERE results

The improved sensitivity from the GAMMASPHERE experiment had a substantial impact on the study of ^{142}Sm band A. There is no question that the γ rays in coincidence with the SD transition are transitions between lower-spin states of ^{142}Sm. The band was extended to a total of 19 transitions, and a detailed intensity profile was established, the results of which are listed in Table 4.3.2. The

^{142}Sm Band A	
E_γ (keV)	I_γ (relative, %)
[679.7 (6)]	[30 (17)]
739.26 (5)	84 (19)
798.81 (7)	85 (5)
859.25 (7)	109 (6)
919.41 (5)	102 (12)
980.08 (8)	95 (5)
1040.46 (9)	111 (6)
1101.17 (9)	93 (5)
1162.42 (10)	94 (5)
1223.76 (10)	106 (6)
1285.49 (11)	82 (5)
1348.16 (12)	66 (4)
1410.6 (2)	58 (4)
1474.1 (2)	52 (4)
1538.2 (2)	31 (3)
1602.5 (3)	21 (3)
1667.7 (5)	12 (2)
1732.0 (9)	6 (2)
1782.9 (14)	4 (2)

^{142}Sm Band B	
E_γ (keV)	I_γ (relative, %)
[724.5 (6)]	[8 (3)]
785.9 (5)	18 (3)
843.3 (5)	19 (3)
900.5 (4)	16 (3)
958.5 (5)	17 (3)
1010.5 (6)	16 (4)
1072.9 (5)	18 (3)
1129.2 (4)	25 (4)
1186.5 (9)	16 (3)
1243.8 (7)	13 (3)
1301.6 (7)	12 (3)
1359.3 (8)	8 (3)
1420 (2)	6 (5)
1474.9 (7)	8 (2)
1535.0 (11)	6 (2)

Table 4.3.2: Energies and relative intensities (normalized to 100% in Band A plateau region) of γ-ray transitions assigned to superdeformed bands A and B in ^{142}Sm, as measured with GAMMASPHERE. Square brackets indicate tentative transitions. Energy uncertainties are statistical only. All measurements were made from γ-γ-γ coincidence data (sums of clean double-gated spectra).

decay from the SD band to states in the non-collective regime was characterized in an attempt to establish the spin of the SD states.

The band was studied in detail in both triple- and quadruple-coincidence data, see Figure 4.3.3. Spectra generated by double-gates on the band transitions were inspected to determine if they were *clean*, that is, to ensure that the counts in the gated spectrum were predominantly from either transitions in the SD band or transitions following the decay-out. If lines were observed in the spectrum which were much more intense than the expected SD lines, then that particular double-gate was deemed *dirty* and rejected from further analysis. The list of clean gates for ^{142}Sm band A is given in Figure 4.3.4, along with example spectra demonstrating clean and dirty double-gates.

From these data, ^{142}Sm band A was extended to a maximum transition energy of 1782 keV. All of the transitions up to 1731 keV were confirmed by placing a single gate on the transition and a second gate, or a clean double-gate, on the rest of the band. The sum of these spectra showed the band, so all of these transitions were confidently assigned to band A. The 1782 keV transition does not follow the constant energy spacing pattern of the rest of the band, which has important consequences on the single-particle structure of this band. Unfortunately there were not enough counts in it to confirm it by the same means as the rest of the transitions. The intensity of that peak could have arisen from one or some small subset of dirty gates. Inspection of clean double-gates rejected this possibility. It could also be that this transition is a previously-unknown branch in the low-spin decay pattern. In the deduced level scheme presented in Appendix A, there is no evidence for such a possibility. On these grounds the 1782 keV transition was assigned to the SD band.

At lower transition energies, the next two transitions which would follow a constant spacing pattern are obscured by low-lying 741 and 677 keV transitions of ^{142}Sm. A sum of triple-gated spectra, where at least two of the gating transitions would form a clean double-gate, was generated and fully subtracted as per Appendix B. Based on the observed intensity of the 201, 253 and 540 keV lines, it was estimated that only $(42 \pm 8)\%$ and $(60 \pm 10)\%$ of the intensity of the 741 and 677 keV lines, respectively, could be accounted for by non-SD decay alone. The excess counts are assigned to SD transitions of 741 and 679 keV with the latter transition remaining tentative.

The intensity profile, plotted as a function of γ-ray energy in Figure 4.3.5, was determined from the sum of clean double-gated spectra extracted from the

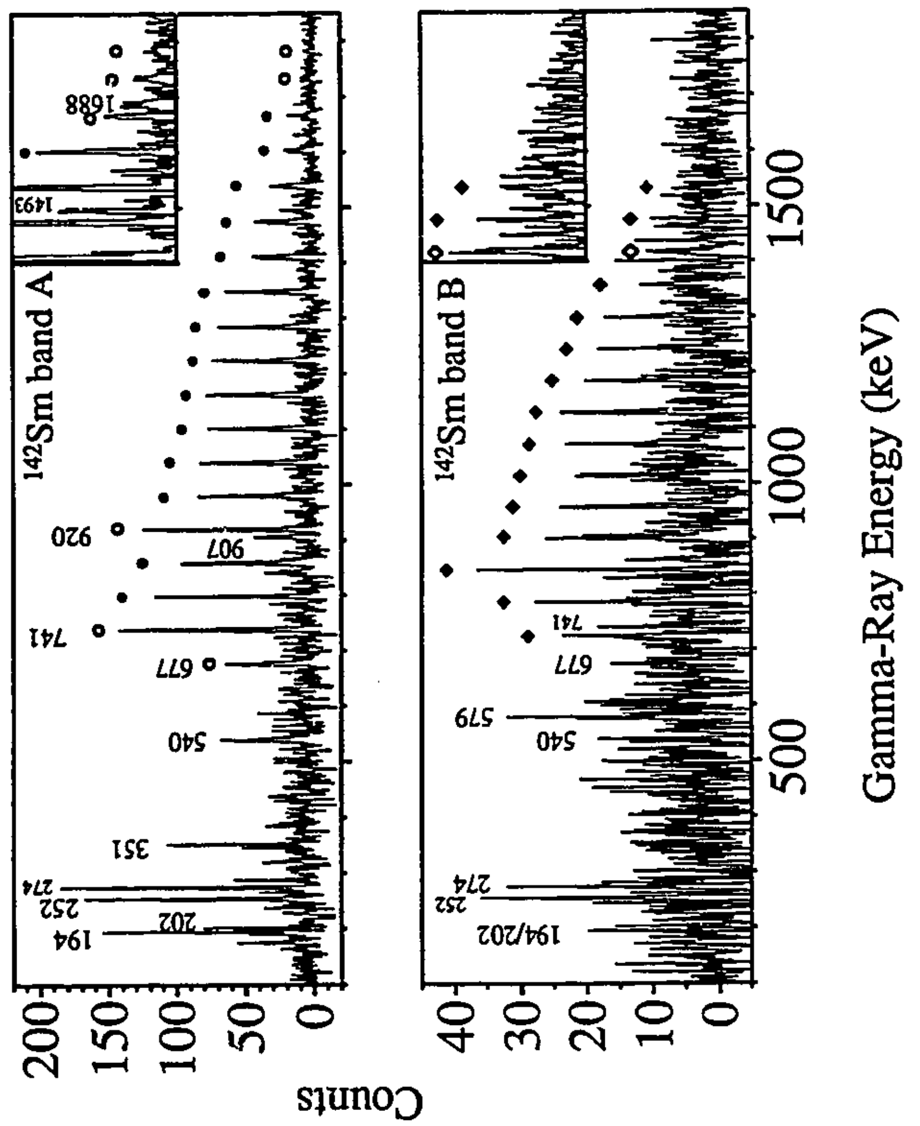

Figure 4.3.3: ^{142}Sm SD bands A and B, γ-ray spectra from triple-gated quadruple-coincidence data measured with GAMMASPHERE. Symbols mark transitions assigned to the SD bands. The symbols are filled if the transition was used in the combinations of triple-gates. A (fold-1) background has been subtracted. Energies of low-lying transitions in ^{142}Sm are identified.

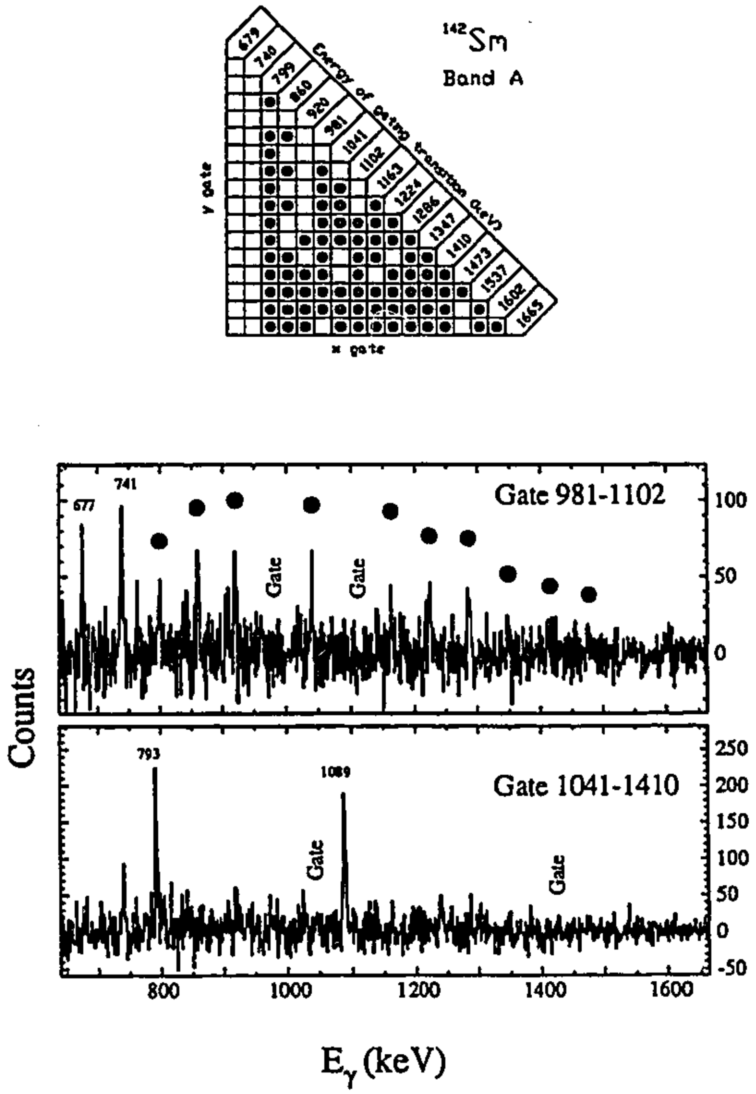

Figure 4.3.4: ^{142}Sm band A, clean gates. Top, clean double gates are indicated on grid by a bullet (•). Middle, partial γ-ray spectrum from a clean double-gate. The only obvious lines are those from the SD band and the 677 and 741 keV low-spin transitions of ^{142}Sm. Bottom, partial γ-ray spectrum from a dirty double-gate. The spectrum is dominated by the 793 and 1089 keV transitions of ^{141}Sm. (Note the change in vertical scale.)

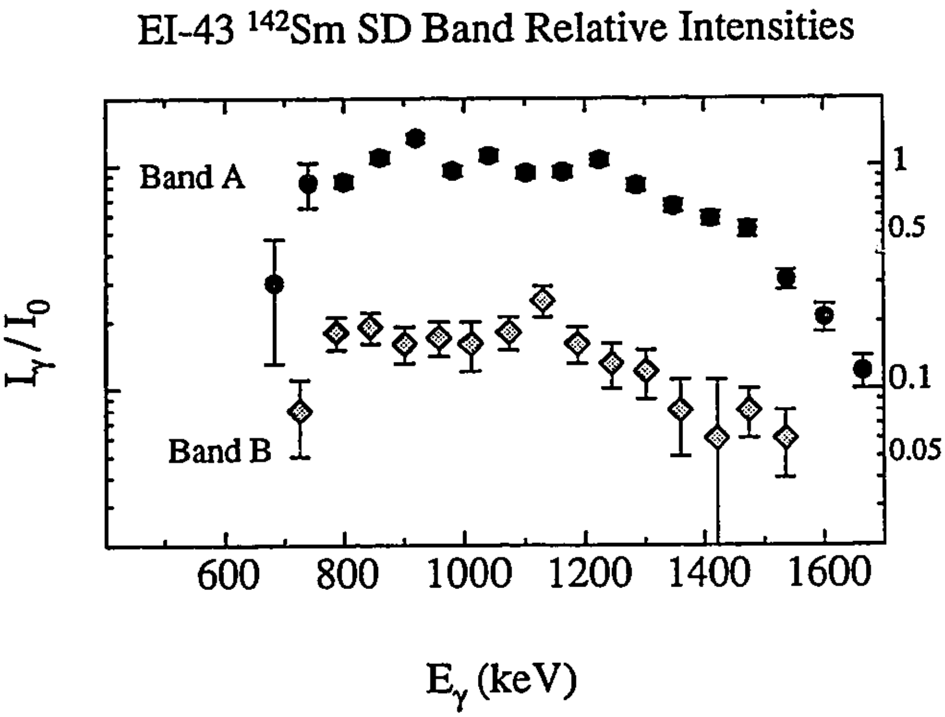

Figure 4.3.5: Relative intensity profiles of ^{142}Sm discrete superdeformed bands, as a function of γ–ray energy, normalized to 1 in the empirical plateau region of the yrast band.

CUBEAID cube, following the semi-automated fitting procedure described in Appendix E. This was then renormalized as input for LEVIT8R analysis. As shown in Figure 4.3.6, all of the decay-out of the SD band was assumed to feed an artificial level, which itself decayed by numerous paths to the near-yrast noncollective states. This model of decay-out through the quasi-continuum between the SD and ground state yrast lines has been applied previously to ^{149}Gd [Fli 95]. The intensities of the decay-out paths were fit manually.

Centroids of intensity-weighted spin distributions showed that, on average, the SD band decayed out $2.0 \pm 0.3\hbar$ above the final state of the 679 keV transition, and that the subsequent decay fed known non-collective states at $18 \pm 1\hbar$. These

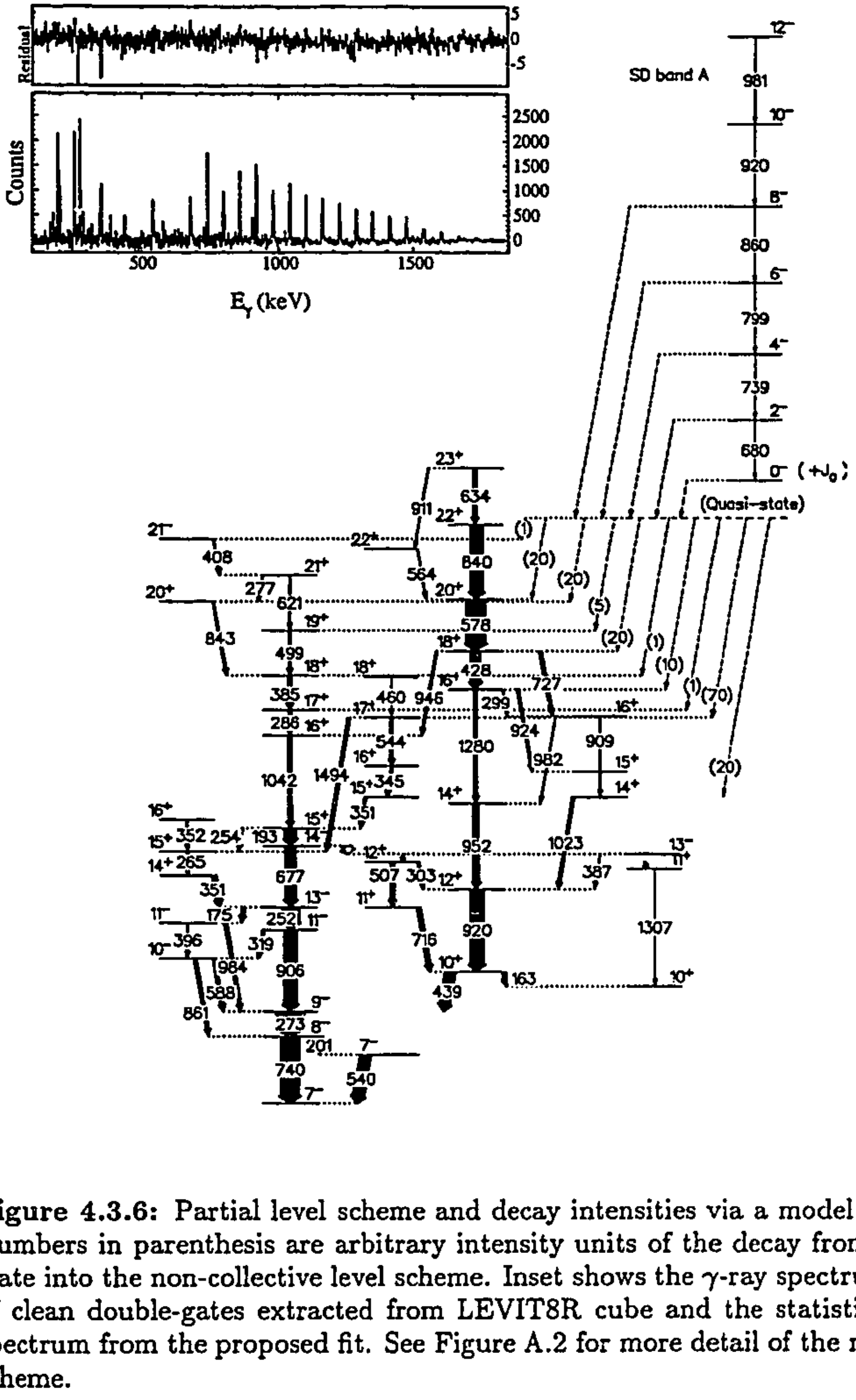

Figure 4.3.6: Partial level scheme and decay intensities via a model quasi-state. Numbers in parenthesis are arbitrary intensity units of the decay from the quasi-state into the non-collective level scheme. Inset shows the γ-ray spectrum of a sum of clean double-gates extracted from LEVIT8R cube and the statistical residual spectrum from the proposed fit. See Figure A.2 for more detail of the non-SD level scheme.

uncertainties reflect confidence in the measured branching ratios of decay-out of the SD band and into the non-collective states. In addition to this uncertainty there could be errors in the deduced non-collective decay scheme. For example, a large component of the feed-in occurs at a $J = 17$ state. In the non-collective decay scheme, the γ rays which de-excite this state are quite strong, but only one weak non-SD transition could be assigned as feeding this state. As such the feed-in which is presently assigned to this $J = 17$ state may indeed proceed through near-yrast states which have yet to be identified. Thus the entry spin reported above should be considered as a lower limit. Based on these measurements, and if one assumes that the decay from the SD band to the normal scheme proceeds by three stretched E1 transitions (cf. [Fli 95]), the 679 keV γ ray would be a $J = 21 \rightarrow 19$ transition. Again, this should be regarded as at best a lower limit of the spins of the SD band states.

4.3.4 ^{142}Sm excited SD band B

A series of exhaustive searches for new superdeformed bands was executed. The code ANDband [HHW 94], described in Appendix C, was used to scan both triple- and quadruple-coincidence list-mode data for possible bands with $640 \leq E_0 \leq 711$ keV, $50 \leq \Delta E_0 \leq 70$ keV, and a non-rigidity parameter $-0.3 \leq \Delta^2 \leq 1.1$ keV. Series of gates were also set corresponding to possible bands with $\mathcal{J}^{(2)}$ values identical to those of known bands in the $A \sim 140$ mass region. Despite these searches, only one very weakly populated new band was found. It is shown in Figure 4.3.3. Once again, clean double-gates were identified and are shown in Figure 4.3.7.

Because this new band is so weak, the evidence of γ rays in coincidence with the band is not as convincing or obvious as it is for ^{142}Sm band A. In both the triple-gated spectrum of Figure 4.3.3 and in sums of clean double-gated spectra, the dominant non-SD transitions are 194, 202, 252 and 274 keV lines. There is also weak evidence of the 540, 677 and 741 keV transitions, although they are obscured

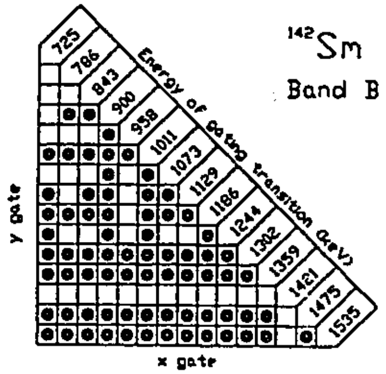

Figure 4.3.7: Clean double-gates used in analysis of ^{142}Sm band B are identified with a bullet (•).

by statistical noise in the triple-gated quadruples spectrum. In addition, the 579 keV line is observed in coincidence with the new band. This line has been assigned as a $J = 20 \rightarrow 18$ transition in ^{142}Sm. Based on this coincidence evidence the cascade is assigned to ^{142}Sm as superdeformed band B. Since the lowest-energy γ rays observed in bands A and B have similar energies, it is unlikely that the spins of the states in the new band could be lower than those band A. Therefore, if band B of Figure 4.3.3 were an excited band in ^{142}Sm then it would most likely feed into higher-spin non-SD states after its decay-out, which explains why the 578 keV transition is observed in strong coincidence with band B but not band A.

The intensity profile has been calculated from the sum of clean double-gates spectrum by the method of Appendix E. This profile has been compared to that of band A. After taking into account this profile and detector efficiency, it is estimated that the empirical plateau region of ^{142}Sm band B is populated with (17±3)% of the intensity of band A, or approximately 0.07% to 0.10% of the ^{142}Sm cross section. The energies and intensities of the transitions in band B are listed in Table 4.3.2. The large uncertainty on the energy and intensity of the ~ 1420 keV SD transition is due to a strong 1418 keV line from ^{141}Sm, since this contaminant line introduces

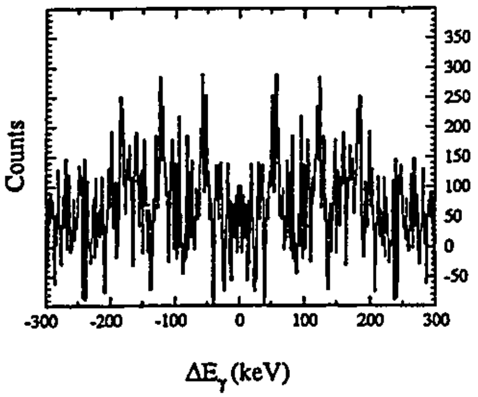

Figure 4.3.8: Ridge projection (see Sect. 2.6.2) of a background-subtracted γ–γ coincidence matrix, $H > 18.5$ MeV, from the 8π experiment. The projection was performed over γ-ray energies between 1.3 and 1.8 MeV, excluding those rows and columns corresponding to the known SD bands in ^{142}Sm.

statistical fluctuations into the background which are much worse than for other transitions in the band.

4.3.5 Quasi-continuum in ^{142}Sm

A superdeformed ridge which was distinct from the yrast SD band was first noted in the original 8π experiment, and is shown in Figure 4.3.8. Indeed, the existence of this ridge was part of the incentive for performing the GAMMASPHERE experiment to search for weaker discrete bands. As was discussed in Sect. 2.6.2, these radiations result from the decays of a large number of rotational structures with the same dynamic moment of inertia $\mathcal{J}^{(2)}$. The high level density in the vicinity of these states permits only a small number of in-band transitions before decay proceeds to other configurations. Since the ridge is observed in γ–γ–($H > 18.5$ MeV) coincidences, it is unlikely that the ridge is associated with the 7-particle evaporation channels, *i.e.* ^{141}Sm or ^{141}Pm. It is most likely that these radiations are associated with ^{142}Sm, by the same arguments as the assignment of the yrast band.

More detailed analysis of the ridge requires the higher statistics of the GAMMASPHERE data set. Two questions of importance are the intensity and centroid of the inner, first-order ridge. This corresponds to $J+2 \rightarrow J \rightarrow J-2$ γ–ray coincidences in the quasi-continuum states. First, a ridge projection was generated by gating on those elements in the matrix where the sum of γ–ray energies corresponds to two consecutive transitions above 1.0 MeV in ^{142}Sm band A, the spectrum of which is shown in the first panel of Figure 4.3.9. There is a peak at 61 keV, which is the average spacing of γ–ray energies in band A. Since the intensity of the transitions which comprise this peak are known, it is used as a reference for subsequent measurements. Next, spectra were generated where the sum of two γ-ray energies were restricted to ranges of 0.3 MeV, excluding those ranges known to include coincidences in either band A or band B. Furthermore, sum-energy gates which would include γ–γ coincidences of non-SD γ-ray transitions differing in energy by ~60 keV were also excluded. The resulting ridge projections should only contain counts at the expected SD position which did not arise either from the known bands or from non-SD decays. These spectra are shown in panels (b) through (f) of Figure 4.3.9. It should be noted that even though these sum-energy gates cover the same energy range, the actual number of positions in the γ–γ matrix which can contribute to the sum depends on how many sum-energy diagonals had to be excluded, so the actual number of counts in the peaks does not correspond directly to the ridge intensity.

The ridge intensity was then calculated by comparing the number of counts in the yrast SD-gated 61 keV peak to the ~ 60 keV peaks in other projections and correcting for excluded sum-energy diagonals. The ridge first appears for average γ-ray energies of ~ 1 MeV, and the ridge reaches a maximum intensity at ~ 1.2 MeV. Beyond that, the ridge intensity is approximately the same as that of the yrast band. (See Figure 4.3.10). It should be noted that this intensity, extracted from the GAMMASPHERE data, would include any quasi-continuum radiations from ^{141}Sm or ^{141}Pm in addition to ^{142}Sm. However, the 8π data have shown that at least some of this intensity is indeed in ^{142}Sm. The centroid of these ridges was typically $\sim 59 \pm 1$ keV, the consequences of which will be discussed more thoroughly

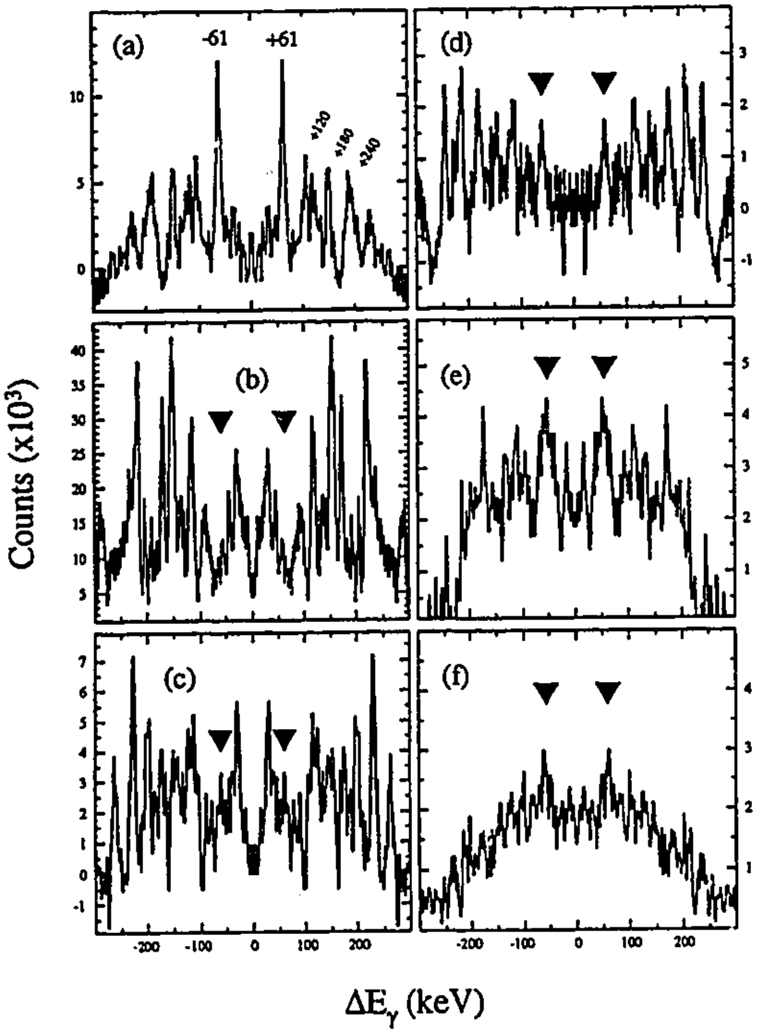

Figure 4.3.9: Ridge projections observed in ^{142}Sm. (a), gated on sum-energy of consecutive transitions in Band A above 1 MeV; (b), gated on sum-energies from 1.9 to 2.2 MeV, excluding sum-energies from known discrete SD bands or non-SD decays; (c), as in (b) from 2.2 to 2.5 MeV; (d), 2.5 to 2.8 MeV; (e), 2.8 to 3.1 MeV; (f), 3.1 to 3.6 MeV. Upside-down triangles indicate ±59 keV.

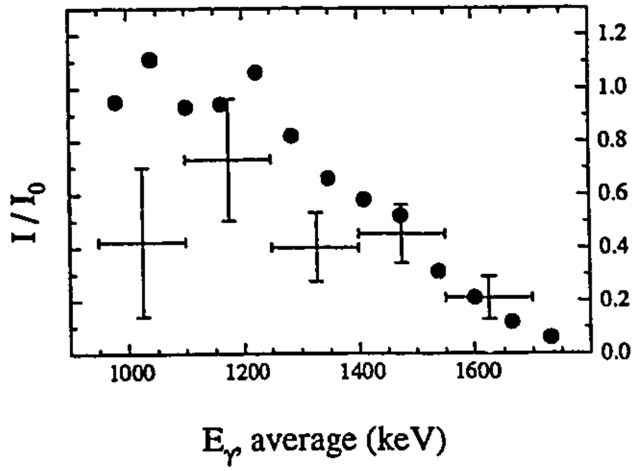

Figure 4.3.10: Ridge intensity, normalized to the plateau region of ^{142}Sm band A. Bullets (•) are the intensities of the ^{142}Sm band A discrete transitions. The measured ridge intensity is at the intersection of the error bars, with the vertical error bar indicates the uncertainty in measured ridge intensity, while the horizontal error bar shows the range of average γ–ray energy (or, 1/2 of the sum-energy) over which it was measured.

in Chap. 5. It is also worth noting that average ridge FWHM of ~ 16 keV is much larger than that of the yrast-band gated projection, which was ~ 9 keV. This may be evidence either of many bands with a wide variety of $\mathcal{J}^{(2)}$ values, or as evidence of significant rotational damping.

Surprisingly, there was no evidence of decay from the SD continuum to the yrast ^{142}Sm band A. A γ–γ matrix was generated from clean double-gates on ^{142}Sm band A. The matrix was gate-corrected by a combination of the double-gated matrix, a single-background-gated matrix, and a background-background matrix, as per Sect. B.2.3. Ridge projections were generated first for the entire matrix, and then for those elements whose sum-energy avoids the yrast SD band. These spectra are shown in Figure 4.3.11. The second of these projections is completely devoid of any evidence of a ~ 60 keV ridge. This implies that the branching ratio through the superdeformed quasi-continuum and subsequently into the yrast band A must

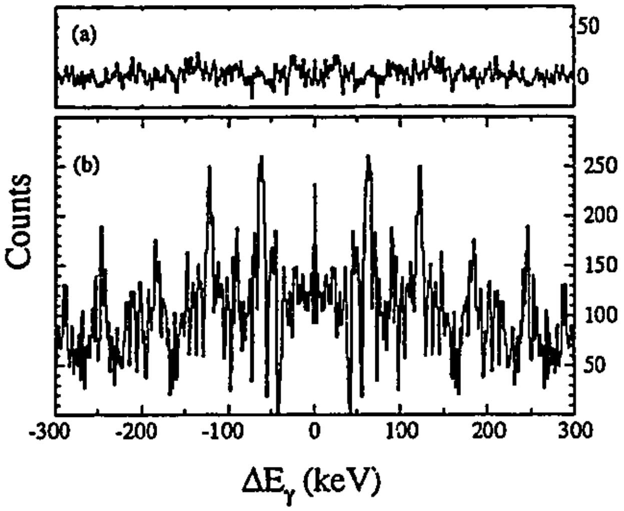

Figure 4.3.11: Ridge projections from a γ–γ matrix, generated from quadruple-γ coincidences by double-gating on discrete transitions of ^{142}Sm. The data were gate-corrected as per Sect. B.2.3. Bottom panel, ridge projection of full matrix; top panel, ridge projection for sum-energies from 2.2 to 3.6 MeV, avoiding elements whose sum-energy includes known SD transitions in either band A or B of ^{142}Sm.

be quite low, or less than ~ 5% of the population of band A. In other words, band A is not fed by superdeformed quasi-continuum states.

4.4. Superdeformation in ^{142}Eu

To study superdeformation in ^{142}Eu, two stacked $\sim$ 500 μg/cm^2 targets of > 98% ^{120}Sn were bombarded with a ^{27}Al beam at 152 MeV. The Pb-Cd-Cu absorbers described in Sect. 3.5 were installed, and the 8π HPGe detectors were calibrated to $b_{\mathrm{nom}} = 0.5$ keV/channel with a ^{88}Y source. BGO ball multiplicity discriminators were set to $K_{\mathrm{hardcut}} \geq 12$ and $K_{\mathrm{p.u.}} \geq 9$, and again the delayed $K_{\mathrm{p.u.}}$ signal was used for post-pile-up rejection. The on-line v/c correction was set to 1.84%, and a total of $\sim 351 \times 10^6$ events were recorded to tape. Efficiency and energy calibrations were performed with a ^{152}Eu source following the experiment.

In this experiment, reaction channels involving evaporated charged particles were clearly evident. Based on the BGO sum-energy spectra gated on γ rays in ^{142}Eu via 5n evaporation, ^{142}Sm via p4n, ^{139}Pm (α4n), ^{141}Eu (6n) and ^{141}Sm (p5n) shown in Figure 4.4.1, the offline γ–γ matrices were sorted for the BGO sum energy conditions $H > 13.1$ and $H > 18.1$ MeV, respectively. The former condition includes most 5-particle events while rejecting about 50% 6-particle events, and the latter excludes almost all 6-particle events while retaining about 50% of the 5-particle channels. Both matrices were scanned with the SDSLICE code, and a salient candidate for a superdeformed band was eventually confirmed. It should be noted that this band is different from that reported by the GA.SP collaboration [Ata 94]. There was no evidence of that cascade in the present data.

The γ–ray spectrum of the band is shown in Figure 4.4.2, and the energies and intensities of the SD transitions are listed in Table 4.4.1. The band consists of a cascade of 15 transitions with an average γ–ray spacing of 60 keV from 700 to 1548 keV. One of these, the 947 keV transition, is an intense γ-ray from the ^{139}Pm decay. Although ^{142}Eu γ rays are observed in the sum-of-gates spectrum, this was not considered a completely reliable means of assigning the structure to that nucleus. The number of counts in the SD peaks, under identical gating conditions, are attenuated by about a factor of 2 in the $H > 18.1$ MeV matrix relative to the

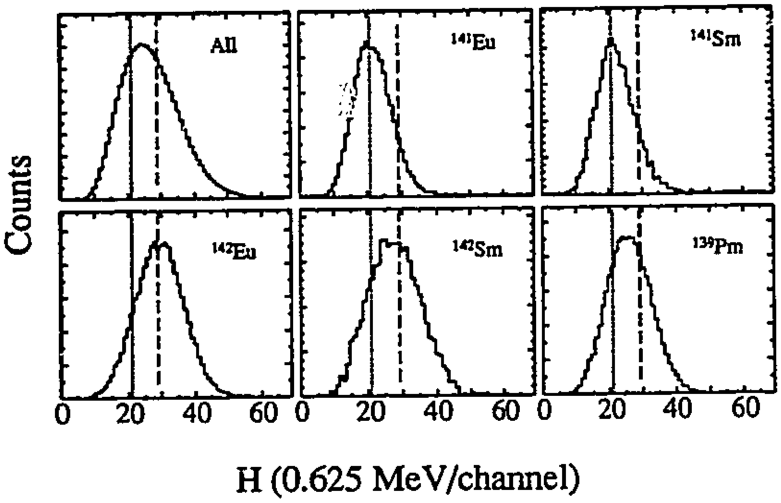

Figure 4.4.1: BGO sum-energy (H) measurements for the ^{142}Eu experiment, for all reactions and for γ rays in coincidence with the dominant reaction channels. The dotted and dashed vertical lines indicate the 13.1 and 18.1 MeV H cuts which were used in off-line analysis.

$H > 13.1$ MeV data. From Figure 4.4.1, this excludes the possibility that this band is in one of the 6-particle evaporation channels. Since the SD bands in ^{142}Sm are already known, that possibility is also discounted. Finally, ^{139}Pm is ruled out by cross-bombardment. A separate high-spin experiment where ^{139}Pm was populated via an xn reaction showed no evidence of the present band. Therefore this band is assigned to ^{142}Eu.

The intensity of the band was, again, measured by taking an empirical plateau region, this time for all γ rays from 700 to 1187 keV. The peak areas were efficiency-corrected and it was determined that the band intensity was 2.4% compared to the intensity of the 419-283 keV γ–γ coincidence. This coincidence carries almost all of the γ-ray flux to the ground state of ^{142}Eu. Since the 283 keV transition de-excites a 9 ns isomeric state, the 419-283 keV coincidence intensity was attenuated, as was discussed in Sect. 4.3.2. A short experiment was performed with a gold-backed target. In such an experiment the recoiling residual nucleus is stopped in the backing material, and hence stays in the focus of the HPGe array.

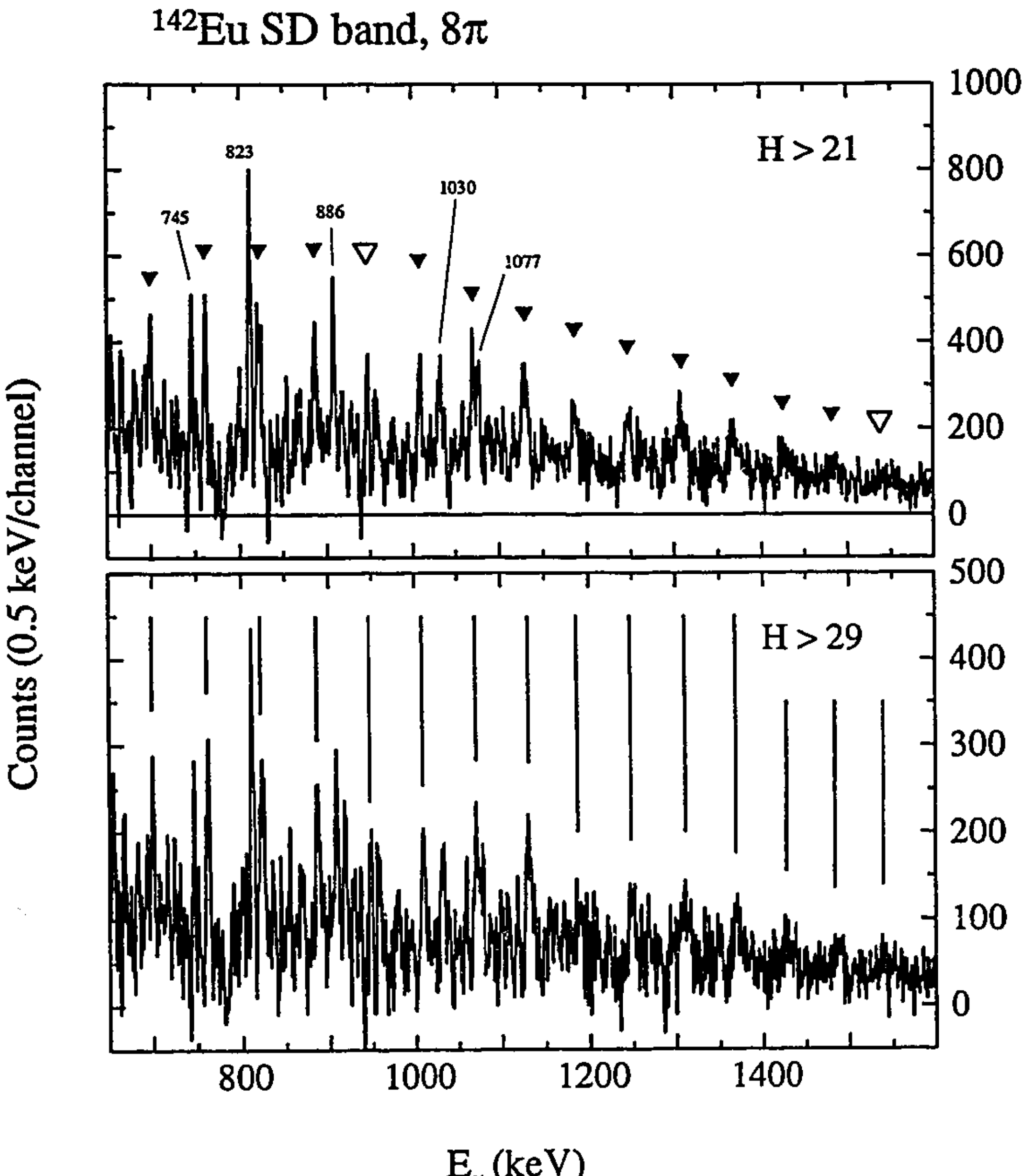

Figure 4.4.2: Partial sum-of-gates γ-ray spectrum of ^{142}Eu SD band. Top panel, spectrum extracted from $H > 13.1$ MeV data. triangles indicate band members, with symbols filled for gating transitions. ^{142}Eu non-SD transitions are identified. Bottom panel, same gating conditions, $H > 18.1$ MeV data.

^{142}Eu Band A	
E_γ (keV)	I_γ (relative, %)
699.6(3)	106(17)
761.8(2)	98(16)
832.0(2)	94(15)
886.3(3)	110(20)
947.0(4)	
1008.2(3)	94(15)
1069.4(3)	100(16)
1128.9(3)	97(16)
1187.0(7)	52(8)
1247.8(8)	53(9)
1307.9(6)	20(3)
1368.4(8)	
1428.0(10)	
1487 (2)	
[1548 (2)]	

Table 4.4.1: Energies and, where measurement was possible, relative intensities (normalized to 100% in the plateau region, 700 to 1129 keV) of γ-ray transitions assigned to the observed superdeformed band in ^{142}Eu, as measured with the 8π spectrometer. Brackets indicate tentative transition. Energy uncertainties are statistical only. All measurements were made from γ-γ coincidence data. The intensity of the 947 keV transition could not be measured reliably because it is a doublet.

This showed that the intensity of the 419-283 keV γ–γ coincidence increased by a factor of two relative to high-spin γ–γ coincidences. The measured intensity of the SD band relative to the ^{142}Eu production cross-section, then, is $1.2 \pm 0.2\%$.

4.5. Superdeformation in ^{144}Eu

The first ^{144}Eu experiment was performed with the 8π spectrometer. An ^{27}Al beam at 142 MeV was directed upon two stacked ~ 500 μg/cm^2 foils of $> 98\%$ ^{122}Sn. With hexagonal Pb-Cd-Cu absorbers, K_{hardcut} and $K_{\mathrm{p.u.}}$ set to 10, the HPGe detectors gain matched with a ^{88}Y source to 0.5 keV/channel, and the CAB v/c correction set at 1.73%, a total of 350×10^6 γ–γ–BGO coincidences were recorded to tape. Following the experiment, a ^{152}Eu source was used for efficiency calibrations.

A ridge projection from an $H > 18.1$ MeV γ–γ matrix showed peaks at ± 59 keV[Mul 93]. Both SDSLICE and the BANDAID correlation grid found a candidate band with that spacing, but a convincing spectrum could not be extracted from the data. However the existence of the ridge was sufficient incentive to perform the experiment with a more sensitive array.

4.5.1 Discovery and Assignment of ^{144}Eu SD Bands

The GAMMASPHERE ^{144}Eu experiment was performed with the identical beam and target conditions as the 8π experiment, and the GAMMASPHERE array was configured exactly as for the ^{142}Sm experiment. A ^{207}Bi source was used to set the HPGe programmable amplifiers for 0.5 keV/channel. The positions of the 492 and 1700 keV transitions of ^{144}Eu were monitored for on-line gain drift corrections. Approximately 1.2×10^9 triple- and higher-fold coincidences were written to tape. Subsequent pre-sorting and sorting (list mode, CUBEAID and LEVIT8R) were performed in the same manner as for the ^{142}Sm data, and the breakdown of events by fold is listed in Table 4.3.1. Subsequent data sorting followed an identical prescription to that used for the ^{142}Sm GAMMASPHERE data. The same parameters for the ANDBAND SD cascade search were also employed.

A total of three new, discrete superdeformed bands were found in these data, and their γ-ray spectra are shown in Figure 4.5.1. The clean double-gate lists which were used for sum-of-gates analysis are shown in Figure 4.5.2. Spectra were extracted from the quadruple-coincidence list data for each possible triple-gate combination in each band. The associated background spectra, described in Sect. B.2, were also generated, taking the background range as all channels between the SD transitions. From these, fully background-subtracted triple-gated spectra were evaluated. A clean triple-gate was defined as a gate where two of the gating transitions would be part of the clean double-gate list, and those clean triple-gated spectra were summed.

For all three new bands, the clean double-gated spectra showed compelling evidence of lines assigned as low-spin ^{144}Eu transitions, especially at 164, 331, 492, 541, 551 and 742 keV [Hae 81]. These transitions were also seen in the sum of clean triple-gates spectra of bands A and B. It is perhaps troubling that the 210 keV transition, which de-excites an 5 ns isomeric state which is fed by the 331 keV transition, is not seen strongly in these spectra. However most of the non-SD transitions are definitely assigned to ^{144}Eu, and the pattern of non-SD transitions is clearly different than that for the ^{143}Eu yrast SD band, which was also observed in this data set. On the evidence of the non-SD transitions in the sums of clean gates, these new bands are assigned to ^{144}Eu as superdeformed bands A, B, and C.

Bands B and C do not follow a regular γ-ray spacing pattern for their entire length. This is evidence for band crossings. Confirming which transitions are really part of the SD cascade is critical to understanding the structure of the band. The first step in identifying a γ ray which was *not* part of the regular spacing pattern was to generate a spectrum from triple-γ coincidences by gating once on the line in question and again on the established transitions of the SD band. If the SD band appeared in this sum of double-gated spectra, then the candidate transition was confirmed and assigned to the band. The 878 keV transition of band C, for example, satisfied this criterion, while and 895 keV line in the sum-of-gates spectrum of band C did not. The latter transition was later identified as a strong transition in the non-SD decay of ^{144}Eu at an appropriate spin that it could be fed by the decay-out of band C, and unlike the low-energy transitions of ^{142}Sm band B,

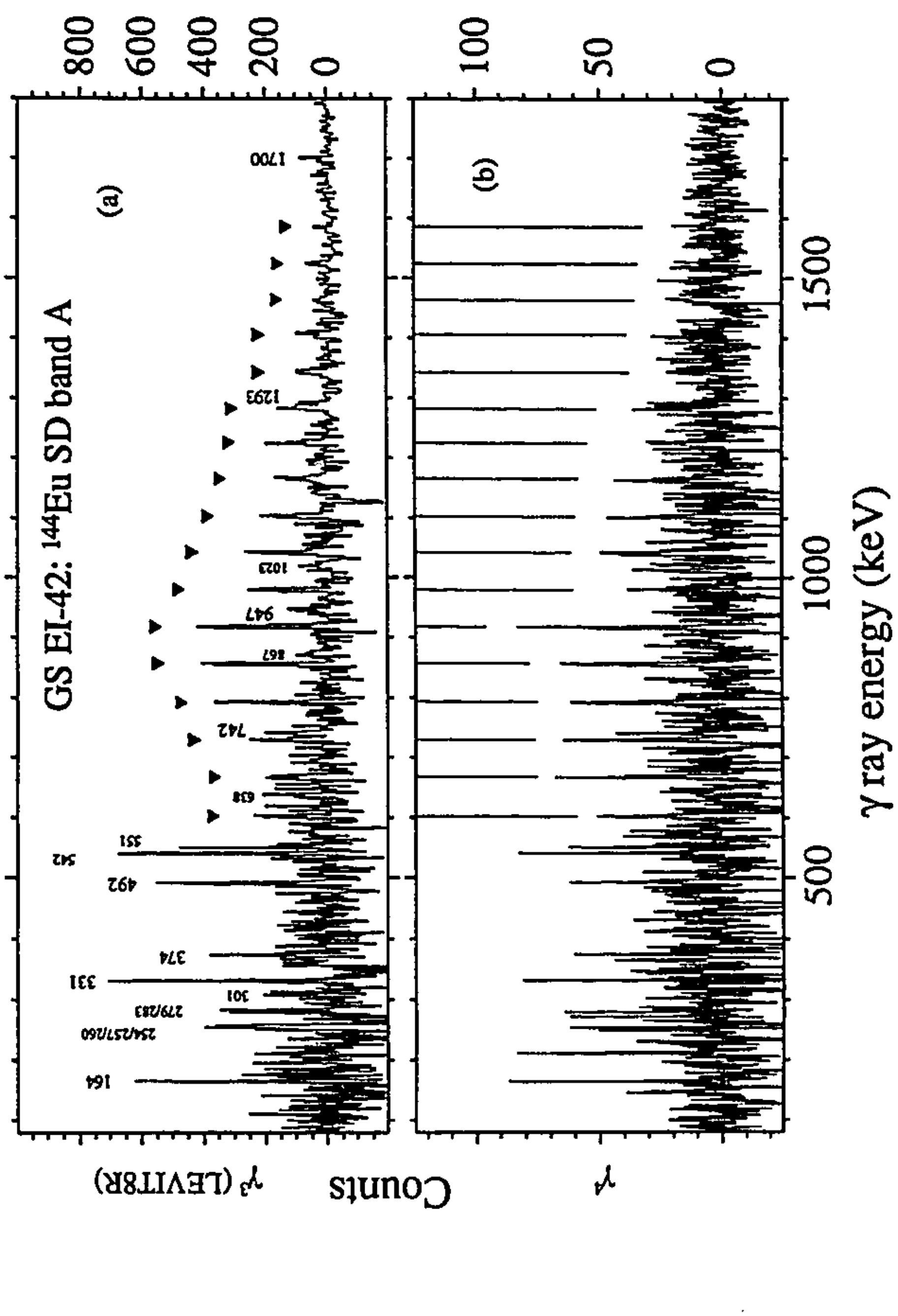

Figure 4.5.1a: ^{144}Eu SD band A spectra observed with GAMMASPHERE. SD transitions labeled with symbols. (a), sum of clean double-gates. (b), sum of clean triple-gates. See text for details.

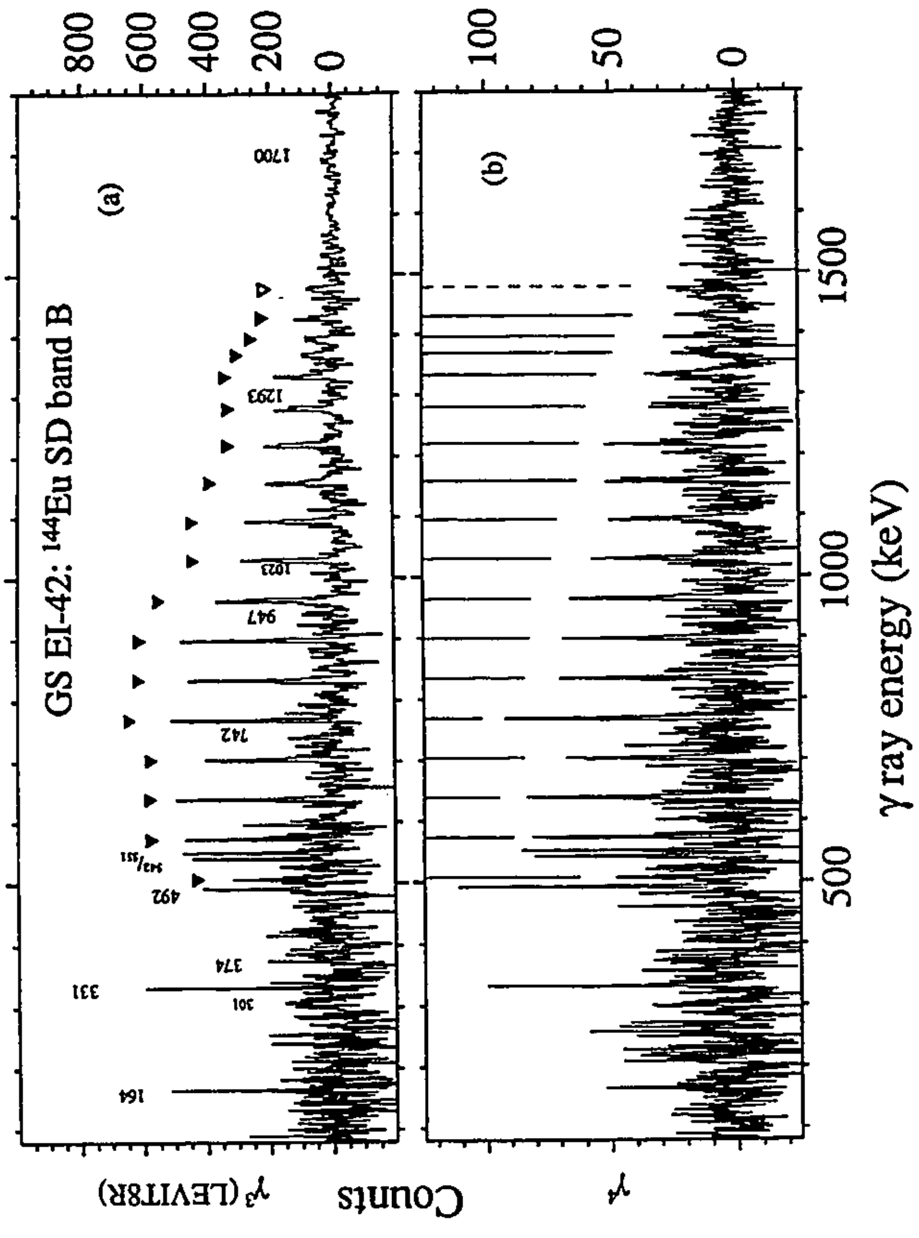

Figure 4.5.1b: ^{144}Eu SD band B spectra observed with GAMMASPHERE. SD transitions labeled with symbols. (a), sum of clean double-gates. (b), sum of clean triple-gates. See text for details.

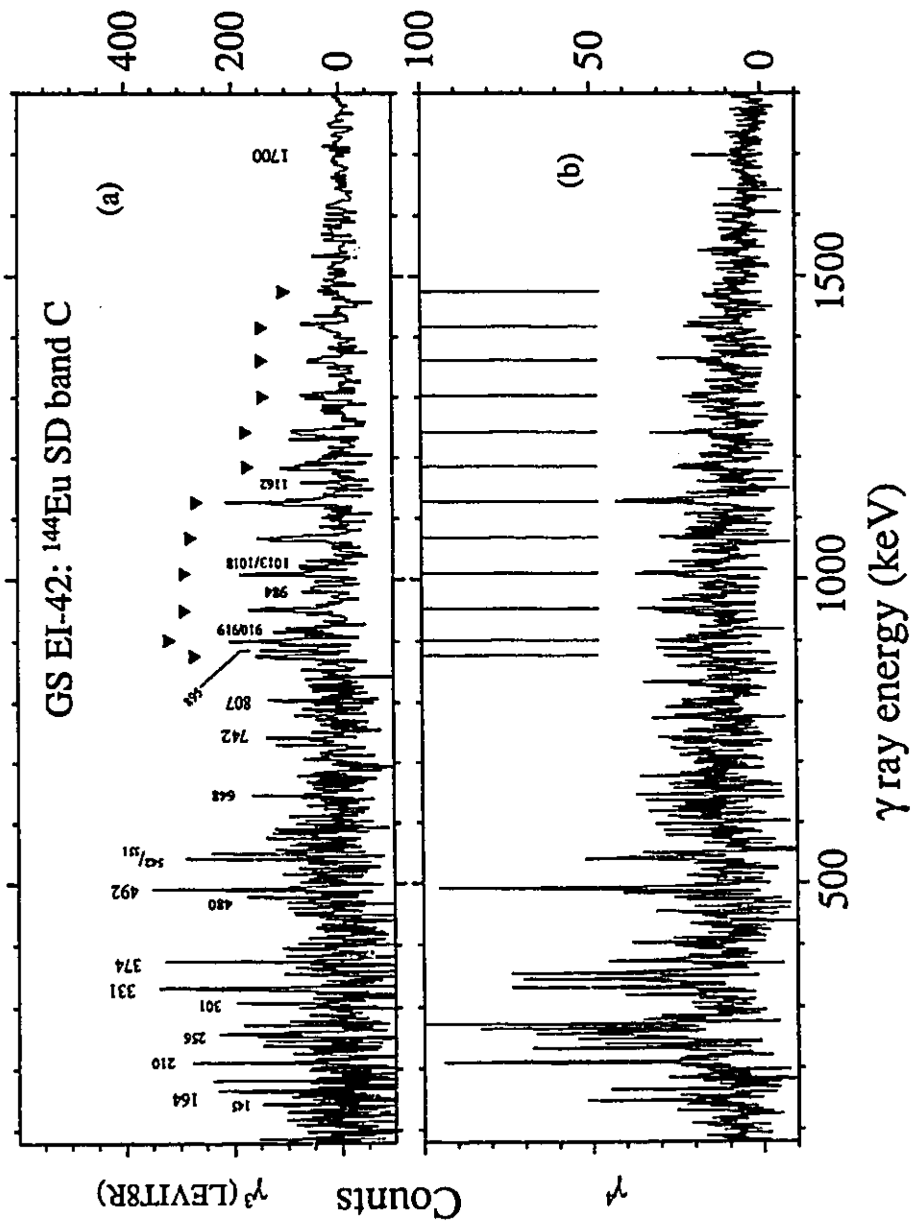

Figure 4.5.1c: ^{144}Eu SD band C spectra observed with GAMMASPHERE. SD transitions labeled with symbols. (a), sum of clean double-gates. (b), sum of clean triple-gates. See text for details.

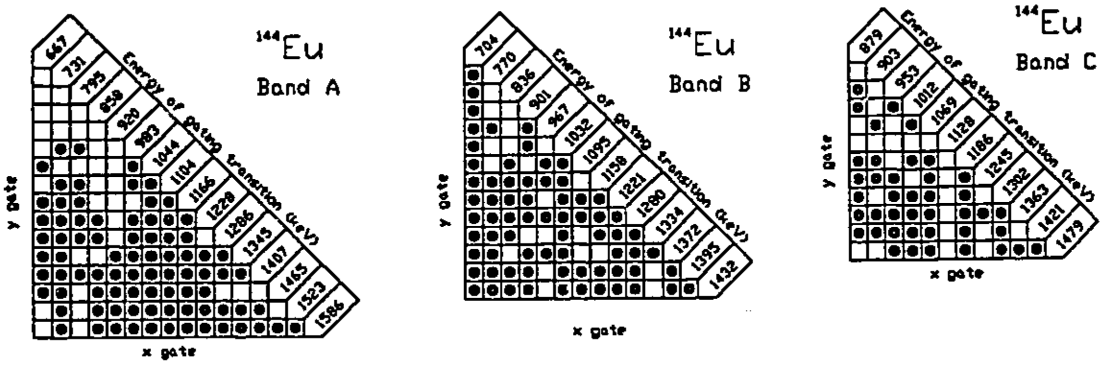

Figure 4.5.2: Defined "clean double-gates" triangle for the three ^{144}Eu SD bands. A bullet (•) indicates that the double-gate was clean and was used in sums-of-gates analysis. Double-gates which were omitted from sums have empty grid locations.

there was no evidence for an excess of counts in the peak which could be attributed to an SD transition. Therefore this 895 keV line was not assinged to band C. The same procedure was followed to extend both bands A and B. A total of 17, 18 and 12 transitions were assigned to bands A, B and C, respectively, in this manner.

4.5.2 Intensities

Centroids and areas of the ^{144}Eu SD peaks were measured from double-gated triples spectra. The energies and intensities of the γ rays assigned to these bands are listed in Table 4.5.1, with the intensity profiles plotted in Figure 4.5.3. Transitions in a region where the spacing is no longer constant, for example where a backbending may occur, are often ordered on the basis of their intensities. The intensity of the transitions should depend on the initial state spin, not the γ-ray energy itself, and in the population region of the SD band the intensity should increase with decreasing spin. The measured intensities of the high-energy transitions of band B are fully consistent with a band crossing that does not backbend.

The intensities of the plateau regions of bands B and C relative to band A are 88±3% and 87±4%, respectively. The latter result may at first seem surprising, since the sum of triple-gated spectra for band C appears to be of much poorer quality

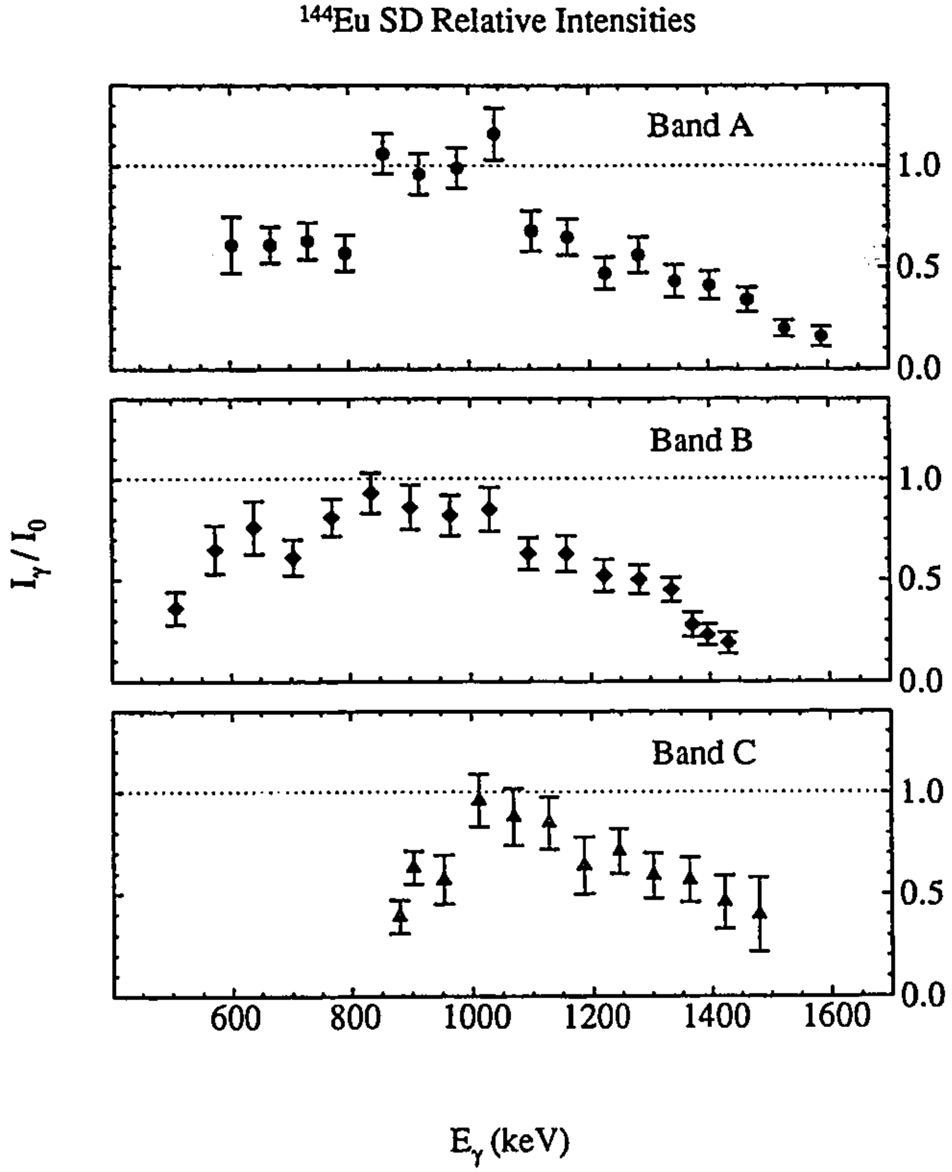

Figure 4.5.3: Relative intensity profiles of ^{144}Eu discrete SD bands as a function of γ–ray energy, normalized to 1 in the empirical plateau region of band A.

^{144}Eu SD Bands					
Band A		Band B		Band C	
		506.9 (3)	36 (8)		
603.2 (4)	61 (14)	572.9 (2)	65 (12)		
668.3 (3)	61 (9)	638.8 (2)	76 (13)		
731.4 (3)	63 (9)	704.1 (3)	61 (9)		
794.7 (4)	57 (9)	770.0 (2)	81 (9)		
857.9 (2)	106 (10)	835.7 (3)	93 (10)	878.6 (6)	39 (8)
920.2 (3)	96 (10)	900.6 (3)	86 (11)	902.7 (4)	63 (8)
982.5 (3)	99 (10)	966.7 (3)	82 (10)	952.7 (6)	57 (12)
1043.8 (3)	106 (13)	1031.8 (3)	85 (11)	1011.7 (5)	96 (13)
1104.2 (5)	68 (10)	1095.1 (5)	63 (8)	1069.3 (6)	88 (14)
1166.0 (5)	65 (9)	1158.1 (5)	63 (9)	1128.0 (6)	85 (13)
1227.5 (7)	47 (8)	1221.1 (6)	52 (8)	1186.1 (7)	64 (14)
1286.4 (7)	56 (9)	1280.5 (5)	50 (7)	1244.9 (6)	71 (11)
1345.5 (9)	42 (8)	1333.8 (5)	45 (6)	1302.2 (8)	59 (11)
1407.0 (8)	41 (7)	1372.3 (8)	28 (6)	1363.3 (9)	57 (11)
1465.3 (9)	34 (6)	1395.5 (9)	23 (5)	1421.4 (12)	46 (13)
1525.7 (11)	20 (4)	1431.8 (11)	19 (5)	1479 (2)	40 (18)
1586 (2)	16 (5)	1467.1 (12)	10 (5)		

Table 4.5.1: Energies and relative intensities (normalized to 100% in Band A plateau region) of γ-ray transitions assinged to superdeformed bands A, B, and C in ^{144}Eu, as measured with GAMMASPHERE. All measurements were made from γ-γ-γ coincidence data (sums of clean double-gated spectra), except for the γ rays with energies below 640 keV and the 1467 keV transition of band B, which were measured in sums of triple-gated spectra.

than those for bands A and B. Since there are only twelve transitions assigned to band C, compared to 18 for band B, there are only about one-third as many triple-gate combinations available for creating the sum-of-gates spectra. Therefore the sum-of-gates spectrum has one-third as many counts in the SD peaks, even though the band itself is populated with the same intensity.

The intensity of population of the SD bands relative to the ^{144}Eu fusion-evaporation cross section was evaluated with LEVIT8R. The calculated profiles for bands A, B and C were used in an input level scheme. These intensities were then adjusted by a multiplicative factor so that the sum of calculated counts in the SD peaks of clean sums-of-double-gates spectra of all three bands equaled the sum of counts experimentally observed. This intensity was then compared to a best fit in the LEVIT8R cube data for the intensities of the transitions feeding the 10^+ state, namely 492, 1132, 1234, 1338 and 1700 keV. The intensity of the plateau region of band A was measured to be $0.22 \pm 0.03\%$ of the sum of those transitions. This value should be taken as an upper limit, however, since it is possible that some of the γ–ray flux from a fusion-evaporation event will not proceed through these transitions. Also, because the angular momentum vector of the residual nucleus is nearly perpendicular to the beam axis, the geometry of the GAMMASPHERE HPGe detectors would enhance the detection probability for stretched E2 transitions relative to a spherically uniform detector arrangement. This enhancement factor is roughly 10% per transition [Yam 67], so a triple-coincidence in a stretched E2 cascade would be enhanced by $\sim$ 32%. The γ rays used for the intensity reference are $\Delta J = 0, 1$ and 2 transitions, and so the total effect of the detector geometry will be assumed to average out to within 10%. Therefore the upper limit on the intensity of the band A plateau region is $0.17 \pm 0.04\%$ of the ^{144}Eu fusion-evaporation cross-section.

4.5.3 Spins

Because these bands were approximately one third as intense as ^{142}Sm band A, it was not possible to do a detailed fit of the decay into the non-collective level scheme for the ^{144}Eu bands. The centroids of the decays-out are $2.8 \pm .7\hbar$, $2.8 \pm .8\hbar$, and $2.06 \pm .8\hbar$ above the final state of the lowest observed transition of bands A, B and C, respectively. Both bands A and B have very similar non-SD transitions in the sum-of gates spectra, in particular the 307 and 947 keV transitions. According to the level scheme of [Pii 95a], this γ–ray de-excites $J = 19$ states in ^{144}Eu. In the band B spectrum there is no evidence of γ rays involving higher-spin states. The band A spectrum, on the other hand, also has evidence of possibly the 261 and 283 keV transitions, which have been assigned as two $\Delta J = 1$ transitions in cascade above the $J = 19$ initial state of the 947 keV transition. By contrast, the γ rays in coincidence with band C include an 1162-984-807 keV cascade which extends up to $J = 30$. In lieu of a more detailed profile of the decay into the non-SD level scheme, it will be assumed that that the centroid of the feed-in spin will be approximately as far *below* the highest initial state of the non-SD transitions observed in the gated spectra, as it is *above* the lowest spin of the SD band. Then taking a $\Delta J = 3$ path of stretched E1 transitions as for ^{142}Sm band A, the final spins of the last transitions of bands A, B and C would be 19, 17 and 29 $\hbar$, respectively. Again these values should be regarded as lower limits with large uncertainties of at least $1\hbar$.

4.6. Search for Superdeformation in ^{141}Pm, ^{144}Sm

Two experiments were also performed to study superdeformation in ^{141}Pm and ^{144}Sm, as indicated in Table 4.2.1.

Extensive searches with SDSLICE of a ^{141}Pm $H > 14$ MeV γ–γ matrix revealed no salient candidates for SD bands. The BANDAID correlation grid technique did uncover one signal, and further BANDAID analysis gave weak evidence of a cascade with energies 941, 1005, 1067, 1123, 1185, 1241, 1297, 1357, 1413 and 1541 keV. These do not comprise a particularly well-behaved, constant-spaced set of transitions, and they could not be confirmed in sums-of-gates spectra on the original matrix. There was no evidence of a ridge in these data.

The ^{144}Sm data set was studied in the same manner. Although there appeared to be a ridge in the γ–γ matrix with a $\sim$ 60 keV spacing, neither BANDAID nor SDSLICE provided any hint of possible SD band candidates.

Nucleus	Band	$I_{\rm SD}$ (%)	Number of Transitions	Proposed J_0
^{142}Sm	A	0.5 (1)	19	> 19
	B	0.08(2)	15	
^{142}Eu	A	1.2 (2)	15	
^{144}Eu	A	0.17(4)	17	> 19
	B	0.14(4)	18	> 17
	C	0.14(4)	12	> 29

Table 4.7.1: Summary of experimental results on the discrete SD bands reported in this section.

4.7. Summary

This concludes the experimental section of this work. Before proceeding with interpretation, it is perhaps worthwhile to summarize the six SD bands measured in this work, and discuss some of the features which may yield important clues as to their structure.

The ^{142}Eu band, ^{142}Sm band B, and ^{144}Eu band A all exhibit constant γ-ray energy spacings, with no anomalous changes in the γ-ray decay patterns. The highest-energy γ ray in ^{142}Sm band A must be a transition between spins of $J \sim 58$, based on the measured feed-in spin. This is well beyond the spins at which pairing is expected to vanish. The same can be said of the anomaly at $E_\gamma \sim 1400$ keV in ^{144}Eu band B, which occurs at $J \sim 50$. On the other hand, the feature in ^{144}Eu band C appears at $J \sim 30$, which is exactly the predicted spin of the phase transition into pairing. The exact nature of these anomalies, however, must await comparison to detailed calculations, which will be discussed in the following chapter.

Chapter 5.
Interpretation: Single-Particle Structure

Six high-spin superdeformed bands have been studied by γ–ray decay and assigned to ^{142}Sm, ^{142}Eu and ^{144}Eu. The valence particle structure of each band will now be discussed. First the $\mathcal{J}^{(2)}$ moments of inertia of these and other SD bands in the N=80 region will be examined for any similarities which may aid in the understanding of single-particle level occupation. Then each band will be discussed in turn by comparing the experimental results with mean-field calculations. Finally, possible configurations will be proposed.

5.1. Dynamic Moments of Inertia

The systematics of a group of rotational bands is often best understood by first organizing the available data, such as plots of $\mathcal{J}^{(2)}$ *vs.* rotational frequency, in a grid of proton number Z *vs.* neutron number N, as in Figure 5.1.1. The data for the ^{142}Sm, ^{142}Eu and ^{144}Eu bands were extracted from experimental values reported in Chapter 4 of this thesis, while the remaining data were based on the γ–ray energies reported in the references of Table 4.2.1.

The $\mathcal{J}^{(2)}$ of ^{142}Sm band A is lower than that of ^{143}Eu. This is not unexpected. Not only is there one less nucleon in the system but the quadrupole deformation coordinate of the SD minimum in the total Routhian surface for ^{142}Sm (Figure 4.1.5) is also somewhat lower, $\beta \sim 0.49$ *vs.* 0.52. As was previously suggested, the upturn in $\mathcal{J}^{(2)}$ at high frequency should be an unpaired band crossing effect, and therefore should be a sensitive test of the single-particle configuration of this band. Two of the bands discussed in this work, ^{142}Eu and ^{144}Eu band C, follow quite closely the $\mathcal{J}^{(2)}$ of ^{143}Eu. Since the high-j orbitals should have the

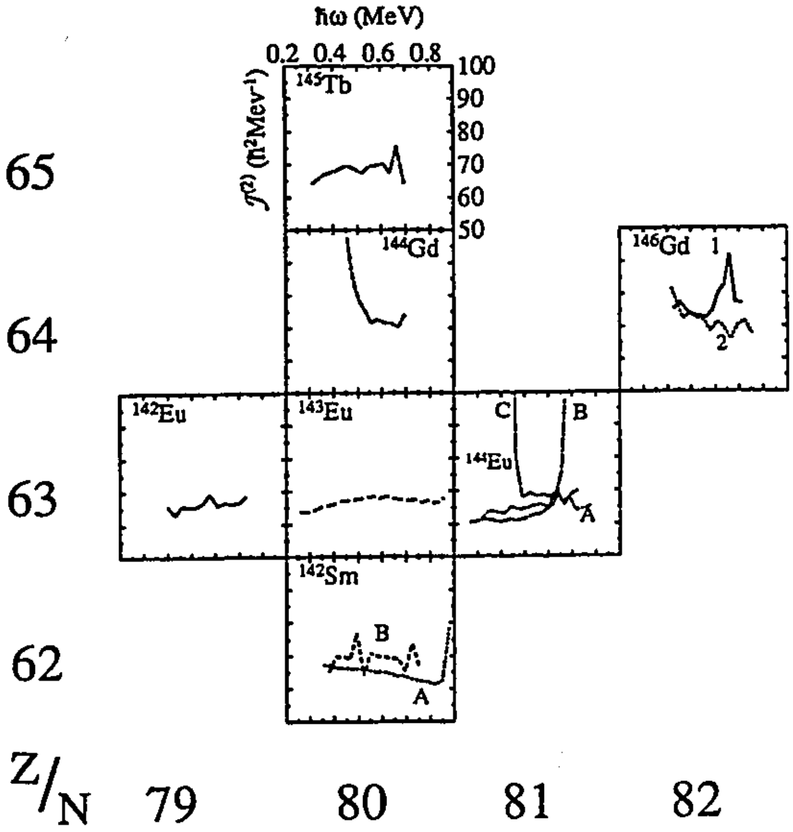

Figure 5.1.1: Dynamic moments of inertia $\mathcal{J}^{(2)}$, plotted on the y–axis of each panel, *vs.* rotational frequency on the x–axis, for known SD bands of nuclei in the vicinity of ^{143}Eu. Panels are arranged for each nucleus by neutron number (N) horizontally and proton number (Z) vertically. The same scale is used on all panels. In ^{142}Sm, ^{144}Eu and ^{146}Gd, the $\mathcal{J}^{(2)}$ curves of the multiple, distinct SD bands within each nucleus are identified by letters or numbers, as they are in the text.

most important additive contribution to $\mathcal{J}^{(2)}$, the similarity in $\mathcal{J}^{(2)}$ implies a common intruder configuration, namely $\pi 6_1$ for these three bands. ^{144}Eu band C also exhibits an anomalous upturn in $\mathcal{J}^{(2)}$ with decreasing rotational frequency, which occurs at the same frequency ($\hbar\omega \simeq 0.45$ MeV) as a band crossing in ^{144}Gd. The latter has been interpreted as the de-alignment of the 6_2 proton as it couples to a $J = 0$ pair with the $\pi 6_1$ orbital. The other two bands of ^{144}Eu, bands A and B, have $\mathcal{J}^{(2)}$ values which are lower than ^{143}Eu. However the anomaly in the $\mathcal{J}^{(2)}$ of band B occurs at the same frequency as that in ^{146}Gd band 1, namely ~ 0.7 MeV. Since this detail in the structure of ^{146}Gd has been interpreted as a consequence of the occupation of an $N_{\rm osc}$=6 neutron orbital above the N=80 gap, this suggests that the same orbital is occupied in the valence configuration of of ^{144}Eu band B. This in turn has consequences for the structure of ^{144}Eu band A and ^{146}Gd band 2.

Perhaps the most surprising result to come out of these experiments is that for frequencies above $\sim$ 0.5 MeV, the $\mathcal{J}^{(2)}$ of ^{142}Sm band B is the same, within experimental uncertainty, as that of ^{146}Gd band 2. In fact, closer inspection reveals that the 1072 keV and higher-energy γ rays of $^{142}_{62}$Sm$_{80}$ band B are *identical* to within 2 keV of γ rays in $^{146}_{64}$Gd$_{82}$ band 2. In other words, one can take ^{146}Gd band 2, remove two protons and two neutrons, and still have a band which behaves macroscopically ($\mathcal{J}^{(2)}$) and microscopically (γ-ray energies) as before. This surprising result is the third example of 2p2n identical bands. The first was reported in [Fli 95], where $^{149}_{64}$Gd$_{85}$ band D was shown to decay by an identical γ-ray pattern to that of $^{153}_{66}$Dy$_{87}$ band 2 [Joh 89]. Structurally, ^{149}Gd band D was assigned the same intruder configuration as the yrast band of ^{152}Dy, namely $\pi 6^4 \nu 7^2$. The particle-hole excitations into these intruder orbitals involve the two $[301]\frac{1}{2}$ proton levels and one $[411]\frac{1}{2}$ neutron level. A second case of 2p2n identical bands in this mass region involves an excited band in ^{148}Gd [DeA 95], which has an identical moment of inertia $\mathcal{J}^{(2)}$ to the yrast SD band of ^{152}Dy. There are some interesting features of these identical bands in nuclei separated by so many particles. First, the $A^{5/3}$ scaling law for moments of inertia, Eq. (2.1.5), implies a difference of 4% in $\mathcal{J}^{(2)}$. Secondly, since the bands in the higher-mass partner of the isospectral pairs (^{153}Dy band 2 and ^{146}Gd band 2) are nearly yrast, the other partner must involve energetically unfavourable particle-hole excitations, which one might expect would result in weaker population than simpler single-particle excitations. Yet in ^{142}Sm, the 2p2n band B was the *only* discrete excited SD band found. In ^{149}Gd, the 2p2n band D intensity was measured to be greater than that of band C, which is a proton excitation band identical to ^{150}Tb, and tose of bands E and F, which are neutron excitations with identical $\mathcal{J}^{(2)}$ to ^{148}Gd. Furthermore, there has been no reports of identical bands based on one-proton one-neutron excitations in $A \sim 150$ superdeformed nuclei [Bea 93, Cur 95, Dag 95, Fal 94, Fli 95].

5.2. A Few Words on Hartree-Fock Calculations

Some of the interpretation which follows is based on state-of-the-art calculations from cranked Hartree-Fock (without pairing) codes developed by Dobaczewski and Dudek [DD 95]. The initial basis $\{\chi\}$ is calculated for a deformed Woods-Saxon potential. In the present studies the deformation parameters are chosen to be near those of the expected final system, *i.e.* $\beta = 0.5$, although the final results of the calculations themselves are insensitive to the initial choice of basis states.

5.2.1 Quadrupole Constraints and Iterations

These HF codes include provisions for macroscopic and microscopic constraints, namely deformation and single-particle occupation. In principle the HF calculation will find the lowest-energy configuration. However, in the Woods-Saxon TRS plots of Figures 4.1.4 and 4.1.5, the SD local minimum is not the absolute minimum, except at the highest frequencies. This implies that the HF calculations will tend to find a non-SD minimum. Since SD states are highly excited relative to the ND yrast line at low spins, it is necessary to put on additional constraints to force the calculations into a "false minimum." This is achieved by adding a quadratic penalty to the energy when the quadrupole moment of the wave function $\langle Q_{20} \rangle$ deviates from some expected value $\tilde{Q}_{20}$,

$$E' = E + C\left(\langle Q_{20}\rangle - \tilde{Q}_{20}\right)^2$$

If the factor C is too large, it will unduly influence the final results, so for each configuration it is selected as the minimum value which would still steer the calculation away from non-SD minima. Microscopically, the levels are grouped by signature and parity and ordered by energy. A theoretical configuration, then, is defined by specifying which of the ordered levels within a group are occupied. Then the calculations are performed for one configuration over a range of cranking frequencies, and the properties of this calculated band can then be compared to an experimentally observed band.

At the end of each iteration of the Hartree-Fock calculations, the energy of the system is calculated in two ways, first by integrating the density of the Hamiltonian with the Skyrme interaction and then by adding up the single-particle energies of occupied levels. The difference between these two calculations gives an indication of the uncertainty in the calculations themselves. If this discrepancy is as small as 1 keV, or roughly the order of the uncertainty of the measured γ-ray energies, the calculations can be compared to experimental data with confidence. The calculations for a given configuration were performed with the same quadrupole constraints C and $\bar{Q}_{20}$ and number of iterations for each cranking frequency. The authors of the code suggested that this was the most consistent means of performing calculations for a single band, but that it was not necessary to use the same conditions for all configurations.

5.2.2 Vacua

In these calculations, an *arbitrary vacuum* was defined as the $n_{(\pi,\alpha)}$ lowest-energy states *at any rotational frequency* for each of the four (π,α) combinations for protons and neutrons. These were selected by using WS and TRS calculations as guides to determine a likely yrast SD configuration. Different configurations are then specified by particle-hole excitations from this arbitrary vacuum. For example, a single particle-hole excitation constrains the calculations such that the $i^{\text{th}}_{(\pi,\alpha)}$ single-particle state, numbered from lowest to highest energy, is occupied, and the $k^{\text{th}}_{(\pi',\alpha')}$ level is empty. In principle, the lowest-energy configuration should have no empty orbitals below the highest-energy filled orbital. However, one of the consequences of the HF self-consistent mean field is that a change in occupation can change the ordering of nearly-degenerate orbitals. For example, in calculations for ^{146}Gd, occupation of one signature of the $[642]\frac{5}{2}$ valence neutron doublet will raise the single-particle energy of the occupied state slightly above that of the empty state, regardless of which signature is occupied.

5.3. ^{142}Sm

Based on both Woods-Saxon and Hartree-Fock calculations of dynamic moments of inertia, the ^{142}Sm yrast band A is most likely a ^{143}Eu core with a hole in an $\alpha = -\frac{1}{2}$ N_{osc}=5 proton level just below the Z=63 cranked shell gap. The identical $\mathcal{J}^{(2)}$ behavior of band B to ^{146}Gd band 2 can be explained by first occupying identical intruder orbitals, which is confirmed by the cranked HF calculations. Such a structure is, however, so highly excited that it might at first seem unlikely that it would be observed in the absence of discrete bands based on less excited configurations. Some of these expected bands may comprise the quasi-continuum.

5.3.1 Yrast configuration: Band A

The Woods-Saxon TRS calculations of Figure 4.1.5 predicted a minimum with a deformation of $\beta \sim 0.49$. Although the energy of the $\pi 6_1$ intruder orbital is sensitive to deformation, cranked WS calculations predicted that even at this lower deformation, this orbital would be at or below the Z=62 level over much of the frequency range that ^{142}Sm band A was observed, $\hbar\omega \geq 0.5$ MeV (cf. Figure 4.1.3). From Figure 4.1.2, the most likely level which would be empty relative to the ^{143}Eu core would be one of the two $[541]\frac{1}{2}$ orbitals. These $K = 1/2$ orbitals will be split even at the lowest rotational frequencies, so the lack of an observed signature partner band is consistent with this possibility, but by no means should be accepted as rigorous proof. As may be seen in Figure 4.1.2, at low frequencies the $\alpha = -\frac{1}{2}$ orbital is at higher energy than the opposite signature orbital, which suggests that a hole in this orbital would be the yrast configuration. However this ordering is inverted beyond $\hbar\omega \gtrsim 0.65$ MeV.

The calculations presented in Figure 5.3.1 for these two configurations were performed with cranked Woods-Saxon and Hartree-Fock codes. Dynamic moments of inertia $\mathcal{J}^{(2)}$ were extracted from these calculations, and are shown in comparison to the experimental values. It should be first noted that none of these calculations can fully reproduce the observed $\mathcal{J}^{(2)}$ of band A, so any conclusions drawn from these (or any other calculations) must be regarded with caution. The HF calculations, which do not include paring correlations, were performed for a ^{143}Eu core, with the $\pi 6_1$ proton intruder occupied, with a hole in one of the two signatures of the $N_{\rm osc}$=5 orbitals. Both HF calculations (denoted HF:a and HF:b) overestimate the average $\mathcal{J}^{(2)}$ of the ^{142}Sm band, but the results for the configuration with the hole in the negative signature $N_{\rm osc}$=5 orbital (HF:b) tends to follow shape of the observed $\mathcal{J}^{(2)}$. That is, the HF:b curve is consistently $\simeq 5\ \hbar^2$MeV^{-1} higher than the observed $\mathcal{J}^{(2)}$. Furthermore, the observed upturn in the $\mathcal{J}^{(2)}$ at $\hbar\omega = 0.85$ MeV occurs at lower frequency and is sharper in the HF:b calculation than HF:a.

The influence of the two proton $N_{\rm osc}$=5 orbitals nearest to the Fermi surface on the calculated $\mathcal{J}^{(2)}$ may be understood from examination of a fixed-deformation Woods-Saxon Routhian plot. A change in the slope of the Routhian,

$$\frac{de'}{d\omega} = -\frac{d}{d\omega}(\omega j_x) = -j_x - \omega\left(\frac{\partial}{\partial\omega} j_x\right),$$

will result in a change in the behavior of $\mathcal{J}^{(2)}$ (see Eqs. (2.3.24) and (2.3.25)). For example, of the two single-particle states described by $[541]\frac{1}{2}$ quantum numbers at zero frequency, the Routhian of the $\alpha = -\frac{1}{2}$ states evolves smoothly with ω. By contrast, the Routhian of the positive signature state of that pair decreases with rotational frequency until it crosses and interacts with the $[532]\frac{5}{2}_{(+)}$ state. It is a well-known result from quantum mechanics that the wave functions will mix and the levels will repel each other, and beyond the crossing the wave functions will be exchanged. In other words, the $\alpha = +\frac{1}{2}$ state whose wave function at $\omega = 0$ was described with $[541]\frac{1}{2}$ quantum numbers will evolve to a cranked $[532]\frac{5}{2}$ wave function. Therefore a configuration with a hole in the negative signature $N_{\rm osc}$=5 orbital will have a smooth $\mathcal{J}^{(2)}$ relative to ^{143}Eu, while the configuration with the

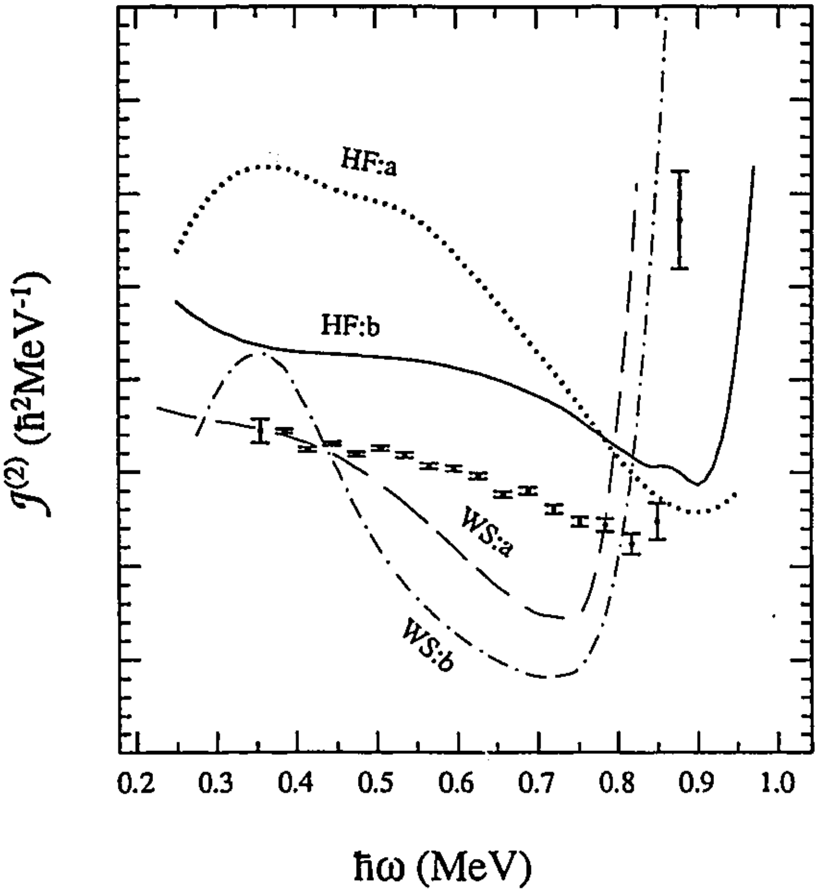

Figure 5.3.1: ^{142}Sm yrast band (band A), experimental (data points) and calculated (curves) $\mathcal{J}^{(2)}$ values. Dotted line, HF:a (no pairing), $^{143}\mathrm{Eu}\otimes[541]\frac{1}{2}_{(+)}{}^{-1}$. Solid line, HF:b (no pairing), $^{143}\mathrm{Eu}\otimes[541]\frac{1}{2}_{(-)}{}^{-1}$. Dashed line, WS:a (proton pairing only), same configuration as HF:b. Dashed-dotted line, WS:b (full pairing), same configuration as HF:b.

positive-signature hole should have a discontinuity in $\mathcal{J}^{(2)}$ at the predicted crossing frequency of $\hbar\omega \sim 0.6$ MeV.

In the HF calculations, the $\mathcal{J}^{(2)}$ of the HF:b configuration follows a smooth, uneventful curve (up to $\hbar\omega = 0.8$ MeV), while the HF:a calculated $\mathcal{J}^{(2)}$ curve changes slope at $\hbar\omega \sim 0.6$ MeV, as predicted for the $[541]\frac{1}{2}_{(+)}$ crossing. Based on these mean-field calculations it is reasonable to propose a $\pi(6^1 \otimes \{[541]\frac{1}{2}_{(-)}\}^{-1})$ valence particle configuration, relative to the $\omega = 0$ shell gaps at Z=62 and N=80, for ^{142}Sm band A.

The $[770]\frac{1}{2}_{(-)}$ neutron intruder orbital ($\nu 7_1$), which will be important in discussions of ^{142}Sm band B and ^{144}Eu band C, first exerts its influence at the very highest frequencies of ^{142}Sm band A. All of the mean field calculations predict an upturn in the $\mathcal{J}^{(2)}$ at high frequency, in agreement with the observation of the last (1782 keV) transition of band A. The $\nu 7_1$ Routhian decreases rapidly with increasing rotational frequency. Eventually it reaches the Fermi surface and interacts with an occupied $(\pi, \alpha) = (-, -\frac{1}{2})$ level, which results in the drastic "accident" in the $\mathcal{J}^{(2)}$.

The role of neutron pairing in the Woods-Saxon calculations is also demonstrated in Figure 5.3.1. A bump in the calculated $\mathcal{J}^{(2)}$ at $\hbar\omega$ = 0.3 MeV (WS:b) arises from the breaking and alignment of the second pair of N_{osc}=6 neutrons. This pair of neutrons should be occupied in all of the N=80 superdeformed bands, yet no evidence for a perturbation in the $\mathcal{J}^{(2)}$ at this frequency has been observed in this band, ^{143}Eu or ^{145}Tb. If the pairing correlations are excluded for the neutrons in the Woods-Saxon calculations (WS:a), the bump disappears and at low frequency the agreement with the experimental $\mathcal{J}^{(2)}$ is somewhat improved. This observation is consistent with the conclusion of [Mul 94] that the N=80 SD shell gap is sufficiently large to attenuate pair scattering across the Fermi surface, that is, to effectively quench any neutron pairing correlations.

The angular momentum parallel to the cranking axis, I_x, has been extracted from the cranked HF wave function. At $\hbar\omega$ = 0.4 MeV the calculations yield $I_x = 33.8\hbar$. Given the parity and signature constraints, this would mean that the 798 keV γ-ray is a $J^\pi = 35^- \rightarrow 33^-$ transition. This would put the spin of the final state of the 679 keV transition at $J_0 = 29\hbar$. By contrast, a simple assumption $\mathcal{J}^{(1)} = \mathcal{J}^{(2)}$ predicts $J_0 \sim (\omega_0 \mathcal{J}^{(2)}) \simeq 25\hbar$, which is also suggested by Nilsson model calculations of Ragnarsson [Rag 93b]. HF calculations performed for the ^{143}Eu yrast SD configuration predicted initial and final spins for the 794 transition of that band which were $4\hbar$ higher than what would be expected based on the assumption of Sect. 4.1.4. The origin of this discrepancy is probably related to the overestimation of $\mathcal{J}^{(2)}$ as well, and will be discussed further in Sect. 5.3.2. Given $J_0 = 25\hbar$, the spin of the highest transition in ^{142}Sm band A is $J^{\pi} = 63^{-} \rightarrow 61^{-}$, which is certainly not unreasonable in light of the entry conditions to the residual system.

5.3.2 Excited band: Band B

The excited band of ^{142}Sm, whose γ-ray decay energies are identical to those of ^{146}Gd band 2, was certainly the biggest surprise to come out of the N=80 SD project. In Figure 5.3.2, the experimental effective alignment Δi_x of ^{142}Sm band B, modulo $2\hbar$, is plotted with ^{146}Gd band 2 as a reference. Spins have been assumed such that the two bands have the same signature, which means that γ rays of identical energy in the two bands are transitions with initial states differing in spin by an integer multiple of $2\hbar$. Since the average γ-ray spacing is 57 keV, each unit of Δi_x corresponds to a γ-ray energy difference of 29 keV. Hence Figure 5.3.2 shows quite vividly how the γ-ray transitions of ^{142}Sm band B above 1073 keV are identical to within 2 keV of ^{146}Gd band 2.

Ragnarsson [Rag 93a] has demonstrated the additive property of $\mathcal{J}^{(2)}$ for the $A\sim150$ superdeformed bands. In simpler terms, bands with identical moments of inertia should have the same occupation of high-N_{osc} orbitals. Over the range that ^{142}Sm band B and ^{146}Gd band 2 have identical γ-ray energies, their $\mathcal{J}^{(2)}$ values must also match. It has been proposed that the high-N_{osc} configuration of ^{146}Gd band 2 is $\pi 6^2 \nu 6^5 \nu 7^1$ [Heb 90, Haa 93]. The Nilsson calculations of [Haa 93] predict that above the 81st neutron state are four N_{osc}=6 neutron levels which arise from the ($\omega = 0$) $[642]\frac{5}{2}$ and $[651]\frac{1}{2}$ orbitals. Four of the five N_{osc}=6 neutrons and one N_{osc}=6 proton intruder are already occupied in the ^{142}Sm band A configuration, but to occupy the $\pi 6_2$ and $\nu 7_1$ intruder orbitals would involve an energetically expensive two-particle, two-hole excitation across the very shell gaps which give the yrast SD band its stability. Figure 4.1.3 demonstrates, with arrows and filled-open these excitations

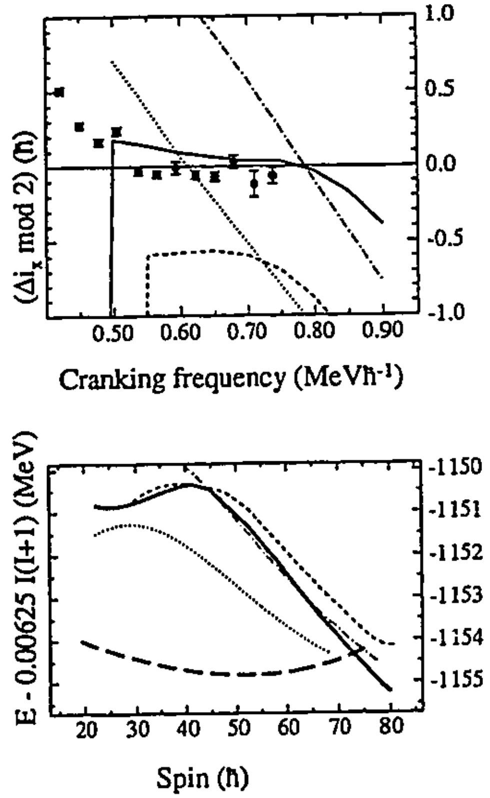

Figure 5.3.2: Comparison of Hartree-Fock [DD 95] calculations to observed ^{142}Sm band B. Top panel, experimental effective alignment *vs.* ^{146}Gd, assuming the same signature, compared with calculated variables for $\nu 7^1 \pi 6^2$ (solid, $\alpha = 1$; dashed-dot, $\alpha = 0$), $\nu 7^1 \pi 6^2 \otimes$"magic" (dashed) and $\nu 7^1$ (dotted) configurations, see text for details. Bottom panel, energy of these configurations compared to the proposed yrast configuration (long dashed curve) minus $\mathcal{J}^{(2)} = 80\hbar^2\text{MeV}^{-1}$ rigid rotor reference.

at $\beta = 0.49$ at high rotational frequency. At lower frequencies these would be still higher-energy excitations. If instead we consider a cranked ^{142}Sm system which is already much more deformed than the yrast SD configuration, for example with $\beta = 0.57$ as is typical of the heavy gadolinium isotopes [Haa 93], then the $\pi 6^2$ and

$\nu 7^1$ orbitals would be brought down in energy so that they are below the Fermi surface.

In addition to reducing the energy of the relevant intruder orbitals, increased deformation also brings certain "magic" orbitals to the Fermi surface. For example, the $\pi[301]\frac{1}{2}$ signature partner orbitals become the 63rd and 64th proton orbitals, respectively. These "magic" orbitals have an asymptotic pseudo-spin decoupling parameter $\tilde{a}_{\text{asymp}} = 1$, and more importantly, have been identified as probable valence orbitals responsible for the identical bands along the $N = 86$ chain of isotones [Byr 90]. Similarly, the $\nu[411]\frac{1}{2}$ orbitals are close enough to the neutron Fermi surface that they could become active valence particles or holes. These orbitals have $\tilde{a}_{\text{asymp}} = -1$, and it has been recently confirmed that the occupation of these "magic" orbitals has no effect on $\mathcal{J}^{(2)}$ [Nis 95]. Therefore to understand both the identical $\mathcal{J}^{(2)}$ and isospectrality of ^{142}Sm band B to ^{146}Gd band 2, it is tempting to assign the ^{142}Sm band B configuration as $^{146}\text{Gd}\otimes\{(\pi[301]\frac{1}{2})^2(\nu[411]\frac{1}{2})^2\}^{-1}$, since holes in these orbitals would contribute $\delta\mathcal{J}^{(2)} = 0$ and $\sum \tilde{a} = 0$ to the ^{146}Gd core.

For a theoretical test of the role of the intruder and "magic" orbitals on these identical bands, it was decided that the calculations based on the Hartree-Fock method would be most appropriate. The TRS calculations based on the Woods-Saxon potential could not give a stable minimum at a sufficiently high β to explain the high $\mathcal{J}^{(2)}$ of ^{142}Sm band B compared to the yrast band, so the deformation input for any calculations would have been, at best, a guess. The two aspects of identical bands, the matching $\mathcal{J}^{(2)}$ and isospectrality, can both be demonstrated from the effective alignment Δi_x. Two bands with identical $\mathcal{J}^{(2)}$ values would have identical γ-ray spacing, which means that the experimentally deduced Δi_x would be constant with rotational frequency. Of course, it is more satisfactory if the HF calculations can also reproduce the observed $\mathcal{J}^{(2)}$ of at least one of the pair of identical bands as well as predicting a constant Δi_x.

In Figure 5.3.3, the HF calculations for the $\mathcal{J}^{(2)}$ of ^{146}Gd are compared to the experimental results for band 2. The intruder configuration in the calculations

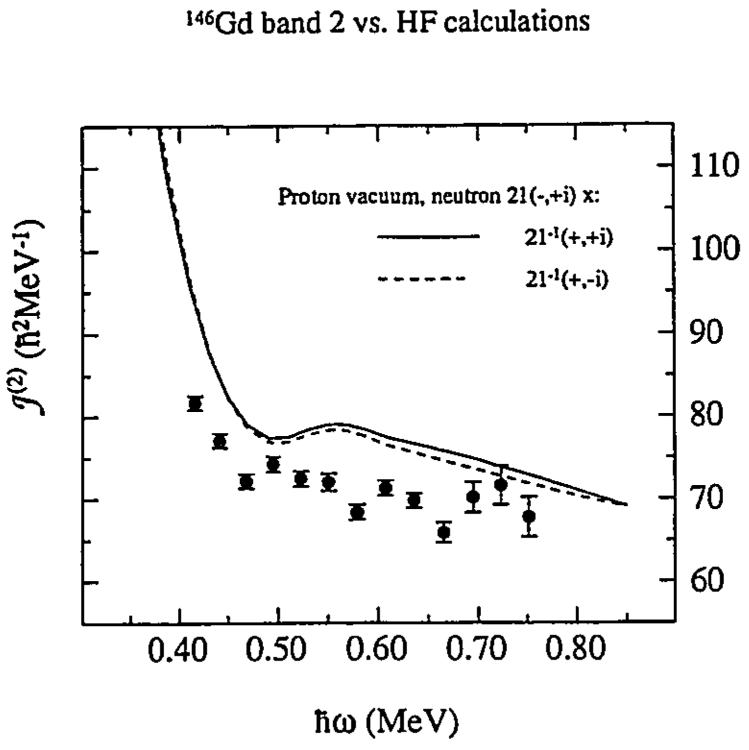
^{146}Gd band 2 vs. HF calculations

Figure 5.3.3: Comparison of the experimental $\mathcal{J}^{(2)}$ of ^{146}Gd band to HF calculations for $\pi 6^2\nu 7^1\otimes$ $[642]\frac{5}{2}_{(\pm)}$ configurations.

was $\pi 6^2\nu 7^1$, with an additional valence neutron in one of two $N_{\rm osc}$=6 states. These nearly-degenerate signature-partner orbitals are the 82^{nd} and 83^{rd} neutron orbitals, although as was mentioned earlier their exact ordering depends on the details of the self-consistent mean field. In both WS and Nilsson calculations for $\beta \sim 0.55$, there are four $N_{\rm osc}$=6 orbitals with, the $[642]\frac{5}{2}$ doublet lying lower than the $[651]\frac{1}{2}$ doublet at $\hbar\omega = 0$. With increasing rotational frequency, the $[651]\frac{1}{2}$ orbitals split, and the negative-signature Routhian is driven to and crosses the $[642]\frac{5}{2}_{(-)}$ level. At higher frequency, the same crossing will occur for the positive signature. In the cranked Nilsson calculations of [Haa 93], the $\alpha = -\frac{1}{2}$ crossing occurs near the frequency of an observed feature in the $\mathcal{J}^{(2)}$ of ^{146}Gd band 1. Hence the $[642]\frac{5}{2}_{(-)}$ orbital was assigned as occupied in this band to give it a total $\alpha = 1$.

For the $\alpha = 0$ signature-partner configuration, the crossing was calculated to be beyond the observed frequency range of ^{146}Gd band 2. In the HF calculations, the occupation of *either* signature of this last $N_{\rm osc}$=6 neutron orbital reproduces the smoothly-varying $\mathcal{J}^{(2)}$ of ^{146}Gd band 2, and much like the calculation for the proposed ^{142}Sm band A configuration, overestimates it by $\sim$ 5 $\hbar^2$MeV^{-1}. This means that if the HF calculations can predict a flat Δi_x for ^{142}Sm relative to one of these ^{146}Gd configurations, then the $\mathcal{J}^{(2)}$ will automatically be reproduced as well. However, it is important to be aware of the discrepancy between these calculations for the $\alpha = 0$ configuration and the Nilsson results. It should also be noted that it has not been possible to reproduce the $\mathcal{J}^{(2)}$ of ^{146}Gd band 1 in the HF calculations yet.

The two questions which the HF calculations have to answer are whether the suggested configuration can reproduce a flat Δi_x, preferably one which will give identical bands, and whether such a configuration would be low enough in energy to be populated. The first target configuration of ^{142}Sm band B has the $\pi 6^2 \nu 7^1$ intruder states occupied, with the remaining nucleons occupying the lowest available single-particle states at a rotational frequency of $\hbar\omega$ = 0.8 MeV. This leads to a configuration with a total signature of $\alpha = 1$. Since the Δi_x deduced from experiment assumes that the signature of the two bands was the same, Δi_x is calculated with the $\alpha = 1$ SD configuration of ^{146}Gd as a reference. For rotational frequencies between about 0.5 and 0.8 MeV, or over the range which the two bands were observed to be isospectral, the calculated Δi_x falls from 2.2 to 2.0. For lower rotational frequencies, the SD minimum is not stable and the calculations converge to a much less deformed configuration at lower spin, hence the sudden drop in Δi_x. The almost-flat Δi_x means that these two configurations will have nearly the same $\mathcal{J}^{(2)}$. Also since $\Delta i_x \sim 2$, this means that the transition $J+2 \rightarrow J$ in ^{142}Sm band B would have identical γ-ray energy to the $J \rightarrow J-2$ transition of ^{146}Gd band 2.

The occupation and evolution of the single-particle Routhians as a function of rotational frequency are shown in Figure 5.3.4. The Routhians for ^{146}Gd would

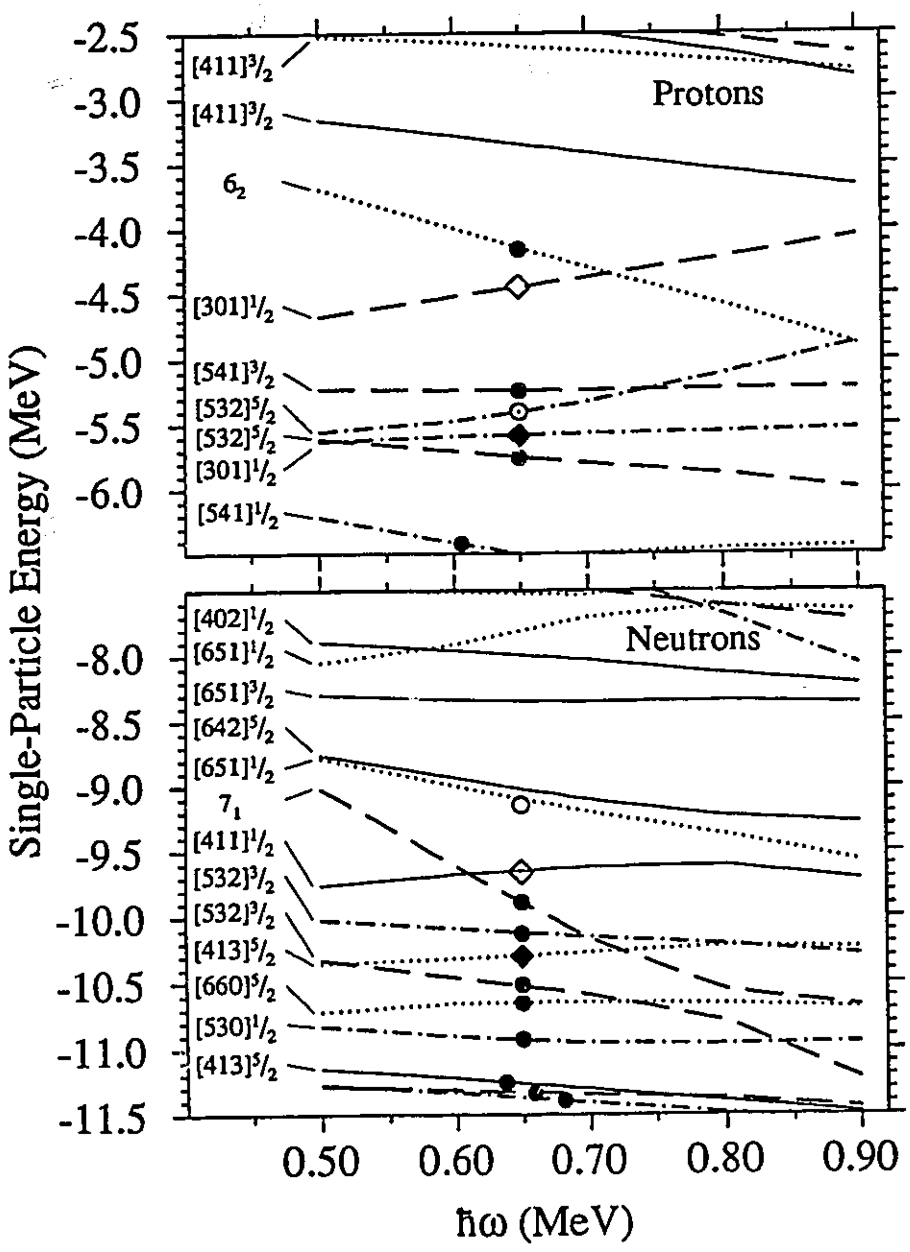

Figure 5.3.4: HF calculated single-particle Routhians for ^{142}Sm excited band (band B) configuration $\nu 7^1 \pi 6^2$. Filled symbols mark occupied orbitals in the preferred configuration for ^{142}Sm band B. Open symbols identify orbitals which would be occupied in ^{146}Gd band 2. Diamonds indicate pseudo-spin "magic" orbitals. The states are labeled by the largest amplitude $\omega = 0$ basis state.

differ in details due to the self-consistency of the mean field, but one can still identify those orbitals which are occupied in an $\alpha = 1$ ^{146}Gd SD configuration. Over the entire range of frequencies there is at least one unoccupied level below the $\pi 6_2$ level. A calculation with the particle from the $\pi 6_2$ level moved to the level labeled $[532]\frac{5}{2}_{(+)}$, however, yields a Δi_x relative to $\alpha = 1$ ^{146}Gd which is not even close to being flat, see Figure 5.3.2. Instead the Δi_x of this configuration drops with increasing rotational frequency, which implies that the $\mathcal{J}^{(2)}$ of this ^{142}Sm configuration is lower than that of ^{146}Gd. This calculated result is consistent with the claim that the same intruder configuration is required to give identical $\mathcal{J}^{(2)}$ for two bands. Calculations with a $\pi 6^2 \nu 7^0$ configuration did not converge to a SD minimum, even with strong quadrupole moment constraints. While this may indicate a flaw in the code, the result can also be interpreted to mean that there is no potential well to stabilize the $\pi 6^2$ configuration in ^{142}Sm, and therefore it could not yield a long discrete-line γ-ray cascade.

A second question is the role of the lower-j orbitals, specifically the "magic" orbitals, in isospectrality. Another set of calculations were performed with one proton moved from the $[541]\frac{3}{2}_{(-)}$ to the $[532]\frac{5}{2}_{(+)}$ level. This configuration has a total signature $\alpha = 0$, and so must be compared to the ^{146}Gd calculation of the same signature. In fact, the calculated function $I(\omega)$ is very nearly the same for both signatures of ^{146}Gd. However, the Δi_x of the ($\alpha = 0$) ^{142}Sm configuration relative to ($\alpha = 0$) ^{146}Gd is almost parallel to that of the $\pi 6^1 \nu 7^1$ configuration relative to ($\alpha = 1$) ^{146}Gd. It is interesting to note that while the $[541]\frac{3}{2}_{(-)}$ orbital is flat and straight, the $[532]\frac{5}{2}_{(+)}$ orbital curves upwards with increasing ω. Because of the subtleties of the self-consistent mean field, it is not straightforward to understand why occupation of these orbitals has such a dramatic effect on Δi_x. However, since Λ is smaller for the latter orbitals, it would be expected to be less "deformation driving" than the former, that is, the decrease in total energy of the system with increasing deformation is greater for the $[541]\frac{3}{2}_{(-)}$ configuration than for $[532]\frac{5}{2}_{(+)}$.

Finally, the last calculated curve plotted on Figure 5.3.2 is for $\pi 6^2 \nu 7^1$, but with the particles from the levels labeled $\pi[301]\frac{1}{2}_{(+)}$ and $\nu[413]\frac{5}{2}_{(-)}$ promoted to $\pi[532]\frac{5}{2}_{(+)}$ and $\nu[651]\frac{1}{2}_{(-)}$, respectively. The labels indicate the largest component of the initial basis state in the HF single-particle wave function, and the level marked as $\nu[413]\frac{5}{2}_{(-)}$ actually evolved from the positive signature level which, at $\hbar\omega = 0$, would be described by the $[411]\frac{1}{2}$ wave function. The is a common feature of these calculations, for example, the $\nu 7_1$ orbital is a pure $[770]\frac{1}{2}_{(-)}$ wave function at $\omega = 0$, but at high rotational frequency the largest basis state component is $[761]\frac{3}{2}_{(-)}$. Therefore the configuration just mentioned corresponds to a ^{146}Gd SD core with holes in all four available "magic" orbitals. This configuration could only converge to the SD minimum for rotational frequencies above 0.55 MeV, but the Δi_x remains flat to within $0.1\hbar$ up to 0.75 MeV. This means that this $\pi 6^2 \nu 7^1 \otimes \{\text{"magic"}\}^{-4}$ configuration can also reproduce the identical $\mathcal{J}^{(2)}$ for ^{142}Sm band B and ^{146}Gd band 2, at least over the range of frequencies where the bands are observed and the calculations converge. It does not, however, give an Δi_x which is an integer multiple of $2\hbar$, which would be required for isospectral bands.

The I_x predicted at $\hbar\omega = 0.65$ MeV for the two $\alpha = 1$, $\pi 6^2 \nu 7^1$ configurations are 62.7 and 62.1 $\hbar$. Given the signature constraint, this means that the 1302 keV transition is most likely $J^\pi = 63^- \rightarrow 61^-$, in either scenario which yields a constant Δi_x. This gives $J_0 = 41\hbar$ for the final spin of the 725 keV transition, or $71\hbar$ for the initial state of the highest-energy transition (1535 keV). This latter figure is at the limit of the highest input angular momentum predicted for these experimental conditions, but based on the comparison between the WS, HF and $\mathcal{J}^{(2)} = \mathcal{J}^{(1)}$ models for band A, it is probably overestimated by $4 - 8\hbar$.

5.3.3 Energetics and the Quasi-Continuum

Although two configurations for ^{142}Sm band B have been identified which will yield identical $\mathcal{J}^{(2)}$ and, in one case, isospectrality with ^{146}Gd band 2, such configurations must not be too highly excited or they could not be populated in the fusion-evaporation reactions. The bottom panel of Figure 5.3.2 shows that all of the configurations considered in Sect. 5.3.2 become yrast near the very highest spins which can be achieved in the selected reaction. The calculated HF energy of the $\pi 6^2 \nu 7^1 \otimes \{\text{magic}\}^{-4}$ configuration is approximately 0.5 MeV higher in excitation energy than that of the simpler $\pi 6^2 \nu 7^1$ configuration. While it is satisfying to see that these configurations do indeed have some possibility of being populated, it is troubling that they then become up to 5 MeV non-yrast at what are still high spins ($\sim$ $45\hbar$). In the present case as well as for ^{149}Gd, these 2p2n bands are populated with $>$ 10% the intensity of the yrast SD bands. In fact the ^{149}Gd 2p2n band is the third most intense of the six discrete bands, even more intense those which are identical to ^{150}Tb (band C) and ^{148}Gd (bands E,F). Both of these excited bands involve single particle-hole excitations to one intruder orbital, not two as in the present case or three as in ^{149}Gd band D. In fact, there has yet to be a report of an identical band pair in the $A{\sim}140$ between nuclei (Z, N) and $(Z+1, N+1)$. The paucity of such pn identical bands, in light of the two 2p2n isospectral and one identical-$\mathcal{J}^{(2)}$ bands, is certainly puzzling. This may indicate the presence of a further correlation which, for some reason, favours those bands which exhibit 2p2n isospectrality. It should be noted that the wave functions of the "magic" orbitals discussed so far are such that their spatial probability distributions are highest near the middle of the nucleus and will have substantial overlap amongst themselves. Clustering of nuclear density into spatial distributions resembling α particles is well established in light nuclei [Bro 85] but any notion of quasi-α correlations amongst the particles occupying the "magic" orbits in heavy nuclei can only be considered as speculation in the absence of a rigorous, formal theory.

It may be that the single-proton excitations, whose study was the initial goal of the GAMMASPHERE experiment, comprise the quasi-continuum ridge intensity discussed in Sect. 4.3.5. With the exception of one point, the $\mathcal{J}^{(2)}$ of the ridge follows that of the ^{143}Eu band quite closely (see Figure 5.3.5). Indeed, this ridge may be

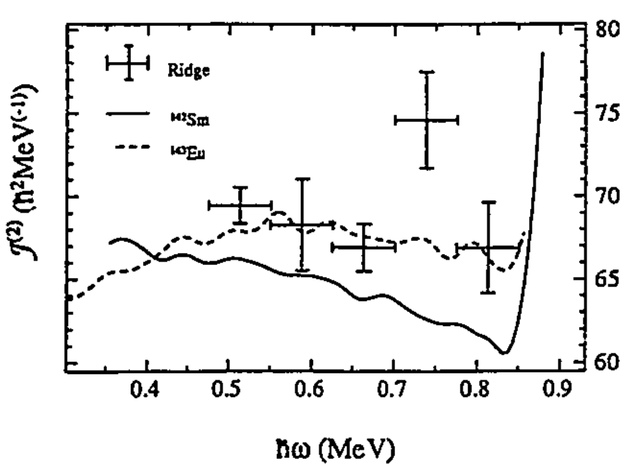

Figure 5.3.5: Data points, dynamic moment of inertia of ^{142}Sm quasi-continuum ridge, with vertical error bars indicating uncertainty in $\mathcal{J}^{(2)}$ and horizontal error bars indicating frequency range over which $\mathcal{J}^{(2)}$ was measured. Curves, $\mathcal{J}^{(2)}$ deduced from experimental data of ^{142}Sm and ^{143}Eu yrast SD bands.

the only available evidence of identical bands based on single-particle excitations of the ^{142}Sm yrast core.

5.3.4 Conclusions for ^{142}Sm

With the HF calculations as a guide, it is proposed that the two ^{142}Sm bands, A and B, have valence particle configurations of $\pi 6^1 \otimes \{[541]\frac{1}{2}_{(-)}\}$ and $\pi 6^2 \nu 7^1 \nu\{N_{\mathrm{osc}}{=}6, \alpha = -\frac{1}{2}\}$, respectively, giving both bands $(\pi, \alpha) = (-, 1)$. Equivalently they could be described in terms of SD configurations in other nuclei, namely $^{143}\mathrm{Eu}\otimes\{\pi[541]\frac{1}{2}_{(-)}\}$ and (^{146}Gd band 2)$\otimes\{\pi[301]\frac{1}{2}_{(-)} \otimes \pi[532]\frac{5}{2}_{(+)} \otimes \nu[413]\frac{5}{2}_{(+)} \otimes \nu[651]\frac{1}{2}_{(-)}\}^{-1}$. Although the (^{146}Gd band 2)$\otimes\pi([301]\frac{1}{2})^{-2}\nu([411]\frac{1}{2})^{-2}$ configuration did not yield the Δi_x value expected for isospectral bands, it should not be ruled out yet.

As with the HF codes, WS calculations with standard parameters overestimate the $\mathcal{J}^{(2)}$ of ^{152}Dy [NWJ 89]. With a nucleon radius of 1.23 fm, about 0.08 fm smaller than the standard values, the calculated $\mathcal{J}^{(2)}$ matched the experimental value, since $\mathcal{J}^{(2)} \propto r_0^2$. The SkM parameter set used in the HF calculations are fit to ground-state and low-energy measurements of nuclear properties, as were the standard WS parameters, so it may be that a similar scaling is necessary for the Skyrme parameter set.

5.4. ^{142}Eu

The SD band in the N=79 nucleus ^{142}Eu would most likely involve the same proton configuration as ^{143}Eu, and would have one hole in one of the valence neutrons below the N=80 shell gap. According to Figure 4.1.2, this neutron hole would most likely be in the 6_4 ($[651]\frac{3}{2}_{(-)}$) level, if the ^{143}Eu core were sufficiently stable that the mean field would be unaffected by the loss of a valence neutron. However, the energy of this level is strongly influenced by deformation, and a shape change to a lower deformation could possibly bring the $[532]\frac{3}{2}_{(\pm)}$ or $[411]\frac{1}{2}_{(+)}$ orbitals into competition with it. The self-consistent HF calculations predict that the $^{143}\mathrm{Eu}\otimes\{\nu 6_4\}^{-1}$ configuration is about 0.7 MeV lower in energy than the other possible configurations (Figure 5.4.1), which means that it is most likely the yrast configuration. The fact that the estimated intensity of the experimentally observed band was quite high compared to the other bands discussed in this work is fairly convincing evidence that this would indeed be the yrast SD band. It would seem, then that ^{142}Eu should provide the first experimental measurement of the alignment of the $\nu 6_4$ orbital.

The experimental Δi_x of the ^{142}Eu SD band relative to ^{143}Eu was first compared to a Nilsson model without pairing [Mul 95]. In this particular set of calculations, the deformation parameters for each configuration at each frequency were first chosen from the TRS SD minimum. In principle this is an improvement on the standard procedure of selecting a fixed deformation over all frequencies, but still is not fully self-consistent. The Δi_x from these calculations are shown for the the $(\nu 6_4)^{-1}$ and $(\nu[532]\frac{3}{2})^{-1}$ configurations relative to ^{143}Eu, Figure 5.4.2, and are compared to the experimental Δi_x of ^{142}Eu band A for assumed final-state spins J_0 of the 699 keV transition from 25 to 27. In these calculations there was no signature splitting of the $[532]\frac{3}{2}_{(\pm)}$ orbitals. The $(\nu 6_4)^{-1}$ configuration, with α=1, gives, on average, the correct Δi_x for J_0 = 27, and the (α = 0) $([532]\frac{3}{2}_{(+)})^{-1}$

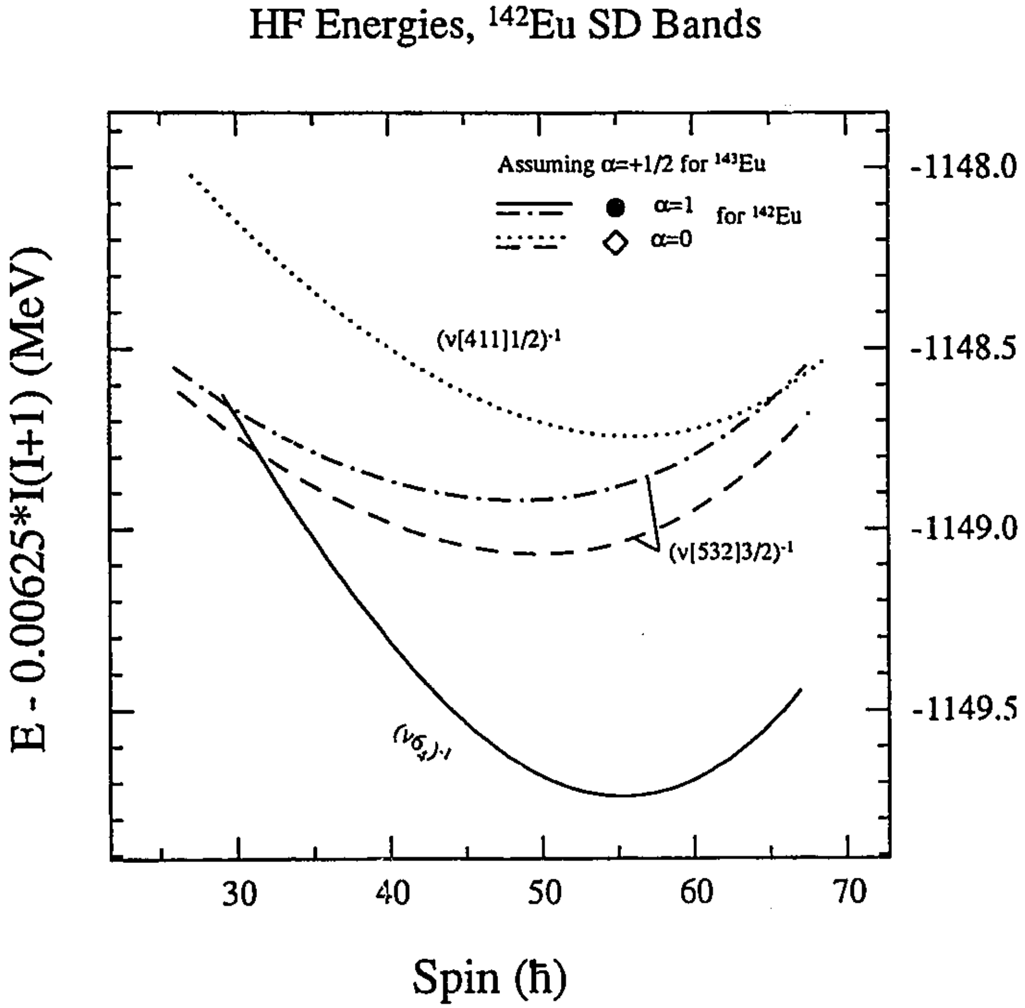

Figure 5.4.1: HF calculated energies, minus a rigid-rotor component of $\mathcal{J} = 80\hbar^2\text{MeV}^{-1}$, for the four lowest-lying SD configurations in ^{142}Eu, corresponding to neutron holes relative to a ^{143}Eu core.

configuration gives similar agreement for $J_0 = 26$, but neither can match the slope of the experimental Δi_x.

The self-consistent HF mean field calculations also predict a drastically different shape of the Δi_x curve for the $^{143}\text{Eu}\otimes(\nu 6_4)^{-1}$ configuration than what was observed experimentally. Instead it appears that the hole relative to the ^{143}Eu

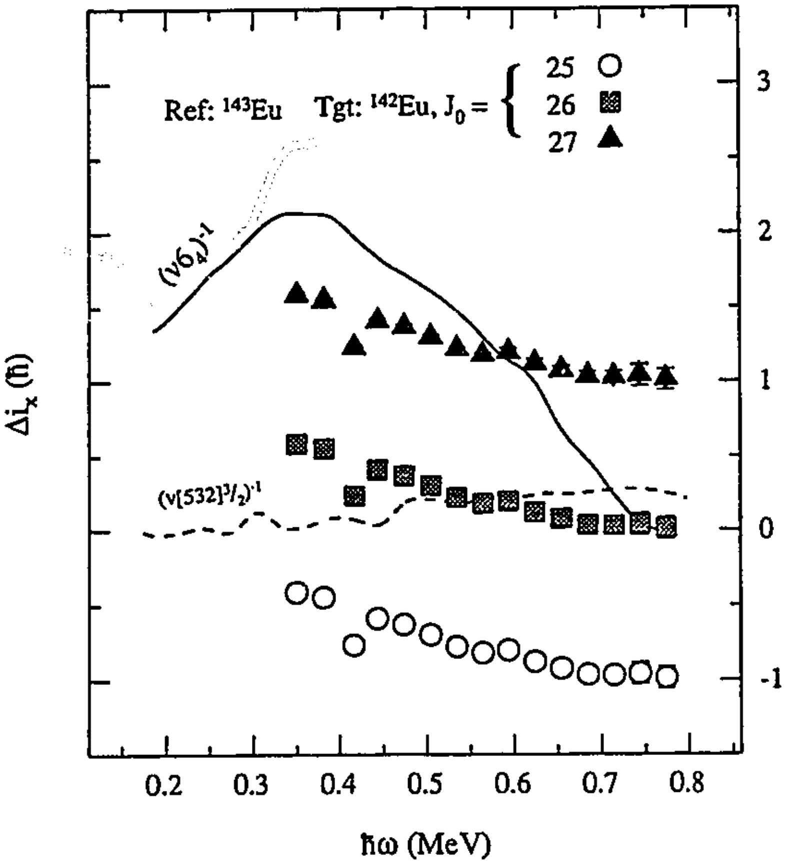

Figure 5.4.2: Effective alignments of ^{142}Eu relative to ^{143}Eu, experimental and and calculated from a Nilsson model, for selected configurations of ^{142}Eu.

core is more likely in one of the $[532]\frac{3}{2}$ levels. Of these, the HF calculation for the configuration $^{143}\mathrm{Eu}\otimes(\nu[532]\frac{3}{2}_{(+)})^{-1}$, with a total $(\pi, \alpha) = (-, 0)$, better reproduces the detailed features of the experimental Δi_x. On this (microscopic) evidence, it is proposed that the ^{142}Eu band's configuration is $^{143}\mathrm{Eu}\otimes(\nu[532]\frac{3}{2}_{(+)})^{-1}$. This is, however, inconsistent with the fact that $(\nu 6_4)^{(-1)}$ should be much more energetically favoured from the (macroscopic) total energy. In this model there is a small Coriolis splitting of the $[532]\frac{3}{2}$ levels. However this splitting is small enough that if the $(\nu N_{\mathrm{osc}}{=}5)^{(-1)}$ configuration is indeed yrast, then the $\alpha = 1$ signature partner band,

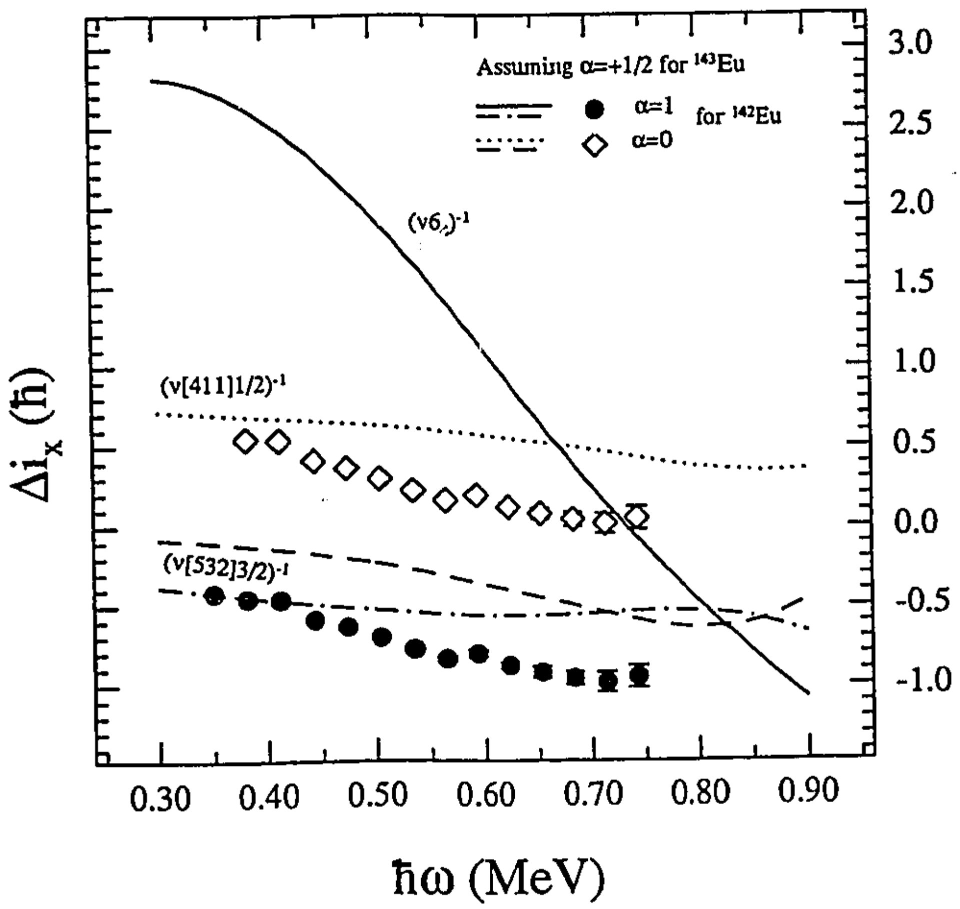

Δi_x, ^{142}Eu-^{143}Eu (HF vs. Exp.)

Figure 5.4.3: SD effective alignments (HF calculated and experimental) for ^{142}Eu with ^{143}Eu as the reference. The assumed spins for $\alpha = 0$ and $\alpha = 1$ experimental points are $J_0 = 26$ and 27, respectively. Calculated curves for a given configuration must be compared with the experimental values based on the same assumed signature.

^{143}Eu$\otimes$($\nu[532]\frac{3}{2}_{(-)}$), would not be a highly excited structure and should have been observed with similar intensity as the known band. It should again be pointed out, though, that the latter is only a weak argument against the ^{143}Eu$\otimes$($\nu[532]\frac{3}{2}_{(+)}$) configuration.

5.5. ^{144}Eu

Because ^{144}Eu has one neutron beyond the N=80 shell gap, it would seem most likely that any SD bands in this nucleus could be based on single neutron particle states coupled to the ^{143}Eu core. Specifically, the most likely orbitals which would be occupied by the last valence neutron are the $\nu 7_1$ orbital and one of the two signatures of N_{osc}=6 orbitals just above the Fermi surface. Although reasonable valence orbital assignments for these bands can be deduced from comparison of $\mathcal{J}^{(2)}$ values amongst bands in neighbouring nuclei, detailed calculations are not as supportive for these particular cases as they have been for other nuclei in this mass region.

5.5.1 Band C Crossing: Pairing or $N_{\text{osc}} = 7$ intruder?

As was discussed in Sect. 4.5, the SD band labeled Band C of ^{144}Eu appears to undergo a crossing at $\hbar\omega \sim 0.5$ MeV, see Figure 5.5.1. The frequency of this crossing matches that of the backbend in ^{144}Gd. Since this backbend is attributed to the Coriolis breaking of the N_{osc}=6 quasi-proton pair, this would suggest a $\pi 6^2$ proton configuration for ^{144}Eu band C, rather than more obvious $\pi 6^1 \otimes \nu 6^5$ or $\pi 6^1 \otimes \nu 6^4 \nu 7^1$ configurations.

Since there was some indication that pairing might indeed play an important role in the detailed behavior of ^{144}Eu band C, it was necessary to use Woods-Saxon codes which include pairing. Paired calculations were performed at a fixed deformation of $(\beta, \gamma) = (0.52, 3°)$, which was the approximate location of the predicted SD minimum of the (π,α)=$(-,-\frac{1}{2})$ TRS calculations. Extracted $\mathcal{J}^{(2)}$ values are compared to experimental results in Figure 5.5.2. The proton quasi-particle crossing in the ^{144}Eu $\pi 6^2$ system does indeed occur at approximately the same frequency as was experimentally observed. However, the $\mathcal{J}^{(2)}$ is also reproduced by a $\pi 6^1 \nu 7^1$ configuration. In this case, the low-frequency feature of $\mathcal{J}^{(2)}$ can be seen from Figure 4.1.2 as a consequence of the interaction of the

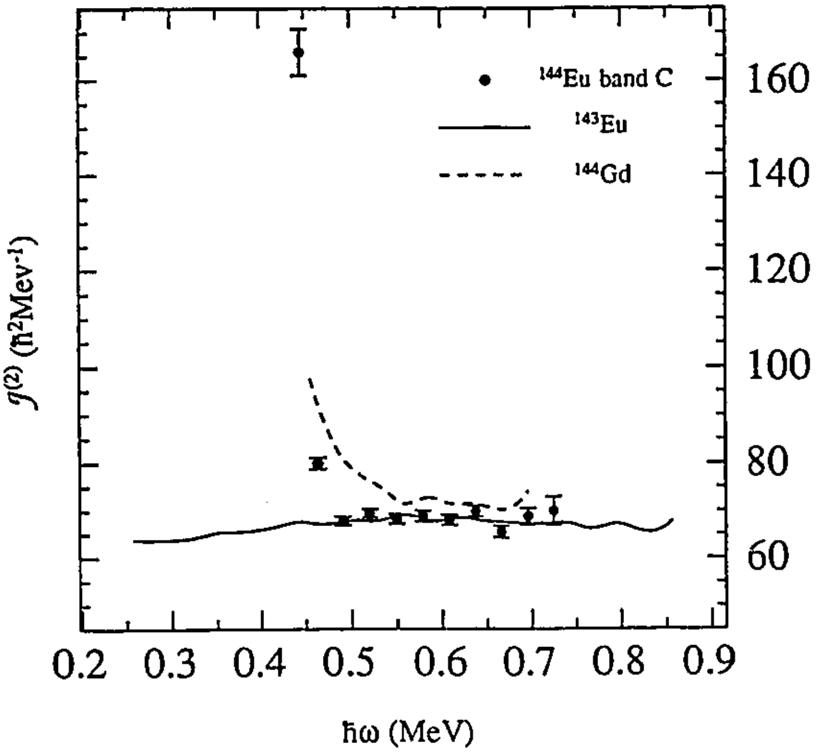

Figure 5.5.1: Experimental dynamic moments of inertia $\mathcal{J}^{(2)}$ of ^{144}Eu band C (data points), ^{143}Eu (solid curve), and ^{144}Gd (dashed curve).

$\nu 7^1$ level, which is the lowest-Routhian single-particle state at high frequencies, with the unoccupied level labeled $[514]\frac{9}{2}_{(-)}$. On this evidence alone it is not possible to distinguish a paired crossing (*i.e.* $\pi 6^2$) from an unpaired crossing ($\nu 7_1$–$[514]\frac{9}{2}_{(-)}$). It is worth noting that the $\nu 7^1$ configuration reproduces the experimental $\mathcal{J}^{(2)}$ somewhat better than the $\pi 6^2$ configuration, specifically the sharpness of the low-frequency feature and also the magnitude of $\mathcal{J}^{(2)}$ at higher frequencies. Turning back to Figure 4.1.2, the 81st neutron will naturally occupy the $\nu 7_1$ single-particle level for rotational frequencies above ~ $0.6\hbar\omega$, whereas the $\pi 6^2$ would involve a particle-hole excitation into the second $N_{\rm osc}$=6 proton even at the highest

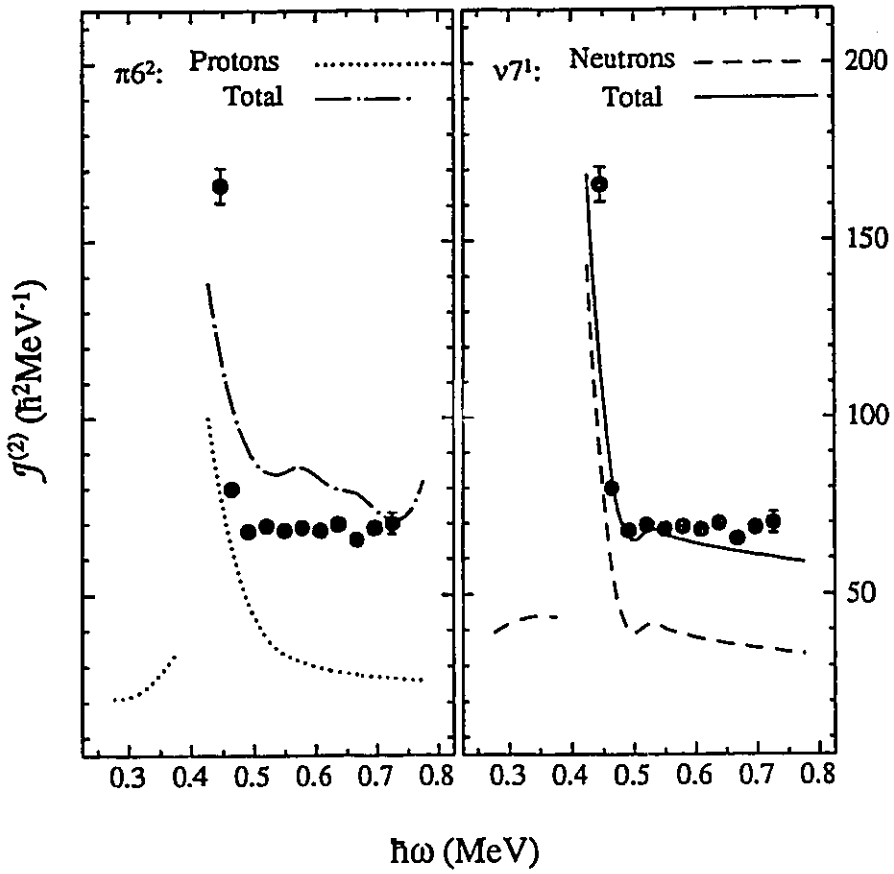

Figure 5.5.2: Woods-Saxon calculations of $\mathcal{J}^{(2)}$ at fixed deformation for ^{144}Eu $\pi 6^2$ (left) and $\nu 7^1$ (right) configurations. Experimental data points from ^{144}Eu band C are compared to total calculated values (dash-dot and solid curves). Also, the proton (left) and neutron (right) contributions to the total $\mathcal{J}^{(2)}$ are plotted separately to demonstrate the contribution of the $\pi 6^2$ and $\nu 7^1$ crossings, respectively.

frequencies observed in $A\sim150$ superdeformed bands. For these reasons the $\nu 7^1$ configuration is the preferred assignment.

It is interesting to note that the $\mathcal{J}^{(2)}$ of ^{144}Eu band C is identical to that of superdeformed ^{143}Eu, which is reflected in a flat Δi_x (see Figure 5.5.3). It was pointed out previously that bands with identical moments of inertia will have the same intruder configurations. This is based largely on the presumption that the addition of a particle into a high $N_{\rm osc}$, high n_z intruder orbital will tend to "polarize" the collective core. In a perhaps simplistic description of the polarization scenario, such a level pulls itself to the lower energy, dragging the deformation of the core along with it. The polarization of the core from the occupation of neutron $N_{\rm osc}$=6 levels was long regarded as a necessary condition for stabilizing the A~130 superdeformed nuclei [Wys 88], and it was generally accepted that the same sort of intruder polarization occurred in the A~150 superdeformed bands. Yet even though the valence configuration of ^{144}Eu band C would most likely be $\pi[660]\frac{1}{2}_{(-)}$ or $\nu[770]\frac{1}{2}_{(-)}$ relative to ^{143}Eu, the $\mathcal{J}^{(2)}$ of band C suggests a pure particle-rotor coupling with no polarization of the core.

A Hartree-Fock calculation of the $\nu 7_1 \otimes ^{143}$Eu configuration, which is also shown in Figure 5.5.3, indeed yields a constant Δi_x with respect to ^{143}Eu. The absolute value of Δi_x is subject to a renormalization of the SkM* parameters which may change the magnitude of the constant difference. This supports the preferred $\pi 6^1 \nu 7^1$ intruder configuration. It would seem that the $\nu 7^1$ orbital has no effect on the ^{143}Eu core, even though the $\nu 6^1$ orbitals do tend to polarize the A~130 superdeformed shapes.

5.5.2 Anomalous Low $\mathcal{J}^{(2)}$ bands A and B

The previous result on ^{144}Eu band C may have given some hope that the ^{143}Eu really is a stable, rigid core in the presence of neutron valence particles. However, Figure 5.5.4 demonstrates that the dynamic moments of inertia of bands A and B are lower than that of ^{143}Eu. The behavior of the relevant neutron orbitals above N=80 is well understood from systematics of the gadolinium isotopes and so the interpretation of these bands will rely on the conclusions of [Haa 93].

At very low frequencies, the γ–ray energies of ^{144}Eu bands A and B are approximately the average of one another, up to about ~ 750 keV. Beyond that frequency the pattern disappears. One possible interpretation of this is that the

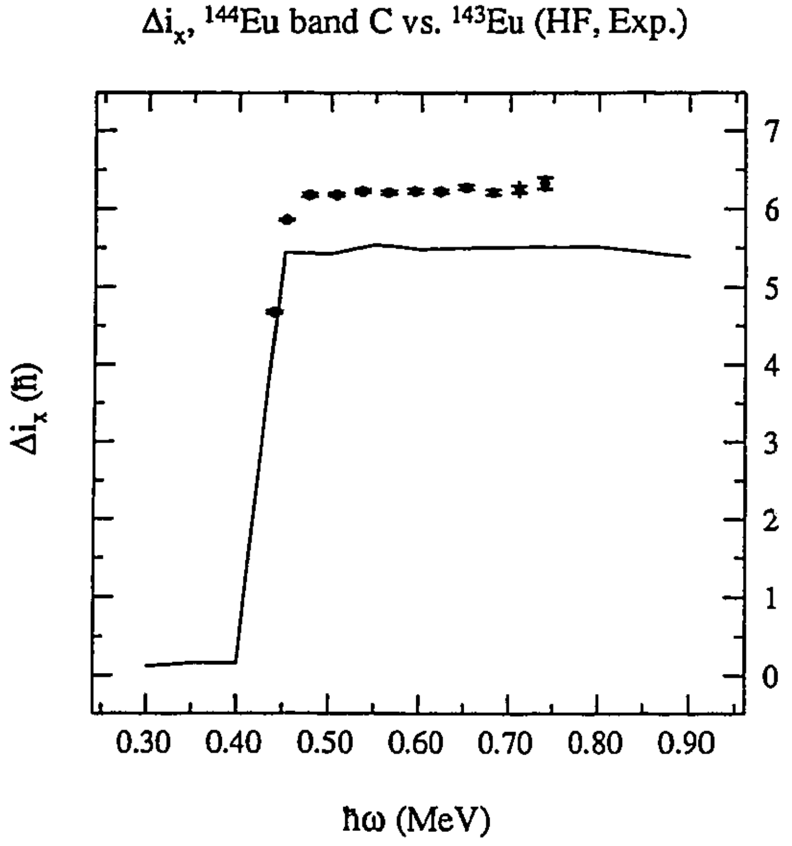

Figure 5.5.3: Effective alignment of ^{144}Eu band C relative to ^{143}Eu yrast band. Spins are assumed such that final state of the 878.6 keV transition of ^{144}Eu band C has a spin $\frac{37}{2}\hbar$ higher than the final state of the 483.7 keV transition of ^{143}Eu. The solid line is a HF calculation of this quantity.

valence neutron beyond the ^{143}Eu core occupies one of two signature-partner orbitals which are degenerate at low frequency but split beyond $\hbar\omega \sim 0.38$ MeV. The two $N_{\rm osc}$=6 orbitals just above N=80, labeled $[642]\frac{5}{2}_{(\pm)}$ in Figure 4.1.2, satisfy these criterion. Furthermore, the violent perturbation in $\mathcal{J}^{(2)}$ at $\hbar\omega \sim 0.7$ MeV resembles a similar but less dramatic effect in ^{146}Gd band 1, which has been attributed [Heb 90, Haa 93] to the interaction of the negative signatures of the (signature-split) $[651]\frac{1}{2}$ and (signature-degenerate) $[642]\frac{5}{2}$ orbitals shown in Figure 5.5.5. This

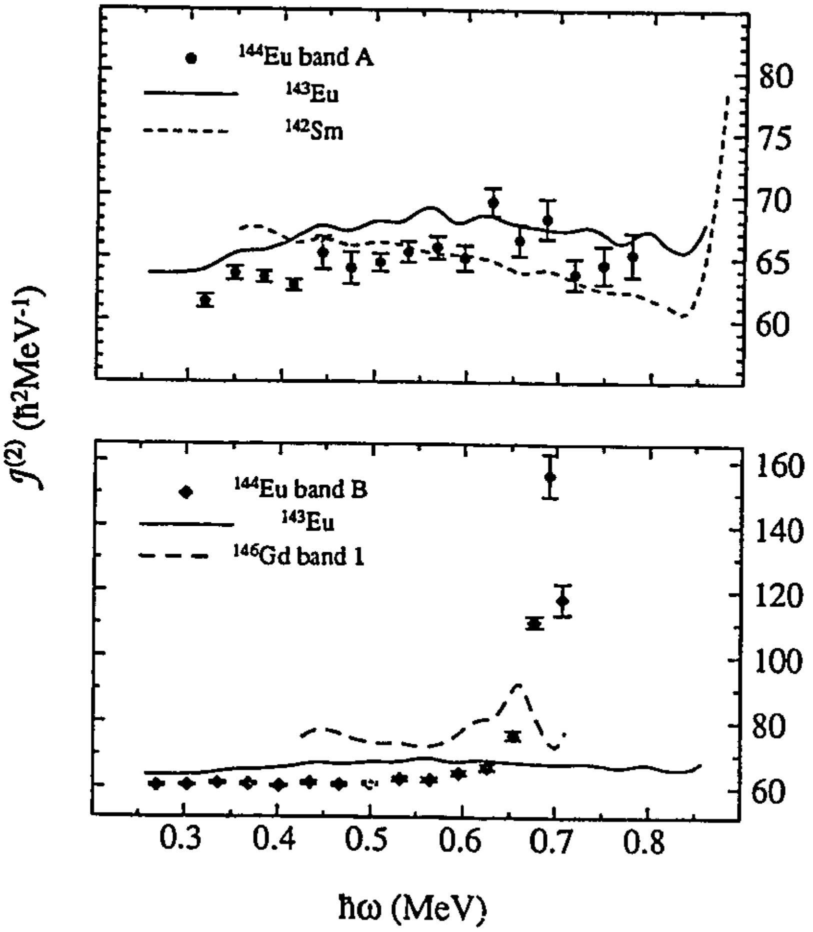

Figure 5.5.4: Experimental dynamic moments of inertia $\mathcal{J}^{(2)}$ of ^{144}Eu bands A and B and selected neighboring nuclei.

has also been recently observed in a ^{145}Gd superdeformed band [DeA 95], which is consistent with the assumption that the crossing is due to neutron valence particles.

The configuration of ^{144}Eu bands A and B, then, is likely an ^{143}Eu core with the 81st neutron occupying one of the positive-parity $N_{\text{osc}}=6$ neutrons. As will be discussed in the following paragraph, the signature of these configurations is

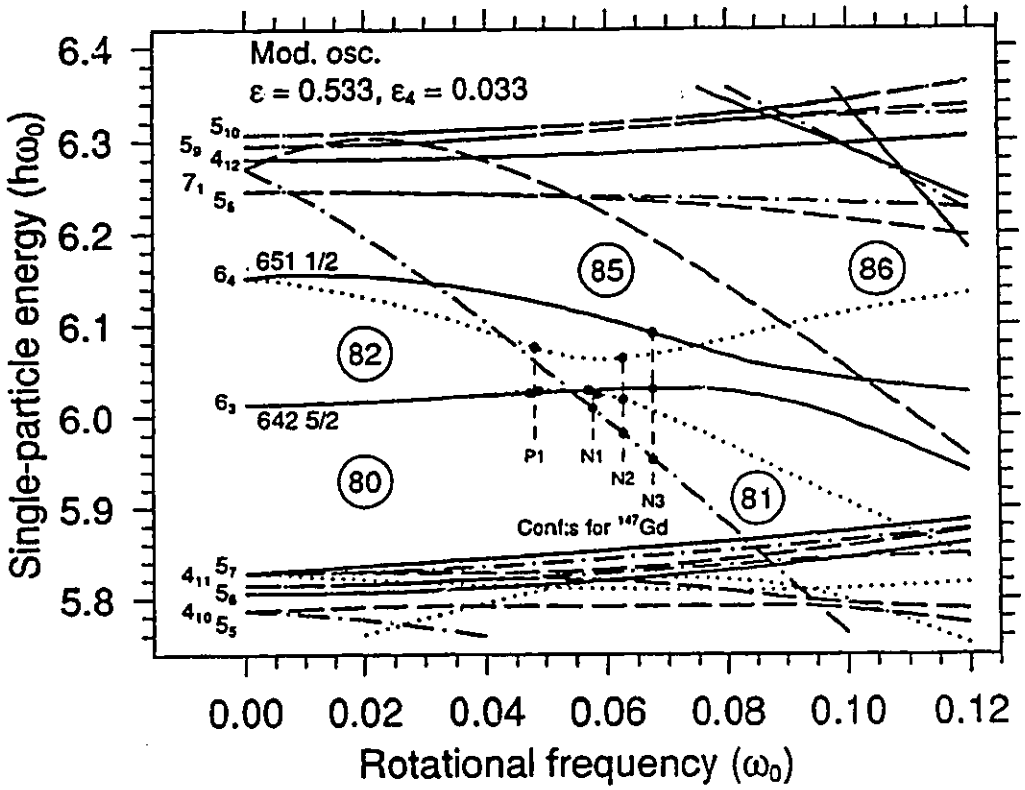

Figure 5.5.5: Neutron single-particle energies in the Nilsson model calculations, reproduced from [Haa 93], showing the crossing of the $[642]\frac{5}{2}$ and $[651]\frac{1}{2}$ orbitals. These calculations, which are specific to ^{147}Gd ($\hbar\omega_0$=7.8 MeV), show qualitatively how this crossing behaves in the $^{146\rightarrow148}$Gd SD bands.

not unambiguous, and so the only statement which can be made with certainty is that N_{osc}=6 neutrons of the same signature are occupied in the pair of bands ^{144}Eu band A and ^{146}Gd band 2, and the opposite-signature N_{osc}=6 neutron is occupied in ^{144}Eu band B and ^{146}Gd band 1.

The reproduction of experimental features by cranking calculations has not been as successful for these two bands as it has for the other structures presented in this work. The $\mathcal{J}^{(2)}$ values shown in Figure 5.5.6, which were calculated with a cranked Woods-Saxon potential, cannot be considered a good reproduction of the data. As was found for the ^{146}Gd, the Hartree-Fock calculations do not give a

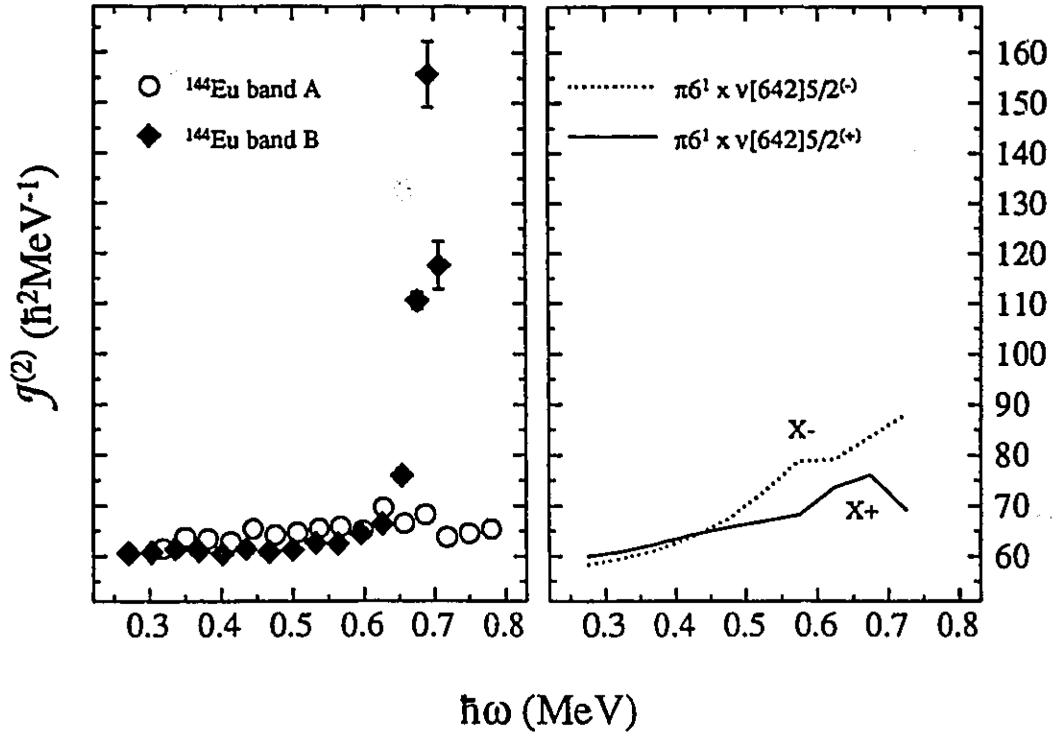

Figure 5.5.6: Experimental $\mathcal{J}^{(2)}$ of ^{144}Eu bands A and B (left panel) compared to paired Woods-Saxon calculations (right panel). $\mathcal{J}^{(2)}$ was calculated at a fixed deformation of $(\beta, gamma) = (.515, 2.9°)$, which was the location of the TRS minima for both the $(\pi, \alpha) = (+, 0)$ and $(\pi, alpha) = (+, 1)$ configurations at $\hbar\omega = 0.6$ MeV. X± marks the crossings discussed in the text.

large perturbation of $\mathcal{J}^{(2)}$ for either of the $\alpha = \pm\frac{1}{2}$ $N_{\rm osc}$=6 neutron crossings. In fact, the Nilsson model as applied in [Heb 90] and [Haa 93] is the most successful in reproducing the experimental data based on the previously-mentioned configurations. In the paired WS calculations of Figure 5.5.6, configurations with either signature of $\nu[642]\frac{5}{2}$ yield small perturbations in $\mathcal{J}^{(2)}$. The $\alpha = -\frac{1}{2}$ crossing only gives an almost negligible perturbation of $\mathcal{J}^{(2)}$, and it occurs at a much lower frequency ($\sim$ 0.5 MeV) than experimentally observed. The second configuration with the $\alpha = +\frac{1}{2}$ $N_{\rm osc}$=6 proton occupied gives a small bump in $\mathcal{J}^{(2)}$ at $\sim$ 0.7 MeV. These same crossings occur 0.2 MeV higher in rotational frequency in the unpaired

Nilsson calculations. This serious discrepancy amongst the various treatments of these $N_{\rm osc}$=6 neutron orbitals – Nilsson, Woods-Saxon and Hartree-Fock – may be symptomatic of a deeper problem with the mean field. At the present time the Nilsson interpretation from the systematic study of gadolinium isotopes in [Haa 93] will be taken as the more probable scenario, especially in light of the reproduction of the magnitude of the crossing in ^{146}Gd band 1 and the lack of an observed crossing in ^{146}Gd band 2. Specifically, it is proposed that the most likely valence particle configurations for bands A and B are $\pi[660]\frac{1}{2}_{(+)} \otimes \nu[642]\frac{5}{2}_{(+)}$ and $\pi[660]\frac{1}{2}_{(+)} \otimes \nu[642]\frac{5}{2}_{(-)}$ respectively.

5.5.3 Spins

Theoretical spins were extracted from the paired WS cranking calculations. The aligned spin I_x of the $\pi6^1\nu7^1$ configuration at $\hbar\omega = 0.65$ MeV was $49.3\hbar$. This corresponds to the artificial state halfway between the initial and final states of the 1302 keV transition of band C. The $[660]\frac{1}{2}_{(+)}$ and $[770]\frac{1}{2}_{(-)}$ orbitals couple to a total $\alpha = 0$, so the states of such a band would have even spins. Therefore it is proposed that the 1302 keV transition is a decay between states $J = 50 \rightarrow 48$, which in turn means that the spin of final state of the 878 keV transition is $32\hbar$. For band A, the spin extracted from the WS calculations at $\hbar\omega = 0.3$ MeV for the $\pi6^1$ calculation coupled to the positive and negative signatures of the $\nu[642]\frac{5}{2}$ orbitals was $21.4\hbar$ and $21.1\hbar$ respectively. Since these correspond to total signatures of $\alpha = 1$ and 0, the lowest-energy 603 keV γ ray of band A would be a $23 \rightarrow 21$ or $22 \rightarrow 20$ transition. This in turn places the final spin of band B at $18\hbar$ or $17\hbar$. The preferred interpretation in Sect. 5.5.2 corresponds to the former of each pair of possible spins. It should be noted that these spins are consistent with the lower limits proposed in Sect. 4.5.3. As in the case of ^{142}Sm band A, the HF calculations for the lowest-spin states of the ^{144}Eu bands are $\sim 4\hbar$ higher than the WS predictions.

5.6. Summary: Is ^{143}Eu A Suitable Core?

The results of the previous sections are summarized in Table 5.6.1. The proposed configurations are the most probable of the ones discussed in the previous sections. It has been possible to describe five of the six bands as particle or hole couplings to ^{143}Eu, and their behavior is close to what would be expected from the calculations of Figure 4.1.2. This would tend to support the suggestion of Sect. 4.1 to use ^{143}Eu as a doubly-magic, rigid superdeformed core. However, ^{142}Sm band B is better considered as multiple holes in a ^{146}Gd band 2 core (see Figure 4.1.3). Furthermore, the behavior of ^{144}Eu bands A and B is quite similar to ^{146}Gd bands 2 and 1 in details, and this is understood by assigning them the same (non-intruder) valence configuration. In light of this, it seems most appropriate to consider the $N{\sim}80$ superdeformed nuclei as an extension of the $A{\sim}150$ region of superdeformation, rather than as a distinct region or as part of the $A{\sim}130$ class of highly deformed bands.

It should be noted that the configurations proposed for ^{142}Sm band B and ^{144}Eu bands A and B depend on the interpretation of ^{146}Gd bands 1 and 2. In particular, the good agreement of the HF calculated Δi_x for ^{142}Sm band B relative to ^{146}Gd band 2 requires a valence particle in the $\alpha = -\frac{1}{2}$ N_{osc}=6 neutron orbital, yet based on the Nilsson model that same orbital has been assigned as the one responsible for the crossing in ^{144}Eu band B. Until these discrepancies between the mean-field calculations are resolved, it might be more appropriate to simply assign common valence configurations without specifying the exact wave function of those particles. In other words, consider the two N_{osc}=6 neutron orbitals which have been invoked in the discussions of ^{146}Gd, ^{142}Sm and ^{144}Eu, simply as orbitals X and Y. The bands which exhibit a crossing at $\hbar\omega \sim 0.7$ keV could be assigned as having X occupied, while Y is occupied in those bands without this crossing. Valence configurations in terms of these unknown particles X and Y are given in Table 5.6.2.

Nucleus	Band	Valence Configuration	(π, α)	I_0 ($\hbar$)
^{142}Sm	A	$\pi 6^1(\nu[541]\frac{1}{2}_{(-)})^{-1}$	$(-,1)$	25
^{142}Sm	B	$\pi 6^2\nu 7^1 \otimes [651]\frac{1}{2}_{(-)} \otimes (2p2n)^{-1}$	$(-,1)$	41
^{142}Eu	A	$\pi 6^1 \otimes (\nu[532]\frac{3}{2}_{(+)})^{-1}$	$(-,0)$	
^{144}Eu	A	$\pi 6^1 \otimes \nu[642]\frac{5}{2}_{(+)}$	$(+,1)$	21
^{144}Eu	B	$\pi 6^1 \otimes \nu[642]\frac{5}{2}_{(-)}$	$(+,0)$	18
^{144}Eu	C	$\pi 6^1\nu 7^1$	$(-,0)$	32

Table 5.6.1: Summary of preferred valence particle configurations of the ^{142}Sm and ^{142,144}Eu SD bands, with respect to the N=80, Z=62 static shell gap. Note that the configurations for ^{144}Eu are based on those proposed in [Haa 93] for ^{146}Gd, while the configuration for ^{142}Sm is based on the HF calculations. The suggested I_0 values are the spins expected from theory of the final states of the lowest energy transitions reported in Tables 4.3.2, 4.4.1 and 4.5.1. (2p2n) is a shorthand notation for the four hole states with total $\alpha = 0$ listed in Sect. 5.3.4.

Nucleus	Band	Valence Configuration
^{146}Gd	1	$\pi 6^2\nu 7^1 \otimes \nu X$
^{146}Gd	2	$\pi 6^2\nu 7^1 \otimes \nu Y$
^{142}Sm	B	$\pi 6^2\nu 7^1 \otimes \nu Y \otimes (2p2n)^{-1}$
^{144}Eu	A	$\pi 6^1 \otimes \nu Y$
^{144}Eu	B	$\pi 6^1 \otimes \nu X$

Table 5.6.2: Configurations for ^{146}Gd, ^{142}Sm band B and ^{144}Eu bands A and B in terms of valence states X and Y, as discussed in the text. (2p2n) is defined as in Table 5.6.1. holes in the ^{142}Sm configuration discussed elsewhere.

Chapter 6.
Conclusions and Future Prospects

6.1. Summary

In conclusion, superdeformation has been found and studied in the nuclei ^{142}Sm, ^{142}Eu and ^{144}Eu. This includes six discrete SD bands:

- ^{142}Sm band A was populated by the ^{124}Sn(^{24}Mg,6n) fusion-evaporation reaction at a beam energy of 145 MeV. It was first discovered with the 8π spectrometer and later studied with GAMMASPHERE, and consists of 19 γ-ray transitions with a maximum intensity of 0.5% of the ^{142}Sm fusion-evaporation reaction channel. The proposed configuration is a $\pi[541]\frac{1}{2}_{(-)}$ hole coupled to an ^{143}Eu core;
- ^{142}Sm band B was populated by the same reaction with an intensity of $\sim$ 0.08% and observed with GAMMASPHERE. It consists of 15 transitions, and for transitions with energies greater than 1073 keV, the energies are identical to those in ^{146}Gd band 2. It has been interpreted as having a $\pi 6^2 \nu 7^1$ intruder configuration, or as a ^{146}Gd core with holes in low-j orbitals;
- ^{142}Eu band A was populated by the ^{120}Sn(^{27}Al,5n) reaction at 152 MeV beam energy, and was studied with the 8π. The 15 transitions have a maximum intensity of 1.2% relative to the ^{142}Eu reaction channel. Based on Δi_x it is propsed that the configuration is most likely a ^{143}Eu core with a hole in the $\nu[532]\frac{3}{2}_{(+)}$ orbital, rather than $\nu 6_4$ which was predicted to be energetically favoured in the mean field calculations;

- ^{144}Eu bands A and B, with 17 and 18 transitions respectively, were populated by ^{122}Sn(^{27}Al,5n) at 142 MeV and observed with GAMMASPHERE. Their intensities are $\lesssim 0.17, 0.14\%$ of the ^{144}Eu cross section. They have been interpreted as signature partners based on the ^{143}Eu core coupled to the same $N_{\mathrm{osc}}=6$ valence neutrons as in ^{146}Gd bands 2 and 1, respectively;
- ^{144}Eu band C, populated and observed as in ^{144}Eu bands A and B, has 13 transitions with an upper limit on intensity of $\lesssim 0.14\%$ of the ^{144}Eu cross section. It has been interpreted as ^{143}Eu coupled to a $\nu[770]\frac{1}{2}_{(-)}$ neutron which does *not* polarize the core.

Also the ^{142}Sm ridge structure arising from SD not associated with the discrete SD bands was found to have a $\mathcal{J}^{(2)}$ identical to ^{143}Eu.

With the exception of ^{142}Sm band B, all of these bands can be understood as couplings to a rigid ^{143}Eu core. Once again it should be pointed out that there is a significant inconsistency in the assignment of valence particles to ^{142}Sm band B, ^{144}Eu bands A and B, and ^{146}Gd bands 1 and 2. Resolution of this problem will be discussed in the following section.

6.2. Future Prospects

There are a number of possible extensions to this project, some (but not all) of which require the ever-increasing sensitivity of evolving γ-ray spectrometers. In addition to trying to extend the systematics with more bands in more nuclei, the question of spins, parities and excitation energies of the known bands must be resolved to clarify the ^{142}Sm band B, ^{144}Eu bands A/B conflict. Lifetime measurements may be of some interest in confirming the nature of the ^{142}Sm band B excitation and in understanding the apparent lack of a polarization effect in ^{144}Eu band C. But perhaps the most interesting challenge raised by the present work is to develop a coherent theoretical explanation of the 2p2n isospectral bands, or at least to propose an empirical model with predictive power.

6.2.1 More Bands, More Nuclei

Preliminary reports of discrete superdeformed bands in ^{145}Gd [DeA 95] are not inconsistent with the scenario presented for the ^{144}Eu bands A and B. This was really the last piece of the puzzle, in terms of a complete systematic picture connecting the ^{143}Eu–like SD bands to the rest of the $A\sim150$ region. The search for more bands in more nuclei is not critical to understanding the configurations of the presently known bands, except for ^{142}Eu to be discussed below. With the exception of possible 2p2n excitations (see Sect. 6.2.4), it is unlikely that there will be any peculiar behavior of new SD bands.

First it is worth pointing out that repeating the same experiments on ^{142}Sm is unlikely to produce new bands. If the ridge of ^{142}Sm actually consists of long, discrete cascades based on holes in the ^{143}Eu core, then their intensity must be extremely low or they must be extremely short. In the latter case the extra gain in sensitivity from high-fold gating will not be significant. This is not to say that ^{142}Sm is a closed case, since that ridge may be useful laboratory for studying rotational damping at superdeformations. Furthermore, at low rotational frequencies ^{142}Sm would be a "bare naked" superdeformed band [Gal 94], which has *no* intruder orbitals occupied. This is the expected SD configuration at $\hbar\omega = 0$, where the $\nu 6_1$ orbital is well above the Fermi surface. However such a configuration would be so highly excited that it may not be possible to populate these states and observe their γ-ray decay.

Of the europium isotopes, it would certainly be worthwhile to study ^{142}Eu for excited bands to try to identify the $^{143}\mathrm{Eu}\otimes(\nu 6_4)^{-1}$ configuration. The fact that the current band is best described by a configuration which is calculated to be non-yrast is certainly troubling. Another experiment with higher sensitivity would hopefully uncover both the $(\nu 6_4)^{-1}$ band and the signature partner of the current band, which in turn could be used to deduce the $\omega = 0$ energy of the $\nu 6_4$ orbital relative to the N_{osc}=5 levels. A further study of ^{144}Eu would not, by itself, have much of an influence on the systematics of SD bands in this region.

6.2.2 Spins and Parities

The problem of the valence particle assignments in ^{142}Sm band B, ^{144}Eu bands A and B, and ^{146}Gd bands 1 and 2 must be resolved experimentally by an absolute measurement of the spins and parities of the SD states. Probably ^{146}Gd would be the best case, since these two bands are the most intense of the set. Such a measurement would have to wait for the full implementation of EUROBALL [NBF 94] or the fourth-generation detector array GRETA.

6.2.3 Deformations and DSAM

The expectation value of the Q_{20} operator, which is related to deformation β by Eq. (2.1.2), can be calculated from the Hartree-Fock wave functions. The results for protons for some of the bands considered in this work are shown in Figure 6.2.1. Since this quantity determines the E2 transition rate (see Sect. 2.6.2), it can be inferred from lifetimes which are deduced from Doppler-shift attenuation method (DSAM) measurements. This would confirm that the core of ^{142}Sm SD band B is indeed much more deformed than that of the yrast band A. A similar measurement has, however, already been made for the 2p2n band in ^{149}Gd, with analysis in progress.

A more interesting DSAM measurement might be ^{144}Eu. By increasing the beam energy of the reaction used in the present study, the ^{143}Eu *and* ^{144}Eu SD bands would be populated with sufficient intensity for DSAM measurements. If the ^{143}Eu core were rigid against addition or removal of specific particles, then the proton $\langle Q_{20} \rangle$ should only change if that particle or hole were itself a proton, and then it would simply scale as $\delta Z/Z$. In the case of ^{144}Eu *vs.* ^{143}Eu this should be zero. The calculations of Figure 6.2.1 predict that $\langle Q_{20} \rangle$ is lower for

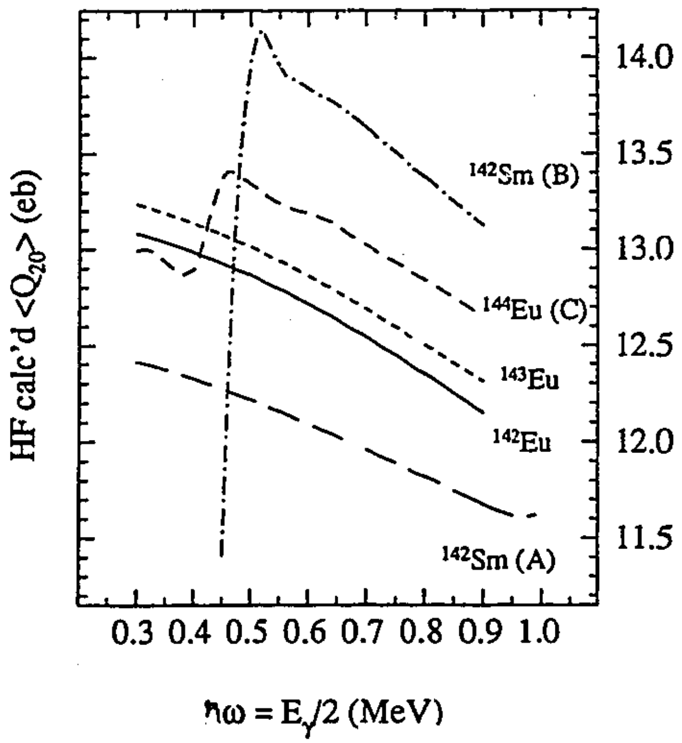

Figure 6.2.1: Expectation value $\langle Q_{20} \rangle$ as a function of cranking frequency of the proton HF wave functions for the configurations proposed in Chap. 5 of this thesis for ^{142}Sm bands A and B, ^{142}Eu, and ^{144}Eu band C, as well as the $\pi 6^1$ configuration of ^{143}Eu.

the ^{143}Eu yrast band than for ^{144}Eu band C, which might suggest that the core is polarized by the N_{osc}=7 neutron particle, so the resulting change in $\mathcal{J}^{(2)}$ must be cancelled by some other effect, such as triaxiality or single-particle degrees of freedom. The predicted difference is of the same order as the uncertainty on current measurements comparing $\langle Q_{20} \rangle$ between different bands in the same experiment, so further improvements in either the sensitivity of the arrays or in the DSAM analysis itself will be necessary to confirm the ridgity of the ^{143}Eu core.

6.2.4 2p2n Identical Bands

It is still not clear why the 2p2n identical bands in the $A{\sim}150$ region are so intense, or what role is played by the low-j valence particles in their proposed configurations. If the "magic" orbitals with $\tilde{a}_{\text{asymp}} = \pm 1$ are responsible for the identical $\mathcal{J}^{(2)}$ and the high intensity, then it would make the most sense to study these orbitals beyond the $A{\sim}150$ region of superdeformation. In Figure 2.2.1, the $[301]\frac{1}{2}$ and $[411]\frac{1}{2}$ orbitals would be near the Fermi surface for systems such as ^{112}Pd and ^{116}Cd at a deformation of $\epsilon \sim 0.3$. These neutron-rich nuclei might be somewhat difficult to study by conventional high-spin fusion-evaporation reactions with stable beams and targets. If the only requirement is availability of low-j states, namely those from s, p or d shells, then the low-spin *first-minimum* rotational bands in the vicinity of ^{236}U would be worthy of closer study. It may be best, however, to continue looking for 2p2n identical bands in the known regions of superdeformation and establish the significance of the phenomenon.

Appendix A.
Non-SD Decay Schemes

Although this thesis concentrated specifically on γ rays associated with superdeformed bands, measurements such as J_0, intensity, and assignment to a specific nucleus require some knowledge of non-SD γ-ray decays and level schemes. Table A.1 lists the most recent published experimental data on non-SD γ-ray decay of high-spin states on ^{142}Sm, ^{142}Eu, ^{144}Eu, and various other nuclei of mass $A \sim 140$. Not all of these nuclei were discussed in the text, but γ rays from all of these nuclei were observed in the data.

Prior to this study, the near-yrast level scheme for ^{142}Sm was only known up to $J \sim 15\hbar$ [Lac 84]. These non-collective low-spin states were described by shell model calculations. The initial motivation to extend the level scheme in the current work was for the measurement of the J_0 of ^{142}Sm SD band A. The high-spin, near-yrast level and γ-ray decay scheme shown in Figure A.2 was deduced from γ^2 and γ^3 coincidence data from the 8π and GAMMASPHERE experiments. Gamma-ray energies and intensities were measured from LEVIT8R best fits to the GAMMASPHERE data, while DCO ratios (to be discussed later) were measured from 8π data.

It should be noted that the experiments all measured *prompt* coincidences. One consequence of the prompt coincidence condition is that it essentially restricts the multipolarity of observed γ rays to those of E2, M1 or E1 multipolarity. Higher-multipole (*e.g.* M2 or E3) transitions of energies $E_\gamma \leq 2.5$ MeV typically have transition rates much longer than the time that the recoiling nucleus remains in view of the collimated HPGe detectors, so only M1, E1 and E2 transitions are observed in prompt coincidence experiments. Furthermore, coincidences involving decays

Table A.1: References to non-SD γ-ray decay schemes for $A{\sim}140$ nuclei.

^{139}Pm	[Xu 87]
^{141}Pm	[GDC 89]
^{142}Pm	[Fun 76]
^{141}Sm	[Car 91] [Lac 93]
^{142}Sm	[Lac 84]
^{143}Sm	[Kow 74]
^{144}Sm	[Ott 94]
^{145}Sm	[Pii 91]
^{141}Eu	[Xu 91]
^{142}Eu	[Biz 90]
^{143}Eu	[Pii 92]
^{144}Eu	[Hae 81] [Pii 95a]
^{145}Eu	[Baz 80]

through states with mean life-times longer than about 1 ns will be attenuated. For example, no decays could be observed from the 10^+ state, which decays with a mean lifetime of 480 ns [Lac 84], nor were any decays observed following the 175 ns 7^- isomer. Hence there is very little observed intensity in the $2^+ \rightarrow 0^+$ 767 keVtransition.

In the new high-spin part of the decay scheme there are three structures of interest:

- establishment of linking transitions from an E2 cascade (428, 578 and 840 keV) to the previously-known decay scheme;
- measurement of an cascade in coincidence with a 1042 keV transition to the $J = 15$ initial state of the 193 keV transition;
- placement of the 1494 keV transition.

All three of these structures, or some part of them, are observed in coincidence with the SD bands, so establishing their place in the decay scheme is essential to determining experimentally the spin of the SD bands. Figure A.1 shows some examples of the quality of the γ^3 GAMMASPHERE data that was available for determining the coincidence relationships and deducing level schemes for these structures.

Part of the high-spin decay scheme of ^{142}Sm includes a branch with intense lines of 428, 578 and 840 keV. From the 8π γ^2 coincidence data it was established that these three γ rays are in coincidence with one another, and the 840 and 579 keV lines are in coincidence with the 193 keV transition but the 428 keV transition is not. With triple-coincidence data it was possible to find a network of linking transitions. The 1280 and 952 keV transitions were both observed in spectra made by double-gates, one on the $12^+ \rightarrow 10^+$ 920 keV transition and the other on the 428, 578 or 840 keV transitions. Furthermore a decay branch from the final state of the 579 keV transition through the 1042 keV line to the 15 → 14 193 keV transition was observed from triple-coincidences, although this decay path could not be resolved in 8π data.

The 1042 keV transition itself was part of a decay branch which turned out to be quite difficult to establish. It was clearly in coincidence with 286 and 385 keV transitions. These had been assigned in [Lac 84] as a short $17 \rightarrow 16 \rightarrow 15$ cascade feeding the 193 keV transition. However these γ rays were not seen in coincidence with the 578 keV line, yet the 1042 keV transition was. After these were re-arranged, the rest of this structure, including a "bubble," were easily established. It appears that this cascade is in coincidence with an 815 keV transition, possibly meaning that it is at least partly fed from states above the initial state of the 579 keV transition.

Finally the 1494 keV transition remains somewhat troublesome. Its proposed placement is based on coincidence or anti-coincidence relationships with a number of γ rays which also happen to be doublets or even triplets, in particular three γ rays with energies $\simeq$351 keV. Also, it has only been possible to assign one weak γ ray (460 keV) which feeds the initial state of this transition, so the γ-ray

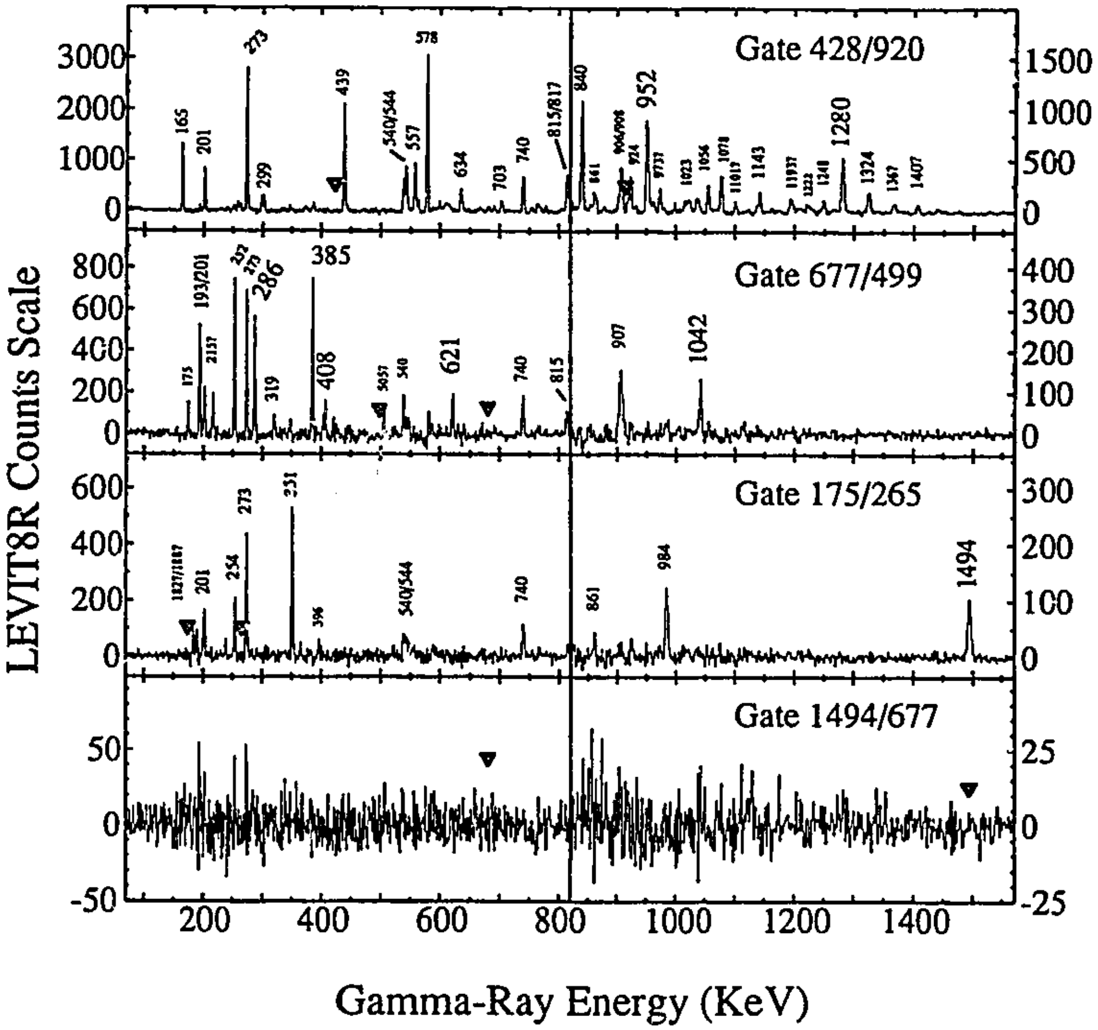

Figure A.1: Selected double-gates from GAMMASPHERE γ^3 LEVIT8R data (non-linear dispersion) demonstrating the quality of data available for deducing the structures described in the text. Note that the vertical scale changes at 820 keV. The bottom panel is a double-gate on two transitions which are not coincident. γ rays which are particularly important in the decay scheme are labeled with larger numbers.

intensity into the state does not even come close to accounting for the intensity out (*i.e.*, ***intensity balance*** is not satisfied). As was discussed in Sect. 4.3.3, this complicates the attempt to establish the spin of the SD bands. This transition is clearly in coincidence with transitions which have been placed at higher spin in the decay scheme, but decay paths connecting these states could not be established.

Spins were deduced based on the well-known one-matrix directional correlation from oriented nuclei (DCO) method. The relevant theory and its application to the 8π detector geometry have been described in [War 91], so only the most essential points will be discussed here. Double-coincidence 8π data were sorted into a correlation matrix (E_x, E_y) where E_x corresponded to a γ ray detected in the HPGe detectors in the rings nearly perpendicular to the beam axis, *i.e.* 79° and 101° (also called the ±79° detectors in 8π jargon), while E_y corresponded to γ rays detected at 37° or 143°(±37°). Spectra are then generated by gating, or "slicing," on γ-ray A and measuring the intensity of γ-ray B,

$$R_{\text{DCO}} = \frac{I_x\,(\text{B})\,(\text{gate on A}_y)}{I_y\,(\text{B})\,(\text{gate on A}_x)}. \qquad (A.1)$$

The advantage of this one-matrix method is that all efficiency factors (detector response, solid angle, number of detectors) cancel, and R_{DCO} reduces simply to the ratio of the number of counts in the peaks. If the gating transition A is a stretched $\Delta J = 2$ E2 transition, *i.e.* a $J{+}2 \rightarrow J$ transition, then R_{DCO} will be 1 if transition B is another $\Delta J = 2$ E2 transition or 2 if transition B is a pure dipole $\Delta J = 1$ transition (either E1 or M1). Unfortunately, it also turns out that the ratio for an unstretched dipole transition, *e.g.* a $J^+ \rightarrow J^-$ E1, would be 2.2, and a mixed E2/M1 transition can vary from 0.8 to 5. Therefore a single measurement is ambiguous and should be considered in conjunction with other available information, such as coincidence relationships. Similar relationships exist for transitions which are measured in a gate on a $\Delta J = 1$ transition, but because $\Delta J = 1$ transitions are often mixed M1/E2, the measurements are not as reliable.

DCO measurements are strictly valid either for consecutive decays, $(J + \Delta J_1) \rightarrow J \rightarrow (J - \Delta J_2)$, or for cascades where the decay paths between the gating transition and the measured transition are all stretched transitions, *i.e.* $J+1 \rightarrow J$ pure dipoles or $J+2 \rightarrow J$ pure quadrupoles. In the case of the 428-578-840 keV structure, it was obvious that these transitions were most consistent with a cascade of stretched E2 transitions. This meant that any or all of these transitions could be used to measure R_{DCO} for the 1280 keV transition. Similarly the 952 keV R_{DCO} transition measured in a 920 keV gate is reliable. These two new transitions, 952 and 1280 keV, were assigned as stretched E2 transitions, which firmly established the multipolarity of other cascades connecting the 428-578-840 keV structure to the rest of the level scheme. In the case of the 1042 keV transition, it was not possible to establish that the path to either the 252 or 906 keV E2 transitions consisted exclusively of stretched transitions, so the R_{DCO} ratio was not reliable. For this case an additional measurement was made from two matrices, $(x, y) = (\pm 37°, \pm 37°)$ and $(\pm 37°, \pm 79°)$. Ratios of *counts* for a transition of interest were measured in spectra gated on the y axis of an arbitrary reference transition. There is no efficiency correction on this ratio, so it is not a true DCO ratio. The purpose of this was simply to attempt to classify the transitions in cascade with the 1042 keV line. First, these ratios were measured for transitions in coincidence with the 428 keV transition, and a clear trend emerged that transitions which had been previously assigned as $\Delta J = 1$ transitions had a ratio of ~ 0.5, while for known $\Delta J = 2$ transitions the ratio was closer to 1. These trends were then compared to the same measurements of transitions in cascade with the 286 keV γ ray. The results, listed in Table A.3, are consistent with assignment of the 1042 keV transition as $\Delta J = 1$, and the 621 and 844 keV transitions are more likely $\Delta J = 2$ E2 transitions.

The structure which includes 428-578-840 keV cascade and higher-spin states in coincidence with it is similar in spin and excitation energy to strong E2 cascades at high spin reported in ^{144}Eu [Pii 95a] and ^{143}Eu [Pii 92]. In the latter case, it was found that the lifetimes of these states were shorter than would be expected for transitions based on non-collective, single-particle re-arrangements. This was interpreted as evidence of some weak form of collectivity [Pii 95b].

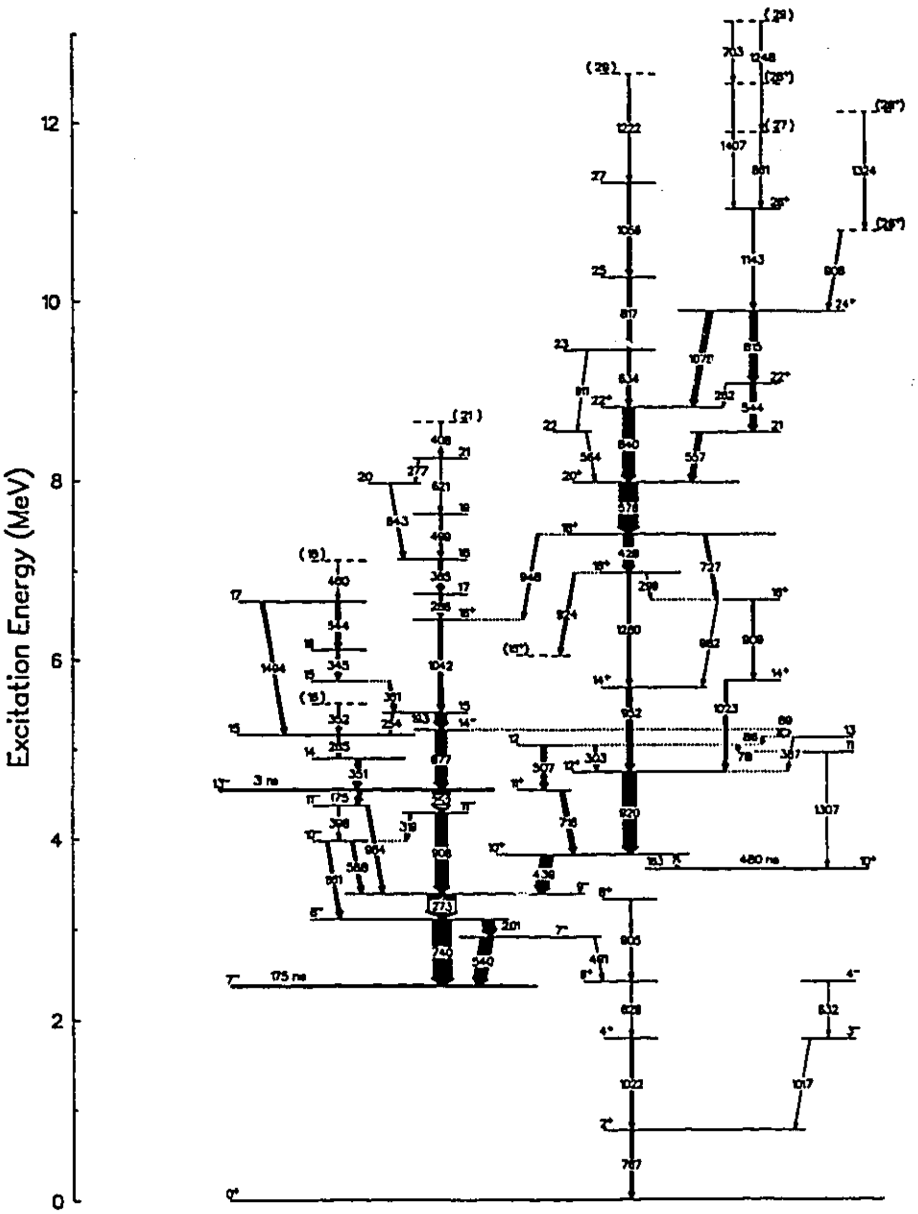

Figure A.2: Proposed γ-ray decay and level scheme for ^{142}Sm, excluding SD states and transitions.

Table A.2a: Characteristics of γ rays observed in ^{142}Sm, excluding those in the superdeformed bands.

E_γ (keV)	E_i (keV)	J_i^π	J_f^π	I_γ	R_{DCO}	Multip.
78.0 [a]	5047.3	12	11	3.0(0.1)		$\Delta J = 1$
85.5 [a]	5132.4	13	12	9.8(0.5)		$\Delta J = 1$
88.8 [a]	5221.3	14^-	13	18.4(0.6)		$\Delta J = 1$
163.5 [b]	3824.8	10^+	10^+	16.7(0.6)		M1
174.5 [b]	4544.6	13^-	11^-	16.4(0.5)		E2
193.4 [a]	5414.8	15	14^-	63.9(2.0)		$\Delta J = 1$
200.7 [b]	3112.6	8^-	7^-	53.6(1.7)	2.1(1) [c]	M1
252.4 [b]	4544.6	13^-	11^-	93.9(2.9)		E2
254.2	5414.8	15	15	9.3(0.3)		
262.4	9084.6	22	22^+	2.6(0.2)		
265.0	5160.8	15	14	10.9(0.5)		
273.3 [b]	3386.0	9^-	8^-	144.1(4.5)	2.0(1) [c]	M1
276.7	8247.7	21	20	5.7(0.2)		
286.4	6742.7	17	16^+	19.5(0.6)		$\Delta J = 1$[d]
298.7	6976.7	16^+	16^+	2.9(0.1)		
302.5 [a]	5047.3	12	12^+	14.1(0.6)		
318.6 [b]	4292.3	11^-	10^-	13.9(0.5)		M1
345.3	6111.1	16	15	14.2(0.5)		
350.9	5765.7	15	15	15.0(0.6)		
351.5	4895.9	14	13^-	29.5(1.2)		
352.4	5513.2	(16)	15	7.2(0.5)		
384.7	7127.4	18	17	24.0(0.8)		$\Delta J = 1$[d]
387.1 [a]	5132.4	13	12^+	3.7(0.3)		E1
396.4 [b]	4370.1	11^-	10^-	5.2(0.3)		M1
408.1	8655.8	(22)	21	9.0(0.3)		
428.3	7404.9	18^+	16^+	54.5(1.8)	1.07(4) [c]	E2
438.5 [b]	3824.8	10^+	9^-	62.7(2.0)	1.6(1) [c]	E1
459.7	7114.4	(18)	17	1.3(0.2)		
491.4 [b]	2911.9	7^-	6^+	4.4(0.4)		E1
499.3	7626.7	19	18	13.4(0.5)		$\Delta J = 1$[d]
506.6 [a]	5047.3	12	11^+	25.8(0.9)		$\Delta J = 1$
539.9 [b]	2911.9	7^-	7^-	68.0(6.8)		M1
543.5	6654.7	17	16	18.9(0.7)		
543.8	9084.6	22	21	32.9(1.1)		

E_γ (keV)	E_i (keV)	J_i^π	J_f^π	I_γ	R_{DCO}	Multip.
557.4	8540.7	21	20^+	32.6(1.1)		
564.3	8547.3	22	20^+	5.0(0.4)		
578.3	7983.1	20^+	18^+	106.8(3.3)	0.97(4) f)	E2
587.8 b)	3973.7	10^-	9^-	17.8(1.0)		M1
620.9	8247.7	21	19	7.2(0.3)		E2 d)
628.2 b)	2418.9	6^+	4^+	4.3(0.5)		E2
631.8 b)	2415.8	4^-	3^-	0.3(0.5)		M1
634.4	9457.1	23	22^+	20.1(0.9)	1.7(1) g)	$\Delta J = 1$
676.7 a)	5221.3	14^-	13^-	64.6(2.0)		M1
702.7	13152.6	(29)	(28^+)	6.1(0.2)		
715.8 b)	4540.7	11^+	10^+	25.5(1.2)		M1
726.7	7404.9	18^+	16^+	18.1(0.6)		E2
740.5 b)	3112.6	8^-	7^-	109.6(3.6)		M1
766.9 b)	766.9	2^+	0^+	0.0(1.0)		E2
815.1	9899.9	24^+	22	40.9(1.3)		
817.1	10274.3	25	23	23.2(0.9)	1.1(1) g)	E2
839.7	8822.7	22^+	20^+	68.4(2.2)	1.02(6) e)	E2
843.2	7971.0	20	18	10.0(1.0)		E2 d)
860.9 b)	3973.7	10^-	8^-	18.4(1.2)		E2
861.2	11904.2	(27)	26^+	7.5(0.4)		
905.4 b)	3324.3	8^+	6^+	9.6(0.7)		E2
906.4 b)	4292.3	11^-	9^-	74.7(2.5)		E2
907.8	10807.7	(26^+)	24^+	10.0(1.0)		
909.0	6678.0	16^+	14^+	8.5(0.6)		E2
910.7	9457.1	23^+	22	3.9(0.3)		
919.8 b)	4744.9	12^+	10^+	76.0(2.5)		E2
924.3	6976.7	16^+	(15)	14.4(0.5)		
945.7	7404.9	18^+	16^+	10.9(0.4)		E2
951.9	5696.8	14^+	12^+	33.4(1.2)	1.2(1) c)	E2
981.6	6678.0	16^+	14^+	3.9(0.3)		E2
983.9 b)	4370.1	11^-	9^-	18.8(1.0)		E2
1017.1 b)	1784.0	3^-	2^+	2.4(0.9)		E1
1022.0 b)	1790.0	4^+	2^+	15.7(1.0)		E2
1023.4	5768.6	14^+	12^+	17.0(0.8)		E2

Table A.2b: Table A.2 (Continued).

E_γ (keV)	E_i (keV)	J_i^π	J_f^π	I_γ	R_{DCO}	Multip.
1041.5	6456.3	16^+	15	24.9(0.9)		$\Delta J = 1$ d)
1055.8	11330.1	27	25	21.3(0.8)	1.2(2) f)	E2
1077.5	9899.9	24^+	22^+	32.2(1.1)	1.0(1) e)	E2
1143.0	11042.9	26^+	24^+	11.8(0.5)	1.1(2) g)	M1
1222.4	12552.5	(29)	27	11.8(0.5)		
1248.4	13152.6	(29)	(27)	7.6(0.3)		
1279.8	6976.7	16^+	14^+	17.0(0.7)	1.1(2) f)	E2
1307.5 a)	4969.0	11^+	10^+	1.1(3.3)		$\Delta J = 1$
1324.0	12131.8	(28^+)	(26^+)	7.5(0.5)		
1407.0	12449.9	(28^+)	26^+	6.5(0.3)		E2
1494.1	6654.7	17	15	18.0(0.6)	0.8(2) h)	E2

a) Placement and ΔJ from [Lac 84].
b) Placement and ΔJ^π from [Lac 84].
c) Gate on 919.8 keV transition.
d) See Table A.3.
e) Gate on 578.8 keV transition.
f) Gate on 428.3 keV transition.
g) Gate on 839.7 keV transition.
h) Gate on 252.4 keV transition.

Table A.2c: Table A.2 (Continued).

E_{gate} (keV)	E_γ (keV)	$\mathcal{R}$	ΔJ
428	634	0.54(9)	1
	740	0.52(6)	1
	840	1.08(8)	2
	1280	1.1(2)	2
286	385	0.58(4)	(1)
	408	0.52(8)	(1)
	421	0.4(1)	(1)
	499	0.46(5)	(1)
	507	0.60(9)	(1)
	621	0.8(1)	(2)
	844	0.9(2)	(2)
	1042	0.48(6)	(1)

Table A.3: Ratio $\mathcal{R}$ of counts in peak E_γ measured at ±37° to counts at ±79° in spectra gated by detection of E_{gate} at ±37°, and known (proposed) ΔJ for E_γ. Gamma-ray energies are approximate.

Appendix B.
Background Subtraction

Modern subatomic physics experiments are typically designed to study processes whose cross-sections are extremely small compared to the total interaction yield of the selected reactions. This is especially true of high energy physics, where processes with picobarn cross-sections must be studied in the background of millibarn scatterings. In fact, characterization of background levels arising from false triggers, cosmic rays and the like comprise the bulk of the intellectual effort in the design and analysis of contemporary high-energy physics experiments. As modern γ–ray detector arrays become more sophisticated and sensitive, it is similarly necessary to develop reliable, reproducible methods for evaluating the contribution of background events to coincidence histograms. It is customary in γ–ray studies to subtract this estimated background level from the histograms prior to rigorous analysis. The resulting data sets (spectra, coincidence matrices, etc.) are referred to as "background subtracted." In this Appendix, a method for evaluating the global background associated with a high-spin experiment is presented for application to high-fold coincidence histograms.

B.1. The Global Operator Method

Following a scheme initially proposed by Palameta [Pal 95], background levels in arbitrary high-fold γ^n coincidence data sets may be evaluated and subtracted by the use of a background operator Φ. This elegant, simple procedure is an approximation which makes use of a normalized, smooth background shape.

B.1.1 Origin of the "Smooth" Background

As was discussed earlier, the dominant source of background is the false energy measurements due to Compton scattering and annihilation photon escape, which will give a feature known as a "Compton tail." In a typical heavy-ion reaction, part of the background will take the shape of Compton tails from the γ-rays emitted by the residual nucleus. In principle the shape of the background will depend on the exact decay path taken, but in a typical high-spin experiment with a γ-ray multiplicity $K \sim 30$, and with hundreds of possible transitions and thousands of possible decay paths, it a suitable approximation to assume that the Compton tails will have a smooth shape which is largely independent of the details of a specific event or decay path. Even from one residual nucleus to another, the shape of this background source should not be substantially different, since all the residual nuclei from a given compound nucleus will have roughly the same level densities and hence transition energies. A closely related but significantly less important source of background comes from Compton scattering of γ rays off of material inside the array, *e.g.* from the target frame or chamber, beam line, or Ge crystal housing. The energy spectrum of the scattered γ rays will again add up to form a smoothly varying background level.

Another source of background which varies smoothly with energy is the transitions of the E2 continuum (the E2 bump) and E1 statistical regimes. The individual γ rays of this continuum are too weak to be resolved individually, but altogether they form a broad distribution. In an experiment which focuses on discrete line spectroscopy, these radiations are themselves often considered to be background. The intensity of the E2 bump depends on the temperature of the residual nucleus following particle evaporation. Consequently, the E2 bump shape may differ dramatically between two nuclei populated by different particle evaporation channels from the same compound system. The difference in E2 continuum between reaction channels may be modeled by the method described in [Rad 95b], but it is often sufficient to treat the E2 bump in an average way as part of the "smooth" background.

The final somewhat "smooth" background we will consider is the neutron bump. When the neutrons produced in the heavy-ion reaction enter the germanium counters or its shield, it may inelastically scatter off of a germanium nucleus. The Ge nucleus recoils after the reaction, and it decelerates by scattering off of the electrons in the detector material, which means that the recoil energy is converted to charge carriers. Furthermore the excited Ge nucleus emits a γ ray, *e.g.* 691 keV from ^{72}Ge and 596 keV from ^{74}Ge. If this γ ray is fully absorbed within the same detector as it originated, the result is a pulse height corresponding to the sum of Ge nucleus recoil energy and the γ ray itself. Because the Ge nucleus is recoiling, the emitted γ ray will be Doppler shifted. The overall result in the γ-ray spectrum is a broadened peak shifted up in energy from the rest-frame germanium γ-ray energy The standard Doppler correction which is normally applied for recoiling residual nuclei will also disperse these counts into a broad bump.

Figure B.1.1 shows the estimated shape of a smooth background for a typical heavy-ion reaction, identifying the E2 and Ge(n,n'γ) contributions. Although this could be evaluated in detail with Monte-Carlo simulations of the detector array, it is customary to estimate this level manually (as was done in this case), that is, by "drawing" a smooth curve under the spectrum. In the following discussion of background subtraction, this curve will be referred to as the (not normalized) smooth background as a function of channel number, ϕ'_i.

B.1.2 Gating on γ rays and the Normalized Smooth Background ϕ

The application of the smooth background may be best introduced by beginning with a discussion of the traditional methods of background subtraction of gates. Consider a gate on a peak E_x which corresponds to a set of ADC or histogram channels $\mathcal{G}$, as shown in Figure B.1.2. The resulting spectrum or sub-set of data $F^{\mathcal{G}}$ will contain events which were truly in coincidence with the photopeak

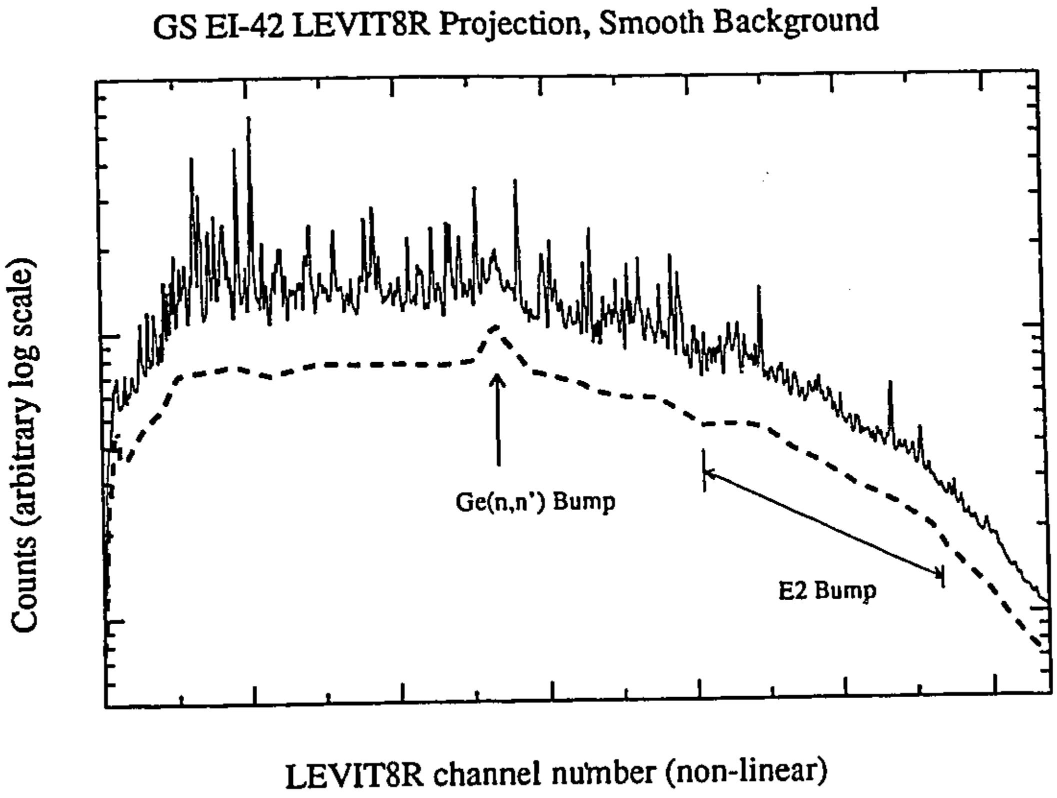

Figure B.1.1: Smooth γ ray background used in LEVIT8R analysis of EI-43 GAMMASPHERE ^{142}Sm experiment. Solid line is projection histogram (non-linear energy vs. channel dispersion) of γ rays from 70 to 1850 keV. Dashed line is smooth background (multiplied by $\frac{2}{3}$ for clarity), with E2 bump and germanium (n,n'γ) components identified.

E_x, but also events "under" the peak which correspond to energy measurements in the smooth background. One straightforward way to estimate the background under the photopeak is to gate on a set of background channels $\mathcal{B}$ which are near $\mathcal{G}$ but which themselves do not contain any discrete photopeaks. It is assumed that the background will be a sufficiently slowly varying function of gating channel number that the sub-data-set $F^{\mathcal{B}}$ gated by channels $\mathcal{B}$ will be a good representation of the

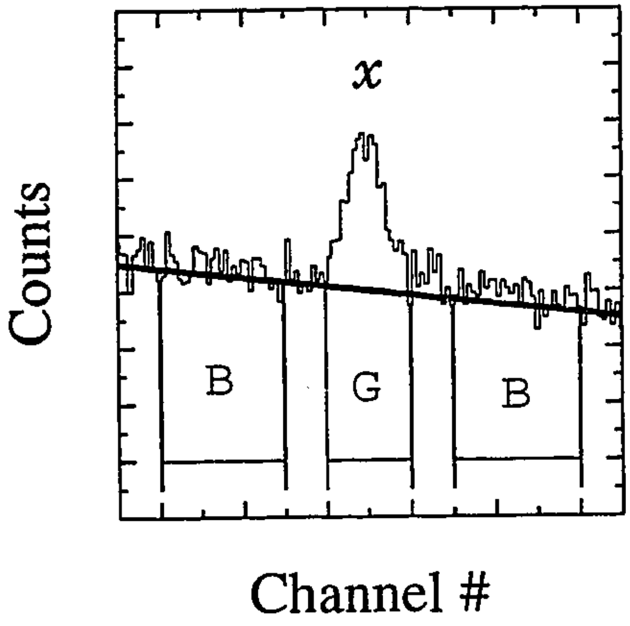

Figure B.1.2: Schematic of gates and smooth ϕ' function for background subtraction.

actual events where a γ-ray from a source other than the photopeak E_x satisfied the gate $\mathcal{G}$. The spectrum truly in coincidence with the photopeak E_x is then given by $\mathcal{F}^{\mathcal{G}} = F^{\mathcal{G}} - F^{\mathcal{B}}$.

A modification of this method may be applied when the number of channels in the background set $\mathcal{B}$ is not equal to the number of channels in the gate set $\mathcal{G}$. Then the background subtracted spectrum is then

$$\mathcal{F}^{\mathcal{G}} = F^{\mathcal{G}} - kF^{\mathcal{B}}, \tag{B.1.1}$$

where k is a normalization factor which ensures that the number of counts removed by the $F^{\mathcal{B}}$ term equals the number of background counts which satisfied the gate $\mathcal{G}$. This is where the smooth background function sees its first application. The number of background counts in $F^{\mathcal{G}}$ is approximately $\sum_{i\in\mathcal{G}} \phi'_i$, while the number of counts in the background spectrum will be approximately $\sum_{i\in\mathcal{B}} \phi'_i$, and k is just the ratio of these two numbers.

The next level of approximation is the assumption that a universal set of background channels $\mathcal{B}$ exists for any gate $\mathcal{G}$. In this case the background spectrum $F^{\mathcal{B}}$ will be the same for all gating conditions. At this point it is convenient to define the normalized smooth background function,

$$\phi_i \equiv \frac{\phi'_i}{\sum\limits_{i\in\mathcal{B}(x)} \phi'_i} \tag{B.1.2}$$

Immediately it can also be seen that this function will give the normalization constant k for a given gate list, so that

$$\mathcal{F}^{\mathcal{G}} = F^{\mathcal{G}} - \left(\sum_{i\in\mathcal{B}(x)} \phi_i \right) F^{\mathcal{B}}. \tag{B.1.3}$$

The discussion to this point has been sufficiently general that F could correspond to any arbitrary measurement in coincidence with γ rays, *e.g.* multiplicity, charged particle spectra, conversion electron spectra, etc. What follows will apply specifically to γ^n coincidence histograms which are symmetrical under the permutation of indices, *e.g.* $M_{ij} = M_{ji}$.

B.1.3 Background Operator in γ^n Coincidence Histograms

If the data set of interest is a high-fold γ^n coincidence histogram $F^n_{ijkl\ldots}$, then the exercise of gating $i \in x$ produces a lower-dimensional data set $F^{(x)n-1}_{jkl\ldots}$, the simplest example being that a gate on a coincidence matrix M_{ij} yields a spectrum,

$$F^x_j = \sum_{i\in x} M_{ij}.$$

A spectrum which contains only counts which were truly in coincidence with the photopeak at E_x is the "gate-corrected" spectrum,

$$\mathcal{F}^x_j = F^x_j - \left(\sum_{j'\in x} \phi_{j'}\right) P^B_j \tag{B.1.4}$$

where

$$P^B_j = \sum_{i\in B} M_{ij} \tag{B.1.5}$$

is a "projection" spectrum over the wide range of universal background channels. The spectrum $\mathcal{F}^x_j$ will contain counts which were truly in coincidence with the photopeak at E_x. This spectrum itself, however, will contain the same smooth background as the one-dimensional projection spectrum, since the photopeaks in coincidence with E_x will have Compton tails, etc. If instead of a matrix, the gate x was placed on one dimension of a triple-coincidence cube histogram C_{ijk}, then we will be left with a matrix,

$$\mathcal{M}^x_{jk} = M^x_{jk} - \phi_x M^B_{jk} \tag{B.1.6}$$

where M^x is a matrix of double-coincidences gated by the photopeak at E_x, M^B is a matrix gated on the background, and the subscript x on ϕ_x is a shorthand notation for a sum over the gate list x. To take a second gate on E_y to produce a double-gated spectrum, the smooth component under the photopeak at y must be corrected,

$$\mathcal{F}^{xy}_k = \sum_{j\in y} \mathcal{M}^x_{jk} - \phi^x_y \sum_{j\in B} \mathcal{M}^x_{jk}, \tag{B.1.7}$$

where ϕ^x is the new normalized smooth background for the matrix $\mathcal{M}$, which may not necessarily have the same shape as ϕ.

For both $\mathcal{F}^x$ and $\mathcal{F}^{xy}$, a final step may be to remove the smooth background which arises from the photopeaks which were truly in coincidence with the gating transitions, as demonstrated for $\mathcal{F}^x$,

$${}^*F^x_j = \mathcal{F}^x_j - \left(\sum_{j'\in B} \mathcal{F}^x_{j'}\right) \phi^x_j \tag{B.1.8}$$

which by the normalization condition for ϕ would result in a spectrum with an average of zero counts in the background region $\mathcal{B}$. One can combine Eqs. (B.1.4) and (B.1.8) to write

$$\begin{aligned}
{}^*F_j^x &= \sum_{i\in x}\left(M_{ij} - \phi_i \sum_{i'\in\mathcal{B}} M_{i'j} - \phi_j \sum_{j'\in\mathcal{B}}\left(M_{ij'} - \sum_{i'\in\mathcal{B}} M_{i'j'}\right)\right) && (B.1.9a)\\
&= \sum_{i\in x}\left(M_{ij} - \phi_i P_j^{\mathcal{B}} - \phi_j P_i^{\mathcal{B}} + \phi_i\phi_j S^{\mathcal{B}\mathcal{B}}\right) && (B.1.9b)\\
&= \sum_{i\in x}\left(1 - \phi_i \sum_{i'\in\mathcal{B}} - \phi_j \sum_{j'\in\mathcal{B}} + \phi_i\phi_j \sum_{i'\in\mathcal{B}}\sum_{j'\in\mathcal{B}}\right) M_{ij} && (B.1.9c)\\
&= \sum_{i\in x} {}^*M_{ij}. && (B.1.9d)
\end{aligned}$$

If the background is, for the most part, uncorrelated, that is, if ϕ_i is independent of j and vice versa, then Eq. (B.1.9a) is a very good estimate of the background subtraction appropriate for this data set. Eq. (B.1.9b) has been re-organized to take advantage of the definition of $P^{\mathcal{B}}$ in Eq. (B.1.5), and a new definition $S^{\mathcal{B}\mathcal{B}} = \sum_{i,j\in\mathcal{B}} M_{ij}$. Eq. (B.1.9b) is exactly the same as the Palameta-Waddington background subtraction method [PW 85]. In Eq. (B.1.9c) it is implied that the sum over a primed index is independent of, and is performed before, any operation involving an unprimed index, and that the primed index should be used in M_{ij} while that sum is performed.

If we now look at Eqs. (B.1.9c) and (B.1.9d) without the gating condition, we find

$$\begin{aligned}
{}^*M_{ij} &= \left(1 - \phi_i \sum_{i'\in\mathcal{B}} - \phi_j \sum_{j'\in\mathcal{B}} + \phi_i\phi_j \sum_{i'\in\mathcal{B}}\sum_{j'\in\mathcal{B}}\right) M_{ij}\\
&= \left(1 - \phi_i \sum_{i'\in\mathcal{B}}\right)\left(1 - \phi_j \sum_{j'\in\mathcal{B}}\right) M_{ij} && (B.1.10)\\
&= (1 - \Phi_i)(1 - \Phi_j)\, M_{ij}
\end{aligned}$$

where we have introduced the background operator,

$$\Phi_\sigma = \phi_\sigma \sum_{\sigma'\in\mathcal{B}} . \qquad (B.1.11)$$

This operator essentially calculates the background along any index $\sigma = i, j, k \ldots$, so the expression for a subtracted γ^n histogram of arbitrary coincidence fold n is given simply by

$$^{*}H_{ijk\ldots} = \prod_{\sigma=ijk\ldots} (1 - \Phi_\sigma) H_{ijk\ldots}.$$

For example, in a triple-coincidence cube,

$$\begin{aligned} ^{*}C_{ijk} &= (1-\Phi_i)(1-\Phi_j)(1-\Phi_k)C_{ijk} \\ &= (1 - \Phi_i - \Phi_j - \Phi_k + \Phi_i\Phi_j + \Phi_i\Phi_k + \Phi_j\Phi_k - \Phi_i\Phi_j\Phi_k)C_{ijk}. \end{aligned}$$

The single Φ operators will result in terms of the form ϕM^{B}, where M^{B}_{ij} is a matrix in coincidence with one background γ ray. The $\Phi\Phi$ operators give $\phi\phi P^{BB}$, where P^{BB}_i is a spectrum in coincidence with two background gamma rays. Finally, the triple-Φ term is $\phi\phi\phi S^{BBB}$, where S^{BBB} is the total number of triple-background counts. This gives

$$\begin{aligned} ^{*}C_{ijk} =& C_{ijk} \\ & - \phi_i \sum_{i' \in B} C_{i'jk} - \phi_j \sum_{j' \in B} C_{ij'k} - \phi_k \sum_{k' \in B} C_{ijk'} \\ & + \phi_i\phi_j \sum_{i',j' \in B} C_{i'j'k} + \phi_i\phi_k \sum_{i',k' \in B} C_{i'jk'} + \phi_j\phi_k \sum_{j',k' \in B} C_{ij'k'} \\ & - \phi_i\phi_j\phi_k \sum_{i',j',k' \in B} C_{i'j'k'} \end{aligned}$$

which reduces to

$$\begin{aligned} ^{*}C_{ijk} =& C_{ijk} \\ & - \left(\phi_i M^{B}_{jk} + \phi_j M^{B}_{ik} + \phi_k M^{B}_{ij}\right) \\ & + \left(\phi_i\phi_j P^{BB}_k + \phi_i\phi_k P^{BB}_j + \phi_j\phi_k P^{BB}_i\right) \\ & - \phi_i\phi_j\phi_k S^{BBB}. \end{aligned} \qquad (B.1.12)$$

This is the result that you would get by combining Eqs. (B.1.7) and (B.1.8) in the same manner as was done for the double-coincidence case, and it is can be shown that if B is the entire range of channels in the histogram, this is exactly the same expression as that used in [Rad 95b]. If m is the number of channels in $\mathcal{B}$, then one can estimate the order of magnitude of the terms in this expression,

$$\begin{aligned} M_{ij}^{\mathcal{B}} &\sim m C_{ijk}, \\ P_i^{\mathcal{B}\mathcal{B}} &\sim m^2 C_{ijk}, \\ S^{\mathcal{B}\mathcal{B}\mathcal{B}} &\sim m^3 C_{ijk}, \\ \phi_i &\sim \left(m^{-1}\right). \end{aligned}$$

In other words, all of the terms are roughly the same size. In fact, in a pure background region (*i.e.*, ijk all $\in \mathcal{B}$), they would all be the same, and hence the sum would be zero within statistical fluctuations.

The operator method becomes especially powerful in still higher-fold coincidence data sets F^n, such as quadruple-coincidences. Rather than follow the tedious procedure in Eqs. (B.1.4) through (B.1.8) for three gating levels on an 4-dimensional coincidence histogram (hypercube) $F^4 = H$, one may start with

$$^*H_{ijkl} = (1 - \Phi_i)(1 - \Phi_j)(1 - \Phi_k)(1 - \Phi_l)\, H_{ijkl}.$$

Immediately one sees that there will be one $H^4 = H$ term, four $-\phi F^3 = -\phi C^{\mathcal{B}}$ terms, six $\phi\phi F^2 = \phi\phi M^{\mathcal{B}\mathcal{B}}$ terms, four $-\phi\phi\phi F^1 = -\phi\phi\phi P^{\mathcal{B}\mathcal{B}\mathcal{B}}$ terms, and one $\phi\phi\phi\phi F^0 = \phi\phi\phi\phi S^{\mathcal{B}\mathcal{B}\mathcal{B}\mathcal{B}}$ term in the subtracted data set,

$$\begin{aligned} ^*H_{ijkl} &= H_{ijkl} \\ &- \left(\phi_i C_{jkl}^{\mathcal{B}} + \phi_j C_{ikl}^{\mathcal{B}} + \phi_k C_{ijl}^{\mathcal{B}} + \phi_l C_{ijk}^{\mathcal{B}}\right) \\ &+ \Big(\phi_i\phi_j M_{kl}^{\mathcal{B}\mathcal{B}} + \phi_i\phi_k M_{jl}^{\mathcal{B}\mathcal{B}} + \phi_i\phi_l M_{jk}^{\mathcal{B}\mathcal{B}} + \\ &\quad \phi_j\phi_k M_{il}^{\mathcal{B}\mathcal{B}} + \phi_j\phi_l M_{ik}^{\mathcal{B}\mathcal{B}} + \phi_k\phi_l M_{ij}^{\mathcal{B}\mathcal{B}}\Big) \\ &- \left(\phi_i\phi_j\phi_k P_l^{\mathcal{B}\mathcal{B}\mathcal{B}} + \phi_i\phi_j\phi_l P_k^{\mathcal{B}\mathcal{B}\mathcal{B}} + \phi_i\phi_k\phi_l P_j^{\mathcal{B}\mathcal{B}\mathcal{B}} + \phi_j\phi_k\phi_l P_i^{\mathcal{B}\mathcal{B}\mathcal{B}}\right) \\ &+ \phi_i\phi_j\phi_k\phi_l S^{\mathcal{B}\mathcal{B}\mathcal{B}\mathcal{B}}. \end{aligned} \qquad (\mathcal{B}.1.13)$$

For quintuple-coincidences, it follows that

$$\begin{aligned}{}^{*}Q_{ijklm} =&Q_{ijklm}\\ &-\left(\phi_i H^{B}_{jklm}+\ldots\right)\text{(5 combinations)}\\ &+\left(\phi_i\phi_j C^{BB}_{klm}+\ldots\right)\text{(10 combinations)}\\ &-\left(\phi_i\phi_j\phi_k M^{BBB}_{lm}+\ldots\right)\text{(10 combinations)}\\ &+\left(\phi_i\phi_j\phi_k\phi_l P^{BBBB}_{m}+\ldots\right)\text{(5 combinations)}\\ &-\phi_i\phi_j\phi_k\phi_l\phi_m S^{BBBBB}.\end{aligned} \qquad (B.1.14)$$

Immediately there would appear to be a technical problem associated with background subtraction of high-fold data sets. To fully characterize the background of an n-fold coincidence data set, you need to know the background-gated $(n-1)$-fold subset and lower-dimension projections. The resources required to store the cube background for a quadruples data set, or the hypercube background for a quintuples data set, are still somewhat too expensive for on-line storage. When one is interested in studying only a small fraction of the high-fold data set, for example, sums-of-triple-gates spectra on quadruple coincidences very little of the information in the background subsets will ever actually be required. The next section discusses simplifications of Eqs. (B.1.12), (B.1.13) and (B.1.14) for specialized applications where it is not necessary to know the contents of the entire $n-1$-fold background set.

B.2. Background Subtraction of Gated Spectra

B.2.1 One $n-1$-gated spectrum

Consider as a first example the triple-coincidence case of a double-gated spectrum on transitions E_y, E_z,

$$F_i^{yz} = \sum_{j\in y, k\in z} C_{ijk}. \tag{B.2.1}$$

The background-subtracted version then is

$$\begin{aligned} {}^*F_i^{yz} &= \sum_{j\in y, k\in z} {}^*C_{ijk} \\ &= \sum_{j\in y, k\in z} \begin{pmatrix} C_{ijk} \\ -\phi_i M_{jk}^{\mathcal{B}} - \phi_j M_{ik}^{\mathcal{B}} - \phi_k M_{ij}^{\mathcal{B}} \\ +\phi_i\phi_j P_k^{\mathcal{BB}} + \phi_i\phi_k P_j^{\mathcal{BB}} + \phi_j\phi_k P_i^{\mathcal{BB}} \\ -\phi_i\phi_j\phi_k S^{\mathcal{BBB}} \end{pmatrix} \end{aligned} \tag{B.2.2}$$

Following the notation $\phi_x \equiv \sum_{i\in x}\phi_i$, some of the terms may be re-written,

$$\begin{aligned} &\phi_y \sum_{k\in z} M_{ik}^{\mathcal{B}} \\ =&\phi_y \sum_{j'\in\mathcal{B}} \sum_{k\in z} C_{ij'k} \\ =&\phi_y F_i^{z\mathcal{B}}, \end{aligned} \tag{B.2.3}$$

where $F_i^{z\mathcal{B}}$ is the spectrum produced by double-gating on triple-coincidence data with one gate on the transition E_z and the second on the background channels $\mathcal{B}$. A permutation of variables yields the same result for the $\phi_z \sum_{j\in y} M_{ij}^{\mathcal{B}}$ term. If one defines $F^{\mathcal{BB}} \equiv P^{\mathcal{BB}}$, then the four terms which do not contain ϕ_i as a factor may be re-written

$$\mathcal{F}_i^{yz} = F_i^{yz} - \phi_y F_i^{z\mathcal{B}} - \phi_z F^{y\mathcal{B}} + \phi_y\phi_z F_i^{\mathcal{BB}}, \tag{B.2.4}$$

which is exactly the same as Eq. (B.1.7) for the gate-corrected spectrum. We could equivalently arrive at this result from the operator notation,

$$\begin{aligned}
\mathcal{F}_i^{yz} =& \sum_{j\in y}\sum_{k\in z}(1-\Phi_j)(1-\Phi_k)\,C_{ijk} \\
=& \sum_{j\in y}\sum_{k\in z}\left(C_{ijk}-\phi_j\sum_{j'\in\mathcal{B}}C_{ij'k}-\phi_k\sum_{k'\in\mathcal{B}}C_{ijk'}+\phi_j\phi_k\sum_{j',k'\in\mathcal{B}}C_{ij'k'}\right) \\
=& \sum_{j\in y,k\in z}C_{ijk}-\phi_y\sum_{j'\in\mathcal{B},k\in z}C_{ij'k}-\phi_z\sum_{k'\in\mathcal{B},j\in y}C_{ijk'}+\phi_y\phi_z\sum_{j',k'\in\mathcal{B}}C_{ij'k'} \\
=& F_i^{yz}-\phi_y F_i^{z\mathcal{B}}-\phi_z F^{y\mathcal{B}}+\phi_y\phi_z F_i^{\mathcal{B}\mathcal{B}}.
\end{aligned}$$

Then to perform the full subtraction procedure,

$$\begin{aligned}
{}^{*}F_i^{yz} &= \sum_{j\in y}\sum_{k\in z}(1-\Phi_i)(1-\Phi_j)(1-\Phi_k)\,C_{ijk} \\
&= (1-\Phi_i)\sum_{j\in y}\sum_{k\in z}(1-\Phi_j)(1-\Phi_k)\,C_{ijk} \\
&= (1-\Phi_i)\,\mathcal{F}_i^{yz} \\
&= \mathcal{F}_i^{yz}-\phi_i\sum_{i'\in\mathcal{B}}\mathcal{F}_{i'}^{yz}.
\end{aligned} \qquad (B.2.5)$$

A triple-gated (E_y, E_z, E_w) spectrum may be evaluated in the same way, by first calculating the gate-corrected spectrum

$$\begin{aligned}
\mathcal{F}_i^{yzw} =& \sum_{j\in y}\sum_{k\in z}\sum_{l\in w}(1-\Phi_j)(1-\Phi_k)(1-\Phi_l)\,H_{ijkl} \\
=& \sum_{j\in y}\sum_{k\in z}\sum_{l\in w}(1-\Phi_j-\Phi_k-\Phi_l+\Phi_j\Phi_k+\Phi_j\Phi_l+\Phi_k\Phi_l-\Phi_j\Phi_k\Phi-l)\,H_{ijkl} \\
=& F^{wzy}-\phi_y F^{zw\mathcal{B}}-\phi_z F^{yw\mathcal{B}}-\phi_w F^{yz\mathcal{B}} \\
&+\phi_y\phi_z F^{w\mathcal{B}\mathcal{B}}+\phi_y\phi_w F^{z\mathcal{B}\mathcal{B}}+\phi_z\phi_w F^{y\mathcal{B}\mathcal{B}}-\phi_y\phi_z\phi_w F^{\mathcal{B}\mathcal{B}\mathcal{B}},
\end{aligned} \qquad (B.2.6)$$

where some tedious algebra has been left out. The full subtraction is then simply

$$\begin{aligned}
{}^{*}F_i^{yzw} &= (1-\Phi_i)\,\mathcal{F}_i^{yzw} \\
&= \mathcal{F}_i^{yzw}-\phi_i\sum_{i'\in\mathcal{B}}\mathcal{F}_{i'}^{yzw}.
\end{aligned} \qquad (B.2.7)$$

So one can fully subtract an individual triple-gated spectrum given the raw (unsubtracted) triple-gated spectrum, three spectra which are double-gated on each pair of triple-gating transitions and single-gated on the background, three spectra which are single-gated on each transition and double-gated on the background, and one spectrum which is triple-gated on the background. The result for a quadruple-gated spectrum on quintuple-coincidence data is obvious,

$$\begin{aligned}
\mathcal{F}_i^{xyzw} =& F_i^{xyzw} \\
& - \phi_x F^{yzw\mathcal{B}} \ldots \qquad \text{(4 permutations)} \\
& + \phi_x \phi_y F^{zw\mathcal{B}\mathcal{B}} \ldots \qquad \text{(6 permutations)} \\
& - \phi_x \phi_y \phi_x F^{w\mathcal{B}\mathcal{B}\mathcal{B}} \ldots \quad \text{(4 permutations)} \\
& + \phi_x \phi_y \phi_z \phi_w F^{\mathcal{B}\mathcal{B}\mathcal{B}\mathcal{B}} \qquad (B.2.8) \\
{}^*F_i^{xyzw} =& \mathcal{F}_i^{xyzw} - \phi_i \sum_{i'} \mathcal{F}_{i'}^{xyzw} \qquad (B.2.9)
\end{aligned}$$

In the present work, gates on the superdeformed band peaks were optimized in triple-coincidences, and then the necessary peak-peak-peak, peak-peak-background, peak-background-background, and background-background-background gated spectra were produced from quadruple-coincidence data in the same replay task. One disadvantage of working with the γ^4 data in this manner is that any time one would want to change the transition gates or background gate list, it would be necessary to perform the replay again. Through judicious choice of parameters, this did not turn out to be necessary. The clear advantage is that it was never necessary to generate and store a background-gated cube. When quintuple-coincidence data are available and useful, this will be an even greater concern.

B.2.2 Sums of Gates

Sums of gates have already been demonstrated as a useful tool for enhancing otherwise weak structures. While it is often possible to observe, for example, the transitions of a superdeformed band in one clean gate in doubles or one clean double-gate in triples, it is rarely possible to extract a useful spectrum from a single triple- or quadruple-gate. In these cases one normally has no choice but to use sums of gates spectra. Since superdeformation studies are of such high interest in contemporary nuclear structure, it is worth discussing a useful approximation for the specific case of sums of gates on a long cascade of γ rays.

For a cascade of γ rays $E_x, x = 1, 2 \ldots n$ one assigns a gate set $\mathcal{G}^x$ for each transition. A sum of single-gated spectra from double-coincidence data for each of these gates,

$$F_i^{(1)} = \sum_{x=1}^{n} \sum_{j \in \mathcal{G}^x} M_{ij}$$

could equivalently be written as a sum over a set which is the the union of gating channels for all of these transitions,

$$F_i^{(1)} = \sum_{j \in \mathcal{G}^{(1)}} M_{ij}$$

where

$$\mathcal{G}^{(1)} = \mathcal{G}^{E_1} \cup \mathcal{G}^{E_2} \cup \ldots \cup \mathcal{G}^{E_n}.$$

A set of double-gating channels $\mathcal{G}^{(2)}$ can similarly generated by the union of all double-gating combinations,

$$\begin{aligned} \mathcal{G}^{(2)} = & \left(j \in \mathcal{G}^{E_1}, k \in \mathcal{G}^{E_2}\right) \cup \ldots \cup \\ & \left(j \in \mathcal{G}^{E_y}, k \in \mathcal{G}^{E_z}\right) \cup \ldots \cup \\ & \left(j \in \mathcal{G}^{E_{(n-1)}}, k \in \mathcal{G}^{E_n}\right), \qquad y < z. \end{aligned}$$

The condition $y < z$ ensures that there is no double-counting in the symmetrized data set and that there are no double-gates on the same transition; in other words, the gates are ordered and non-diagonal. Note that the number of elements in $\mathcal{G}^{(2)}$ is less than the number of elements in a set defined simply as the outer product of the gates, *i.e.*, $j \in \mathcal{G}^{(1)}, k \in \mathcal{G}^{(1)}$.

In the expression for the gate-corrected double-gated spectrum,

$$\mathcal{F}_i^{(2)} = \sum_{(jk)\in\mathcal{G}^{(2)}} (1-\Phi_j)(1-\Phi_k)\, C_{ijk}, \qquad (B.2.10)$$

the first term will reduce trivially to $F_i^{(2)}$. The remaining terms can be written in a somewhat more transparent manner if the sum over (jk) could be written as independent sums over j and k,

$$\sum_{(jk)\in\mathcal{G}^{(2)}} \simeq \kappa \sum_{j\in\mathcal{G}^{(1)}} \sum_{k\in\mathcal{G}^{(1)}} .$$

This corresponds to substituting the outer product of the single-gate lists for the correct double-gate list. This substitution justified by first noting that the goal of this procedure is to *estimate* the background level. If there are no $j-k$ correlations in the smooth component of the background, and if there are no photopeaks in the diagonal $(y = z)$ gates, then the effect of this substitution will simply be to overestimate the background level calculated in this term. This can be seen clearly if one considers the number of individual double-gates available on an n transition band. There are only $n(n-1)/2$ possible ordered, non-diagonal combinations of transitions which contribute to $\mathcal{G}^{(2)}$, compared to a full n^2 if the simple outer product is taken instead. The attenuation factor κ is defined as

$$\kappa = \frac{\sum_{(jk)\in\mathcal{G}^{(2)}} \phi_j\phi_k}{\left(\sum_{j\in\mathcal{G}^{(1)}} \phi_j\right)^2} \simeq \frac{n-1}{2n} \sim \frac{1}{2}$$

to correct for the fact that the independent sum over j and k includes more channels than are in the proper, ordered, non-diagonal double-gate list.

If this "separation of background variables" approximation is applied to all but the first term of the sum-of-double-gates spectrum, then Eq. (B.2.10) becomes approximately

$$\begin{aligned}
\mathcal{F}^{(2)} \simeq & F^{(2)} - \kappa \sum_{j\in\mathcal{G}^{(1)}} \sum_{k\in\mathcal{G}^{(1)}} \left(\phi_j \sum_{j'\in\mathcal{B}} + \phi_k \sum_{k'\in\mathcal{B}} - \phi_j\phi_k \sum_{j',k'\in\mathcal{B}}\right) C_{ijk} \\
= & F^{(2)} \\
& - \kappa \left(\sum_{j\in\mathcal{G}^{(1)}} \phi_j\right)\left(\sum_{k\in\mathcal{G}^{(1)},j'\in\mathcal{B}} C_{ij'k}\right) \\
& - \kappa \left(\sum_{k\in\mathcal{G}^{(1)}} \phi_k\right)\left(\sum_{j\in\mathcal{G}^{(i)},k'\in\mathcal{B}} C_{ijk'}\right) \\
& + \kappa \left(\sum_{j,k\in\mathcal{G}^{(1)}} \phi_j\phi_k\right)\left(\sum_{j',k'\in\mathcal{B}} C_{ij'k'}\right) \\
= & F^{(2)} - 2\kappa\phi^{(1)}F^{(1)\mathcal{B}} + \kappa\left(\phi^{(1)}\right)^2 F^{\mathcal{B}\mathcal{B}}
\end{aligned} \qquad . \qquad (B.2.11)$$

The gate-corrected spectrum, then, is a combination of the raw double-gated spectrum, a spectrum gated once with the 1-D gate list and once with the background, and a spectrum gated twice on the background. Full subtraction can be achieved in same manner as Eq. (B.2.5).

The same sort of approach can be taken with a sum-of-triple-gates spectrum extracted from quadruple-coincidence data. In this case, the sum is over an ordered, non-diagonal triple-gate list $\mathcal{G}^{(3)}$,

$$\begin{aligned}
\mathcal{G}^{(3)} = & \left(j \in \mathcal{G}^{E_1}, k \in \mathcal{G}^{E_2}, l \in \mathcal{G}^{E_3}\right) \cup \ldots \\
& \ldots \cup \left(j \in \mathcal{G}^{E_y}, k \in \mathcal{G}^{E_z}, l \in \mathcal{G}^{E_w}\right) \cup \ldots \\
& \ldots \cup \left(j \in \mathcal{G}^{E_{(n-2)}}, k \in \mathcal{G}^{E_{(n-1)}}, l \in \mathcal{G}^{E_n}\right), \qquad y < z < w,.
\end{aligned}$$

corresponding to $(n)(n-1)(n-2)/6$ combinations of transitions. Once again one starts with the gate-corrected spectrum,

$$\mathcal{F}^{(3)} = \sum_{(jkl)\in\mathcal{G}^{(3)}} (1-\Phi_j)(1-\Phi_k)(1-\Phi_l)H_{ijkl}. \qquad (B.2.12)$$

For the Φ_j term, the sum over $\mathcal{G}^{(3)}$ can be separated into the single-gate list $\mathcal{G}^{(1)}$ over the j index and the double-gate $\mathcal{G}^{(2)}$ over the (k,l) indices,

$$\sum_{(jkl)\in\mathcal{G}^{(3)}} \simeq \kappa_{(2)} \left(\sum_{j\in\mathcal{G}^{(1)}}\right)\left(\sum_{(kl)\in\mathcal{G}^{(2)}}\right).$$

Here there are roughly three times as many elements in the fully ordered sum as there are in the separated sum, so

$$\kappa_{(2)} = \frac{\sum_{(jkl)\in\mathcal{G}^{(3)}} \phi_j\phi_k\phi_l}{\left(\sum_{j\in\mathcal{G}^{(1)}} \phi_j\right)\left(\sum_{(kl)\in\mathcal{G}^{(2)}} \phi_k\phi_l\right)} \simeq \frac{n(n-1)(n-2)/6}{(n)(n)(n-1)/2} = \frac{n-2}{3n} \sim \frac{1}{3}.$$

This gives

$$\kappa_{(2)} \sum_{j\in\mathcal{G}^{(1)}} \sum_{(kl)\in\mathcal{G}^{(2)}} \left(\phi_j \sum_{j'\in\mathcal{B}}\right) H_{ij'kl} = \phi^{(1)} F^{(2)\mathcal{B}},$$

and there will be two terms of the same form for the Φ_k and Φ_l terms. For the rest of the terms in Eq. (B.2.12), $\mathcal{G}^{(3)}$ is decomposed into three sums over $\mathcal{G}^{(1)}$,

$$\sum_{(jkl)\in\mathcal{G}^{(3)}} \simeq \kappa_{(1)} \sum_{j\in\mathcal{G}^{(1)}} \sum_{k\in\mathcal{G}^{(1)}} \sum_{l\in\mathcal{G}^{(1)}}$$

with

$$\kappa_{(1)} = \frac{\sum_{(jkl)\in\mathcal{G}^{(3)}} \phi_j\phi_k\phi_l}{\left(\sum_{j\in\mathcal{G}^{(1)}} \phi_j\right)^3} \simeq \frac{n(n-1)(n-2)/6}{n^3} = \frac{(n-1)(n-2)}{6n^2} \sim \frac{1}{6}.$$

A little bit of straightforward algebra gives

$$\mathcal{F}_i^{(3)} = F_i^{(3)} - 3\kappa_{(2)}\phi^{(1)}F_i^{(2)\mathcal{B}} + 3\kappa_{(1)}\left(\phi^{(1)}\right)^2 F_i^{(1)\mathcal{BB}} - \kappa_{(1)}\left(\phi^{(1)}\right)^3 F_i^{(0)\mathcal{BBB}}. \quad (B.2.13)$$

and the fully-subtracted, sum-of-triple-gates spectrum is

$$^{*}F_i^{(3)} = \mathcal{F}_i^{(3)} - \phi_i \sum_{i'\in\mathcal{B}} \mathcal{F}_{i'}^{(3)}. \quad (B.2.14)$$

So a good approximation to a properly background-subtracted sum-of-triple-gates spectrum can be achieved knowing only the raw triple-gated spectrum, a spectrum double-gated on the band and gated once on the background, a spectrum single-gated on the band and twice on the background, and a spectrum triply-gated on the background.

The prescription and algebra of the separation of variables for a sum-of-quadruple-gates spectrum from quintuple-coincidence data is nearly the same, and the expression is

$$^{*}F_i^{(4)} = \mathcal{F}_i^{(4)} - \phi_i \sum_{i' \in \mathcal{B}} \mathcal{F}_{i'}^{(4)},$$

$$\begin{aligned}
\mathcal{F}_i^{(4)} = & F_i^{(4)} \\
& - 4\kappa_{(3)} \phi^{(1)} F_i^{(3)\mathcal{B}} \\
& + 6\kappa_{(2)} \left(\phi^{(1)}\right)^2 F_i^{(2)\mathcal{B}\mathcal{B}} \\
& - 4\kappa_{(1)} \left(\phi^{(1)}\right)^3 F_i^{(1)\mathcal{B}\mathcal{B}\mathcal{B}} \\
& + \kappa_{(1)} \left(\phi^{(1)}\right)^4 F_i^{(0)\mathcal{B}\mathcal{B}\mathcal{B}\mathcal{B}}
\end{aligned} \tag{B.2.15}$$

with the new attenuation coefficients

$$\begin{aligned}
\kappa_{(1)} = & \frac{\sum_{(ijkl) \in \mathcal{G}^{(4)}} \phi_i \phi_j \phi_k \phi_l}{\left(\sum_{i \in \mathcal{G}^{(1)}} \phi_i\right)^4} \sim \frac{1}{24}, \\
\kappa_{(2)} = & \frac{\sum_{(ijkl) \in \mathcal{G}^{(4)}} \phi_i \phi_j \phi_k \phi_l}{\left(\sum_{(ij) \in \mathcal{G}^{(2)}} \phi_i \phi_j\right) \left(\sum_{k \in \mathcal{G}^{(1)}} \phi_k\right)^2} \sim \frac{1}{12}, \\
\kappa_{(3)} = & \frac{\sum_{(ijkl) \in \mathcal{G}^{(4)}} \phi_i \phi_j \phi_k \phi_l}{\left(\sum_{(ijk) \in \mathcal{G}^{(3)}} \phi_i \phi_j \phi_k\right) \left(\sum_{l \in \mathcal{G}^{(1)}} \phi_l\right)} \sim \frac{1}{4}.
\end{aligned}$$

The beauty of Eqs. (B.2.13) and (B.2.15) is that spectra can be extracted from quadruple- and quintuple-coincidence data sets without explicitly generating a background cube or hypercube. For example, if the data are stored in a sequential list mode, a properly-subtracted spectrum can be generated by merely generating the four (or five) spectra specified in Eqs. (B.2.13) and (B.2.15).

B.2.3 Gated Matrices

The examples in Sect. B.2.2 can equally well be applied to gated matrices. Consider a γ–γ matrix which is generated by double-gating on quadruple-coincidence data with the two transitions E_z and E_w. In operator notation, the fully-subtracted, gated data set is given by

$$\begin{aligned} {}^{*}M_{ij}^{zw} &= \sum_{k\in z}\sum_{l\in w}\left((1-\Phi_i)(1-\Phi_j)(1-\Phi_k)(1-\Phi_l)\,H_{ijkl}\right) \\ &= (1-\Phi_i)(1-\Phi_j)\left(\sum_{k\in z}\sum_{l\in w}(1-\Phi_k)(1-\Phi_l)\right)H_{ijkl}. \end{aligned}$$

Considering the operations over k and l yields a gate-corrected matrix,

$$\begin{aligned} \mathcal{M}_{ij}^{zw} &= \left(\sum_{k\in z}\sum_{l\in w}(1-\Phi_k)(1-\Phi_l)\right)H_{ijkl} \\ &= \sum_{k\in z}\sum_{l\in w}H_{ijkl} \\ &\quad -\sum_{k\in z}\sum_{l\in w}\phi_k\sum_{k'\in B}H_{ijk'l} \\ &\quad -\sum_{k\in z}\sum_{l\in w}\phi_l\sum_{l'\in B}H_{ijkl'} \\ &\quad +\sum_{k\in z}\sum_{l\in w}\phi_k\phi_l\sum_{k',l'\in B}H_{ijk'l'} \\ &= M_{ij}^{zw} - \phi_z M_{ij}^{wB} - \phi_w M_{ij}^{zB} + \phi_z\phi_w M_{ij}^{BB}. \end{aligned}$$

The matrix $\mathcal{M}^{zw}$ corresponds to all γ–γ coincidences which were in double-coincidence with the photopeaks E_z and E_w. Then the final operation, $(1-\Phi_i)(1-\Phi_j)$, removes the smooth background from that matrix.

B.3. The Operator Method in Action

There are some concerns regarding the practical application of the operator method which affect its appropriateness as a model for the background. Throughout the discussion of this method it has been assumed that the smooth background is a function in only one dimension, and that the contributions from multiple non-photopeak coincidences (*e.g.*, background-background events in a matrix) are independent of any correlations in these coincidences and that their shape is well reproduced as the product of the one-dimensional smooth background ϕ. An immediate example of a background source which violates this condition would be a case where a γ ray of energy E_γ scatters from one Ge detector, passes through two sets of anti-Compton shields without interacting, and then is fully absorbed in a second Ge detector. The resulting pulses will be interpreted as a double-γ-ray coincidence by the array, and for a fixed E_γ will appear as a line along $E_x + E_y = E_\gamma$ in the γ–γ coincidence histogram. In such a case, the background-background shape which is currently treated as $\phi_i\phi_i$ might better be modeled by a function in two variables $\phi(i,j)$. At first this may seem to be a fundamental and possibly tragic flaw. However it has been pointed out by Radford [Rad 95b] that in the present method, terms which contain background-gated projection factors, such as M_{ij}^{BB} in the hypercube expression, will already contain such correlations. Hence these terms will largely compensate for deviations from a separable $\phi_i\phi_j$ behavior.

It has been presumed throughout that the coincidence data are symmetrical, *i.e.*, $H_{ijk\ldots} = H_{jik\ldots}\cdots$. For an n-dimensional coincidence data set, a single n-fold coincidence event increments $(n!)$ bins in the histogram corresponding to all possible permutations. Furthermore, a higher m-fold coincidence event must be unpacked into $\binom{m}{n}$ combinations before the $n!$ permutations are taken. This is straightforward for a static data set, *i.e.* a histogram stored on disk. However it is important (and potentially quite time-consuming) to ensure that the permutations and combinations are treated fully symmetrically in gating algorithms which read list-mode data.

Finally there is the question of the choice of smooth background function shape ϕ and channels $\mathcal{B}$. In the present investigations the photopeak density is so high that no subset of channels dispersed throughout the total projection could be assigned as practical background channels which would be suitable under all gating conditions. For the present work, low-fold analyses were performed by selecting the full range of the histogram (matrices and cubes) as the background region and drawing the smooth background to fit the total projection. This is in the spirit of a truly global background applicable in all cases, and is the option recommended in [Rad 95b]. By contrast, the detailed work with quadruple-coincidence data (*i.e.*, triple-gated spectra) was performed with a different $\mathcal{B}$ and ϕ for each band under investigation. After generating a raw triple-gated spectrum for a given band, a ϕ function was drawn to this spectrum and the background channels were assigned as those channels in the energy range of the gates ($\sim 600 - 1600$ keV) which were did not seem to have any photopeaks in them. This is closer to the detailed, fold-by-fold prescription. This choice to deal with triple-coincidence data globally and quadruple-coincidence data locally was empirical. However it can be understood why one might wish to differentiate between the two cases. In double- and triple-coincidence data, the density of photopeaks is still large enough, that any candidate local background regions are still contaminated with counts from proper photopeak measurements. In quadruple-coincidence data the hyper-peaks arising from true four-fold photopeak measurements are sufficiently sparse that a local background becomes meaningful again.

This work provides ample evidence of the application and success of these methods in three- and four-fold coincidence data. The separation-of-background-variables technique for four- and five-fold data have also been tested on data from a commissioning run on EUROGAM phase II. The results, reported in Ref. [HW 95], are summarized here.

The superdeformed yrast band of ^{149}Gd was populated in a ^{124}Sn(^{30}Si,5n) reaction at 162 MeV bombarding energy. The suppressed energies were gain matched off-line and written to tape in a compressed format. In a subsequent replay, high-fold γ-ray coincidence events were unpacked to quadruples and quintuples, and the unpacked events were treated symmetrically by the gating program. Gates were placed on all members of the superdeformed cascade below 1672 keV [Fli 93] except the 712, 808 and 1167 keV members which are well-known doublets. Background channels $\mathcal{B}$ were defined as the energy region from 550 keV to 1950 keV.

The top panel of Figure B.3.1 is the uncorrected sum of triple-gates, which was used as a guide to draw the ϕ' function suitable for quadruples analysis. From this the attenuation coefficients were extracted and the gate-corrected spectrum $\mathcal{F}^{(3)}$ was produced. For the next step to full subtraction, the background channels were selected with the $\mathcal{F}$ spectrum as a guide. The resulting, fully-subtracted triple-gated spectrum is shown in the lower panel of Figure B.3.1. The same steps were followed to perform the subtraction on the quadruple-gated quintuples data, with the unsubtracted and fully subtracted spectra shown in Figure B.3.2. In both figures, the superdeformed band transitions are identified with diamonds, filled for the gating transitions. Crosses identify the locations of transitions which are assigned only to ^{148}Gd. These contaminant peaks do not appear in either the triple- or quadruple-gated fully subtracted spectra, nor are they over-subtracted. The remaining peaks which are eliminated by the full subtraction procedure are transitions between states in ^{149}Gd which are not fed through the decay out of the superdeformed band (see [Fli 95]).

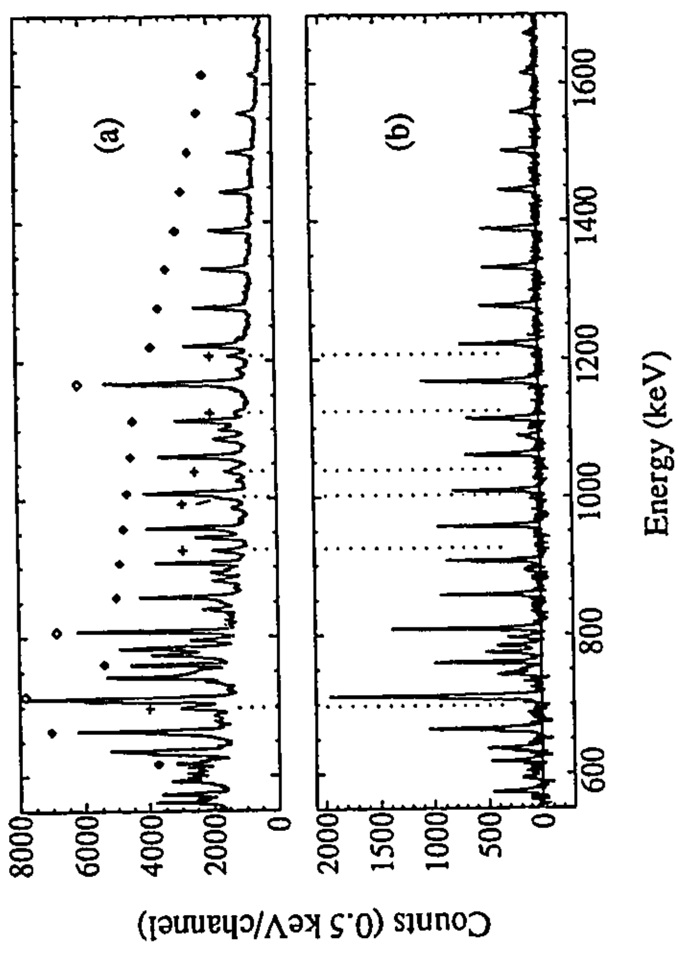

Figure B.3.1:

Partial γ-ray spectra of ^{149}Gd yrast SD band obtained from EUROGAM phase 2 commissioning run quadruple-coincidence data by setting ordered, non-diagonal triple gates on members of band. (a), unsubtracted spectrum $F_i^{(3)}$. (b), fully subtracted spectrum $^*F_i^{(3)}$.

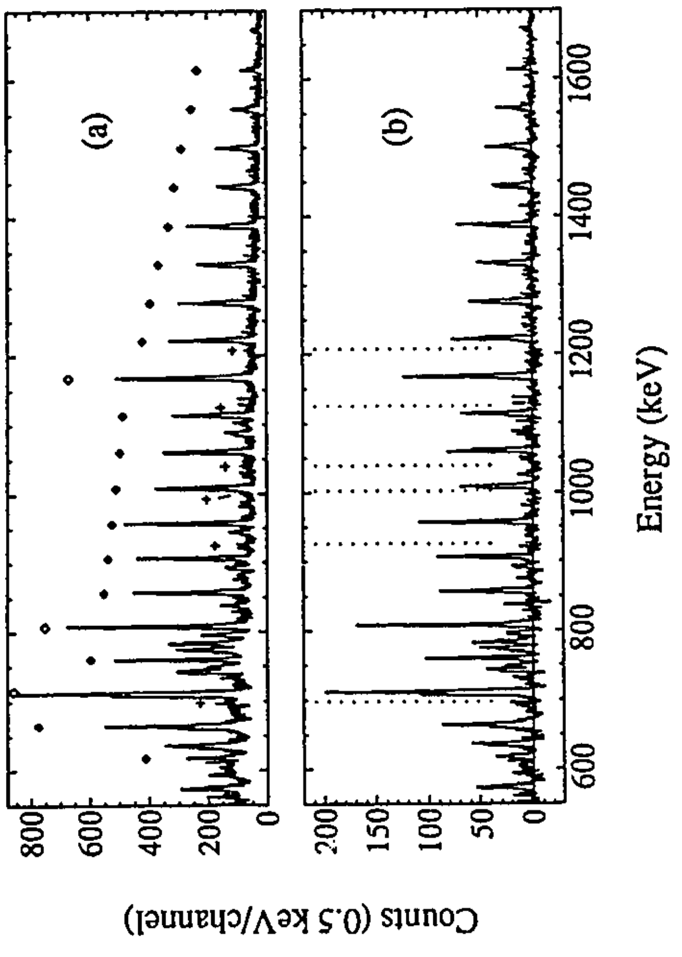

Figure B.3.2:

Partial γ-ray spectra of ^{149}Gd yrast SD band obtained from EUROGAM phase 2 commissioning run quadruple-coincidence data by setting ordered, non-diagonal quadruple gates on members of band. (a), unsubtracted spectrum $F_i^{(4)}$. (b), fully subtracted spectrum $^*F_i^{(4)}$.

Appendix C.
SD Search Algorithm

Two closely-related algorithms were used to search for SD bands, SD-SLICE [JW 88] on 8π γ^2 data and ANDBAND (see [HHW 94] for a more detailed discussion) on GAMMASPHERE γ^3 and γ^4 data. Both algorithms are based on the principle that, in a sum-of-gates spectrum of an SD band:

- there will be peaks at each gating location;
- the peaks will have the roughly the same (preferably large) number of counts in them.

First, a set of n arbitrary gates $(x_1, x_2 \ldots x_n)$ comprising part of a *candidate band* is selected, and a background-subtracted sum-of-gates spectrum $\mathcal{F}_i^k$ is generated, where k is the gating fold. Then the number of counts in each gate is evaluated, $C_j = \sum_{i \in x_j} \mathcal{F}_i^k$. One measure of the quality of the band, of course, is the average number of counts in the expected peak locations. This does not by itself identify a good candidate for a band, since a spectrum with one large peak in one of the gating locations would give a large number as would a real band. One method for discriminating against such an unbalanced distribution of counts is to require that the geometrical mean and the arithmetic mean are nearly the same, that is,

$$Q \equiv \frac{(|C_1 \times C_2 \times \ldots \times C_n|)^{1/n}}{(1/n) \cdot (C_1 + C_2 + \ldots + C_n)} \simeq 1. \qquad (C.1)$$

If only a small subset of C_i is large, then the figure of merit Q will tend to be much smaller than 1, while if all C_i's are approximately the same, Q will approach unity. "Good" candidates are those with $(1 - Q) \leq \delta Q$, where δQ is some threshold on the figure of merit. This method for screening candidate bands was first reported in [Joh 89].

The inputs to SDSLICE are a number of transitions n, a range of constant γ–ray spacings ΔE, a minimum starting energy E_0, a gate width w, and a background spectrum $\mathcal{B}$. A single candidate band is defined by the union of gate sets x_i which included all channels from $E_i - \frac{w}{2}$ to $E_i + \frac{w}{2}$, with

$$E_i = E_0 + E_0' + (i-1)\,\Delta E, \tag{C.2}$$

where $0 \leq E_0' < \Delta E$. In essence, the range of ΔE defines a range of possible $\mathcal{J}^{(2)}$ values, while the variation of E_0' over the given range is equivalent to a variation of possible Δi_x values in an interval of $2\hbar$.

In practice, SDSLICE takes finite steps through the ranges of ΔE and E_0'. The sum of gates spectrum $F^{(1)}$ is then generated from a γ–γ matrix, Rather than consider the full background-subtraction method, the spectrum $\mathcal{F}^{(1)}$ is simply given by $\mathcal{F}^{(1)} = F^{(1)} - k\mathcal{B}$, where k is calculated such that the total number of counts in spectrum $\mathcal{F}_i^{(1)}$ is zero. Such a procedure inevitably gives an oversubtracted spectrum. For a legitimate band, this would only result in a lower value of the average number of counts in each peak, and to first order the figure of merit Q would be unaffected. In the 8π experiments described in Chapter 4, SDSLICE was run with typical values of $n = 5$ or 6, 50 keV$< \Delta E <$70 keV, E_0 between 500 and 900 keV, $w \sim 5$ keV, and $\mathcal{B}$ taken as the total projection of the relevant matrix.

In higher-fold coincidence data, both the generation of candidate bands and the problem of background subtraction are more complicated. Here the case for γ^4 coincidence data will be considered. Early experience with high-fold data from third-generation arrays showed that a believable (although not strictly correct) background subtraction of a k-fold sum-of-gates spectrum could be approximated by subtracting a fraction of the $(k-1)$-fold sum-of-gates spectrum. For example, a subtracted triple-gated SD spectrum $\mathcal{F}^{(3)}$ can made by subtracting a fraction of the double-gated spectrum $F^{(2)}$ from the triple-gated spectrum $F^{(3)}$ so that the channels with no obvious peaks have, on average, zero counts. This corresponds to the first two lines of Eq. (B.2.13) with arbitrary normalization. In the γ^4 version of

ANDBAND, "pseudo-spectra" are generated where, rather than incrementing two real spectra, events which satisfy the appropriate gating conditions are histogramed directly into peak bins C_i^g or background bins B^g, where $g = 2$ or 3 for the double- or triple-gated pseudo-spectra. Then a normalization factor $k = B^3/B^2$ is used to correct the gate bins, $C_i = C_i^3 - kC_i^2$. This requires 2(n+1) storage locations per candidate band, rather than typically 10^3 locations each for the triple- and double-gated spectra.

Minimizing storage per candidate band is essential because in high-fold data you need to consider more candidate bands. Consider a set of gates (1) on a band, where each gate is centred exactly at the peak location and which covers the full width of each peak. A second set of gates, $(1')$, can be made by displacing each gate by exactly one half of the peak width. In γ^2 coincidence data, a sum-of-displaced-gates spectrum $\mathcal{F}^{(1')}$ would have exactly half as many counts in each peak as in the sum-of-centred-gates spectrum $\mathcal{F}^{(1)}$. Furthermore the gate itself only includes half of whatever peak is there, so the total number of counts in a gate which goes into evaluating the figure of merit Q is only 1/4 of that in the properly centred gates. In $(n-1)$-fold gating on γ^n coincidence data, the number of counts would go as $(0.5)^n$, so there would only be $1/16^{\text{th}}$ as many counts in the gates of a sum of shifted triple-gates spectrum $\mathcal{F}^{(3')}$ as in the centred gates $\mathcal{F}^{(3)}$. This example demonstrates that a high-fold search algorithm will be less tolerant of "near-misses" than a low-fold search. Having said that, a lower-fold search would not exploit the maximum sensitivity of a third-generation spectrometer. Therefore a more thorough search must be performed. First of all, the steps in ΔE and E_0' must be smaller. Furthermore, since many bands (*e.g.* the gadolinium isotopes) have $\mathcal{J}^{(2)}$ values which vary smoothly with ω, this must be reflected by allowing ΔE to change with i as well. In the ANDBAND code, a candidate band is defined by

$$E_1 = E_0 + E_0';$$

$$E_i = E_{i-1} + \Delta E_{i-1}, \qquad i > 1,$$

where

$$\Delta E_i = \Delta E_{i-1} + \Delta^2 E, \qquad i > 1.$$

To speed up computation, each candidate band is expressed as a bit stream where bits are set corresponding to gating channels. Then the data are scanned in a list mode, and each event is encoded as a bit stream. The two bit streams are logically ANDed with each candidate band (hence the name ANDBAND). Since logical ANDs are the fastest possible digital computations, this provides a quick check of how many gates are satisfied in a given event before incrementing the pseudo-spectra.

Appendix D.

8π *vs.* GAMMASPHERE: Sensitivity

The sensitivity of a detection apparatus can be considered as the smallest measurable decay branch which occurs for some fraction α of all reactions, *e.g.* a particular γ ray or cascade of γ rays. This will involve not only the rate of detection of γ rays but also their quality (P/T, FWHM etc.) The GAMMASPHERE array is substantially more sensitive that the 8π array. The question is how much more sensitive is GAMMASPHERE than the 8π, and how one best exploits this increased sensitivity. Naturally this will depend on the exact nature of the experiment, so we will consider only those experiments which involve fusion-evaporation reactions employed to study high-spin behavior where the residual nucleus recoils out of a self-supporting target.

Aside from monetary constraints, the two most fundamental variables in the design of a modern γ-ray spectrometer array are the distance of the HPGe detectors from the target position and the total coverage of the 4π solid angle. If a detector has an absolute photopeak detection efficiency of ϵ and is positioned to subtend a solid angle Ω as seen from the target position, then an array of N such detectors will have a total photopeak detection efficiency of $N\epsilon\Omega$. The efficiency for k-fold coincidences then is $(N\epsilon\Omega)^k$. From this relationship alone, it would seem that efficiency and hence sensitivity of the array increases when the solid angle is maximized, that is, when the detectors are mounted close to the target. As the detectors move in closer, however, there are a number of effects which degrade the quality of the detected γ rays:

- Doppler broadening – as the opening angle of the detector increases, the difference in Doppler shift from one side of the detector to the other increases and the peaks get wider;
- Double hits – the chance of two γ rays entering the detector and giving a false measurement increases, so the overall P/T decreases;
- Compton scattering – as the HPGe crystals get closer together there is less space for the anti-Compton shields and so the suppression efficiency, and consequently the P/T, decreases.

A quantity often referred to as *gain per fold* includes this Doppler broadening degradation,

$$R = (\Delta E_\gamma/\mathrm{FWHM}) \cdot \mathrm{P/T}, \tag{D.1}$$

where ΔE_γ is the average spacing between γ rays in a typical decay path. In addition there is an R_0 which estimates the overall ability of the array to use information other than just the HPGe γ-ray energy measurements; the 8π BGO ball can be used for channel selection, and so is rated $R_0 = 3.0$, while the GAMMASPHERE coincidence electronics at best favour fusion-evaporation reactions over fusion-fission and so is rated $R_0 = 1.5$. Then the overall systematic sensitivity is $R_0 R^k$, k being the coincidence fold used in off-line analysis. The design of a new device involves balancing the overall detection efficiency $N\epsilon\Omega$ with the gain per fold R.

These concepts can be applied in analyzing the arrays used in the present work and attempting to quantify the relative sensitivity of the two instruments, The parameters for a typical experiment and for the characteristics of the arrays are taken from the analysis of Radford in the TRIGAM proposal [Dra 92]. The conditions of Radford's archetypical experiment, a 3-day high-spin study employing heavy-ion fusion-evaporation reactions, are actually very close to those in the experiments of the present work, so the degradation factors calculated in this reference for double-γ or neutron detections are appropriate as is the FWHM. A 34-detector GAMMASPHERE is considered in addition to the 110-detector final implementation. The sensitivity at a given fold is inversely proportional to the branching ratio of the weakest observable structure, *i.e.*, $S^k \propto (\alpha_{\min})^{-1}$.

One popular criterion for deeming a peak "real" is when it is above a 95% confidence level, *i.e.*, two standard deviations (2σ). When the counting rate is sufficiently high (*e.g.* at low coincidence fold), the limiting factor on sensitivity is the uncertainty in the background, and a real peak should have at least twice as many counts in it than the uncertainty in the background level. Radford estimates this uncertainty to be $\sim 5\%$. At the other limit of high-fold, the background level approaches zero, but the number of counts in the peaks rapidly falls off as well. Here the 2σ limit strictly implies that a peak is real if it has more than four counts in it. These limits were applied for the present analysis, and at intermediate folds they are added in quadrature. The *optimal fold* is the fold at which the sensitivity is highest, which implies that the statistical and systematic uncertainties are almost equal.

Table D.1 compares the sensitivity of the 8π spectrometer to GAMMASPHERE for various folds. It should be emphasized that these sensitivities are estimates which will vary with different experimental conditions. The first comparison is for the sensitivity to individual γ^k coincidences measurements. In double-coincidences, the sensitivity of the 8π is actually estimated to be superior to GAMMASPHERE largely due to channel selection from the BGO core. However in triple coincidences, the GAMMASPHERE early implementation configuration is three times as sensitive as the 8π in doubles. The full GAMMASPHERE is also shown for comparison, and at its optimal fold of 4, its sensitivity is expected to be fifteen times greater that the 8π in doubles.

This first set of sensitivities is relevant to studies where individual k-fold coincidences are the primary study tool, for example, deduction of a non-collective level scheme. For the special cases of rotational, and especially superdeformed, bands, sums of gates spectra will tend to be even more useful for high-fold coincidence data. For an N-transition band there are $n = \binom{N}{k-1}$ multiple-gated spectra.

		GAMMASPHERE	
	8π	Early	Full
No. HPGe's	20	34	110
Photopeak prob.	0.15	0.24	0.24
HPGe crystal dia. (cm)	5.3	7.1	7.1
Dist. tgt. to HPGe (cm)	25	25	25
Doppler-broad'nd FWHM (keV)	3.6	4.1	4.1
$N\epsilon\Omega$	0.007	0.034	0.110
Degraded $N\epsilon\Omega$	0.006	0.028	0.091
Basic P/T	0.55	0.68	0.68
Degraded P/T	0.46	0.58	0.58
R	7.5	8.4	8.4
"Ball" R_0	3.0	1.5	1.5
Ball efficiency	0.7	0.7	0.7
For individual k-fold coincidences:			
Doubles (S^2)	960	620	620
Triples (S^3)	540	2900	3900
Quadruples (S^4)	90	1600	13900
Quintuples (S^5)	10	590	11000
For sums of $(k-1)$-gated spectra on 15 transitions:			
Doubles (S^2)	1000	620	620
Triples (S^3)	4000	4000	4000
Quadruples (S^4)	2000	20000	26000
Quintuples (S^5)	500	21000	150000
As above, Stephens statistical limit:			
Doubles (S^2)	900	620	620
Triples (S^3)	1000	3600	4000
Quadruples (S^4)	400	6500	24000
Quintuples (S^5)	110	4300	73000

Table D.1: Comparison of 8π and GAMMASPHERE (early and full implementation) spectrometer sensitivities, parameters from [Dra 92].

Haslip [Has 94] has considered this problem in detail, but for the present purposes the naive approach will be taken of replacing the 4-count statistical limit at high fold with $4/n$. Then a peak would be declared valid if it appears with more than four counts in the sum-of-gates spectrum. The second set of sensitivities in Table D.1 were calculated for a 15-transition band, and show that for all three detector arrays under consideration, the optimal fold increases by one (possibly more for the full GAMMASPHERE). The maximum sensitivity is now a factor of 5 greater for GAMMASPHERE early implementation compared to the 8π in the optimal fold. An interesting feature of this calculation, first pointed out by [Has 94] and confirmed in this specific model, is that the optimal fold of the 8π for detecting superdeformed bands in the archetypical experiment is triple-coincidences, not double-coincidences as have been traditionally used.

The four-count-per-peak statistical limit is perhaps generous. Stephens [Ste 92] uses a 100-count limit instead in his calculations, which it may be argued is somewhat too high. However it is instructive to see that with the Stephens statistical limit, GAMMASPHERE early implementation is still roughly six to seven times more sensitive than the 8π for sums-of-gates studies. Also the difference between doubles and triples for the 8π and between triples and quadruples in GAMMASPHERE are less dramatic. For the GAMMASPHERE estimates this is certainly consistent with the current results.

Appendix E.
Intensity Measurements

Measurement of the intensity of superdeformed bands is not always straightforward. In γ–γ coincidence data, it is complicated by poor statistics and risk of contamination in the γ–ray peaks. In high-fold data, the only useful spectra are sums-of-gates spectra, so care must be taken to properly account for the way in which sums-of-gates are taken. In this Appendix, a model for the intensity of the γ–ray decay of SD bands is proposed. All intensities reported in this thesis were based on this model, and further details of its application are also presented.

E.1 Model SD Band Intensity Profile

The intensity of the γ rays in SD bands is characterized by a profile with three distinct regions as shown in Figure E.1. At very high spin, the intensity increases monotonically as spin and γ–ray energy decrease. This is the feed-in region, where the decay from non-yrast states to the SD states competes with decays to non-collective or less-deformed states. The probability of populating a given SD state is the sum of the probability populating higher-spin SD states plus the probability of a quasi-continuum to SD transition, so the intensity of the γ rays which then de-excite the given state rises. Eventually the SD states are far enough above the non-SD states that the level density of the latter states reduces the probability of a decay from quasi-continuum to SD to almost zero. The γ-ray intensity remains constant in the plateau region. At low spin, the transition rate out of the band begins to compete with in-band transitions, so the intensity of subsequent γ rays at lower spin decreases. In the present model it will be assumed ratio of feeding of an SD state from the next higher-spin SD states to total feeding

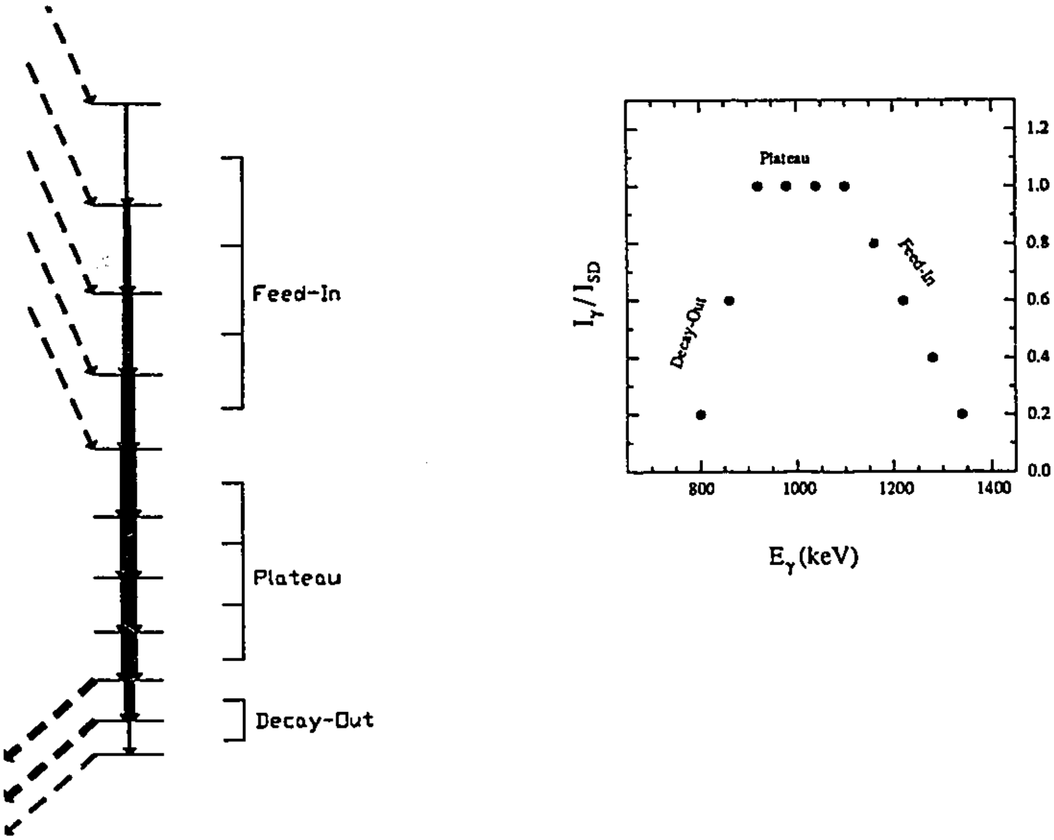

Figure E.1: Schematic of intensity profile for the γ–ray decay of an SD band, showing the states and γ–ray intensities associated with feed-in, plateau, and decay-out regions. Widths of arrows indicate γ-ray intensity, vertical scale is level energy.

is < 1 *only* in the feed-in region. Furthermore it is assumed that the branching ratio for decay from one SD state to another SD state is 1 everywhere *except* in the decay-out region.

If a total of N fusion-evaporation events in a given nucleus resulted in N_{SD} events where SD states were populated, then the intensity of the band is simply $I_{\mathrm{SD}} = N_{\mathrm{SD}}/N$. Since the γ–ray cascade from these events must proceed through the plateau region, N_{SD} of each of the γ rays of that region are *emitted* but not necessarily detected. The intensity of the γ rays in the plateau is exactly the cross-section for population of SD states relative to fusion-evaporation reactions in that channel. In the discussion which follows, the intensity of SD population I_{SD} will be the only one which is directly related to the branching ratio of SD transitions *vs.* total fusion-evaporation. Individual γ-ray intensities will be expressed then in terms of a relative intensity, $I_i = N_{E_{\gamma i}}/N_{\text{SD}} \equiv N_i/N_{\text{SD}}$. In the plateau region, $I_i = 1$.

The coincidence intensity is a little bit more complicated. Consider a state which is fed by γ rays i and j, and then decay-out by γ rays k and l. To conserve the flux into and out of the state (intensity balance),

$$(I_i + I_j) = (I_k + I_l) \equiv I_J$$

where I_J is, essentially, the population intensity of state J. Also, all intensities must be zero or positive. The I_{ik} coincidence intensity, for example, will be a product of the branching-in and branching-out ratios by these transitions,

$$I_{ik} = \left(\frac{I_i}{I_i + I_j}\right) \cdot \left(\frac{I_k}{I_k + I_l}\right) \cdot I_J$$

In the present model, i and k will be taken as the in-band transitions, and j and l are the feeding or decay-out transitions, respectively. The decay-out intensity I_l is non-zero only in the decay-out region, similarly I_j is zero everywhere except in the feed-in region; in the plateau, $I_l = I_j = 0$. These conditions mean that the branching-out ratio is zero, except in the decay-out regime.

If one considers coincidence emissions where the γ–ray i associated with the highest spin was in the feed-in region, then one has defined a decay path which incorporates $N_i = I_i \cdot N_{\text{SD}}$ of all events. According to the model, the decay from one such state can only proceed to another SD state through the rest of the feed-in region and into the plateau. Thus there will be $N_{ik} = I_i \cdot N_{\text{SD}}$ subsequent emissions of γ ray k where k is in the feed-in or plateau below i. It can be shown quite easily that this expression applies for i in the plateau as well, remembering that $I_i = 1$ in the plateau. Beyond the plateau, the intensity of γ ray k' essentially measures how much of the decay has not branched out relative to the lowest plateau transition, so the total number of coincidences when i is in the plateau or feed-in region is

$N_{ik'} = I_i \cdot I_{k'} \cdot N_{\text{SD}}$. If both i' and k' are in the decay-out regime, only the latter is relevant; independent of i', there are $N_{k'} = I_{k'} \cdot N_{\text{SD}}$ emissions of γ ray k', and since all decays through k' must first proceed through i', $N_{i'k'} = I_{k'} \cdot N_{\text{SD}}$.

Therefore, if i is a transition at higher spin than k, and I_i and I_k are their respective relative singles intensities, the relative coincidence intensities are:

- if i is a feed-in γ ray and k is a decay-out γ ray, $I_{ik} = I_i \cdot I_k$;
- if i is a feed-in γ ray and k is it not a decay-out γ ray, $I_{ik} = I_i$;
- if i is *not* a feed-in γ ray and k is a decay-out γ ray, $I_{ik} = I_k$;
- otherwise, $I_{ik} = 1$.

The default condition only applies to plateau-plateau coincidences. It should be noted that even for triple-coincidence intensities I_{ijk} or higher-fold coincidences, the coincidence intensity depends only on the singles intensities of the top and bottom γ rays. Taking into account the energy-dependent photopeak efficiency ϵ, the total number of counts in a given photopeak triple-coincidence $N_{ijk}(i > j > k)$, expressed in terms of the total population of the residual nucleus, is

$$N_{ijk} = N \cdot I_{\text{SD}} \cdot I_{ik} \cdot \epsilon_i \epsilon_j \epsilon_k.$$

E.2 Implementation

In the double-coincidence data from the 8π spectrometer, application of this method is straightforward if a suitable plateau region $\mathcal{P}$ can be established. The number of counts in peak i in gate j, where $j \neq i$, is $N_{ij} = N \cdot I_{\text{SD}} \cdot \epsilon_i \epsilon_j$. In a sum-of-gates spectrum on the plateau $\mathcal{P}$, the total number of counts in all of the peaks is

$$\begin{aligned} N_{\mathcal{P}} &= \sum_{i \in \mathcal{P}} \sum_{j \in \mathcal{P}}^{i \neq j} (N \cdot I_{\text{SD}} \cdot \epsilon_i \epsilon_j) \\ &= (N \cdot I_{\text{SD}}) \cdot \left(\sum_{i \in \mathcal{P}} \sum_{j \in \mathcal{P}}^{i \neq j} \cdot \epsilon_i \epsilon_j \right) \\ &= (N \cdot I_{\text{SD}}) \cdot \mathcal{E}_{\mathcal{P}}, \end{aligned} \tag{E.1}$$

where the sum over efficiencies has been conveniently expressed as a single factor $\mathcal{E}_{\mathcal{P}}$. Since the double-coincidence intensity of any peak i with a plateau peak just reduces to $I_{i\mathcal{P}} = I_i$, the number of counts in peak i of the sum-of-gates spectrum is

$$\begin{aligned} N_i =& \sum_{j\in\mathcal{P}} (N \cdot I_{\mathrm{SD}} \cdot I_i \epsilon_i \epsilon_j) \\ =& I_i \cdot (N \cdot I_{\mathrm{SD}}) \cdot \sum_{j\in\mathcal{P}} \epsilon_i \epsilon_j \end{aligned}$$

and the intensity of that peak I_i can be calculated by substituting for $(N \cdot I_{\mathrm{SD}})$ from Eq. (E.1),

$$I_i = \frac{N_i}{\sum_{j\in\mathcal{P}} \epsilon_i \epsilon_j} \cdot \frac{\mathcal{E}_{\mathcal{P}}}{N_{\mathcal{P}}}.$$

The total number of reactions N can be calculated from low-spin transition coincidences, taking into account efficiencies and, as in the case of ^{142}Eu, attenuation of the coincidence intensity due to isomers. Then

$$I_{\mathrm{SD}} = \frac{N}{\left(\sum_{i\in\mathcal{P}} \sum_{j\in\mathcal{P}}^{i\neq j} \cdot \epsilon_i \epsilon_j\right)}.$$

For higher-fold data, the first step was to establish an intensity function which is consistent with the proposed decay model. Specifically, the intensity I_i of the i^{th} transition in an n-transition band was modeled by ramp functions in the feed-in and decay-out regions and unity in the plateau. This function ${}^{*}I(i)$ of transition number i has four parameters for the boundaries of the three regions. Although it would be possible to fit these parameters to the number of counts in individual triple-coincidences, it was more convenient to work with the sum of spectra from the clean double-gate list $\mathcal{G}$. For a given peak i, the double-coincidence intensities ${}^{*}I_{ij}$ were calculated from the trial intensity function ${}^{*}I(i)$ and the number of counts in peak i was calculated as

$${}^{*}N_i = (NI) \sum_{jk\in G}^{i\neq j,k} {}^{*}I_{[ijk]} \epsilon_i \epsilon_j \epsilon_k,$$

where ${}^*I_{[ijk]}$ is actually the double-coincidence intensity of the upper and lower transitions of the triple-coincidence set. For example, if $i < j < k$, then ${}^*I_{[ijk]} = {}^*I_{ik}$. The normalization factor (NI) was then chosen so that the sum of counts in the calculated spectrum $\sum_i {}^*N_i$ equaled the number of counts in the observed spectrum $\sum_i N_i$. The parameters demarcating the three regions were then adjusted by an interactive program to find a least-squares fit of ${}^*N_i$ to N_i. The actual intensities I_i were then measured from sums-of-gates spectra based on this proposed intensity function ${}^*I(i)$,

$$I_i = {}^*I\,(i) \cdot \frac{N_i}{{}^*N_i}.$$

The ratio of intensities of two bands A and B could also be evaluated,

$$\frac{I_{\mathrm{SD,A}}}{I_{\mathrm{SD,B}}} = \frac{\frac{\sum_i {}^*N_{i,\mathrm{A}}}{\mathcal{E}_\mathrm{A}}}{\frac{\sum_i {}^*N_{i,\mathrm{B}}}{\mathcal{E}_\mathrm{B}}}, \tag{E.2}$$

where the efficiency and intensity correction factor

$$\mathcal{E}_\mathrm{X} = \sum_{i\in X} \sum_{jk\in\mathcal{G}_\mathrm{X}}^{i\neq j,k} {}^*I^{\mathrm{X}}_{[ijk]}\epsilon_i\epsilon_j\epsilon_k$$

is evaluated separately for bands A and B.

Appendix F.
Symbols

α	Signature (exponential) (Eq. (2.3.21))
$\alpha_{\lambda\mu}$	Spherical harmonic coefficient (Sect. 2.1.1)
β	Quadrupole deformation (Sect. 2.1.1)
γ	Quadrupole deformation (Sect. 2.1.1)
Γ	Self-consistent mean field (Eq. (2.2.18))
	Transition width (Eq. (2.6.4))
Δ	Pairing gap (Sect. 2.4)
ϵ	Nilsson deformation parameter (Sect. 2.2.1)
ϵ_k	Single-particle energy (Sect. 2.2.4)
	Detector efficiency (App. D,E)
ϕ_i	Smooth background function (Eq. (B.1.2))
$\|\phi\rangle$	Single-particle wave function, HF basis (Sect. 2.2.4)
Φ_i	Smooth background operator (Eq. (B.1.11))
Λ	$\vec{l}$ projection onto 3-axis (Figure 2.1.2)
ν	Neutron particle, hole or quasi-particle
π	Proton particle, hole or quasi-particle
	Parity
ρ_{ij}	HF density matrix (Sect. 2.2.4)
Σ	$\vec{s}$ projection onto 3-axis (Figure 2.1.2)
τ	Isospin (Sect. 2.2.4)
	Transition mean lifetime (Eq. (2.6.4))
$\|\chi\rangle$	Single-particle trial wave function (Sect. 2.2.4)
Ξ	Nuclear surface (Sect. 2.2.2)

ω	Rotational frequency (Sect. 2.3)
Ω	$\vec{j}$ projection onto 3-axis (Figure 2.1.2)

a	Decoupling parameter (Eq. (2.1.12))
a_{asymp}	Decoupling parameter in asymptotic limit (Eq. (2.5.1))
$\tilde{a}_{\text{asymp}}$	Decoupling parameter, pseudo-spin asymptotic limit (Sect. 2.5)
A	Nuclear mass number ($N + Z$)
b_{nom}	Nominal ADC gain (Sect. 3.4.1)
e	Generic single-particle energy (Sect. 2.4)
E	Generic energy
E^*	Excitation energy
$\mathcal{F}$	Gate-corrected data set (App. B)
$^*F$	Fully-subtracted data set (App. B)
$g(e)$	Level density (Sect. 2.2.3)
h	Generic single-particle Hamiltonian (Chap. 2)
H	Generic Hamiltonian (Chap. 2)
	BGO sum-energy (Chaps. 3,4)
i_x	Aligned spin (Eq. (2.3.18))
Δi_x	Incremental alignment (Eq. (2.3.28))
I	Angular momentum in a rotational model (Chap. 2,5)
I or I_γ	Intensity (Chap. 4, Appendix E)
I_0	Plateau or other reference intensity
I_x	Projection of $\vec{I}$ on cranking axis (Eq. (2.3.12c))
J	Angular momentum of a physical state (Chaps. 2,4,5)
J_0	Spin of final state of lowest-lying γ ray in band (Chaps. 4,5)
$\mathcal{J}$	Generic rotational inertial parameter
$\mathcal{J}^{(1)}$	Kinetic moment of inertia (Eq. (2.3.26))
$\mathcal{J}^{(2)}$	Dynamic moment of inertia (Eq. (2.3.27))

K	Projection of $\vec{I}$ onto 3-axis (Figure 2.1.2)
	BGO multiplicity (Chaps. 3,4)
l_{max}	Maximum heavy-ion reaction input angular momentum (Eq. (2.6.1))
n_z	Oscillator quanta along symmetry axis (Sect. 2.2.1)
N	Neutron number
N_{osc}	Major oscillator shell number (Sect. 2.2.1)
$N\epsilon\Omega$	Array photopeak detection efficiency (Appendix D)
P/T	Peak to total ratio (Sect. 3.1.1)
r	Signature (eigenvalue) (Eq. (2.3.20))
r_0	Phenomenological nucleon radius ($\sim$ 1.3 fm)
$\hat{r}$	Single-particle Routhian operator (Eq. (2.3.9))
R	Sensitivity gain per fold (Appendix D)
R_0	Spherical nuclear radius ($= A^{1/3}r_0$)
	Ball sensitivity (App. D)
$\hat{R}$	Routhian operator (Eq. (2.3.10))
$\vec{R}$	Collective rotational angular momentum (Figure 2.1.2)
S^k	Sensitivity for γ^k coincidences (Appendix D)
t_{ij}	Kinetic energy matrix element (Sect. 2.2.4)
$\bar{v}_{ijkl}$	Two-body interaction matrix element (Sect. 2.2.4)
Z	Proton number

References

[AFN 90] S. Åberg, H. Flocard and W. Nazarewicz, Ann. Rev. Nuc. Part. Sci. **40**, 439 (1990).

[AHS 69] A. Arima, M. Harvey and K. Shimizu, Phys. Lett. **B30**, 517 (1969).

[And 76] G. Andersson, S.E. Larsson, G. Leander, P. Möller, S.G. Nilsson, I. Ragnarsson, S. Åberg, R. Bengtsson, J. Dudek, B. Nerlo-Pomorska, K. Pomorski, and Z. Szymański, Nucl. Phys. **A268**, 205 (1919).

[Ata 93] A. Ataç, M. Piiparinen, B. Herskind, J. Nyberg, G. Sletten, G. de Angelis, S. Forbes, N. Gjørup, G. Hagemann, F. Ingebretsen, H. Jensen, D. Jerrestam, H. Kusakari, R.M. Lieder, G.M. Marti, S. Mullins, D. Santonocito, H. Schnare, K. Strahle, M. Sugawara, P.O. Tjøm, A. Virtanen and R. Wadsworth, Phys. Rev. Lett. **70**, 1069 (1993).

[Ata 94] A. Ataç, S. Petzold, J. Nyberg, M. Piiparinen, C. Rossi Alvarez, G. de Angelis, D. de Acuna, R.A. Bark, D. Bazzacco, G. Lo Bianco, R. Burch, A. Buscemi, B. Herskind, S. Leoni, S. Lunardi, G. Maron, B. Million, D. Napoli, M. de Poli, X. Rico, G. Sletten and G. Vedovato, Z. Phys. **A348**, 251 (1994).

[Bar 82] J. Bartel, P. Quentin, M. Brack, C. Guet and H.B. Håkansson, Nucl. Phys. **A386**, 79 (1992).

[Baz 80] D. Bazzacco, A.M.I. Haque, K.O. Zell, P. von Brentano and C. Protop, Phys. Rev. C **21**, 222 (1980).

[BCS 57] J. Bardeen, L.N. Cooper, and J.R. Schreiffer, Phys. Rev. **108**, 1175 (1957).

[Bea 93] C.W. Beausang, P. Fallon, S. Clarke, F.A. Beck, Th. Byrski, D. Curien, P.J. Dagnall, G. deFrance, G. Duchêne, P.D. Forsythe, B. Haas, M.J. Joyce, A.O. Machiavelli, E.S. Paul, J.F. Sharpey-Schafer, J. Simpson, P.J. Twin and J.P. Viven, Phys. Rev. Lett. **71**, 1800 (1993).

[Ben 75] R. Bengtsson, S.E. Larsson, G. Leander, P. Möller, S.G. Nilsson, S. Åberg and Z. Szymański, Phys. Lett. **B57**, 301 (1975).

[Ben 81] T. Bengtsson, M.E. Faber, G. Leander, P. Möller, M. Ploszajczak, I. Ragnarsson and S. Åberg, Physica Scripta **24**, 200 (1981).

[BF 79] R. Bengtsson and S. Frauendorf, Nucl. Phys. **A327**, 139 (1979).

[BFH 87] P. Bonche, H. Flocard and P.-H. Heenen, Nucl. Phys. **A467**, (1987).

[BFH 91] P. Bonche, H. Flocard and P.-H. Heenen, Nucl. Phys. **A523**, 300 (1991).

[BHM 82] A. Bohr, I. Hamamoto and Ben R. Mottelson, Physica Scripta **26**, 267 (1982).

[Biz 90] A.M. Bizetti-Sona, P.G. Bizetti, F. Banci Buonamici, D. Bazzacco, S. Lunardi, F. Soramel, G. Lo Bianco, N. Molho, G. De Angelis and J. Simpson, Z. Phys. **A337**, 235 (1990).

[BM 75] A. Bohr and B. Mottelson, *Nuclear Structure*, Benjamin, New York, 1975, Vol. 2.

[BMP 58] A. Bohr, B. Mottelson, and D. Pines, Phys. Rev. **110**, 936 (1958).

[Bog 58] N.N. Bogolyubov, Nuovo Cimento Series 10 **7**, 794 (1958).

[Bro 85] D.A. Bromley, *Proceedings of the Fourth International Conference on Clustering Aspects of Nuclear Structure and Nuclear Reactions* (J.S. Lilley and M.A. Nagarajan, eds.), Reidel, Dordrecht, p. 1 (1985).

[Byr 90] Th. Byrski, F.A. Beck, D. Curien, C. Schuck, P. Fallon, A. Alderson, I. Ali, M.A. Bentley, A.M. Bruce, P.D. Forsyth, D. Howe, J.W. Roberts, J.F. Sharpey-Schafer, G. Smith and P.J. Twin, Phys. Rev. Lett. **64**, 1650 (1990).

[Cam 94] J.A. Cameron, M.A. Bentley, A.M. Bruce, R.A. Cunningham, W. Gelletly, H.G. Price, J. Simpson, D.D. Warner and A.N. James, Phys. Rev. C **49**, 1347 (1994).

[Car 91] M.A. Cardona, G. de Angelis, D. Bazzacco, M. De Poli and S. Lunardi, Z. Phys. **A340**, 346 (1991).

[Cas 90] R.F. Casten, *Nuclear Structure from a Simple Perspective*, Oxford University Press, New York (1990).

[Cur 95] D. Curien, G. de. France, C.W. Beausang, F.A. Beck, T. Byrski, S. Clarke, P. Dagnall, G. Duchêne, S. Flibotte, S. Forbes, P.D. Forsythe, B. Haas, M.A. Joyce, B. Kharraja, B.M. Nyakó, C. Schück, J. Simpson, C. Theisen, P.J. Twin, J.P. Vivien and L. Zolnai, Phys. Rev. Lett. **71**, 2559 (1993).

[Dag 95] P.J. Dagnall, C.W. Beausang, P.J. Twin, M.A. Bentley, F.A. Beck, Th. Byrski, S. Clarke, D. Curien, G. Duchene, G. de France, P.D. Forsythe, B. Haas, J.C. Lisle, E.S. Paul, J. Simpson, J. Styczen, J.P. Vivien, J.N. Wilson and K. Zuber, Phys. Lett. **B335**, 313 (1995).

[DD 88] M.A. Deleplanque and R.M. Diamond, *GAMMASPHERE* proposal, LBL-PUB-5202 (1988).

[DD 95] J. Dobaczewski and J. Dudek, submitted to *Computer Physics Communications.*

[DeA 95] G. de Angelis, D. Bazzacco, W. Gast, A. Georgiev, H.M. Jager, R.M. Lieder, S. Lunardi, R. Menegazzo, G. Rossi-Alvarez, T. Rzaca-Urban and S.Uzelmann, Julich Annual Report 1995, 109 (1995).

[DeA 95] G. de Angelis, *Conference on Physics from Large γ-ray Detector Arrays* vol. 1 (ed. M.A. Deleplanque), LBL-35687, Berkeley, 16 (1995).

[DN 85] J. Dudek and W. Nazarewicz, Phys. Rev. **C31**, 298 (1985).

[Dra 92] T.E. Drake, J.C. Waddington, H.R. Andrews, D.C. Radford and D. Ward, *The TRIGAM Spectrometer: Gamma-Ray Spectroscopy Through the Next Decade* (1992, unpublished).

[DS 80] R.M. Diamond and F.S. Stephens, Ann. Rev. Nuc. Part. Sci **30**, 85 (1980).

[DSW 81] J. Dudek, Z. Szymański and T. Werner, Phys. Rev. C **23**, 920 (1981).

[Dud 82] J. Dudek, A. Mahjofer, W. Nazarewicz and Z. Scymański, Phys. Lett. **B112**, 1 (1982).

[EH 75] Y.A. Ellis and B. Harmatz, Nulc. Data Sheets **16**, 135 (1975).

[Eng 75] Y.M. Engel, D.M. Brink, K. Goeke, S.J. Kreiger and D. Vautherin, Nucl. Phys. **A249**, 215 (1975).

[Fal 94] P. Fallon, C.W. Beausang, S. Clarke, P.J. Twin, F.A. Beck, Th. Byrski, D. Curien, P.J. Dagnall, G. deFrance, G. Duchêne, P.D. Forsythe, B. Haas, M.J. Joyce, A.O. Machiavelli, E.S. Paul, J.F. Sharpey-Schafer, J. Simpson, J.P. Viven, S. Åberg and W. Nazarewicz, Phys. Rev. Lett. **73**, 782 (1994).

[Fli 93] S. Flibotte, H.R. Andrews, G.C. Ball, C.W. Beausang, F.A. Beck, G. Belier, T. Byrski, D. Curien, P.J. Dagnall, G. de France, D. Disdier, G. Duchêne, Ch. Finck, B. Haas, G. Hackman, D.S. Haslip, V.P. Janzen, B. Kharraja, J.C. Lisle, J.C. Merdinger, S.M. Mullins, W. Nazarewicz, D.C Radford, V. Rauch, H. Savajols, J. Styczen, Ch. Theisen, P.J. Twin, J.P. Vivien, J.C. Waddington, D. Ward, K. Zuber and S. Åberg, Phys. Rev. Lett. **71**, 4299 (1993).

[Fli 95] S. Flibotte, G. Hackman, I. Ragnarsson, Ch. Theisen, H.R. Andrews, G.C. Ball, C.W. Beausang, F.A. Beck, G. Bélier, M.A. Bentley, T. Byrski, D. Curien, G. de France, D. Disdier, G. Duchêne, B. Haas, D.S. Haslip, V.P. Janzen, P.M. Jones, S.M. Mullins, E.S. Paul, D. Prévost, D.C. Radford, V. Rauch, J.F. Smith, J. Styczen, P.J. Twin, J.P. Vivien, J.C. Waddington, D. Ward and K. Zuber, Nucl. Phys. **A584**, 373 (1995).

[Flo 95] H. Flocard, P. Bonche, P.H. Heenen, R. Mehrem and M.S. Weisss, *Conference on Physics from Large γ-ray Detector Arrays* vol. 2 (ed. M.A. Deleplanque), LBL-35687, Berkeley, 165 (1995).

[Foc 30] V.A. Fock, Z. Phys. **61**, 126 (1930).

[Fun 76] L. Funke, W. D. Fromm, H. J. Keller, R. Arlt, and P. M. Gopytsch, Nucl. Phys. **A274**, 61 (1976).

[Gal 94] A. Galindo-Uribarri, D. Ward, T. Drake, G. Hackman, V.P. Janzen, S.M. Mullins, S. Pilotte, D.C. Radford, I. Ragnarsson, N.C. Schmeing and J.C. Waddington, Phys. Rev. C **50**, R2655 (1994).

[GDC 89] E. Gülmez, M.W. Drigert, and J.A. Cizewski, Phys. Rev. C **39**, 1809 (1989).

[HA 69] K.T. Hecht and A. Adler, Nucl. Phys. **A137**, 129 (1969).

[Haa 88] B. Haas, P. Taras, S. Flibotte, F. Banville, J. Gascon, S. Cornoyer, S. Monaro, N. Nadon, D. Prévost J.K. Johansson, D.M. Tucker, J.C. Waddington, H.R. Andrews, G.C. Ball, D. Horn, D.C. Radford, D. Ward, C. St. Pierre and J. Dudek, Phys. Rev. Lett. **60**, 503 (1988).

[Haa 93] B. Haas, V.P. Janzen, D. Ward, H.R. Andrews, D.C. Radford, D. Prévost, J.A. Kuehner, A. Omar, J.C. Waddington, T.E. Drake, A. Galindo-Uribarri, G. Zwartz, S. Flibotte, P. Taras and I. Ragnarsson, Nucl. Phys. **A561**, 251 (1993).

[Hac 93] G. Hackman, S.M. Mullins, J.A. Kuehner, D. Prévost, J.C. Waddington, A. Galindo-Uribarri, V.P. Janzen, D.C. Radford, N. Schmeing and D. Ward, Phys. Rev. C **47**, R433 (1993).

[Hac 95] G. Hackman, R. Wadsworth, D.S. Haslip, R.M. Clark, J. Dobaczewski, J. Dudek, S. Flibotte, K. Hauschild, I.M. Hibbert, I.-Y. Lee, S.M. Mullins, A.O. Macchiavelli, S. Pilotte, A.T. Semple, I. Thorslund, J. Tiniar, P. Vaska, J.C. Waddington and L. Walker, accepted for publication in PRC , Rapid Communications (1995).

[Hae 81] D.R. Haenni, H. Beuscher, B. Bochev, T. Kutsarova, T. Morek, M. Muller-Veggian, A. Neskakis and C. Mayer-Boricke, Nucl. Phys. **A365**, 229 (1981).

[Har 28] D.R. Hartree, Proc. Camb. Phi. Soc. **24**, 89 (1928).

[Har 65] S.M. Harris, Phys. Rev. **138**, B509 (1965).

[Has 94] D.S. Haslip, private communication.

[Heb 90] G. Hebbinghaus, K. Strähle, T. Rzaca-Urban, D. Balabanski, W. Gast, R.M. Lieder, H. Schnare, W. Urban, H. Wolters, E. Ott, J. Theuerkauf, K.O. Zell, J. Eberth, P. von Brentano, D. Alber, K.H. Maier, W. Schmitz, E.M. Beck, H. Hübel, T. Bengtsson, I. Ragnarsson and S. Åberg, Phys. Lett. **B240**, 311 (1990).

[Hen 94] R.G. Henry, T. Lauritsen, T.L. Khoo, I. Ahmad, M.P. Carpenter, B. Crowell, T. Doøssing, R.V.F. Janssens, F. Hannachi, A. Korichi, C. Schuck, F. Azaiez, C.W. Beausang, R. Beraud, C. Bourgeois, R.M. Clark, I. Deloncle, J. Duprat, B. Gall, H. Hubel, M.J. Joyce, M. Kaci, Y. Lecoz, M. Meyer, E.S. Paul, N. Perrin, N. Poffe, M.G. Porquet, N. Redon, H. Sergolle, J.F. Sharpey-Schafer, J. Simpson, A.G. Smith, R. Wadsworth and P. Willsau, Phys. Rev. Lett. **73**, 777 (1994).

[HHW 94] D.S. Haslip, G. Hackman and J.C. Waddington, Nucl. Instr. and Meth. **A345**, 534 (1994).

[Hil 79] D.L. Hillis, J.D. Garrett, O. Christensen, B. Fernandez, G.B. Hagemann, B. Herskind, B.B. Back, F. Folkman, Nucl. Phys. **A325**, 216 (1979).

[Hof 56] R. Hofstadter, Rev. Mod. Phys. **28**, 214 (1956).

[HW 53] D.L. Hill and J.A. Wheeler, Phys. Rev. **89**, 1102 (1953).

[HW 95] G. Hackman and J.C. Waddington, Nucl. Instr. and Meth. **A357**, 559 (1995).

[Ing 54] D.R. Inglis, Phys. Rev. **96**, 1059 (1954).

[Jan 93] V.P. Janzen, H.R. Andrews, B. Haas, D.C. Radford, D. Ward, A. Omar, D. Prévost, M. Sawicki, P. Unrau, J.C. Waddington, T.E. Drake, A. Galindo-Urribari and R. Wyss, Phys. Rev. Lett. **70**, 1065 (1993).

[Joh 87] J.K. Johansson, M.Sc. thesis, McMaster University, Hamilton (unpublished) (1987).

[Joh 89] J.K. Johanson, H.R. Andrews, T. Bengtsson, A. Djaafri, T.E. Drake, S. Flibotte, A. Galindo-Uribarri, D. Horn, V.P. Janzen, J.A. Kuehner, S. Monaro, N. Nadon, S. Pilotte, D. Prévost, D.C. Radford, I. Ragnarsson, P. Taras, A. Tehami, J.C. Waddington, D. Ward and S. Åberg, Phys. Rev. Lett. **63**, 220 (1989).

[JRH 72] A. Johnson, H. Ryde, and S.A. Hjorth, Nucl. Phys. **A179**, 753 (1972).

[JRS 71] A. Johnson, H. Ryde, and J. Sztarkier, Phys. Lett. **34B**, 605 (1971).

[JW 88] J.K. Johansson and J.C. Waddington, private communication (1988).

[Kno 89] G.F. Knoll, *Radiation Detection and Measurement*, 2nd edn., John Wiley & Sons, New York (1989).

[Kow 74] J. Kownacki, J. Ludziejewski, S. Sujkowski, H. Arnold and H. Ryde, Nucl. Phys. **A236**, 125 (1974).

[KPW 92] J.A. Kuehner, D. Prévost and J.C. Waddington, in *International Conference Nuclear Structure at High Spin* vol. 2 (eds. D. Ward and J.C. Waddington), AECL-10613, Ottawa, 413 (1992).

[Lac 84] M. Lach, J. Styczen, R. Julin, M. Piiparinen, H. Beuscher, P. Kleinheinz and J. Blomqvist, Z. Phys. **A319**, 235 (1984).

[Lac 93] M. Lach, P. Kleinheinz, J. Blomqvist, A. Ecran, H.J Hahn, D. Wahner, R. Julin, M. Zupancic, F. Cigoroglu and G. De Angelis, Z. Phys. **A345**, 427 (1993).

[Lee 90] I.Y. Lee, Nucl. Phys. **A520**, 641c (1990).

[Lee 94] I.Y. Lee, private communication, 1994.

[LS 78] C.M. Lederer and V.S. Shirley, eds., *Table of Isotopes*, 7th. edn., John Wiley & Sons, New York (1978).

[Lun 94] S. Lunardi, D. Bazzacco, C. Rossi-Alvarez, P. Pavan, G. de Angelis, D. De Acuna, M. De Poli, G. Maron, J. Rico, O. Stuch, D. Weil, S. Utzelmann, P. Hoernes, W. Satula and R. Wyss, Phys. Rev. Lett. **72**, 1427 (1994).

[Lun 95] S. Lunardi, R. Venturelli, D. Bazzacco, C.M. Petrache, C. Rossi-Alvarez, G. de Angelis, G. Vedovato, D. Bucurescu and C. Ur, Phys. Rev. C **52**, R6 (1995).

[Mar 87] J.P. Martin, D.C. Radford, M. Beaulieu, P. Taras, D. Ward, H.R. Andrews, G. Ayotte, F.J. Sharp, J.C. Waddington, O. Häusser and J. Gascon, Nucl. Instr. and Meth. **A527**, 301 (1987).

[Moo 89] E.F. Moore, R.V.F. Janssens, R.R. Chasman, I. Ahmad, T.L. Khoo, F.L.H. Wolfs, D. Ye, K.B. Beard, U. Garg, M.W. Drigert, Ph. Benet, Z.W. Grabowski and J.A. Cizewski, Phys. Rev. Lett. **63**, 360 (1989).

[Mul 91] S.M. Mullins, R.A. Wyss, P. Fallon, T. Byrski, D. Curien, S.A. Forbes, Y.–J. He, M.S. Metcalfe, P.J. Nolan, E.S. Paul, R.J. Poynter, P.H. Regan and R. Wadsworth, Phys. Rev. Lett. **66**, 1677 (1991).

[Mul 93] S.M. Mullins, G. Hackman, A. Galindo-Uribarri, D.C. Radford, J.C. Waddington and D. Ward, Z. Phys. **A346**, 251 (1994).

[Mul 94] S.M. Mullins, N.C. Schmeing, S. Flibotte, G. Hackman, J.L. Rodriguez, J.C. Waddington, L. Yao, H.R. Andrews, A. Galindo–Uribarri, V.P. Janzen, D.C. Radford, D. Ward, J. DeGraaf, T.E. Drake, S. Pilotte and E.S. Paul, Phys. Rev. C **50**, R2261 (1994).

[Mul 95] S.M. Mullins, S. Flibotte, G. Hackman, J.L. Rodriguez, J.C. Waddington, A.V. Anasjev, I. Ragnarsson, H.R. Andrews, A. Galindo–Uribarri, V.P. Janzen, D.C. Radford, D. Ward, M. Cromaz, J. DeGraaf, T.E. Drake and S. Pilotte, Phys. Rev. C 52, 99 (1995).

[Naz 90] W. Nazarewicz, P.J. Twin, P. Fallon, and J.D. Garret, Phys. Rev. Lett. **64**, 1654 (1990).

[NBF 94] P.J. Nolan, F.A. Beck, and D.B. Fossan, Ann. Rev. Nuc. Part. Sci. 44, 561 (1994).

[Nee 75] K. Neergård and V.V. Pashkevich, Phys. Lett. **B59**, 218 (1975).

[NGT 85] P.J. Nolan, D.W. Gifford, and P.J. Twin, Nucl. Instr. and Meth. **A236**, 95 (1985).

[Nil 55] S. G. Nilsson, K. Dan. Vidensk. Selsk. Mat. Fys. Medd **16**, 1 (1955).

[Nis 95] D. Nisius, R.V.F. Janssens, P. Fallon, B. Crowell, I. Ahmad, C.W. Beausang, M.P. Carpenter, B. Cederwall, P.J. Daly, M.A. Deleplanque, R.M. Diamond, D. Gassmann, Z.W. Grabowski, R.G. Henry, T.L. Khoo, T. Lauritsen, I.Y. Lee, A.O. Machiavelli, R.H. Mayer, F.S. Stephens and P.J. Twin, Phys. Lett. **B346**, 15 (1995).

[Nol 85] P.J. Nolan, A. Kirwan, D.J.G. Love, A.H. Nelson, D.J. Unwin and P.J. Twin, J. Phys. G **11**, L17 (1985).

[NWJ 89] W. Nazarewicz, R. A. Wyss, and A. Johnson, Nucl. Phys. **A503**, 285 (1989).

[Nya 84] B.M. Nyakó, J.R. Creswell, P.D. Forsyth, D. Howe, P.J. Nolan, M.A. Riley, J.F. Sharpey-Schafer, J. Simpson, N.J. Ward and P.J. Twin, Phys. Rev. Lett. **52**, 507 (1984).

[Ott 94] E. Ott, M. Schimmer, R. Wirowski, H. Wolters, I. Jansen, A. von der Werth, A. Dewand and P. von Brentano, Z. Phys. **A348**, 57 (1994).

[Pal 95] G. Palameta, private communication.

[PB 75] M.A. Preston and R.K. Bhaduri, *Structure of the Nucleus*, Addison-Wesley, Reading (1975).

[Pii 91] M. Piiparinen, Y. Nagai, P. Kleinheinz, M.C. Bosca, B. Rubio, M. Lach and J. Blomqvist, Z. Phys. **A338**, 417 (1991).

[Pii 92] M. Piiparinen, A. Ataç, G. De Angelis, S. Forbes, N. Gjorup, G. Hagemann, B. Herskind, F. Ingebretsen, H. Jensen, D. Jerrestam, H. Kusakari, R. Lieder, G.M. Marti, S.M. Mullins, J. Nyberg, D. Santonocito, H. Schnare, G. Sletten, K. Strahle, M. Sugawara, P.O. Tjom, A. Virtanen and R. Wadsworth, Z. Phys. **A343**, 367 (1992).

[Pii 95a] M. Piiparinen, private communication.

[Pii 95b] M. Piiparinen, A. Ataç, S.J Freeman, R. Julin, S. Juutinen, A. Lampinen, T. Lönnroth, D. Muller, J. Nyberg, G. Sletten, P. Tikkanen, S. Törmänen, A. Virtannen, C.T. Zhang and R. Wyss, Phys. Rev. C **52**, R1 (1995).

[Pol 62] S.M. Polikanov, V.A. Druin, V.A. Karnaukhov, V.L. Mikheev, A.A. Pleve, N.K. Skobelev, V.G. Subbotin, G.M. Ter-Akop'yan and V.A. Fomichev, Sov. Phys. JETP **15**, 1016 (1962).

[Pre 92] D. Prévost, private communication.

[PW 85] G. Palameta and J. C. Waddington, Nucl. Instr. and Meth. **A234**, 476 (1985).

[Rad 85] D.C. Radford, private communication..

[Rad 95a] D.C. Radford, TASCC preprint TASCC-P-94-29 (unpublished).

[Rad 95b] D.C. Radford, TASCC preprint TASCC-P-94-28 (unpublished).

[Rag 93a] I. Ragnarsson, Nucl. Phys. **A520**, 67c (1990).

[Rag 93b] I. Ragnarsson, private communication..

[RS 80] P. Ring and P. Schuck, *The Nuclear Many-Body Problem*, Springer-Verlag, New York, 1980.

[Rza 91] T. Rzaca-Urban, K. Strähle, G. Hebbinghaus, D. Balabanski, W. Gast, R.M. Lieder, H. Schnare, W. Urban, P. von Brentano, A. Dewald, J. Eberth, E. Ott, J. Theuerkauf, H. Wolters, K.O. Zell, D. Alber, K.H. Maier, E.M. Beck, H. Hübel and W. Schmitz, Z. Phys. **A339**, 421 (1991).

[Sch 87] Y. Schutz, C. Baktash, I.Y. Lee, M.L. Halbert, D.C. Hensley, N.R. Johnson, M. Oshima, R. Ribas, J.C. Lisle, L. Adler, K. Honkanen, D.G. Sarantities, A.J. Larabee and J.X. Saladin, Phys. Rev. C **35**, 384 (1987)..

[Sky 56] T.H.R. Skyrme, Phil. Mag. **1**, 1043 (1956).

[Sky 59] T.H.R. Skyrme, Nucl. Phys. **9**, 615 (1959).

[SRN 72] R.K. Sheline, I. Ragnarsson and S.G. Nilsson, Phys. Lett. **B41**, 115 (1972).

[SS 72] F.S. Stephens and R.S. Simon, Nucl. Phys. **A183**, 257 (1972).

[SS 88] J.F. Sharpey-Schafer and J. Simpson, Prog. Nuc. Part. Sci. **21**, 293 (1988).

[Ste 90] F.S. Stephens, Nucl. Phys. **A520**, 91c (1990).

[Ste 92] F.S. Stephens, Proceedings of the Int. Conf. on Nuclear Structure at High Spin, Ottawa (May 1992, unpublished).

[Str 67] V.M. Strutinski,Nucl. Phys. **A95**, 428 (1967).

[Str 68] V.M. Strutinsky, Nucl. Phys. **A122**, 1 (1968).

[Szy 83] Z. Szymański, *Fast Nuclear Rotation*, Clarendon Press, Oxford, 1983.

[Tar 83] P. Taras, J.C. Waddington, H.R. Andrews and D. Ward, *The 8π Spectrometer* (proposal) (1983).

[Tar 88] P. Taras, S. Flibotte, J. Gascon, B. Haas, S. Pilotte, D.C. Radford, D. Ward, H.R. Andrews, G.C. Ball, F. Banville, S. Cournoyer, D. Horn, J.K. Johansson, S. Monaro, N. Nadon, D. Prévost, C. Pruneau, D. Thibault, D.M. Tucker and J.C. Waddington, Phys. Rev. Lett. **61**, 1348 (1988).

[Twi 86] P.J. Twin, B.M. Nyakó, A.H. Nelson, J. Simpson, M.A. Bentley, H.W. Cramer-Gordon, P.D. Forsyth, D. Howew, A.R. Mokhtar, J.D. Morrison, J.F. Sharpey-Schafer and G. Sletten, Phys. Rev. Lett. **57**, 811 (1986).

[VB 73] D. Vautherin and D.M. Brink, Phys. Rev. C **7**, 626 (1973).

[Viv 86] J.P. Vivien, A. Nourreddine, F.A. Beck, T. Byrski, C. Gehringer, B. Haas, J.C. Merdinger, D.C. Radford, Y. Schutz, J. Dudek and W. Nazarewicz, Phys. Rev. C **33**, 2007 (1986).

[War 91] D. Ward, V.P. Janzen, H.R. Andrews, D.C. Radford, G.C. Ball, D. Horn, J.C. Waddington, J.K. Johansson, F. Banville, J. Gascon, S. Monaro, N. Nadon, S. Pilotte, D. Prévost, P. Taras and R. Wyss, Nucl. Phys. **A529**, 315 (1991).

[WD 85] R. Werner and J. Dudek, Atomic Data and Nuclear Data Tables **50**, 179 (1992).

[Wil 94] J.N. Wilson, Ph.D. thesis, University of Liverpool (unpublished) (1994).

[WS 54] R.D. Woods and D.S. Saxon, Phys. Rev. **95**, 577 (1954).

[Wys 88] R. Wyss, J. Nyberg, A. Johnson, R. Bengtsson and W. Nazarewicz, Phys. Lett. **B215**, 211 (1988).

[Xu 87] N. Xu, C.W. Beausang, E.S. Paul, W.F. Piel, Jr., P.K. Weng, D.B. Fossan, E. Gülmez and J.A. Cizewski, Phys. Rev. C **36**, 1649 (1987).

[Xu 91] N. Xu, C.W. Beausang, J.R. Hughes, Y. Liang, R. Ma, E.S. Paul, W.F. Piel, Jr., S. Shi, D.B. Fossan Phys. Rev. C **43**, 2189 (1991).

[Yam 67] T. Yamazaki, Nucl. Data **A3**, 1 (1967).